METAL PLASMONIC AS A MECHANISM TO IMPROVE THE PERFORMANCE OF THIN FILM POLYMER SOLAR CELL: DEVICE FABRICATION AND CHARACTERIZATION

Ph.D. Thesis

By

Jude Nodebechukwunso Ike

Under the supervision of

Professor Genene Tessema Mola

A thesis submitted in fulfillment of the academic requirements for a Doctor of Philosophy

In

Physics

School of Chemistry and Physics

College of Agriculture, Engineering, and Science

University of KwaZulu-Natal

Pietermaritzburg campus

South Africa

April 2024

ABSTRACT

This thesis discusses the results of the investigations on the use of plasmon metal nanoparticles (NPs) to enhance the performance of polymer solar cells, which are promising alternative solar energy converters to silicon-based solar cells. Polymer solar cells offer a cost-effective, flexible solar panel using a solution processing method for the generation of power from solar sources. Several key factors are considered to achieve this goal, including optical absorption, nano-morphology, and charge carrier mobility. The thesis focuses on investigating the potential of various dopants, such as solvent additives, thermal annealing, and metal nanoparticles (NPs), to improve the performance of thin-film organic solar cells (TFOSCs) by enhancing the charge transport processes. This research employed conventional device architectures to study the effectiveness of the active and buffer layers on charge transport and stability. The results have already been published in several internationally referred journals.

In this thesis, the synthesized metal NPs were employed as mechanisms to improve the performance of TFOSC incorporated with poly-3-hexylthiophene (P3HT) as the donor material and [6,6]-phenyl-C61-butyric acid methyl ester (PC61BM) as the acceptor material. The popular metal NPs such as nickel, (Ni), zinc (Zn), silver (Ag), calcium (Ca), sulfur (S), and cobalt (Co) were used to synthesize various bimetallic composites. Bimetallic nanoparticles such as-nickel-doped with zinc bimetallic (Ni/Zn), silver-doped with calcium (Ag/Ca), silver-doped with cobalt (Ag/Co), and silver-doped zinc sulfide (ZnS/Ag) were employed at different functional layers of solar cell structure. Hence, the study employed various spectrometers such as high-resolution transmission and scanning electron microscopy (HRTEM and HRSEM), X-ray diffraction, Ultraviolet-Visible (UV-Vis) spectroscopy to investigate the size, morphology, elemental mapping, and optical properties of synthesized metal NPs. HRTEM is indeed a powerful technique for characterizing nanoscale materials, and it can provide valuable insights for confirming the presence of core-shell structures in NPs.

Compared to the pristine reference, the blend of metal NPs with active and buffer layers at different concentrations plays a crucial role in augmenting the optical and electrical properties in TFOSC devices. Such increment of optical and electrical properties in this thesis is due to improved short-circuit current (J_{sc}), fill factors (FFs), and charge carrier mobility, which are significant to enhance the power conversion efficiency (PCE) values in the polymer solar cells. These prominent

improvements are due to the presence of localized surface plasmonic resonance (LSPR) effect of TFOSCs. Finally, this thesis provides a series of experimental works fabricated with several metal NPs in TFOSCs at different concentrations.

PREFACE

The present thesis represents research undertaken by the candidate during his tenure in the Physics Discipline, within the School of Chemistry and Physics, in the College of Agriculture, Engineering and Science, at the University of KwaZulu-Natal, Pietermaritzburg Campus. The conduct of this research was made possible by the generous financial backing of my esteemed cousin, Dr. Collins Nwokedi.

This work is unequivocally original and has not been previously submitted to any other university. Nevertheless, the findings reported here are based on the candidate's own investigative efforts, although any references to the work of other authors have been properly cited and recognized in the text.

Signature: ____ [redacted] ___ Date: April 2024

Ike Jude Nodebechukwunso (Student)

Signature:___ [redacted] Date: April 2024

Professor Genene Tessema Mola (Supervisor)

DECLARATION: PLAGIARISM

Within the pages of this thesis, lies a detailed account of the academic journey undertaken at the esteemed School of Chemistry and Physics, University of KwaZulu-Natal, Pietermaritzburg Campus. The research work, which started from January in the year 2020 to the end of December 2023, was supervised under the expert guidance of Professor Genene Tessema Mola.

"I attest that this thesis represents my original work, with proper referencing and acknowledgment of the contributions of others in this study. No part of this dissertation has been presented or submitted, in any shape or form, for any academic degree or evaluation to any other institution of higher learning."

(a) Their words have been rewritten but the general information assigned to them has been referenced to acknowledge the original source to avoid any ethical or legal issue related to plagiarism.

(b) Where their exact words have been used, their writing has been placed inside the quotation mark and reference to give credit to the original author for their insights.

(c) Where I have used the material for which the publication followed, I have exhibited the details of my role in the work.

(d) This thesis primarily consists of materials that I authored as journal articles, and presented in various formats, including oral and online presentations.

Signed (Student):__  ___ on this __ April 2024

I hereby certify that this statement is correct.

Signed (Supervisor):____  _____

Professor Genene Tessema Mola

DECLARATION: PUBLICATIONS

In this thesis, contribution to publications form part and/or include research presented in this thesis published provide details of the contributions of each author to experimental work and writing of each publication.

(1) Jude N. Ike, Mohammed S.G. Hamed, Genene Tessema Mola. Effective energy harvesting in thin-film organic solar cells using Ni/Zn as bimetallic nanoparticles. Journal of Physics and Chemistry of Solids, 161, (2022), 110405.

(2) Jude N. Ike, Mpilo Wiseman Dlamini, Ram P. Dwivedi, Yong Zhang, Genene Tessema Mola. Plasmon-assisted optical absorption and reduced charge recombination for improved device performance in polymer solar cells. Journal of Physics and Chemistry of Solids, 165, (2022), 110662.

(3) Jude N. Ike, Michael A. Adedeji, Genene Tessema Mola. Silver-doped ZnS core-shell nanocomposites to promote photon harvesting in polymer cells. Physica B: Condensed Matter, 646, (2022), 414347.

(4) Jude N. Ike, Jili Ncedo, Kumar Amit, Sharma Gaurav, Genene Tessema Mola. The impact of Ag/Co nanocomposite on organic charge transport medium for improved photocurrent in polymer solar cells. Journal of Polymer Science (2023).

In the published articles, my role was to carry out all the experimental works, analyze the data, and write the manuscripts with guidance and contributions through my supervisor (Prof. G.T. Mola). I am also indebted to the contributions of other co-authors in terms of assisting data analysis, interpretations, and editorial works.

Signed:……  ……

Date:……April 2024……..

PUBLICATIONS I HAVE CONTRIBUTED TO BUT NOT INCLUDED IN THE THESIS.

(1) Mohammed S.G. Hamed., Jude N. Ike. and Genene Tessema Mola. Plasmonic nanoparticles mediated energy harvesting in thin-film organic solar cells. Journal of Physics D: Applied Physics, 55(1), (2021) 015102. My role in this article was to fabricate solar cells, Manuscript Editing.

(2) Genene Tessema Mola, Abdalla. Y.A. Ahmed, Jude N. Ike, Ming Liu, Mohammed S.G. Hamed, and Yong Zhang. Engineering non-fullerene acceptors as a mechanism to control film morphology and energy loss in organic solar cells. Energy & Fuels, 36(9), (2022), 4691-4707. My role was to paraphrase and add more value to make the article much more attractive to read.

(3) Abdalla. Y.A. Ahmed, Jude N. Ike, Mohammed S.G. Hamed. and Mohammed S.G. Hamed. Silver decorated magnesium doped photoactive layer for improved collection of photo-generated current in polymer solar cell. Journal of Applied Polymer Science, 140(14), (2023), e53697. My role in this article was to fabricate and analyze the data.

(4) Solomon Ashagre, Abiodun Kazeem Ogundele, Jude N. Ike, Bizuneh Gebremichael, Mulugeta Bekele, Ganesh D. Sharma. and Genene Tessema Mola. Synergistic contribution of potassium sulfide doped with silver nanoparticles on the performance of thin film organic solar cells. Journal of Physics and Chemistry of Solids, 177, (2023), 111290. My role in this article was synthesizing nanoparticles (NPs), fabricate solar cells, and analyzing the data correctly.

(5) Mohammed S.G. Hamed Jude N. Ike, Yilin Wang, Ke Zhou, Wei Ma. and Genene Tessema Mola. Reducing Energy Loss in Polymer Solar Cell through Optimization of Novel Metal Nanocomposite. Energy & Fuels, 37(8), (2023), 6129-6137. My role in this article is to synthesize and characterize the NPs.

Signed:……  ……

DEDICATION

To my parents

To my lovely mother (Mrs. Augustina Uzoigwe) and my amazing father who has left a good legacy behind (late Chief Alphonsus Uzoigwe)

To my lovely cousin, brothers, and sister

Dr. Collins Nwokedi, Emeka, Virtus, Kosi, Chiboy, Udochukwu, and Uju

Thank you for being a part of my life and for being the amazing individuals that you are. I hold every one of you dear to my heart, and I am truly blessed to have you by my side.

I dedicated this great work to you all.

ACKNOWLEDGEMENTS

With utmost gratitude, I extend my heartfelt appreciation to Professor Genene Tessema Mola, whose insightful guidance and contributions have been invaluable throughout the completion of this thesis. His enormous expertise, patience, and mentorship have been instrumental in the success of this research endeavor. I am equally grateful to the University of KwaZulu-Natal for providing a development and supportive environment that facilitated the smooth execution of this research project.

I am deeply thankful for the financial backing up from my lovely cousin (Dr. Collins Nwokedi) and may God uplift him to a new level. The instrumental role was played by Pastor Richard Ubani, Pastor Favour Ubani, and Pastor Steve Tai Oladosu. My family members also deserve my heartfelt appreciation for their steadfast support. Ultimately, the glory and potential of my faith belong solely to the Almighty God.

LIST OF FIGURES

LIST OF TABLES

LIST OF ACRONYMS

A	Acceptor
A-D-A	Acceptor-Donor-Acceptor
A-D	Acceptor-Donor
AFM	Atomic force microscopy
Ag	Silver
Al	Aluminum
Am	Air mass
a-Si	Amorphous silicon
Au	Gold
BHJ	Bulk heterojunction
BDT	Benzodithiophene
BMNPs	Bimetallic nanoparticles
BT	2,1,3-Benzothiadiazole
Ca	Calcium
C_{60}	Buckminsterfullerene
CdTe	Cadmium telluride
CIGS	Copper indium gallium selenide
Co	Cobalt
CO_2	Carbon dioxide
CT	Charge transfer state
D	Donor
DSSCs	Dye-synthesized solar cells

DTC	Dithienocyclopenta
DTS	Dithienosilole
EDX	Energy dispersive X-ray
Eg	Energy gap
EMF	Electromagnetic field
ETL	Electron transport layer
EQE	External quantum efficiency
FF	Fill factor
FLM	Fluorescence light microscopy
FTIR	Fourier transform infrared region
FWHM	Full width at half maximum
H_2O	Hydrogene-2-oxide
HCl	Hydrochloric acid
HNO_3	Trinitrate-5-acid
HOMO	Highest occupied molecular orbital
HRTEM	High-resolution transmission electron microscopy
HRSEM	High-resolution scanning electron microscopy
HTL	Hole transport layer
ICBA	Indium-fullerene bis-adduct
IDT	Indacenodithiophene
ITO	Indium tin oxide
IQE	Internal quantum efficiency
J_{sc}	Short circuit current

J-V	Current density-voltage curve
LiF	Lithium fluoride
LSPR	Localize Surface Plasmonic Resonance
LUMO	Lowest unoccupied molecular orbital
MJSC	Multi-junction solar cell
MoO_3	Molybdenum oxide
NaBH4	Sodium borohydride
NC	Nanocomposite
Ni	Nickel
NIR	Near infrared region
NPs	Nanoparticles
NREL	National Renewable Energy Laboratory
ODSs	Optical density of states
OLEDs	Organic light-emitting diode
OSCs	Organic solar cells
P3HT	Poly-(3-hexylthiophene)
PCE	Power conversion efficiency
PCBM	[6-6]-phenyl-C61-butyric acid methyl ester
PEDOT/PSS	Poly(ethylene-3-4-dioxy thiophene)/Polystyrene sulphonate
PL	Photoluminicense
P_{max}	Maximum power
PSCs	Polymer solar cells
PTB7	Poly-4,6-(2-Ethylhexyl-3-fluorothieno[2,3-b]thiophene-2-carboxylate)

	alt-2,6(4,8-bis(2-ethylhexyloxy) benzo[1,2-b/4,5-b]dithiophene)
PV	Photovoltaic
q	Electron charge
SCLC	Space charge limited current
SEM	Scanning electron microscopy
SERS	Surface-enhance Raman spectroscopy
SMs	Small molecules
SPPs	Surface plasmon polaritons
R_s	Series resistance
TEM	Transmission electron microscopy
TFOSCs	Thin-film organic solar cells
UV-Vis	Ultraviolet-visible
V_{max}	Maximum voltage
V_{oc}	Open circuit voltage
XRD	X-ray diffraction
Zn	Zinc
ZnO	Zinc oxide

Table of Contents

CHAPTER 1

INTRODUCTION AND BACKGROUND THEORY

1.1 Introduction

In 1977, Meinel A.B. and Meinel, M.P observations brought to light the solar cell's photovoltaic effect [1]. The p-n Junction solar cell made of silicon was first unveiled by Chapin *et al.* in 1954 [2-4], marking a significant milestone in the history of solar energy. Notably, this electronic device harnesses the photovoltaic effect to transform photon energy into electrical power [5]. The device utilization of selenium-based solar cells has unveiled the first solid-state photovoltaic devices [6]. Solar power has the potential to act as a crucial alternative to fossil fuels, effectively addressing the limitations of non-renewable sources like coal, crude oil, and etc, which have proven unsustainable and damaging to the environment. Given the limited availability of these sources, solar energy emerges as a desirable option, offering a sustainable solution that can help control environmental degradation. The Earth operates as a solar energy climate engine, harnessing an average of 240 watts of solar energy per square meter across its land surfaces, oceans, and atmosphere throughout the year [7]. Earth's energy equilibrium reflects the harmonious interplay of solar energy absorption and radiative energy emission into space. Solar energy as resources gives numbers for the energy deposited on the earth from the sun, this is the Earth's energy budget, and it could justify why the solar energy is highly potential resource for renewable energy. The envelope of gas encircling our planet, known as the Earth's atmosphere, plays a vital role in safeguarding life forms. It shields us from solar radiation’s harmful effects by absorbing or weakening ultraviolet rays. Additionally, the atmosphere works as a natural thermostat by retaining heat, which maintains a comfortable temperature for life to thrive. It also moderates the temperature fluctuations between day and night, justifying extreme conditions. The advent of the Industrial Revolution has propelled humanity towards cutting-edge technologies, resulting in escalated energy demands [8]. Consequently, this flow in energy consumption has culminated into excessive discharge of carbon dioxide into the atmosphere of our planet, thereby triggering the ominous phenomenon of global warming [9]. Hence, it is likely that the constraints of the initial and subsequent repetitions of solar cells have propelled the beginning of a new type of the third generation, which is known as the thin-film organic solar cells (TFOSCs). A thorough account of the first, second, and third generations of solar cells is clarified in chapter two of this thesis.

The focus of growing attention among researchers is on TFOSCs based on organic materials, which are noted for their low device fabrication costs, flexibility, portability, and lightweight [10-15]. These devices utilize conjugated polymer materials as electron-donating agents, and fullerene-based derivative materials as electron acceptors [16]. Although the advantages highlighted earlier are considerable, TFOSCs' commercialization has been hindered by their inferior power conversion efficiency (PCE) compared to traditional inorganic solar cells [17]. The PCE of TFOSCs is limited by the low electrical conductivity, charge mobility, and light absorption range of most organic materials [18]. Furthermore, the susceptibility of organic materials-based solar cell devices to degradation due to environmental exposure and photo-oxidation induced by light illumination cannot be overlooked. The fundamental structure of conventional TFOSCs is composed of two primary layers, namely the photoactive layer and the charge transport buffer layer [19]. To achieve maximum PCE in TFOSCs, the photoactive layer should exhibit excellent exciton generation with high optical absorption and efficient charge mobility to prevent recombination during carrier transport to the electrodes [20]. Achieving high electrical conductivity with selective charge retention and precise bandgap alignment within the charge transport layer is vital for maximizing the durability of unfettered charge carriers. An encouraging avenue for addressing the constraints of TFOSCs involves the integration of metal nanoparticles (NPs) and graphene [21]. Graphene outperforms conducting polymers in terms of mobility and conductivity, thus provides exceptionally conductive channels for carrier transport. Moreover, graphene-derived materials present effortless solution processability, better optical transparency, robust environmental and chemical stability, and uniform microstructures, making them a preferred choice in various applications. The conjunction of graphene and polymers creates an interface that induces spatial segregation of charges from photo-excited carriers within the solar absorber layer [22]. As a result, graphene can serve as both an active photoactive layer and buffer layer, as well as a transparent conductive electrode in the construction of solar cell devices. In recent years, metallic nanoparticles (NPs) have been introduced into solar cells to increase photon harvesting using the localized surface plasmonic resonance (LSPR) of metallic NPs [23] while keeping the active layer thin. The bimetallic nanoparticles (BMNPs) may be easier and cheaper to fabricate, or exhibit a higher performance compared to dielectric light scattering approaches [24]. When incorporated close to the interface between the photoactive and hole transport layers, the NPs lead to concentrated optical electric fields near the junction [24, 25], which enhances exciton creation within an exciton diffusion length away from the active layer medium [24]. This phenomenon is associated with comparatively small NPs, much smaller than the wavelength

of the incident light. The near-field light concentration holds great promise, it comes with a trade-off in the form of significant ohmic losses from the NPs, ultimately dissipating as heat [26]. In the light of this, incorporation of BMNPs in the photoactive and hole transport layers, is aimed at improving the photons absorption either by localized surface plasmonic resonance (LSPR) effect or by way of near and far field scattering, which growths the optical path length within a photoactive medium [27]. It has been reported that the incorporation of plasmonic BMNPs into thin film organic solar cells can significantly improve the PCE of solar cells by multiple folds due to photons trapping through scattering and near-field effects [28-34]. Plasmonics is an emerging field that makes use of the nanoscale properties of metals [28], which are considered as the collective oscillation of conduction electrons upon irradiation with light of certain wavelength [35]. The excitation of the LSPR effect can be achieved when the frequency of the incident light matches with oscillation frequency of metal surface electron plasma, resulting in a strong near-field around the interface between the dielectric and metallic NPs [32, 36, 37]. The resonance frequency of LSPR depends on the size, shape, and dielectric environment within the metallic NPs [28, 32, 38]. Therefore, by manipulating the size, shape and dielectric environment of the metallic NPs, the surface plasmon resonance and associated properties can be tuned depending on the applications [28].

Figure 1: Structure of flexible solar panels that can play a vital role in producing electricity for domestic use in our societies. Reproduced with permission, figure from Ref. [29].

1.2 Justifications

As time continues, the human race is predicted to require twice as much energy as is currently being consumed, underscoring the importance of responsible energy management and conservation. The utilization of fossil fuels as an energy source is paving the way for severe risk of global warming, with devastating consequences. The solution to this problem stands out as truly desirable: harnessing renewable energy offers a myriad of benefits, from reducing costs and boosting the efficacy of solar cells to promoting environmental stability, inspiring global action against climate change, and prompting entrepreneurial innovation. In addition, the utilization of organic photovoltaic cells has enormous potential to enhance the integration of renewable energy sources, owing to their notable advantages, including possible solution processability on flexible substrates and plenty of surface area suitable for large-scale applications.

1.3 Objectives of the Thesis

The primary objective of this thesis is to examine the role of metal NPs in harvesting solar energy using polymer blend solar absorber films. The metal NPs play a significant role in photon harvesting in TFOSCs polymer medium, which is advantageous for promoting exciton dissociation and improving charge transport processes due to the occurrence of localized surface plasmonic resonance (LSPR) effect and light scattering properties in the dielectric medium. The optimization of metal NPs can be attained by integrating various active and buffer layers within the device structure.

1.4 Aim of the Thesis

This thesis sets out to explore the potential of metal NPs in binary molecules (P3HT/PCBM) photoactive and buffer layers of TFOSC based on fullerene derivative. Our specific objectives are as follows:

- Synthesis and characterization of metal NPs through wet chemical procedure that has good optical and electrical properties for solar energy harvesting.
- Fabricating efficient polymers based solar cell using metal NPs into the active layer or /and charge transport buffer layers (hole transport layer (HTL)) to enhance their optical

and electrical properties, thereby augmenting their power conversion efficiency in fullerene derivative.

1.5 Methodological Approach

This research mainly involves the experimental investigation of the issues under consideration, with a particular emphasis on the fabrication of thin-film solar cells using sol-gel processes. By means of the I-V measuring system, we will examine the device's electrical properties under both dark and illuminated conditions. Exploration of the active layer's optical absorption shall be conducted using UV-VIS spectroscopic analysis. The high-resolution scanning electron microscope (HRSEM), high-resolution transmission electron microscope (HRTEM), and high-resolution energy-dispersive X-ray spectroscopy (HREDX) will be employed to explore the morphology of the active layer, and X-ray diffractometry (XRD) will be utilized to determine the crystal structure.

1.6 Resources

The Material Science program at the University of KwaZulu-Natal, Pietermaritzburg Campus is adequately equipped with state-of-the-art research instruments, including the Edward Auto 306 Deposition unit, SS5AAA Solar Simulator, I-V measuring system, Spin Coater, High-temperature furnace, Low-temperature Oven, Ultrasonicator, and Glovebox model MD200MOD. We are fortunate to have access to a wide range of other university facilities that can support our academic endeavors. This includes access to advanced technologies like Scanning Electron Microscopy (SEM), Transmission Electron Microscope (TEM), and X-ray diffraction, which can be used to further our understanding of complex scientific concepts.

1.7 Outline of this Thesis

This thesis is structured as follows: Chapter 1 provides a brief general introduction to solar energy, including the motivation, justification, aim of the thesis, objectives of the thesis, methodological approach, and resources.

Chapter 2 focuses on the description of the literature review. It covers the TFOSCs, bulk-heterojunction (BHJ), basic working principles of TFOSCs, basic characteristics of TFOSCs devices, basic limiting factors for high PCE, and routes of optimizing TFOSCs performance.

Chapter 3 provides a brief introduction to the fundamental theory of plasmonic. It further covers the plasmonic nanomaterials, surface plasmon-polaritons effect, localized surface plasmonic resonance effect, and light scattering effect.

Chapter 4 is a published article that deals with effective energy harvesting in thin-film organic solar cells using Ni/Zn as bimetallic nanoparticles.

Chapter 5 is a published article that explores plasmon-assisted optical absorption and reduced charge recombination for improved device performance in polymer solar cells.

Chapter 6 is a published article that deals with silver-doped ZnS core-shell nanocomposites to promote photon harvesting in polymer cells.

Chapter 7 is a published article that explores the impact of Ag/Co nanocomposite on organic charge transport medium for improved photocurrent in polymer solar cells.

Chapter 8 provides the summary and conclusion by presenting the key research findings in the previous chapters and provides a general conclusion and future work of this study.

References

[1] A.B. Meinel. and M.P. Meinel. Applied solar energy: an introduction. NASA STI/Recon Technical Report A, 77, (1977), 33445.

[2] D.M. Chapin., C.S. Fuller. and G.L. Pearson. A new silicon p-n junction photocell for converting solar radiation into electrical power. Journal of applied physics, 25(5), (1954), 676.

[3] S. Kouijzer. Photoactive and interface layers in polymer solar cells. (2014).

[4] S. Kouijzer., W. Li., M.M. Wienk. and R.A. Janssen. Charge transfer state energy in ternary bulk-heterojunction polymer–fullerene solar cells. Journal of Photonics for Energy, 5(1), (2015), 057203-057203.

[5] N.E. Widjonarko. Physics of Nickel Oxide Hole Transport Layer for Organic Photovoltaics Application (Doctoral dissertation, University of Colorado at Boulder), (2013).

[6] G.A. Chamberlain. Organic solar cells: A review. Solar cells, 8(1), (1983), 47-83.

[7] K.E., Trenberth. and L., Cheng. A perspective on climate change from Earth's energy imbalance. Environmental Research: Climate, 1(1), (2022), 013001.

[8] S. Yu. Performance enhancement of organic photovoltaic cells through nanostructuring and molecular doping, (2015).

[9] S. Khelifi., K. Decock., J. Lauwaert., E. Voroshazi., T. Aernouts., H. Vrielinck., A. Belghachi. and M. Burgelman. Electrical characterization of P3HT: PCBM organic solar cells by admittance spectroscopy: Defect Investigation. In E-MRS 2011 Spring Meeting; Symposium S: Organic photovoltaics-science and technology (OPV), (2011), 5-5.

[10] V. Saini., O. Abdulrazzaq., S. Bourdo., E. Dervishi., A. Petre., V.G. Bairi., T. Mustafa., L. Schnackenberg., T. Viswanathan. and A.S. Biris. Structural and optoelectronic properties of P3HT-graphene composites prepared by in situ oxidative polymerization. Journal of Applied Physics, 112(5), (2012), 054327.

[11] J. Min., Y.N. Luponosov., C. Cui., B. Kan., H. Chen., X. Wan., Y. Chen., S.A. Ponomarenko., Y. Li. and C.J. Brabec. Evaluation of electron donor materials for solution-processed organic solar cells via a novel figure of merit. Advanced Energy Materials, 7(18), (2017), 1700465.

[12] M.C. Scharber. and N.S. Sariciftci. The efficiency of bulk-heterojunction organic solar cells. Progress in polymer science, 38(12), (2013), 1929-1940.

[13] A. Polman., M. Knight., E.C. Garnett., B. Ehrler. and W.C. Sinke. Science, 352, (2016), 307.

[14] A. Polman., M. Knight., E.C. Garnett., B. Ehrler. and W.C. Sinke. Photovoltaic materials: Present efficiencies and future challenges. Science, 352(6283), (2016), 4424.

[15] J. Hou., O. Inganäs., R.H. Friend. and F. Gao. Organic solar cells based on non-fullerene acceptors. Nature Materials, 17(2), (2018), 119-128.

[16] D. Chen., A. Nakahara., D. Wei., D. Nordlund. and T.P. Russell. P3HT/PCBM bulk heterojunction organic photovoltaics: correlating efficiency and morphology, Nano Lett. 11(2), (2011), 561-567,

[17] M. El. Gemayel., A. Narita., L.F. Dössel., R.S. Sundaram., A. Kiersnowski., W. Pisula., M.R. Hansen., A.C. Ferrari., E. Orgiu., X. Feng. and K. Müllen. Graphene nanoribbon blends with P3HT for organic electronics. *Nanoscale, 6*(12), (2014), 6301-6314.

[18] S.E. Root., M.N. Alkhadra., D. Rodriquez., A.D. Printz. and D.J. Lipomi. Measuring the glass transition temperature of conjugated polymer films with ultraviolet-visible spectroscopy. Chemistry of Materials, 29(7), (2017), 2646-2654.

[19] P. Tonui. and G.T. Mola. Improved charge extraction in polymer solar cell using metal nanocomposite. Physica E: Low-dimensional Systems and Nanostructures, 107, (2019),154-159.

[20] A.K. Chauhan., S.K. Gupta., D. Taguchi., T. Manaka., P. Jha., P. Veerender., C. Sridevi., S.P. Koiry., S.C. Gadkari. and M. Iwamoto. Enhancement of the carrier mobility of conducting polymers by the formation of their graphene composites, RSC Adv. 7 (2017) 11913-11920.

[21] P. Robaeys., F. Bonaccorso., E. Bourgeois., J. D'Haen., W. Dierckx., W. Dexters., D. Spoltore., J. Drijkoningen., J. Liesenborgs., A. Lombardo. and A.C. Ferrari. Enhanced performance of polymer: fullerene bulk heterojunction solar cells upon graphene addition. Applied Physics Letters, 105(8), (2014), 136_1.

[22] A.J. Marsden., D.G. Papageorgiou., C. Valles., A. Liscio., V. Palermo., M.A. Bissett., R. J. Young. and I.A. Kinloch. Electrical percolation in graphene-polymer composites, 2D Materials. 5(3), (2018), 032003.

[23] L. Lu., Z. Luo., T. Xu. and L. Yu. Cooperative plasmonic effect of Ag and Au nanoparticles on enhancing performance of polymer solar cells. Nano letters, 13(1), (2013), 59-64.

[24] M. Song., H. Kim., C.S. Kim., J. Jeong., C. Cho., J. Lee., S. Jin., D. Choi. and D. Kim. ITO-free highly bendable and efficient organic solar cells with Ag nanomesh/ZnO hybrid electrodes. Journal of Materials Chemistry A, 3(1), (2015), 65-70.

[25] S. Fujimori., R. Dinyari., J.Y. Lee. and P. Peumans. Plasmonic light concentration in organic solar cells. Nano Letters, (2009).

[26] B. Cai., B. Jia., Z. Shi. and M. Gu. Near-field light concentration of ultra-small metallic nanoparticles for absorption enhancement in a-Si solar cells. Applied Physics Letters, 102(9), (2013), 093107.

[27] J. Zhu., X. Zhu., R. Hoekstra., L. Li., F. Xiu., M. Xue., B. Zeng. and K. L. Wang. Metallic nanomesh electrodes with controllable optical properties for organic solar cells, (2012).

[28] S. Pillai. and M. A. Green. Plasmonics for photovoltaic applications. Solar Energy Materials and Solar Cells, 94(9), (2010), 1481-1486.

[29] L.M. uller-Meskamp., Y.H. Kim., T. Roch., S. Hofmann., R. Scholz., S. Eckardt., K. Leo. and A.F. Lasagni. Efficiency enhancement of organic solar cells by fabricating periodic surface textures using direct laser interference patterning. Advanced Materials, 24(7), (2012), 906-910.

[30] Z. Tang., W. Tress. and O. Inganas. Light trapping in thin film organic solar cells. Materials today, 17(8), (2014), 389-396.

[31] S.W. Baek., J. Noh., C.H. Lee., B. Kim., M.K. Seo. and J.Y. Lee. Plasmonic forward scattering effect in organic solar cells: a powerful optical engineering method. Scientific reports, 3, (2013), 1726.

[32] X.H. Liu., L.X. Hou., J.F. Wang., B. Liu., Z.S. Yu., L.Q. Ma., S.P. Yang. and G.S. Fu. Plasmonic-enhanced polymer solar cells with high efficiency by addition of silver nanoparticles of different sizes in different layers. Solar energy, 110, (2014), 627-635.

[33] J.G. Smith., J.A. Faucheaux. and P.K. Jain. Plasmon resonances for solar energy harvesting: a mechanistic outlook. Nano Today, 10(1), (2015), 67-80.

[34] H. Shen, P. Bienstman and B. Maes. Plasmonic absorption enhancement in organic solar cells with thin active layers. Journal of Applied Physics, 106(7), (2009), 073109.

[35] H. Shen., P. Bienstman. and B. Maes. Solid-state plasmonic solar cells. Chemical reviews, 118(6), (2017), 2955-2993.

[36] D.H. Wang., K.H. Park., J.H. Seo., J. Seifter., J.H. Jeon., J.K. Kim., J.H. Park., O.O. Park. and A.J. Heeger. Enhanced power conversion efficiency in PCDTBT/PC70BM bulk heterojunction photovoltaic devices with embedded silver nanoparticle clusters. Advanced Energy Materials, 1(5), (2011), 766-770.

[37] H. Choi., J.P. Lee., S.J. Ko., J.W. Jung., H. Park., S. Yoo., O. Park., J.R. Jeong., S. Park. and J.Y. Kim. Multipositional silica-coated silver nanoparticles for highperformance polymer solar cells. Nano letters, 13(5), (2013), 2204-2208.

[38] J.A. Schuller., E.S. Barnard., W. Cai., Y.C. Jun., J.S. White. and M.L. Brongersma. Plasmonics for extreme light concentration and manipulation. Nature materials, 9(3), (2010), 193-204.

[39] M. Pagliaro., R. Ciriminna. and G. Palmisano. Flexible solar cells. ChemSusChem: Chemistry & Sustainability Energy & Materials, 1(11), (2008), 880-891.

CHAPTER 2

LITERATURE REVIEW

2.1 Introduction

The sun maintains a reliable and consistent level of solar energy emission, as evidenced by numerous sources [1, 2]. This attribute makes it an excellent resource for evaluating the PCE of various devices, in addition to serving as a formidable source of illumination. The importance of photovoltaics (PVs) as an energy source is unmatched, serving as a luminous standard against which the efficacy of energy-producing devices must be evaluated in a noteworthy application [3, 4]. The practicality of sunlight's impact on the earth's surface depends upon a myriad of factors, including but not limited to atmospheric conditions such as precipitation and cloud cover, and temporal influences like the time of day and season, resulting in a highly fluctuating incident intensity of sunshine across various regions. Thus, a viable solution to enable consistent and repeatable measurements within the laboratory is to employ a light source that can be always utilized, yet easily switched off when required [4]. Solar energy, a renewable energy source with massive potential, serves as a source of inspiration for many scientists in this fascinating field. Huang, H., and J. Huang's recent findings highlight the manifold benefits of solar cells as a sustainable and justifiable solution to global energy demands and environmental issues [5]. Renewable sources of energy such as solar, hydropower, geothermal, biomass, and wave power are quickly gaining ground as cost-effective alternatives, with their consumption skyrocketing [6]. In 2019, renewable energy accounted for over two-thirds of the world's newly installed electricity capacity [7]. As renewable energy sources continue to be enhanced and augmented, it is becoming increasingly clear that the days of widespread fossil fuel consumption - including coal, oil, and gas are numbered [8, 9]. Despite the undeniable benefits of fossil fuels, it cannot be overlooked that their usage has resulted in a host of environmental issues. Several recent studies have indicated that increased carbon dioxide emissions, irregular weather patterns, and air pollution have led to the exacerbation of greenhouse effects and subsequent global warming [10]. The pressing need to replace environmentally damaging fossil fuels has propelled the use of renewable energy sources to the forefront of the energy sector. Among these sources, solar energy stands out as the leading contender meeting the fast-growing energy needs of nations across the world. Fascinatingly, this invention leaves no damaging

environmental footprint and boasts an absence of mechanical components disposed to malfunction, demanding better maintenance and supervision, and has a life of about 20-30 decades without much expensive cost. In 1931, Bruno Lange, a German scientist, successfully pioneered the utilization of Selenium based solar cell panels to increase the absorption of solar energy and convert it into electricity through the PV effect. Regrettably, the solar panel fashioned from Selenium proved insufficiently resilient and inefficient under intense sunlight. However, in 1953, researcher in Bell Laboratories pioneered the utilization of silicon in PV cells, which proved far more productive than their Selenium counterparts, capable of generating plentiful amounts of electricity. During their investigation, the initial devices of the first generation, comprising both mono and polycrystalline cells, were made utilizing a solitary p-n junction. It was speculated that by utilizing crystalline cells produced from single crystalline silicon, an efficiency rating of 23% could potentially be attained [10]. It is noteworthy that the production of polycrystalline silicon cells is much, and cost effective compared to that of their monocrystalline counterparts. These cells boast efficiency values of up to 20.4% [1, 11], making them a compelling option. Initially, solar cells of the first generation boasted higher efficiencies and longer lifetimes. However, the significant costs associated with fabricating these cells prompted scholars to explore the development of second-generation solar cells [12]. Solar energy generation has come a long way with the advent of second-generation thin-film solar cells. These include amorphous silicon (a-Si), copper indium gallium selenide (CIGS), and cadmium telluride (CdTe) cells, which are highly profitable in large-scale PV power stations [13]. Silicon in its a-Si non-crystalline form reigns supreme among thin-film technologies, boasting cell efficiencies that clock in at a formidable 6-8% [14]. Surprisingly, the formation of a-Si panels could entail the deposition of a minute, one-micrometer-thick layer of silicon onto a substrate material, be it metal or glass, via the process of vaporization. Conversely, the CdTe cell presents a sleek semiconductor layer specifically designed to assimilate and transmute solar power into electrical energy, exhibiting a commendable efficiency rate of 19.6% [4,15]. Moreover, CIGS stands out as a leading contender among solar cell materials, boasting impressive efficiency rates of up to 21% [16]. The fabrication process involves the deposition of a slender CIGS layer on glass or plastic, while electrodes are integrated at the front and back to improve the electricity produced. Due to its high absorption coefficient and the consequential strong absorption of photon energy, the use of a significantly thinner film is required when compared to other semiconductor materials.

Over the past decade, extensive research efforts have been directed toward creating more cost-effective thin-film solar cells, known as second-generation solar cells. This development aims to reduce the semiconductor material and fabrication expenses of PVs and overcome the associated costs of first-generation solar cells [17]. For this reason, the sustainable benefit of the second-generation thin film is their ability to fabricate the above cells as quickly as possible without any expensive costs like that of the crystalline silicon PVs. To enter the third generation of solar technology, we can turn to three exciting options: (i) the multi-junction solar cell (MJSC), which increases multiple layers of semiconductors to harvest a broader spectrum of light; (ii) the dye-sensitized cell (DSC), which employs colorful pigments to absorb light and convert it into electricity; and (iii) the thin-film organic solar cell (TFOSC), which uses lightweight and flexible materials to create a solar panel that can bend and twist with ease. Interestingly, these growing PVs embody a novel approach toward the realization of economically viable solar energy. The MJSCs' mission is to enhance the efficiency of solar energy conversion by optimizing the power-to-cost ratio. To achieve this, a layer cake of several cells is constructed, each one containing a unique semiconductor material with varying bandgaps. By tuning the bandgaps, MJSCs can capture a greater portion of the solar spectrum, resulting in more effective photovoltaic performance. A stack of cells tailored to match the solar emission spectrum could potentially surpass the Shockley-Queisser limit, boasting a theoretical maximum efficiency of 66% when exposed to concentrated sunlight [18]. Furthermore, DSCs appear to be the optimum choice for third-generation solar cells, performing a crucial function in the conversion of visible light into electricity, boasting an impressive efficiency rating of 10.4% [19]. The invention of DSCs was attributed to recent research conducted at Ecole Polytechnique Federale de Lausanne (EPFL) [13].

Additionally, TFOSCs are electronic devices, showcasing reasonable potential in converting solar cells into electrical energy through the PV effect. With rigorous research efforts and significant strides in low-cost fabrication techniques, TFOSCs have witnessed notable advancements, paving the way for a sustainable energy future. Unfortunately, TFOSCs face two formidable obstacles: low PCEs and shortened lifetimes stemming from degradation. Bulk heterojunction (BHJ) devices create the fundamental dynamics that underlie the exceptional performance of most TFOSCs that thus illuminate the operational principles of TFOSCs. A comprehension of this mechanism has acted as a driving force for diverse avenues of material innovation, architectural conception, and interfacial manipulation, all of which have significantly boosted the PCE of TFOSCs [20-25]. In the year 2022, the National

Renewable Energy Laboratory (NREL) documented an unparalleled accomplishment in PV cells' efficiency, over several years as depicted in figure 2.

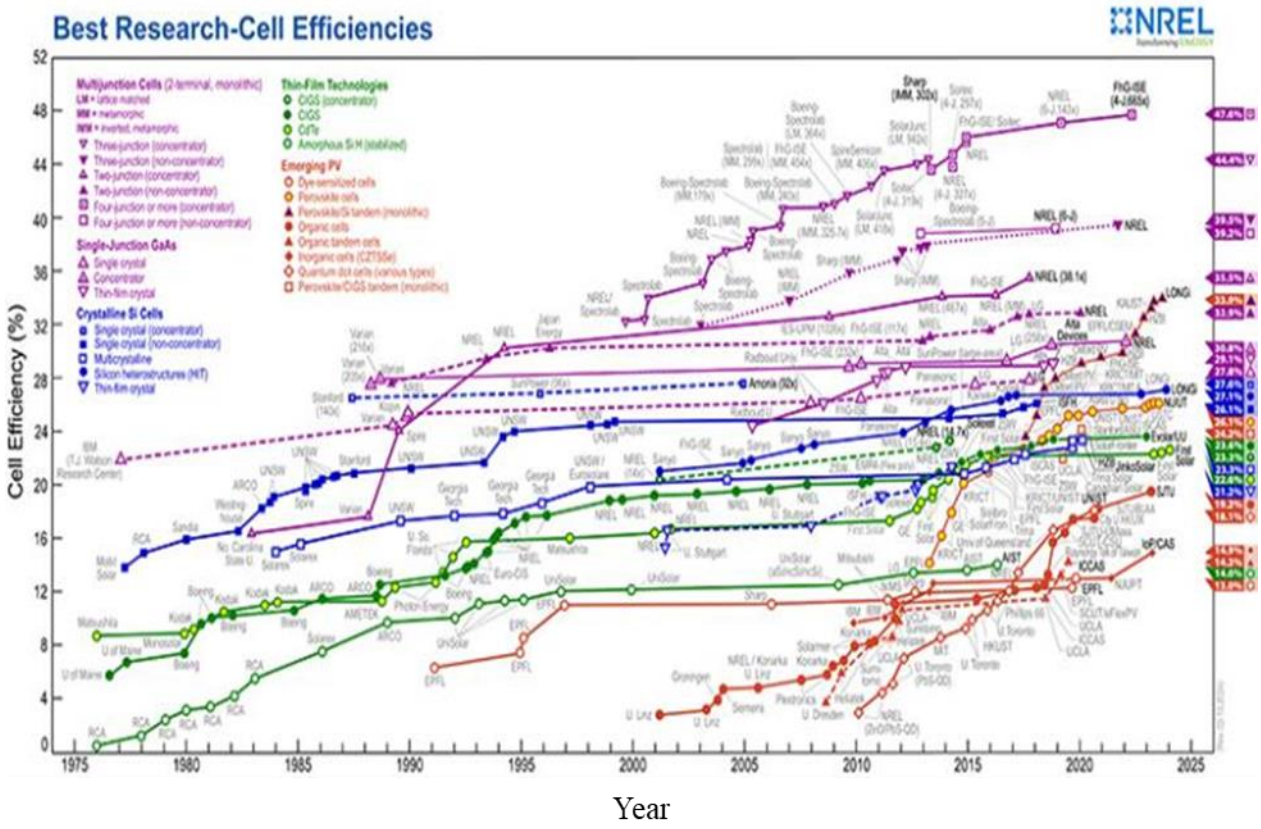

Figure 2.1: The highest record progress of power conversion efficiency of solar cell devices reviewed by NREL. Reproduced with permission, figure from Ref [26].

2.2 Thin-film organic solar cell development

It is to be noted that renewable energy has explored a beneficial interest in TFOSCs, drawing significant research efforts from both academia and industry over the past few decades. This is due to their potential to provide cost-effective solutions, mechanical flexibility, easy processing, and sustainable applications, making them a highly sought-after technology today [27-29]. TFOSCs have emerged as a cost-effective alternative for boosting potential energy from the sun [30]. In contrast to their inorganic counterparts, TFOSCs offer an excess of benefits. An avenue for compensation involves leveraging the interpenetrating network of donor and acceptor material, thereby enhancing absorption coefficients, and improving charge carrier collection [30, 31]. Although the PCEs of silicon-based solar cells remain higher, ongoing research aims to enhance the efficiencies of TFOSCs. Notably, advanced techniques such as bilayer, tandem, and BHJ methods are expected to be employed in examining the best TFOSC devices. The BHJ technique involves amalgamating a donor molecule and a soluble

fullerene derivative acceptor molecule, which are then spin-coated onto a conductive substrate to fabricate an incorporated network for excitons to thrive [32]. As the BHJ technique does not demand stringent conditions such as high pressure or temperature, it emerges as the optimal choice for the mass fabrication of flexible TFOSCs.

2.2.1 Bulk-heterojunction

In TFOSCs, three distinct devices are encountered: the single layer, the bilayer, and the BHJ shown in figure 2.2. The single-layer setup boasts a singular organic material layer sandwiched between two electrodes, devoid of any donor-acceptor pairing. In a bilayer configuration, the donor and acceptor exist as distinct strata, stacked upon one another. The drawback of organic bilayer PVs is their poor charge conveyance, due to the limited travel range of excitons relative to the thickness of the layer mandated for effective light absorption. The BHJ concept can be thought of as a mixture between a conjugated polymer donor and a soluble fullerene acceptor, spun together in a bulk volume. This indicates that each donor/acceptor interface is positioned within an exciton diffusion length, allowing for optimal absorption at every step of the site [33]. Figure 2.2 also shows a schematic diagram of a BHJ device, showcasing energy level alignments and interface effects. The BHJ device corresponds to a bilayer mechanism based on the donor/acceptor concept. However, it reveals an augmented interfacial area, leading to an increase in charge separation [34]. The BHJ architecture exemplifies a distinctive set of physical properties: an exceptional capacity for absorbing light in the solar spectrum optimized for efficient solar energy conversion; a seamlessly interconnected network with a domain width that surpasses the exciton diffusion length promoting efficient charge transfer; and an expansive donor-acceptor interface that facilitates the separation of excitons and the efficient charge transport to the corresponding electrodes through the percolation of phase-separated polymer domains, culminating in their collection.

Moreover, in a BHJ architecture, the donor and acceptor materials interpenetrate and yet remain distinct, creating an advantageous interface with sufficient separation to minimize recombination. Consequently, the efficiency of the BHJ is intimately dependent on its morphology. The affinity of a material for electrons and the ionization potential of the hole-bearing material are conducive to the dissociation of excitons, resulting in a pronounced tendency for electron transfer. Recent studies have highlighted that the BHJ design for TFOSCs was initially uncovered through the utilization of a solar absorber layer comprised of a MEH-PPV/C60 blend, serving as the electron donor and acceptor, respectively [35]. Indium-tin-oxide

(ITO) coated glass substrates can serve as a reasonable host for the solution consisting of a 10:1 wt% ratio of these substances. The application process can be achieved through spin-coating, ensuring uniformity of the mixture. Upon exposure to light, the solution displays exceptional performance with a PCE of 0.04% under an irradiance of 1 mW/cm^2, as indicated in the literature [35].

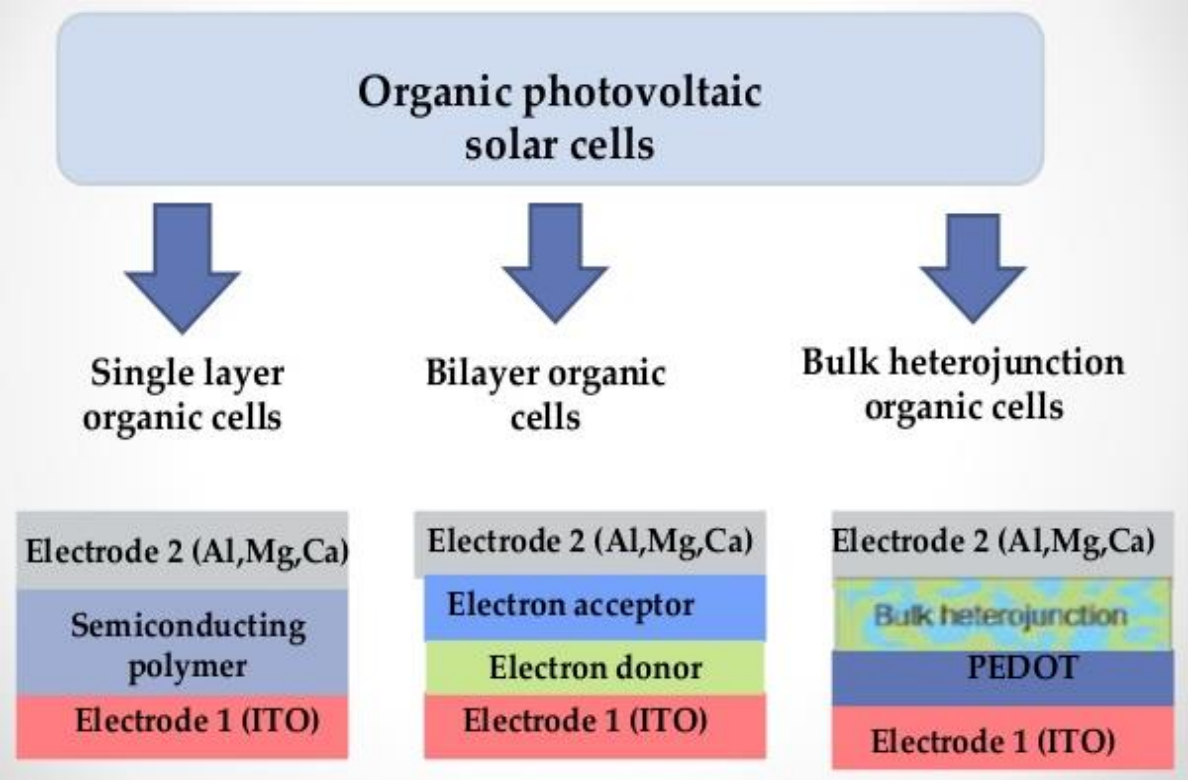

Figure 2.2: The phase-separated domain and path of percolation (a), single layer (b), bi-layer, and (c) bulk-heterojunction organic solar cells, figure taken from Ref. [36].

2.2.2 Donor

The TFOSC preparation relies on organic material as an electron donor that absorbs photon energy. Among the various groups of conjugated polymers employed for this purpose, the 2,1,3-Benzothiadiazole (BT), polythiophenes, and Thienthiopene stand out as the most popular choices. Polythiophenes and their derivatives have emerged as leading electron donors among conjugated polymers, attracting substantial attention in the field of PV research. Out of all the conjugated polymers known to date, it is the poly(3-hexylthiophene) (P3HT) molecules belonging to the polythiophene group that find the most frequent usage in the fabrication of TFOSCs [37]. Scholars have been captivated by P3HT's stability in ambient conditions, its amenability to solubility in a variety of organic solvents, and its uncomplicated

chemical composition, which lends itself to thorough computational modeling and in-depth analysis of the molecule's behavior [37]. Figure 2.3 illustrates the chemical structures of donor molecules that are commonly used in TFOSCs. Additionally, P3HT exhibits superior polymer properties with a narrow bandgap measuring 650 nm (equivalent to 1.9 electron volts), allowing it to absorb as much as 22.4% of incident photons [37,38]. The potential for enhanced light-harvesting efficiency in TFOSCs makes the low bandgap an auspicious attribute.

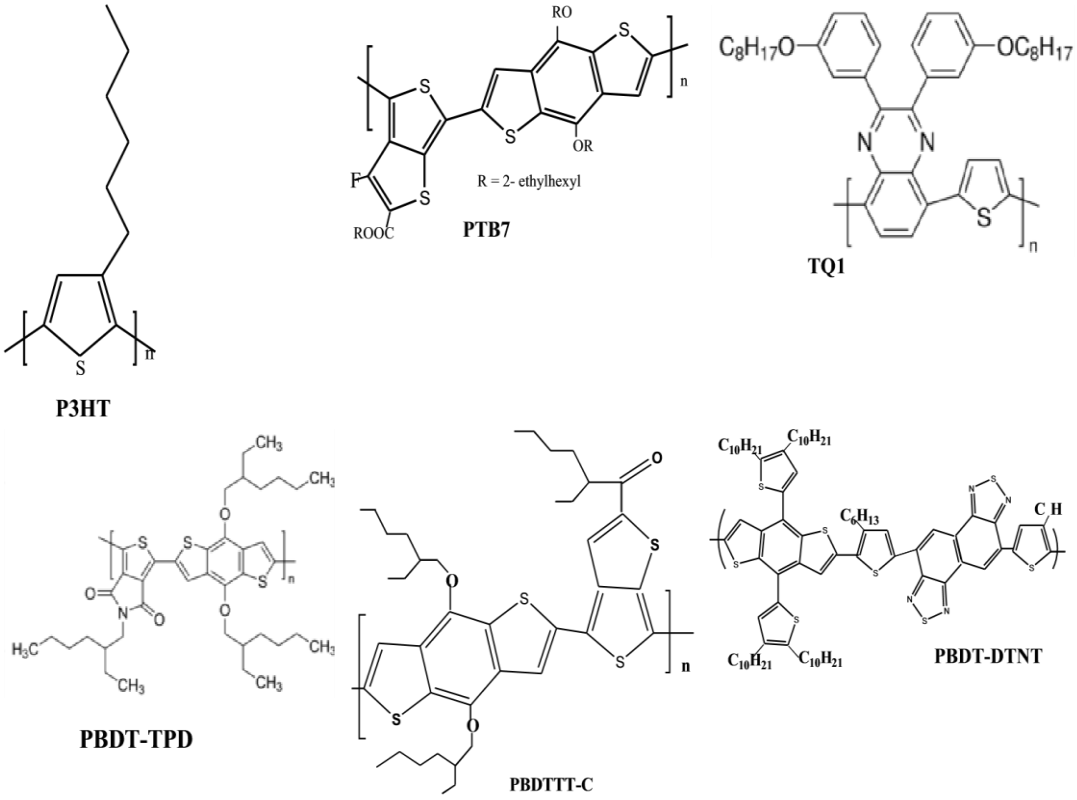

Figure 2.3: Chemical structures of representative donor molecules mostly used in TFOSC.

2.2.3 Acceptor

The fullerene material is a soluble organic solvent and assumes the role of an electron acceptor. The electrons and donor materials in TFOSCs share several defining behaviors, such as expedited exciton diffusion towards an active interface, high mobility of charge carriers, and effective charge separation. Moreover, fullerene C_{60} derivatives were first discovered in 1985 and have since been widely utilized as electroactive materials. The organic solvent displays low solubility towards the C_{60} derivative, due to its lowest unoccupied molecular orbital (LUMO) energy level that is triply degenerate and could potentially accept up to 6 electrons while in solution [39]. The C_{60} is not soluble but C_{60} derivatives are soluble because

of the attached on the sphere-like structure. The introduction of a model electron acceptor in this research has contributed enormously and attracted much attention to augment solubility and modulate the electronic property tuning capabilities. Intriguingly, the most prominent fullerene materials observed so far by researchers are methanol-fullerene derivatives of [6,6]-phenyl-C60-butyric acid methyl ester (PC60BM), [6,6]-phenyl-C70-butyric acid methyl ester (PC70BM), and [6,6]-phenyl-C71-butyric acid methyl ester (PC71BM). Thus, PCBM has the potential to mitigate the drawbacks of C_{60} caused by its tendency to aggregate or form crystals in films comprising both donor and acceptor materials [40]. Figure 2.4 provides the chemical structures of acceptor molecules, frequently improved to fabricate TFOSCs with the better efficiency.

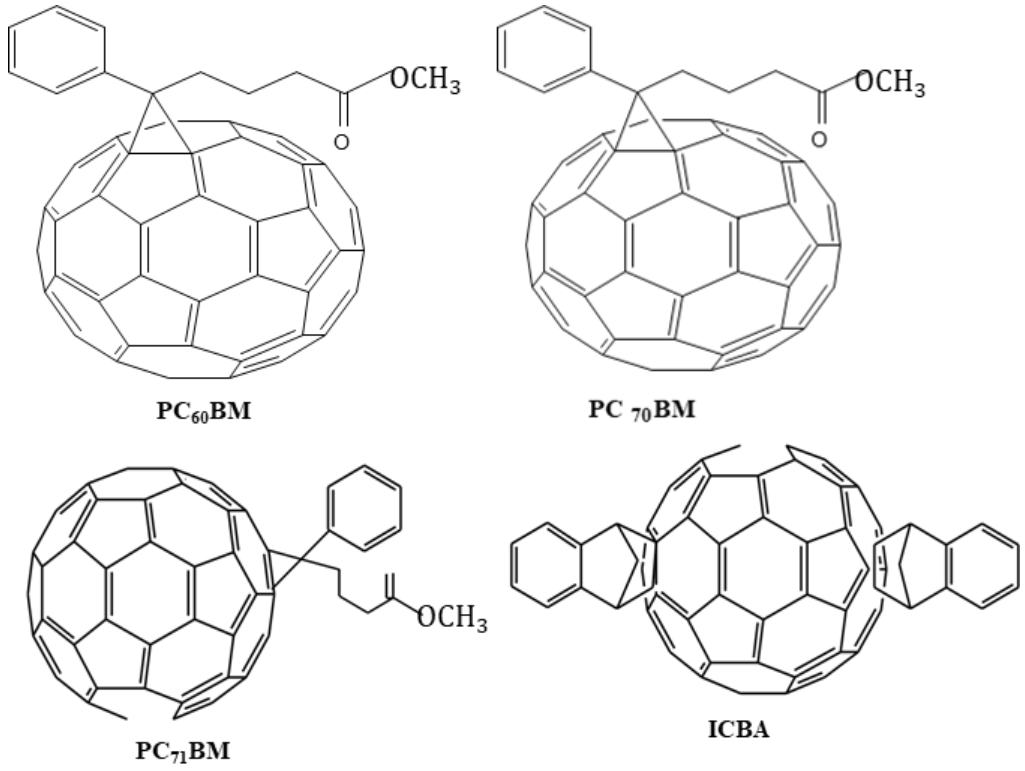

Figure 2.4: Chemical structures of representative acceptor molecules mostly used in TFOSC.

Additionally, the bisadduct (ICBA) of fullerenes can be utilized in TFOSC for creating high V_{oc} devices, due to their desirable elevated LUMO levels in comparison to $PC_{60}BM$ [41,42]. However, ICBA is promising in terms of augmenting the performance of poly (3-hexylthiophene) (P3HT) with PCE of about 6.5% indene-C60 bisadduct (IC60BA) and as well as 6.7% indene-C70 bisadduct (IC70BA).

2.3 Basic working principles of TFOSCs

The key to successful TFOSC function lies in the photoactive medium, which serves as the primary and milestone factor for a substantial alteration of the photon-to-charge carrier conversion mechanism. The TFOSC's solar absorber layer is a mixture of both donor (D) and acceptor (A) materials, functioning as the primary energy-absorbing layer. However, by incorporating a blend of donor and acceptor molecules in the solar absorber layer of TFOSCs, excitons can be efficiently generated upon the absorption of photons, thereby improving the harvesting of electron-hole pairs. In organic molecules, excitons possess a unique characteristic of low dielectric permittivity. The dielectric permittivity is a property of the material, which determines the nature of the exciton. This feature contributes significantly to the notable increase in binding energy, which ranges from 0.5 to 1 eV. This range is considerably higher than the thermal energy K_BT, which amounts to only about 0.026 eV, and is attainable when breaking bonds at room temperature. To achieve the crucial task of splitting excitons into free charge carriers, it is desirable to maintain donor-acceptor (D-A) interfaces within the range of 6-10 nm, as this creates an impressive internal field that can efficiently break up any excitons at the donor-acceptor interfaces [43-45].

2.3.1 Principles of photon-to-charge carrier transfiguration in TFOSCs

TFOSCs can convert solar energy into useful electricity through a series of four sequential steps: Interestingly, the incorporation of organic materials in TFOSCs results in the generation of free charge carriers from sunlight, offering a promising avenue for the advancement of renewable energy technologies. The operational mechanism of TFOSCs is demonstrated in Fig. 2.5 and is commonly abbreviated as:

- From the first point of view, as an electron situated in the highest occupied molecular orbital (HOMO) of an organic material, which absorbs the energy of a photon and becomes excited, transitioning to the lowest unoccupied molecular orbital (LUMO). This process leads to the creation of excitons, which signify a cohesive pair of an electron and a hole [43].
- The second stage involves the diffusion of excitons towards the interface of two organic materials, namely the donor and acceptor, where they eventually dissociate into charge carriers [4].

- In the third step, the excitons dissociate into free holes and electrons. Amazingly, the difference between the two electron affinity levels is the driving force required for the exciton separation.
- Finally, the free holes and electrons are transported to the relevant electrodes, where they are harnessed through donors and acceptors to generate potential electricity [46].
-

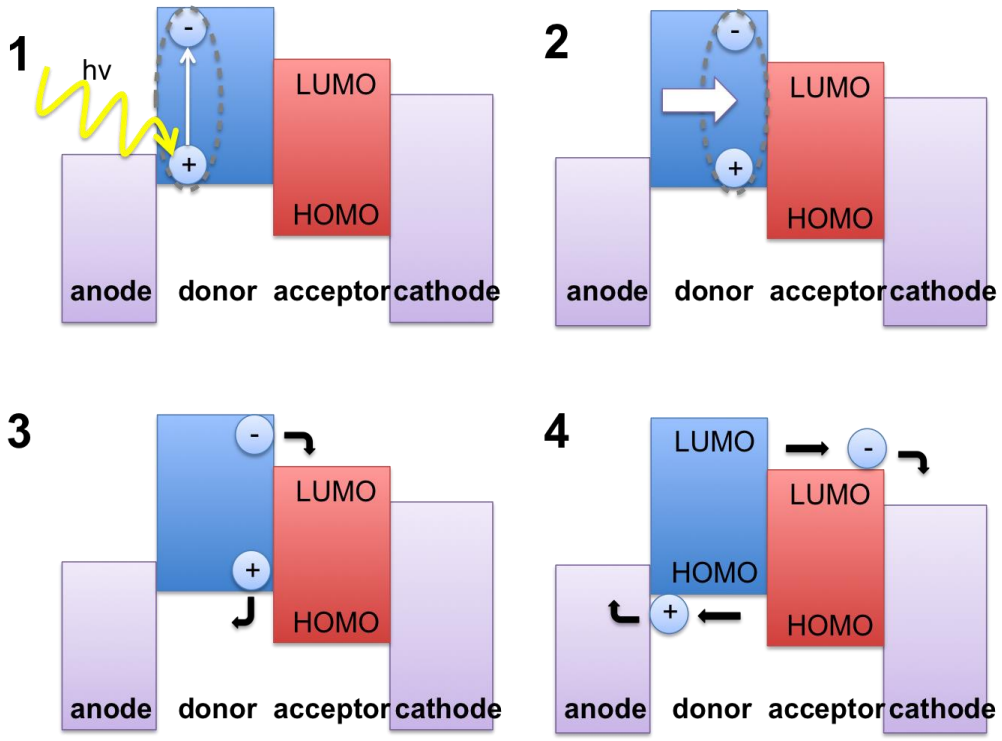

Figure 2.5: The schematic diagram of photon-to-charge carrier conversion in OSCs, figure taken from Ref. [46].

2.3.2 External quantum efficiency in TFOSCs

The TFOSCs have improved progressively in efficiency over the last decades. Interestingly, one of the parameters that determines the efficiency of a solar absorber to convert the incident photons to electrons is the external quantum efficiency (EQE) of a solar cell, which is the ratio of the number of charge carriers collected by the device to the number of incident photons at a given wavelength. Conversely, EQE can be defined as the proportionality between the density of short-circuit current and the density of incident photon flux at a particular wavelength. In mathematical terms, this can be expressed as:

$$EQE(\lambda) = \frac{J_{sc}(\lambda)}{eJ_{ph}(\lambda)} \times 100\%. \quad (2.1)$$

here, e is an electron charge carrier with a value of $e = 1.6 \times 10^{-19}$ Coulombs, λ denotes the wavelength of the incident-photon, while J_{sc} and J_{ph} represent the short-circuit current density, and incident-photon flux density, respectively. The EQE also exhibited better results when combined with the parameters, demonstrating stability and efficiency. This advantageous combination has the potential to enhance device performance during the production of TFOSCs.

2.4 Basic characteristics of TFOSC devices

The TFOSC devices exhibit several distinguishing features, which can be represented by a set of parameters namely, open circuit voltage (V_{oc}), short circuit current (J_{sc}), fill factor (FF), and power conversion efficiency (PCE), respectively. Several parameters are taken into account in figure. 2.6, which showcase the J-V characteristics of TFOSC devices.

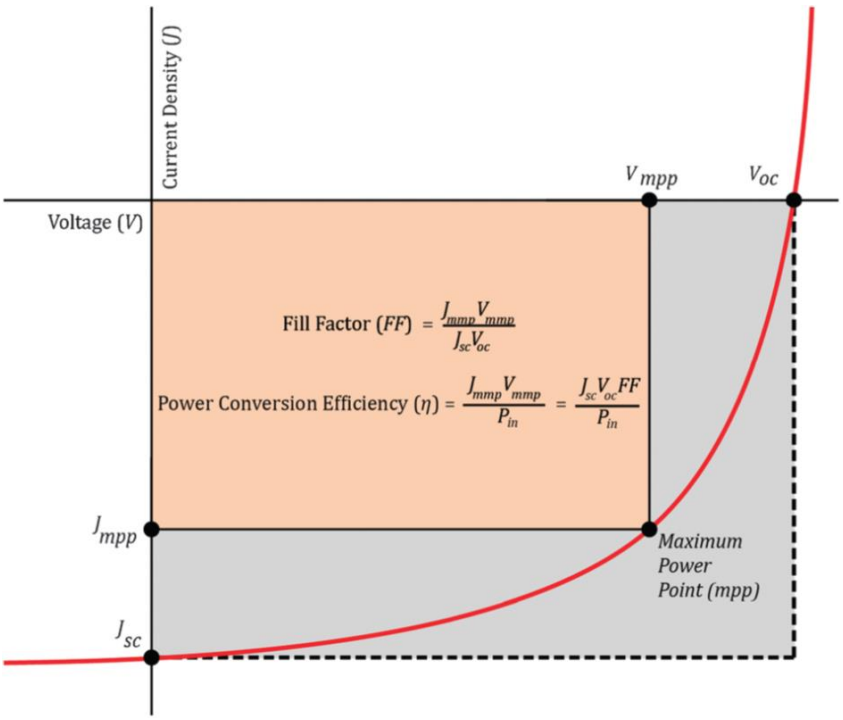

Figure. 2.6: Schematic of current density-voltage (J-V) curve for organic solar cells. Reproduce with permission from (Physical Chemistry Chemical Physics, 14(12), (2012), 4043-4057.), figure from Ref. [47].

The J-V curve can be expressed as the current-voltage characteristics of an illuminated bulk heterojunction of photovoltaic device. The key points of the graph are the V_{oc} (open circuit voltage), J_{sc} (short circuit current), V_{mpp} (voltage at maximum power), and J_{mpp} (current at

maximum power). The fill factor (FF) is a quantitative determination of the squareness of the J-V curve. The power conversion efficiency (η) of a photovoltaic cell is given by the ratio of maximum power output to the power input (P_{in}).

2.4.1 Short-circuit current density in TFOSCs

The maximum current generated by a solar cell is referred to as the short-circuit current density (J_{sc}), which is attained when the voltage across the device is zero. The attainment of the J_{sc} is dependent on various factors, among them being the surface area of the solar cell, the number of incident photons (photon flux), the spectral composition of the incident light, and the optical characteristics of the cell. The J_{sc} advancement is mainly due to the increased optical thickness of the solar cell, as reported by recent studies [48]. Additionally, the J_{sc} value mostly relies on the device's EQE. To determine J_{sc}, one can calculate the integral of the EQE, represented as $\eta_{EQE}(\lambda)$, across the air mass 1.5 global spectra (also known as AM 1.5G spectrum), which is illustrated in equation 2.2:

$$J_{sc} = \int_{A.M.1.5} e\eta EQE(\lambda) N_{ph}(\lambda) d\lambda. \quad (2.2)$$

Here, λ denotes the wavelength, and $N_{ph}(\lambda)$ is the photon flux density in the incident spectrum, while e represents the electronic charge. Assuming a total intensity of 100 mW/cm^2, we can express this as $N_{ph}(\lambda) = (100\ mW/cm^2) / (hv/\lambda)$, where hv is the energy of a single photon. It is interesting to note that the boundary points of the integral in equation (2.2) can be derived by integrating from the domain of shorter wavelengths (indicative of heightened photon energy) to the wavelength that corresponds with the optical bandgap of the photoactive material constituting the medium. As the optical bandgap decreases, a notable flow in the potential J_{sc} value is observed [49]. To determine J_{sc} experimentally, the J-V curve (depicted in figure 2.6) can be utilized by illuminating the sample. The point on the J-V curve corresponding to zero voltage (i.e., J(V = 0)) indicates the achievable J_{sc} value.

2.4.2 Open-circuit voltage in TFOSCs

The voltage that a solar cell can provide when no current flows, also known as the open-circuit voltage (V_{oc}). At this point, the splitting of an electron and a hole in the quasi-Fermi energy levels, as demonstrated in equation 2.3, generates the maximum voltage that a solar cell can offer to an external circuit. Interestingly, the V_{oc} serves as a crucial parameter that defines the upper limit of a solar cell's output capacity.

$$V_{oc} = \frac{1}{q}\left(E_{Fn} - E_{Fp}\right). \tag{2.3}$$

In the experimental findings' summary, the empirical estimation of V_{oc} holds promise as it correlates with the energy level disparity between the HOMO of the donor (D) substance and the LUMO of the acceptor (A) substance, denoted as E_{Fp} and E_{Fn}, respectively, q is the charge in Equation shown below:

$$V_{oc} = \frac{1}{q}(E_{HOMO-D} - E_{LUMO-A} - 0.3\ eV). \tag{2.4}$$

According to equation (2.4), it becomes evident that the temperature-dependent quasi-Fermi energy levels have been experimentally confirmed to yield a precise value of 0.3 eV [50, 51]. To optimize the V_{oc} value, there are a few key factors to consider. Firstly, it is possible to decrease the HOMO of the donor material or elevate the LUMO of the acceptor material. Additionally, tuning the work functions of both the anode and the cathode can also have a significant impact on V_{oc} [52].

2.4.3 Fill factor in TFOSCs

Notably, J_{sc} and V_{oc} denote the maximum current and voltage output of a solar cell, respectively. Consequently, the solar cell's power output is zero at both operating points. Nonetheless, the parameter known as "FF" or fill factor, in combination with V_{oc} and J_{sc}, determines the maximum power obtainable from a solar cell. Interestingly, equation 2.5 probably captures the presence of FF, which is the solar cell's maximum power ratio to the product of J_{sc} and V_{oc}. On the other hand, FF can be defined mathematically as:

$$FF = \frac{P_{max}}{V_{oc} \times J_{sc}}. \tag{2.5}$$

Within the substantial use of solar technology, the high-point of power output is represented by P_{max}, the maximum power-point. However, the potential of solar absorber films is severely

reduced by the nanoscale morphology of their surfaces, which in turn directly or indirectly limits their FF. This is predominantly due to the low mobility of charge carriers, coupled with a substantial discrepancy in the mobility of holes and electrons, which are responsible for transporting the build-up of space charge [53].

2.4.4 Power Conversion Efficiency in TFOSCs

The PCE is a function of the J_{sc}, V_{oc}, and FF, respectively. These factors can be extracted from the current-voltage curve and their product determines the overall efficiency of power conversion. Alternatively, the PCE can be expressed as the proportion of converted energy that is utilized, with "useful" output and input serving as the numerator and denominator, respectively. In other words, the PCE represents the efficiency of energy conversion can be expressed as:

$$PCE = \eta = \frac{V_{oc} \times J_{sc} \times FF}{P_{in}}. \quad (2.6)$$

It is to be noted that the average solar radiation received on the earth's surface is given as 100 mW/cm^2. We can consider the power input P_{in} to be equivalent to the AM 1.5 solar spectrum. This implies that the incident solar power is being improved at its full potential, corresponding to the optimal absorption rate of solar cells.

2.5 Basic limiting factors for high PCE

The TFOSCs exhibit a promising potential to replace the bulky, rigid, and exorbitantly priced inorganic silicon-based solar cells. Therefore, it is imperative to address the limitations and challenges of TFOSCs, and it is hoped that they will be effectively resolved. The Shockley-Queisser limit, also known as the detailed balance limit, defines the maximum theoretical efficiency of a single-junction solar cell. In 1961, William Shockley and Hans Queisser performed the first calculation of its kind, determining the maximum PCE of a single-junction solar cell under ideal conditions. According to their model, which considers zero avoidable losses, the theoretical upper limit for PCE is approximately 33% [54]. Therefore, this value is achievable based on the following assumptions, as described below:

- The photons with energy, E, much greater than the optical gap, E_g, are strongly absorbed.
- There is an absence of non-radiative recombination pathways (i.e., the device radiates just like a blackbody).

- ❖ The internal quantum efficiency (IQE) is unity (that is, each net absorbed photon results in one electron in the external circuit).

The extracted electrons have the difference in the quasi-Fermi levels of the separately thermalized populations of holes and electrons, μ given as:

$$\mu = qV. \tag{2.7}$$

Where q and v are charge and voltage, respectively. Upon examination of this equation, it becomes apparent that the proposed model's condition of detailed balance is subject to a multitude of semi-empirical and experimental assessments by numerous scholars. Through consensus, it has been determined that for a single junction in TFOSC, when an energy offset of 0.3 eV is present, the PCE is approximately 20%, as evidenced by prior investigations [55-58]. Even though the highest certified efficiency for a single junction in TFOSC is equivalent to 11.0% [54, 59], the reported efficiencies often fall short of this limit. In the following subsections, we will explore the possible factors that contribute to this discrepancy.

2.5.1 Basic photon absorption and photon generation in TFOSCs

It is interesting to note that the complex nature of the photocurrent generation poses a significant obstacle to the advancement of TFOSC devices, making it an intriguing observation. TFOSCs, in contrast to inorganic p-n junction solar cells, do not generate charge carriers spontaneously upon photon absorption. Instead, their performance is limited by the initial generation of photon excitons due to the organic material's inherent electronic states and low dielectric permittivity. The fundamental solar cell efficiency limits are illustrated in figure 2.7, which often presents the day records as a function of the respective band gaps. The energy of the BHJ in the bi-continuous interpenetrating network, with its D-A interfaces and charge-transfer states, surpasses that of excitons, enabling the conversion of excitons into free carriers. Due to the localization of charge states, which results in both low charge carrier mobility and limited electrode contact selectivity in TFOSC, the probability of charge recombination increases, ultimately impeding the collection of photocurrents at the relevant electrodes. Consequently, this is likely to result in low J_{sc} and FF values [55].

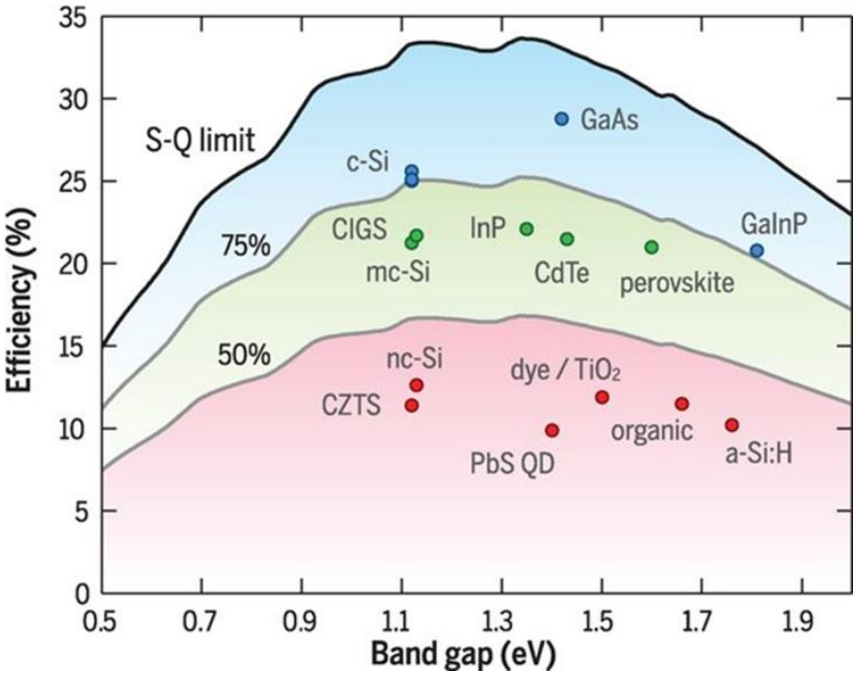

Figure 2.7: Theoretical Shockley-Queisser (detailed-balance) efficiency limit as a function of the bandgap (black line) while 75% and 50% of the limit (gray lines). The record efficiencies for different materials are plotted for the corresponding bandgap, figure from Ref. [54].

2.5.2 Recombination Mechanisms in TFOSCs

It is noteworthy that the efficacy of TFOSCs is frequently challenged by a competition between the internal field's expulsion of dissociated free carriers to the electrodes and the loss of photo-generated excitons, along with the dissociated free carriers, to recombination [60]. Once a photon is absorbed in TFOSCs, the exciton embarks on a fleeting journey to meet the donor-acceptor interface, with only a few nanoseconds to spare before it settles back into its grounded state. Assuming a domain size is much greater than the exciton diffusion length, the probability of electron-hole pair recombination surpasses their separation likelihood [61]. Despite reaching a D-A interface and triggering the formation of a charge transfer (CT) state, the excitons exhibit a non-negligible likelihood of recombination rather than dissociating into free charge carriers [62]. The pictorial representation of recombination mechanisms in TFOSCs is shown in figure 2.8.

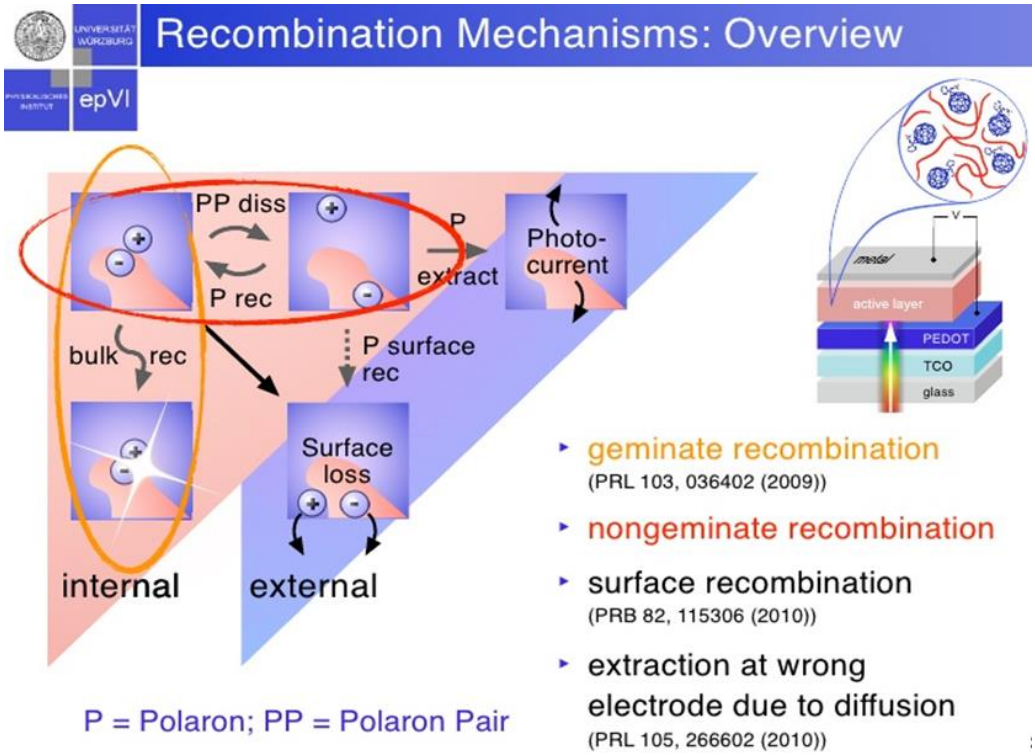

Figure 2.8: The influence of trap-assisted recombination on polymer-fullerene solar cells, figure from Ref. [63].

Geminate recombination describes the attractive process in which an electron and a hole recombine, having originated from the same photon event. In addition, the correlation between the intensity of the intrinsic field and the carrier sweep-out indicates carrier depletion's dependence on their charge carrier mobility. The internal field, which is carrier mobility dependent, is given by

$$E_{int} = \frac{(V_{oc} - V_{applied})}{d}. \tag{2.8}$$

where d exemplifies the thickness of the photoactive layer of BHJ in TFOSCs, V_{oc} is open-circuit voltage, $V_{applied}$ is the applied voltage, and E_{int} represents the internal field. In addition, the transient photoconductivity experiment revealed that the decay of photocurrent is predominantly influenced by the sweep-out of charge carriers under high E_{int} conditions, and by recombination under low E_{int} conditions, as reported in reference [64]. There is a fascinating relationship between the thickness of the active layer and the speed at which mobile carriers drift. The result of this intricate technology is the distinctive sweep-out time τ_{sw}, which can be defined as the ratio between the two aforementioned factors.

$$V_d = \frac{\mu E_{int}}{d}. \quad (2.9)$$

Here, μ signifies the average carrier mobility. Therefore,

$$T_{sw} = \frac{d^2}{2\mu E_{int}}. \quad (2.10)$$

The recombination mechanisms of charge carriers in TFOSCs can be categorized into three parts, as discussed below:

1. **Geminate Recombination:** It is conceivable that geminate recombination might transpire due to a hole and electron deriving from the same photon, recombining before separating into free charges. The relative dielectric constant of organic materials hampers the effective separation of an excited electron-hole pair into readily collectible charge carriers, thereby impeding charge carrier generation in various instances. As a result of this, the enthusiastic electron-hole pairs engage in geminate recombination, a process in which they reunite back to the ground state, before eventually parting ways to become free charge carriers once again. It should be highlighted that in numerous works, the application of geminate recombination is restricted only to the recombination of geminate pairs (GPs) situated at a donor-acceptor (D-A) interface.

2. **Non-Geminate Recombination:** Non-geminate recombination refers to the attractive process in bimolecular recombination where free holes and electrons, after dissociation, could meet again and combine into the ground state. Unlike geminate recombination, where the holes and electrons recombine immediately after dissociation, the non-geminate recombination process involves an intermediate step where the particles are free to move around and potentially encounter each other again before recombining. As soon as incident photons strike the surface, their energy scatters away, causing a decline in the number of carriers at the electrodes. This phenomenon becomes the principal source of loss in TFOSCs, in which the build-up of high charge carrier concentrations can limit the FF and lower PCE [60]. If the charge photo-generation is efficient, but the charge extraction to the electrodes is slower compared to the non-geminate recombination,

3. **Trap-Assisted Recombination:** This mechanism can be described as monomolecular recombination, whereby a single electron and a one-hole combine through a highly localized energetic trap. Despite the involvement of two carriers, this process remains

monomolecular since only one carrier is present at any given time due to the trap-assisted nature of the recombination event. Initially, trapping is the first carrier, followed by a search mission for the second carrier, which bears an opposite charge. The ultimate determination of the recombination rate rests upon the number of sites that function as traps, as well as on how quickly the free carrier can discover the trapped carrier. According to the literature [65], the Shockley-Read-Hall (SRH) recombination model has been etched as the definitive framework for trap-assisted recombination in inorganic semiconductors since its establishment in 1952. In a fascinating turn of events, this same model has found application in organic solar cells, as reported in recent literature [66]. Typically, the recombination of photo-induced charge carriers within TFOSCs imposes constraints on J_{sc}, FF, V_{oc}, and ultimately PCE, depending upon the system and the magnitude of incident light intensity. Fortunately, the refined nano-morphology and fabrication parameters hold great potential in reducing the effect of recombination, thereby boosting the efficiency of TFOSCs.

2.5.3 Nano-morphology mechanisms in TFOSCs

The nano-morphology mechanism plays a critical role in determining the PV properties of TFOSCs. A significant amount of research was invested in improving efficiency during the performance of morphological studies. To improve efficiency, it is crucial to gain a more comprehensive understanding of the methods for predicting and controlling nano-morphology. Interestingly, the nano-morphology of the interface is the key factor influencing the PCE of BHJ devices. Achieving a PCE of 10% requires the optimization of nano-morphology in tandem with the development of low-bandgap materials. The magnitude and nano-morphology of the donor-acceptor (D-A) interface are challenging to control due to the difficulty in predicting the properties and implications of charge transport on a given D-A interface through theoretical means [67].

Researchers have utilized various processing conditions and post-treatments in recent years to refine and enhance charge dissociation. One can achieve nano-morphology control through a variety of techniques, such as manipulating the solvent (e.g., varying its polarity and boiling point) [68], utilizing mixed solvent systems [69], incorporating additives [70], employing post-deposition solvent annealing [71], and implementing thermal annealing. To effectively control the nano-morphology, it is crucial to have the capability to monitor the intricate details of the nano-scale morphology. This can be accomplished through the utilization of diverse characterization techniques, including but not limited to, high-resolution scanning electron

microscopy (HRSEM), high-resolution transmission electron microscopy (HRTEM), high-resolution energy-dispersive X-ray spectroscopy (HREDX), fluorescence light microscopy (FLM) with a camera, and atomic force microscopy (AFM). The nano-morphology of the D-A interface, critical for the efficient functioning of TFOSCs, depends on the polymer and fullerene's intrinsic properties and their intermolecular interaction. The resultant crystallinity and morphology then influence the charge recombination and dissociation, leading to an improved overall device performance [72].

2.5.4 Basic degradation in TFOSCs

The problem of stability remains the foremost challenge in TFOSCs that needs to be tackled urgently. Despite impressive advances in their design and functionality, achieving long-lasting stability under different operational conditions is vital for their sustainable performance. Therefore, the consistent challenge TFOSCs face has been their devices' durability, specifically the chemical stability and degradation of polymers. Despite numerous attempts, a comprehensive degradation concept and process in TFOSCs has remained elusive. The contributing mechanisms and factors have been extensively deliberated, with a focus on individual functional layers or the entire device. The degradation mechanism of TFOSCs, comprising of reaction with oxygen, water (humidity), and electrode materials (such as Aluminum and Calcium), has recently been elucidated by researchers [73]. Due to the immense importance of air exposure, the degradation of TFOSCs divides into two distinct types - intrinsic and extrinsic degradation. The thermal diffusion of constituent materials at interfaces gives rise to the intrinsic degradation of TFOSCs, which manifests through a range of processes, including phase separation at the organic-cathode interface and intrinsic stress and inter-diffusion at buffer layer interfaces [74-75]. According to recent research, the inter-diffusion of aluminum or indium tin oxide (ITO) and organic layers during production has been found to cause negligible degradation [76].

Moreover, the interaction between oxygen and water is the primary reason for extrinsic degradation. Scholars frequently debate the significance of these two factors in the literature, even though TFOSCs and organic light-emitting diodes (OLEDs) use the same materials, they can be degraded by various mechanisms. According to reference [74], OLEDs experience their primary extrinsic degradation because of moisture content. In certain TFOSCs, oxygen reigns supreme in driving extrinsic degradation through a confluence of factors. Foremost among these is the hydrophobic nature of fullerene/acceptor, rendering it unreactive with aqueous molecules. For this reason, aluminum, though susceptible to water-induced corrosion, may acquire passivation when an acceptor is present, as stated in reference [77]. Furthermore, the

electron transport chain of the acceptor experiences significant impairment upon exposure to atmospheric oxygen. Nevertheless, despite previous reports indicating that fabricated TFOSCs consisting of ITO/ZnO/PCBM/P3HT/PEDOT/PSS/Ag structures are vulnerable to degradation by oxygen, recent findings suggest that the degradation is more obvious in encapsulated TFOSCs. Conversely, unencapsulated TFOSCs are significantly affected by degradation caused by both water and oxygen [78]. Following this discovery, PEDOT/PSS was identified as a primary source behind device degradation. As a result, researchers are actively exploring alternative hole transport layers. Generally, the PEDOT/PSS has the ability to expedite the degradation of unencapsulated devices, which can be attributed to its hygroscopic properties instead of its acidity [79]. Moreover, the degradation source from electrochemical reactions occurring at the electrodes is acknowledged as an additional contributing factor. In desirable configurations, aluminum serves as the remarkable electrode but tends to undergo oxidation and hydrolysis upon exposure to oxygen and water. As oxygen diffuses into the cell, an insulating oxide layer could form between the aluminum electrode and the active material, ultimately leading to cell deterioration [80].

2.6 Routes of Optimizing TFOSCs

It should be emphasized that numerous research endeavors have been dedicated to enhancing the power conversion stability of TFOSCs. This involves surmounting the challenges to attain vital operational dynamics, reaching a vital 20% PCE, and a five-year stability milestone that must be met for triumphant commercialization. In the forthcoming subsections, we will discuss and summarize various pathways that have been implemented to boost the dynamics of photon-to-photocurrent in TFOSCs.

2.6.1 Molecular engineering

It is noted that synthetic design has the potential to intensify and elevate certain aspects of TFOSCs through molecular-level augmentation and enhancement. Typically, light absorption is mostly exhibited by the donor/polymer material, with the absorbing acceptor/fullerene offering the immense potential to augment the photocurrent. Notably, the poor match between the absorption spectrum of the solar absorber layer materials and the solar spectrum may serve as an advantageous constraint on the electrical current density for solar cell harvesting. Interestingly, by utilizing the low bandgap of the solar absorber layer materials, one can attain a more optimal match, resulting in an augmented expansive absorption spectrum range and a heightened V_{oc} value. The absorption of light can also depend on the thickness of the layer and

the characteristic properties of its constituent molecules, influencing the step in which it is captured. Achieving a high better crystallinity is frequently mandatory for novel materials, as it guarantees superior charge carrier mobility, decreased recombination, and an impressive FF [81].

2.6.2 Device architectural and interfacial engineering

It is to be noted that exploring the synthesis and potential application of metal oxides with high exceptional functionality holds great promise for elevating the overall performance in the new architectural designs. The utilization of semiconducting metal oxides under the top electrodes has been widely employed to augment the stability of both inverted and conventional (normal) thin-film organic solar cells (TFOSCs). The three metal oxides that we frequently employ consist of zinc oxide, which functions as an electron transport layer (ETL), molybdenum trioxide, which serves as a hole transport layer (HTL), and titanium oxide, which is also employed as an ETL. Moreover, the implementation of the tandem cell structure established the groundwork for double and triple junction cells, ultimately resulting in a boosted PV efficiency. In tandem cells, by virtue of their design, offer an expanded room for capturing a wide spectrum of optical absorption bandwidth. The utilization of a ternary blend, comprising multiple donors or acceptors possessing matching energy levels, has vastly augmented the range of optical absorption bandwidth [82].

2.6.3 Doping methods

Doping is an essential process in the manufacturing of semiconductor devices, such as transistors and diodes, which are the building blocks of modern electronics. Interestingly, the solvent additives or metal NPs show promising potential as doping techniques for the solar absorber and interfacial layers in TFOSCs. However, scholars have acknowledged and demonstrated the effectiveness of utilizing solvent additives and related techniques to optimize both the nanoscale morphology and charge transport process [83-84]. The betterment of TFOSC advancement is credited to the solvent-doping of interfacial layer materials, as it has been found to heighten conductivity, enhance charge selectivity, and reduce the leakage of free charge carriers to an unsuitable electrode [85]. Surprisingly, the integration of both metallic and semiconducting NPs has emerged as a noteworthy doping approach, which has been proven to enhance device performance. Hence, the synergistic interplay between the plasmonic and scattering phenomena of metallic NPs, the widened

absorption spectrum, and the semiconducting NPs' optical spacer properties have boosted PCE by intensifying photon capture, separating, and mobilizing charges, and facilitating their transport upon NP integration [86].

2.7 The non-fullerene acceptors

It is to be noted that for more than two decades, researchers have directed their focus toward fullerene based TFOSCs, resulting in a breakthrough achievement of nearly 13% PCE [87]. The fullerene-based TFOSCs suffer from several limitations: their narrow-band optical absorption, the steep costs of synthesizing and purifying fullerene molecules, and the limited scope for functionalizing fullerenes to adjust their energy levels. In addition, the acceptor/donor (A/D) interface experienced energy loss in the presence of fullerenes, while poor morphological stability resulted from their diffusion, and fast air degradation was also observed [88-90]. In organic solar cells, non-fullerene acceptors (NFAs) have emerged as a game-changer, exhibiting a desirable efficiency beyond 19% as opposed to their fullerene-based counterparts, as noted by several studies [91-95]. Interestingly, it is noteworthy that the NFAs have managed to preserve a multitude of advantageous traits in contrast to their fullerene-based counterparts. With these advancements, we can now effortlessly synthesize small molecules, and tunable energy bandgaps for amplified optical absorption in the visible and near-infrared spectrum (NIR), and low energy loss to intensify V_{oc}. Moreover, the inflexible central core of NFA compounds offers a strategic advantage in upholding planarity and crystal structure, thereby enhancing the efficiency of charge transfer mechanisms and device functionality [96].

The introduction of electron pulls, and push polymers synthesis route referred to here as acceptor -donor (A-D). Such breakthrough paves the way for the exploration of innovative materials for polymer-based electronics [97-106]. The small molecule (SM) polymers can be synthesized through two primary molecular configurations: the electron-deficient (A-D-A) acceptor molecule, which can also be expressed as acceptor-donor-acceptor while the electron-rich donor (D-A-D) donor molecule can also be expressed as donor-acceptor-donor [107-113], as shown in figure 2.9. Understanding and optimizing these factors contribute to the development of efficient organic electronic devices. Researchers continually explore new materials and configurations to enhance the performance, stability, and scalability of organic electronics for diverse applications. Numerous interesting results have been achieved in recent years from the use of highly efficient SMs in all-polymer OSCs. In all-polymer organic solar cells, the employment of desirable efficient small molecules has yielded a result of intriguing

findings in recent years. The A-D-A acceptor molecules, composed of a single electron-donating moiety sandwiched between two electron-acceptor moieties, make up the class of electron-deficient small-molecule acceptors. Effective PV properties rely heavily on the core donor molecule's structure and chemical properties, which play a critical role in fine-tuning the electron-deficient A-D-A molecule. In search of the most useful electron-rich donor, the following cores reign supreme: thiophene, benzodithiophene (BDT), dithienosilole (DTS), dithienocyclopenta (DTC), indacenodithiophene (IDT), perylene diimide (PDI), etc. Interestingly, the A-D-A framework's end groups are pivotal players in molecular packing within BHJ films, consequently shaping the morphology of molecules in the active layer and influencing device performance. On this note, figure 2.9 shows the schematic diagram of electron-deficient and rich small molecule structure. (b) An example of the oligothiophene-based A-D-A electron-deficient small molecules is where A stands for possible acceptor blocks. On the other hand, the summary of organic solar cells device parameters and its energy loss for both binary and ternary non-fullerene acceptors using different electron polymers as the suitable donor material are shown below in Table 2.1. Table 2.1 further contains important device parameters of the various non-fullerene acceptors based on OSCs. The symbols are defined as $\Delta H = HOMO_{Acceptor}-HOMO_{Donor}$, whereas $\Delta L = LUMO_{Acceptor}-LUMO_{onor}$, and E_{loss} signifies the energy loss in small molecule non-fullerene acceptor in OSCs.

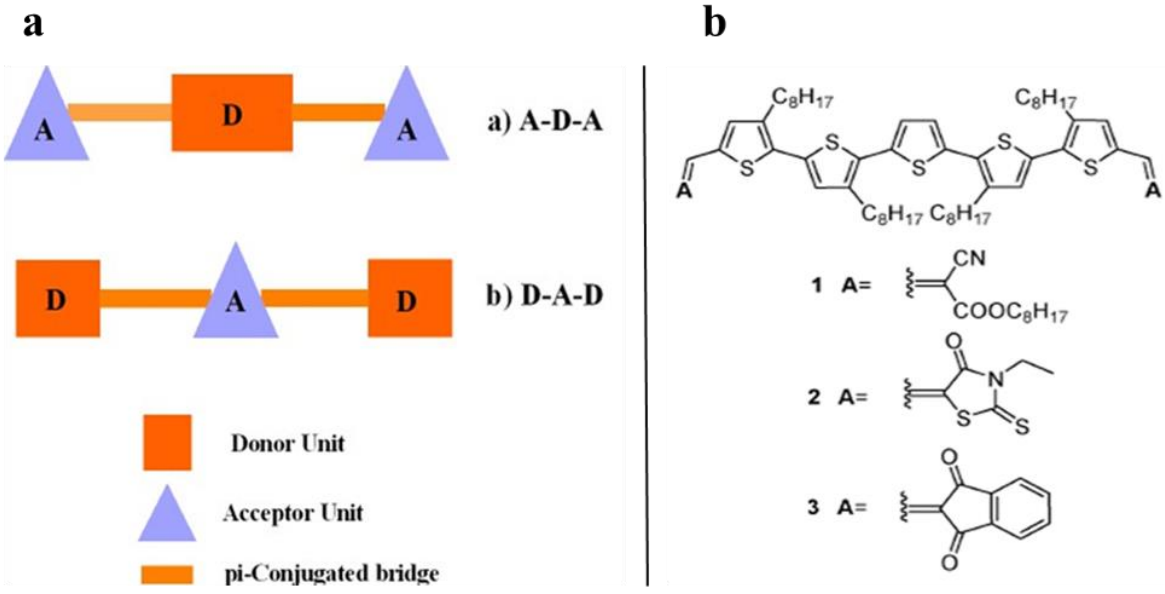

Figure 2.9: (a) Schematic representation of electron-deficient and rich small molecule structure. (b) An example of the oligothiophene-based A-D-A electron-deficient small molecules is where A stands for possible acceptor blocks, figure from Ref. [114].

The chemical structure of the most prominent donor and acceptor molecules of non-fullerene are shown below.

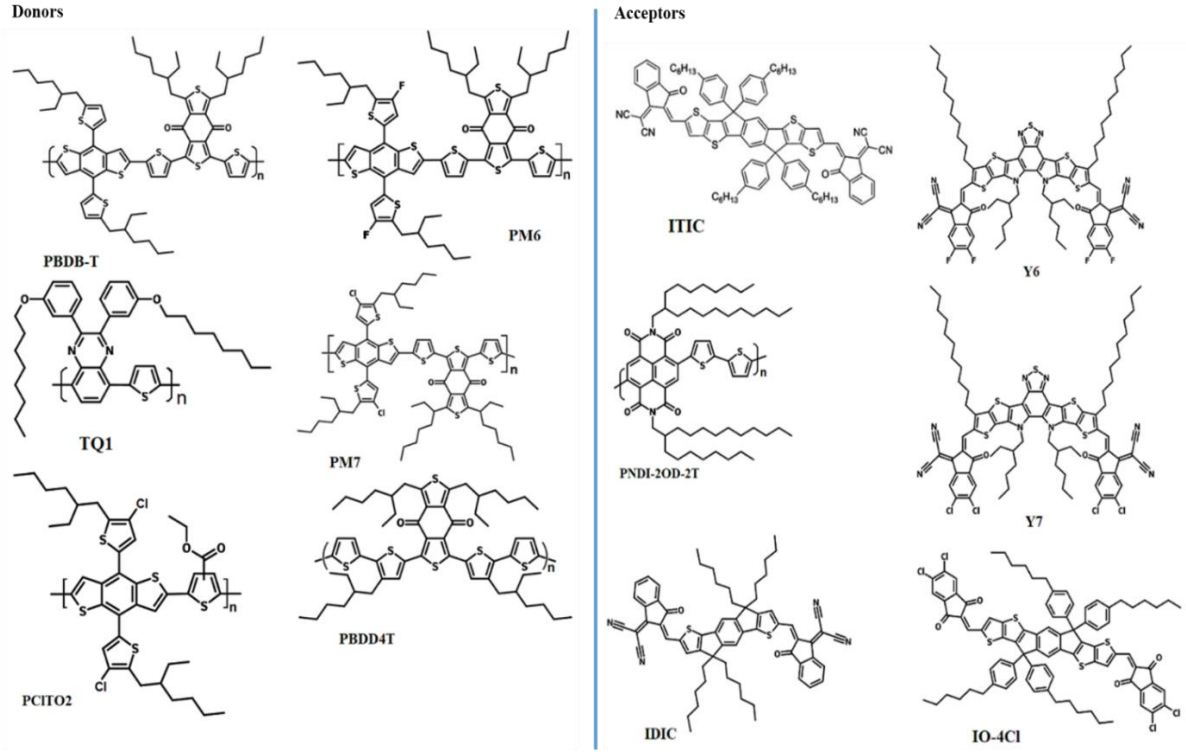

Figure 2.10: The chemical structure of the most prominent donor and acceptor molecules of non-fullerene.

Table 2.1: The summary of OSCs device parameters and energy loss for binary and ternary non-fullerene acceptors using different electron polymers as the suitable donor materials.

Device Stracture Donor-Acceptor	**V_{oc} [V]**	**J_{sc} $mAcm^{-2}$**	**FF [%]**	**$\triangle H$ [eV]**	**$\triangle L$ [eV]**	**E_{loss} [eV]**	**PCE [%]**	**Ref**	**Year**
D18/L8-BO	0.89	26.70	80.00	0.45	0.60	0.50	19.00	115	2022
D18/Y6	0.86	27.70	76.60	0.14	1.33	0.98	18.22	116	2020
PM6/Y6/FBTIC	0.87	24.60	77.90	0.14	0.35	0.60	16.70	117	2020
PM6/FBTIC	0.91	14.60	66.60	0.14	0.34	0.60	8.84	117	2020
PBDB-TF/AQx-1	0.89	22.18	67.14	0.03	0.21	0.52	13.31	118	2020
PBDB-TF/AQx-2	0.86	25.38	76.25	0.06	0.24	0.54	16.64	118	2020

Z5/BPF-4F	0.85	22.10	67.40	0.08	1.05	0.56	12.60	114	2020
SZ5/BPT-4F	0.85	24.80	79.10	0.09	1.08	0.56	16.80	114	2020
SZ5/BPS-4F	0.82	25.40	77.90	0.04	1.08	0.56	16.30	114	2020
PBDB-TF/BTP-eC7	0.84	24.10	73.50	.....	1.92	0.55	14.90	53	2020
PBDB-TF/BTP-eC9	0.84	26.20	81.10	.....	1.92	0.55	17.80	119	2020
PBDB-TF/BTP-eC11	0.85	25.70	77.50	……	1.92	0.55	16.90	119	2020
PM7/BDSe-4Cl	0.83	22.50	74.10	0.39	0.56	0.56	13.83	120	2020
PM7/BDSe-2(BrCl)	0.83	22.91	76.50	0.40	0.57	0.56	14.54	120	2020
PM7/BDSe-4Br	0.83	22.12	71.50	0.41	0.58	0.56	13.12	120	2020
PM6:Y18	0.84	25.71	76.50	0.05	0.41	0.53	16.52	121	2020
PM6/TPQx-4F	0.94	15.42	54.52	0.02	0.06	0.70	7.75	122	2020
PM6/TPQx-6F	0.92	22.37	72.16	0.10	0.12	0.64	14.62	122	2020
PM6/Y6	0.84	25.91	76.00	0.25	0.60	0.56	16.61	123	2021
PM6/L8-BO	0.87	25.72	81.50	0.19	0.43	0.55	18.32	123	2021
PM6/L8-HD	0.88	25.08	78.80	0.22	0.43	0.55	17.39	123	2021
PM6/L8-OD	0.89	24.57	74.60	0.22	0.44	0.53	16.26	123	2021
PM6/Y6	0.86	25.73	76.80	0.12	0.28	0.48	16.94	124	2021
PM6/Y6/AQx-3	0.87	26.82	77.20	0.06	0.24	0.47	18.01	124	2021
PM6/Y6/BTP-M	0.88	26.56	73.46	0.05/0.05	0.49/0.49	0.45	17.03	125	2020
PBD-TF/HDO-4Cl/eC9	0.87	27.05	80.51	0.03/0.09	0.19/0.35	0.26	18.86	126	2021
PM6/L8-BO-F/BTP-eC9	0.85	27.35	80.00	0.03/0.03	0.35/0.48	0.51	18.66	127	2021
PM6/Y6/SN	0.83	27.63	75.90	0.05/0.32	0.05/0.32	0.54	17.50	128	2021
P3TEA/pCP-FPDI4	1.17	13.84	57.00	0.27	0.21	0.51	9.06	129	2020
PM6/PDFC	0.97	15.93	81.30	0.03	0.16	0.41	12.56	130	2020
PDBT-TI/SF-4PDI-O	1.01	12.44	70.60	0.69	0.46	0.52	8.90	131	2020
PDBT-TI/SF-4PDI-S	1.05	10.79	68.90	0.64	0.38	0.55	7.82	131	2020
PDBT-TI/SF-4PDI-Se	1.06	10.53	68.40	0.57	0.36	0.57	7.63	131	2020

References

[1] G.T. Mola., X.G. Mbuyise., S.O. Oseni., W.M. Dlamini., P. Tonui., E.A. Arbab., K. Kaviyarasu. and M. Maaza. Nanocomposite for solar energy application. In Nano Hybrids and Composites (Vol. 20, (2018). 90-107). Trans Tech Publications Ltd.

[2] Y. Tong., Z. Xiao., X. Du., C. Zuo., Y. Li., M. Lv., Y. Yuan., C. Yi., F. Hao., Y. Hua. and T. Lei. Progress of the key materials for organic solar cells. Science China Chemistry, 63(6), (2020), 758-765.

[3] V. Ivasyshyn., V. Ivasyshyn., G. Ye., G. Ye., S. Rousseva., S. Rousseva., J.C. Hummelen., J.C. Hummelen., R.C. Chiechi. and R.C. Chiechi. Increasing the Dielectric Constant of Organic Materials for Photovoltaics. Emerging Photovoltaic Materials: Silicon & Beyond, (2018), 401-441.

[4] M.S.G. Hamed. The effects of nanocomposites in bulk heterojunction thin-film organic solar cells (Doctoral thesis at University of KwaZulu-Natal). (2020).

[5] H. Huang. and J. Huang. Organic and Hybrid Solar Cells. Springer, (2014).

[6] S.H. Bae., H. Zhao., Y.T. Hsieh., L. Zuo., N. De Marco., Y.S. Rim., G. Li. and Y. Yang. Printable solar cells from advanced solution-processible materials. Chem, 1(2), (2016), 197-219.

[7] Z. Zhongming., L. Linong., Y. Xiaona., Z. Wangqiang. and L. Wei. Renewable Energy Now Accounts for a Third of Global Power Capacity, (2019).

[8] A. Bedeloglu. Progress in organic photovoltaic Fiber research. Solar Cells-New Aspects and Solutions, (2011), 255-286.

[9] J.J. Lee., S.H. Lee., F.S. Kim., H.H. Choi. and J.H. Kim. Simultaneous enhancement of the efficiency and stability of organic solar cells using PEDOT: PSS grafted with a PEGME buffer layer. Organic Electronics, 26, (2015), 191-199.

[10] J. Farinhas., R. Oliveira., Q. Ferreira., J. Morgado. and A. Charas. Enhanced Efficiency of PTB7: PC61BM Organic Solar Cells by Adding a Low Efficient Polymer Donor. International Journal of Photo energy, (2017).

[11] M.M.A. Gamel., H.J. Lee., W.E.S.W.A. Rashid., P.J. Ker., L.K. Yau., M.A. Hannan. and M.Z. Jamaludin. A Review on Thermophotovoltaic Cell and Its Applications in Energy Conversion: Issues and Recommendations. Materials, 14(17), (2021), 4944.

[12] M.A. Green., K. Emery., Y. Hishikawa. and W. Warta. Solar cell efficiency tables (version 36). Progress in photovoltaics: research and applications, 18(5), (2010), 346-352.

[13] A.M. Bagher., M.M.A. Vahid. and M. Mohsen. Types of solar cells and application. American Journal of optics and Photonics, 3(5), (2015), 94-113.

[14] Bernede, J., Organic photovoltaic cells: history, principle, and techniques. Journal of the Chilean Chemical Society, 2008. 53(3): p. 1-23.

[15] I.S.E. Fraunhofer. Photovoltaics report. Fraunhofer ISE, Freiburg, (2014).

[16] R. Ganesamoorthy., G. Sathiyan. and P. Sakthivel. Fullerene-based acceptors for efficient bulk heterojunction organic solar cell applications. Solar Energy Materials and Solar Cells, 161, (2017), 102-148.

[17] A.L.D. Yonkeu. Dendritic poly (3-hexylthiophene) star copolymer systems for next-generation bulk heterojunction organic photovoltaic cells, (2018).

[18] M. LoCascio. Application of semiconductor nanocrystals to photovoltaic energy conversion devices. Evident Technologies, Troy, NY, (2002),1.

[19] A. Martin., K.E. Green., H. Yoshihiro. and W. Wilhelm. Progress in photovoltaics: Research and applications Prog. Prog Photovolt Res Appl, 19, (2011), 84-92.

[20] M. Green., E. Dunlop., J. Hohl-Ebinger., M. Yoshita., N. Kopidakis. and X. Hao. Solar cell efficiency tables (version 57). Progress in photovoltaics: research and applications, 29(1), (2021), 3-15.

[21] R. Zhou., J. Xu., P. Luo., L. Hu., X. Pan., J. Xu., Y. Jiang. and L. Wang. Near-Infrared Photoactive Semiconductor Quantum Dots for Solar Cells. Advanced Energy Materials, 11(40), (2021), 2101923.

[22] Q. Wang., Y. Xie., F. Soltani-Kordshuli. and M. Eslamian. Progress in emerging solution-processed thin film solar cells-Part I: Polymer solar cells. Renewable and Sustainable Energy Reviews, 56, (2016), 347-361.

[23] S. Devasahayam. and C.M. Hussain. Thin-film nanocomposite devices for renewable energy current status and challenges. Sustainable Materials and Technologies, 26, (2020), e00233.

[24] C.H.M. Chuang., P.R. Brown., V. Bulović., and M.G. Bawendi. Improved performance and stability in quantum dot solar cells through band alignment engineering. Nature Materials, 13(8), (2014), 796-801.

[25] N. Marinova., S. Valero. and J.L. Delgado. Organic and perovskite solar cells: Working principles, materials, and interfaces. Journal of Colloid and interface science, 488, (2017), 373-389.

[26] J.J. Cook., E. O'Shaughnessy., K. Xu., S. Jena., M.S. Qasim. and S. Crew. SolarAPP+ Performance Review: 2021 Data (No. NREL/TP-6A20-83046). National Renewable Energy Lab. (NREL), Golden, CO (United States), (2022).

[27] H. Yao., F. Bai., H. Hu., L. Arunagiri., J. Zhang., Y. Chen., H. Yu., S. Chen., T. Liu., J.Y.L. Lai. and Y. Zou. Efficient all-polymer solar cells based on a new polymer acceptor achieve 10.3% power conversion efficiency. ACS Energy Letters, 4(2), (2019), 417-422.

[28] A. Singh., A. Dey. and P.K. Iyer. Influence of molar mass ratio, annealing temperature, and cathode buffer layer on the power conversion efficiency of P3HT: PC71BM based organic bulk heterojunction solar cell. Organic Electronics, 51, (2017), 428-434.

[29] P. Tonui., S.O. Oseni., G. Sharma., Q. Yan. and G.T. Mola. Perovskites photovoltaic solar cells: An overview of current status, Renew. Sustain. Energy Rev., 91, (2018) 1025-1044.

[30] G. Tessema. Charge transport across bulk heterojunction organic thin film. Applied Physics A, 106(1), (2012), 53-57.

[31] C. Deibel. and V. Dyakonov Polymer–fullerene bulk heterojunction solar cells. Reports on Progress in Physics, 73(9), (2010), 096401.

[32] B. Xu., G. Sai-Anand., G.E. Unni., H.M. Jeong., J.S. Kim., S.W. Kim., J.B. Kwon., J.H. Bae. and S.W. Kang. Pyridine-based additive optimized P3HT: PC61BM nanomorphology for improved performance and stability in polymer solar cells. Applied Surface Science, 484, (2019), 825-834.

[33] J. Nelson. Polymer: fullerene bulk heterojunction solar cells. Materials Today, 14(10), (2011).462-470.

[34] G.D. Spyropoulos., M.M. Stylianakis., E. Stratakis. and E. Kymakis. Organic bulk heterojunction photovoltaic devices with surfactant-free Au nanoparticles embedded in the active layer. Applied Physics Letters, 100(21), (2012), 213904.

[35] G. Williams. Advances in organic photovoltaics and methods for effective solar cell parameter extraction. review, University of Waterloo. Waterloo, ON Canada. N2L 3G1, (2013).

[36] M. Wright., R. Lin., M.J. Tayebjee. and G. Conibeer. Effect of blend composition on bulk heterojunction organic solar cells: a review. Solar Rrl, 1(3-4), (2017).1700035.

[37] L.X. Chen., J. Guo., J.M. Szarko., Y. Liang., B.S. Rolczynski., B. Lee., H.J. Son. and L. Yu. Structure, dynamics, and power conversion efficiency correlations in new low bandgap polymer: PCBM solar cells. In ACS National Meeting Book of Abstracts. American Chemical Society, (2010 December).

[38] H.J. Jhuo., P.N. Yeh., S.H. Liao., Y.L. Li., Y.S. Cheng. and S.A. Chen. Review on the recent progress in low band gap conjugated polymers for bulk hetero-junction polymer solar cells. Journal of the Chinese Chemical Society, 61(1), (2014), 115-126.

[39] C.J. Brabec., M. Heeney., I. McCulloch. and J. Nelson. Influence of blend microstructure on bulk heterojunction organic photovoltaic performance. Chemical Society Reviews, 40(3), (2011), 1185-1199.

[40] F.C. Jamieson., E.B. Domingo., T. McCarthy-Ward., M. Heeney., N. Stingelin. and J.R. Durrant. Fullerene crystallization as a key driver of charge separation in polymer/fullerene bulk heterojunction solar cells. Chemical Science, 3(2), (2012), 485-492.

[41] Z. Xiao., X. Geng., D. He., X. Jia. and L. Ding. Development of isomer-free fullerene bisadducts for efficient polymer solar cells. Energy & Environmental Science, 9(6), (2016), 2114-2121.

[42] H. Lee., J. Mun., N.N. Nguyen., J. Rho. and K. Cho. The open-circuit voltage of organic solar cells: Effect of energetically and spatially nonuniform distribution of molecular energy levels in the photoactive layer. Nano Energy, 78, (2020), 105336.

[43] Y.W. Su., S.C. Lan. and K.H. Wei. Organic photovoltaics. Materials Today, 15(12), (2012), 554-562.

[44] C. Deibel. and V. Dyakonov. Polymer-fullerene bulk heterojunction solar cells. Reports on Progress in Physics, 73(9), (2010), 096401.

[45] S.R. Cowan., N. Banerji., W.L. Leong. and A.J. Heeger. Charge formation, recombination, and sweep-out dynamics in organic solar cells. Advanced Functional Materials, 22(6), (2012), 1116-1128.

[46] M. Kaushik. and B. Kaushik. Organic solar cells: design, synthesis, and characterization. Int. J. Eng. Sci, 2, (2013), 310-319.

[47] B.C. Popere., A.M. Della Pelle., A. Poe. and S. Thayumanavan. Macromolecular architectures for organic photovoltaics. Physical Chemistry Chemical Physics, 14(12), (2012), 4043-4057.

[48] A. Gaur. and P. Kumar. An improved circuit model for polymer solar cells. Progress in Photovoltaics: Research and Applications, 22(9), (2014), 937-948.

[49] V. Coropceanu., X.K. Chen., T. Wang., Z. Zheng. and J.L. Brédas. Charge-transfer electronic states in organic solar cells. Nature Reviews Materials, 4(11), (2019), 689-707.

[50] S. R.Cowan., A. Roy. and A.J. Heeger. Recombination in polymer-fullerene bulk heterojunction solar cells. Physical Review B, 82(24), (2010), 245207.

[51] W. Taouali., M.E. Casida., S. Znaidia. and K. Alimi. Rational design of (DA) copolymers towards high efficiency organic solar cells: DFT and TD-DFT study. Journal of Molecular Graphics and Modelling, 89, (2019), 139-146.

[52] M.D. Perez., C. Borek., S.R. Forrest. and M.E. Thompson. Molecular and morphological influences on the open circuit voltages of organic photovoltaic devices. Journal of the American Chemical Society, 131(26), (2009), 9281-9286.

[53] N. Zhou. and A. Facchetti. Charge transport and recombination in organic solar cells (OSCs). In Organic and Hybrid Solar Cells (2014, 19-52). Springer, Cham.

[54] A. Polman., M. Knight., E.C. Garnett., B. Ehrler. and W.C. Sinke. Photovoltaic materials: Present efficiencies and future challenges. Science, 352, (2016).

[55] R.A. Janssen. and J. Nelson. Factors limiting device efficiency in organic photovoltaics. Advanced Materials, 25(13), (2013), 1847-1858.

[56] R.R. Lunt., T.P. Osedach., P.R. Brown., J.A. Rowehl. and V. Bulović. Practical roadmap and limits to nanostructured photovoltaics. Advanced Materials, 23(48), (2011), 5712-5727.

[57] N.C. Giebink., G.P. Wiederrecht., M.R. Wasielewski. and S.R. Forrest. Thermodynamic efficiency limit of excitonic solar cells. Physical Review B, 83(19), (2011), 195326.

[58] J. Gilot., M.M. Wienk. and R.A. Janssen. Optimizing polymer tandem solar cells. Advanced Materials, 22(8), (2010), E67-E71.

[59] M.A. Green., K. Emery., Y. Hishikawa., W. Warta. and E.D. Dunlop. Solar cell efficiency tables (Version 45), Progress in Photovoltaics: Research and Applications, 23 (2015) 1-9.

[60] D. Bartesaghi., I.D.C. Pérez., J. Kniepert., S. Roland., M. Turbiez., D. Neher. and L. Koster. Competition between recombination and extraction of free charges determines the fill factor of organic solar cells. Nature Communications, 6(1), (2015), 1-10.

[61] C. M.Proctor., M. Kuik. and T.Q. Nguyen. Charge carrier recombination in organic solar cells. Progress in Polymer Science, 38(12), (2013), 1941-1960.

[62] M. List., T. Sarkar., P. Perkhun., J. Ackermann., C. Luo. and U. Würfel. Correct determination of charge transfer state energy from luminescence spectra in organic solar cells. Nature Communications, 9(1), (2018), 1-8.

[63] M. Nyman., O.J. Sandberg. and R. Österbacka. The effect of 2D-Langevin and trap-assisted recombination on the open circuit voltage in organic solar cells. In Organic Photovoltaics XVI (Vol. 9567, (2015), 5-13). SPIE.

[64] S.R. Cowan., R.A. Street., S. Cho. and A.J. Heeger. Transient photoconductivity in polymer bulk heterojunction solar cells: Competition between sweep-out and recombination. Physical Review B, 83(3), (2011), 035205.

[65] S. Ryu., N.Y. Ha., Y.H. Ahn., J.Y. Park. and S. Lee. Light intensity dependence of organic solar cell operation and dominance switching between Shockley-Read-Hall and bimolecular recombination losses. Scientific Reports, 11(1), (2021), 1-10.

[66] G.J.A. Wetzelaer, M. Kuik. and P.W. Blom. Identifying the nature of charge recombination in organic solar cells from charge-transfer state electroluminescence. Advanced Energy Materials, 2(10), (2012), 1232-1237.

[67] L.M. Chen., Z. Hong., G. Li. and Y. Yang. Recent progress in polymer solar cells: manipulation of polymer: fullerene morphology and the formation of efficient inverted polymer solar cells. Advanced materials, 21(14-15), (2009), 1434-1449.

[68] W.T. Choi., J. Song., J. Ko., Y. Jang., T.H. Kim., Y.S. Han., J. Lim., C. Lee. and K. Char. Effect of solvent additives on bulk heterojunction morphology of organic photovoltaics and their impact on device performance. Journal of Polymer Science Part B: Polymer Physics, 54(2), (2016), 128-134.

[69] B. Schmidt-Hansberg., M. Sanyal., N. Grossiord., Y. Galagan., M. Baunach., M.F. Klein., A. Colsmann., P. Scharfer., U. Lemmer., H. Dosch. and J. Michels. Investigation of non-halogenated solvent mixtures for high throughput fabrication of polymer–fullerene solar cells. Solar Energy Materials and Solar Cells, 96, (2012), 195-201.

[70] S.J. Lou., J.M. Szarko., T. Xu., L. Yu., T.J. Marks. and L.X. Chen. Effects of additives on the morphology of solution phase aggregates formed by active layer components of high-efficiency organic solar cells. Journal of the American Chemical Society, 133(51), (2011), 20661-20663.

[71] M.T. Fontana., H. Kang., P.Y. Yee., Z. Fan., S.A. Hawks., L.T. Schelhas., S. Subramaniyan., Y.J. Hwang., S.A. Jenekhe., S.H. Tolbert. and B.J. Schwartz. Low-vapor-pressure solvent additives function as polymer swelling agents in bulk heterojunction organic photovoltaics. The Journal of Physical Chemistry C, 122(29), (2018), 16574-16588.

[72] C.M. Proctor., M. Kuik. and T.Q. Nguyen. Charge carrier recombination in organic solar cells. Progress in Polymer Science, 38(12), (2013), 1941-1960.

[73] H. Cao., W. He., Y. Mao., X. Lin., K. Ishikawa., J.H. Dickerson. and W.P. Hess. Recent progress in degradation and stabilization of organic solar cells. Journal of Power Sources, 264, (2014), 168-183.

[74] M. Hermenau., M. Riede., K. Leo., S.A. Gevorgyan., F.C. Krebs. and K. Norrman. Water and oxygen-induced degradation of small molecule organic solar cells. Solar Energy Materials and Solar Cells, 95(5), (2011), 1268-1277.

[75] R.P. Xu., Y.Q. Li. and J.X. Tang. Recent advances in flexible organic light-emitting diodes. Journal of Materials Chemistry C, 4(39), (2016), 9116-9142.

[76] J. Song., P. Tyagi., K. An., M. Park., H. Jung., N. Ahn., M. Choi., D. Lee. and C. Lee. Degradation of electrical characteristics in low-bandgap polymer solar cells associated with light-induced aging. Organic Electronics, 81, (2020), 105686.

[77] H. Cao., W. He., Y. Mao., X. Lin., K. Ishikawa., J.H. Dickerson. and W.P. Hess. Recent progress in degradation and stabilization of organic solar cells. Journal of Power Sources, 264, (2014), 168-183.

[78] K. Norrman., M.V. Madsen., S.A. Gevorgyan. and F.C. Krebs. Degradation patterns in water and oxygen of an inverted polymer solar cell. Journal of the American Chemical Society, 132(47), (2010), 16883-16892.

[79] H.J. Son., H.K. Park., J.Y. Moon., B.K. Ju. and S.H. Kim. Thermal degradation related to the PEDOT: PSS hole transport layer and back electrode of the flexible inverted organic photovoltaic module. Sustainable Energy & Fuels, 4(4), (2020), 1974-1983.

[80] O. Oklobia., S. Komilian. and T. Sadat-Shafai. Impedance spectroscopy and capacitance-voltage measurements analysis: Impact of charge carrier lifetimes and mapping vertical segregation in bulk heterojunction P3HT: PCBM solar cells. Organic Electronics, 61, (2018), 276-281.

[81] X. Liu., S. Wang., H. Zheng., X. Cheng. and Y. Gu. Retracted Article: Comprehensive insights into the charge dynamics process and excellent photoelectric properties of heterojunction solar cells. Physical Chemistry Chemical Physics, 18(35), (2016), 24299-24306.

[82] N. Gasparini., L. Lucera., M. Salvador., M. Prosa., G.D. Spyropoulos., P. Kubis., H.J. Egelhaaf., C.J. Brabec. and T. Ameri. High-performance ternary organic solar cells with thick active layers exceeding 11% efficiency. Energy & Environmental Science, 10(4), (2017), 885-892.

[83] W. Chen. and S.B. Darling. Understanding the role of additives in improving the performance of bulk heterojunction organic solar cells. *Microscopy and Microanalysis*, *21*(S3), (2015), 2439-2440.

[84] S.O. Oseni. and G.T. Mola. The effect of uni-and binary solvent additives in PTB7: PC 61 BM based solar cells, Solar Energy, 150 (2017) 66-72.

[85] C.J. Huang., K.L. Chen., Y.J. Tsao., D.W. Chou., W.R. Chen. and T.H. Meen. Study of solvent doped PEDOT: PSS layer on small molecule organic solar cells. Synthetic metals, 164, (2013), 38-41.

[86] J.M. Lee., J. Lim., N. Lee., H.I. Park., K.E. Lee., T. Jeon., S.A. Nam., J. Kim., J. Shin. and S.O. Kim. Synergistic concurrent enhancement of charge generation, dissociation, and transport in organic solar cells with plasmonic metal-carbon nanotube hybrids. Advanced Materials, 27(9), (2015), 1519-1525.

[87] Y. He and Y. Li. Fullerene derivative acceptors for high-performance polymer solar cells. Phys. Chem. Chem. Phys. 13(6), (2011), 1970-1983.

[88] L. Song., W.J. Wang., E. Barabino., D. Yang., V. Korstgens., P. Zhang., S.V. Roth. and P. Muller- Buschbaum. Composition morphology correlation in PTB7-Th/PC71BM blends films for organic solar cells. ACS Appl Mater Interfaces, 11(3), (2019), 3125–3135.

[89] W. Yanbin., Z. Changlong., F. Yawen., Y. Huang. and W. Biaobing. Various roles of dye molecules in organic ternary blend solar cells. Dyes and Pigments, 176, (2020), 108231.

[90] W. Li., H. Yao., H. Zhang., S. Li. and J. Hou, J. Potential of non-fullerene small molecules with high photovoltaic performance. Chemistry–An Asian Journal, 12(17), (2017), 2160-2171.

[91] Y. Cui., Y. Xu., H. Yao., P. Bi., L. Hong., J. Zhang., Y. Zu., T. Zhang., J. Qin., J. Ren. and Z. Chen. Single-junction organic photovoltaic cell with 19% efficiency. Advanced Materials, 33(41), (2021), 2102420.

[92] Z. Luo., R. Ma., T. Liu., J. Yu., Y. Xiao., R. Sun., G. Xie., J. Yuan., Y. Chen., K. Chen., G. Chai., H. Sun., J. Min., J. Zhang., Y. Zou., C. Yang., X. Lu., F. Gao. and H. Yan. Fine-tuning energy levels via asymmetric end groups enables polymer solar cells with efficiencies of over 17%. Joule, 4 (6), (2020), 1236−1247.

[93] R. Ma., T. Liu., Z. Luo., Q. Guo., Y. Xiao., Y. Chen., X. Li., S. Luo., X. Lu., M. Zhang. and Y. Li. Improving open-circuit voltage by a chlorinated polymer donor endows binary organic solar cells efficiencies of over 17%. Science China Chemistry, 63(3), (2020), 325-330.

[94] T. Wang., R. Sun., M. Shi., F. Pan., Z. Hu., F. Huang., Y. Li. and J. Min Solution-Processed Polymer Solar Cells with over 17% Efficiency Enabled by an Iridium Complexation Approach. Adv. Energy Mater. 10 (22), (2020), 2000590.

[95] M.B. Salim., R. Nekovei. and R. Jeyakumar. Organic tandem solar cells with 18.6% efficiency. Solar Energy, 198, (2020), 160-166.

[96] D. Baran., R.S. Ashraf., D.A. Hanifi., M. Abdelsamie., N. Gasparini., J.A. Röhr., S. Holliday., A. Wadsworth., S. Lockett., M. Neophytou. and C.J. Emmott. Reducing the efficiency-stability-cost gap of organic photovoltaics with highly efficient and stable small molecule acceptor ternary solar cells. Nature Materials, 16(3), (2017), 363-369.

[97] Y. Huo., H.L. Zhang. and X. Zhan. Nonfullerene all-small-molecule organic solar cells. ACS Energy Letters, 4(6), (2019), 1241-1250.

[98] W. Ye., Y. Yang., Z. Zhang., Y. Zhu., L. Ye., C. Miao., Y. Lin. and S. Zhang. Non-fullerene All-Small-Molecule Organic Solar Cells: Prospect and Limitation. Solar RRL, 4(11), (2020), 2000258.

[99] Z. Genene., W. Mammo., E. Wang. and M.R. Andersson. Recent Advances in n-Type Polymers for All-Polymer Solar Cells. Advanced Materials, 31(22), (2019), 1807275.

[100] G. Wang., F.S. Melkonyan., A. Facchetti. and T.J. Marks. All-Polymer Solar Cells: Recent Progress, Challenges, and Prospects. Angewandte Chemie International Edition, 58(13), (2019), 4129-4142.

[101] J. Hou., O. Inganäs., R.H. Friend. and F. Gao. Organic solar cells based on non-fullerene acceptors. Nature Materials, 17(2), (2018), 119-128.

[102] R.S. Gurney., D.G. Lidzey. and T. Wang. A review of non-fullerene polymer solar cells: from device physics to morphology control. Reports on Progress in Physics, 82(3), (2019), 036601.

[103] S. Dey. Recent progress in the molecular design of fused ring electron acceptors for organic solar cells. Small, 15(21), (2019),1900134.

[104] P. Cheng., G. Li., X. Zhan. and Y. Yang. Next-generation organic photovoltaics based on non-fullerene acceptors. Nature Photonics, 12(3), (2018), 131-142.

[105] J. Hou., O. Inganäs., R.H. Friend. and F. Gao. Organic solar cells based on non-fullerene acceptors. Nature Materials, 17(2), (2018), 119-128.

[106] C. Yan., S. Barlow., Z. Wang., H. Yan. and A. Jen., KY.; Marder, SR; Zhan, X. Non-fullerene acceptors for organic solar cells. Nat. Rev. Mater, 3, (2018), 18003.

[107] D.K. Sagdullina., I.E. Kuznetsov., A.V. Akkuratov., L.I. Kuznetsova., S.I. Troyanov. and P.A. Troshin. New alternating thiophene-benzothiadiazole electron donor material for small-molecule organic solar cells and field-effect transistors. Synthetic Metals, 250, (2019), 7-11.

[108] H. Lee., H. Jo., D. Kim., S. Biswas., G.D. Sharma. and J. Ko. The effect of acceptor end groups on the physical and photovoltaic properties of A–π–D–π–A type-oligomers with the same S, N-hetero pentacene central electron donor unit for solution-processed organic solar cells. Dyes and Pigments, 129, (2016), 209-219.

[109] Z. Zhang., J. Yuan., Q. Wei. and Y. Zou. Small-Molecule electron acceptors for efficient non-fullerene organic solar cells. Frontiers in chemistry, 6, (2018), 414.

[110] J. Chen., Q. Liu., H. Li., Z. Zhao., Z. Lu., Y. Huang. and D. Xu. Density functional theory investigations of DAD'structural molecules as donor materials in organic solar cell, Frontiers in Chemistry, 6, (2018), 200.

[111] C.L. Chochos., P. Chávez., I. Bulut., P. Lévêque., M. Spanos., E. Tatsi., A. Katsouras., A. Avgeropoulos., V.G. Gregoriou. and N. Leclerc. Experimental and theoretical investigations on the optical and electrochemical properties of π-conjugated donor-acceptor-donor (DAD) compounds toward a universal model. The Journal of chemical physics, 149(12), (2018), 124902.

[112] H.Y. Chung., J. Oh., J.H. Park., I. Cho., W.S. Yoon., J.E. Kwon., D. Kim. and S.Y. Park. Spectroscopic studies on intramolecular charge-transfer characteristics in small-molecule organic solar cell donors: a case study on ADA and DAD triad donors. The Journal of Physical Chemistry C, 124(34), (2020), 18502-18512.

[113] G. Zhang., J. Zhao., P.C. Chow., K. Jiang., J. Zhang., Z. Zhu., J. Zhang., F. Huang. and H. Yan. Nonfullerene acceptor molecules for bulk heterojunction organic solar cells. Chemical Reviews, 118(7), (2018), 3447-3507.

[114] G. Chai., J. Zhang., M. Pan., Z. Wang., J. Yu., J. Liang., H. Yu., Y. Chen., A. Shang., X. Liu. and F. Bai. Deciphering the Role of Chalcogen-Containing Heterocycles in Nonfullerene Acceptors for Organic Solar Cells. ACS Energy Letters, 5(11), (2020), 3415-3425.

[115] D. Li., N. Deng., Y. Fu., C. Guo., B. Zhou., L. Wang., J. Zhou., D. Liu., W. Li., K. Wang. and Y. Sun. Fibrillization of Non-Fullerene Acceptors Enables 19% Efficiency Pseudo-Bulk Heterojunction Organic Solar Cells. Advanced Materials, (2022), 2208211.

[116] L. Zhan., S. Li., T.K. Lau., Y. Cui., X. Lu., M. Shi., C.Z. Li., H. Li., J. Hou. and H. Chen. Over 17% efficiency ternary organic solar cells enabled by two non-fullerene acceptors working in an alloy-like model. Energy & Environmental Science, 13(2), (2020), 635-645.

[117] G. Cai., Y. Li., J. Zhou., P. Xue., K. Liu., J. Wang., Z. Xie., G. Li., X. Zhan. and X. Lu. Enhancing Open-Circuit Voltage of High-Efficiency Non-Fullerene Ternary Solar Cells with a Star-Shaped Acceptor. ACS Applied Materials & Interfaces, 12(45), (2020), 50660-50667.

[118] Z. Zhou., W. Liu., G. Zhou., M. Zhang., D. Qian., J. Zhang., S. Chen., S. Xu., C. Yang., F. Gao. and H. Zhu. Subtle molecular tailoring induces significant morphology optimization enabling over 16% efficiency organic solar cells with efficient charge generation. Advanced Materials, 32(4), (2020),1906324.

[119] Y. Cui., H. Yao., J. Zhang., K. Xian., T. Zhang., L. Hong., Y. Wang., Y. Xu., K. Ma., C. An. and C. He. Single-junction organic photovoltaic cells with approaching 18% efficiency. Advanced Materials, 32(19), (2020), 1908205.

[120] S.S. Wan., X. Xu., Z. Jiang., J. Yuan., A. Mahmood., G.Z. Yuan., K.K. Liu., W. Ma., Q. Peng. and J.L. Wang. A bromine and chlorine concurrently functionalized end group for benzo [1, 2-b: 4, 5-b′] diselenophene-based non-fluorinated acceptors: a new hybrid strategy to balance the crystallinity and miscibility of blend films for enabling highly efficient polymer solar cells. Journal of Materials Chemistry A, 8(9), (2020), 4856-4867.

[121] C. Zhu., J. Yuan., F. Cai., L. Meng., H. Zhang., H. Chen., J. Li., B. Qiu., H. Peng., S. Chen. and Y. Hu. Tuning the electron-deficient core of a non-fullerene acceptor to achieve over 17% efficiency in a single-junction organic solar cell. Energy & Environmental Science, 13(8), (2020), 2459-2466.

[122] Y. Zhao., H. Chen., C. Zhu., J. Yuan., Y. Li., J. Hai., Y. Hu., L. Jiang., G. Chen. and Y. Zou. Fine-tuning the energy levels and morphology via fluorination and thermal annealing enable high-efficiency non-fullerene organic solar cells. Materials Chemistry Frontiers, 4(11), (2020), 3310-3318.

[123] C. Li., J. Zhou., J. Song., J. Xu., H. Zhang., X. Zhang., J. Guo., L. Zhu., D. Wei., G. Han. and J. Min. Non-fullerene acceptors with branched side chains and improved molecular packing to exceed 18% efficiency in organic solar cells. Nature Energy, 6(6), (2021), 605-613.

[124] F. Liu., L. Zhou., W. Liu., Z. Zhou., Q. Yue., W. Zheng., R. Sun., W. Liu., S. Xu., H. Fan. and L. Feng. Organic Solar Cells with 18% Efficiency Enabled by an Alloy Acceptor: A Two-in-One Strategy. Advanced Materials, (2021), 2100830.

[125] L. Zhan., S. Li., T.K. Lau., Y. Cui., X. Lu., M. Shi., C.Z. Li., H. Li., J. Hou. and H. Chen. Over 17% efficiency ternary organic solar cells enabled by two non-fullerene acceptors working in an alloy-like model. Energy & Environmental Science, 13(2), (2020), 635-645.

[126] P. Bi., S. Zhang., Z. Chen., Y. Xu., Y. Cui., T. Zhang., J. Ren., J. Qin., L. Hong., X. Hao. and J. Hou. Reduced non-radiative charge recombination enables organic photovoltaic cells to approach 19% efficiency. Joule, 5(9), (2021), 2408-2419.

[127] Y. Cai., Y. Li., R. Wang., H. Wu., Z. Chen., J. Zhang., Z. Ma., X. Hao., Y. Zhao., C. Zhang. and F. Huang. A well-mixed phase formed by two compatible non-fullerene acceptors enables ternary organic solar cells with an efficiency of over 18.6%. Advanced Materials, 33(33), (2021), 2101733.

[128] W. Liu., S. Sun., L. Zhou., Y. Cui., W. Zhang., J. Hou., F. Liu., S. Xu. and X. Zhu. Design of Near-Infrared Nonfullerene Acceptor with Ultralow Nonradiative Voltage Loss for High-Performance Semitransparent Ternary Organic Solar Cells. Angew. Chem. (2022), e202116111.

[129] H. Yu., L. Arunagiri., L. Zhang., J. Huang., W. Ma., J. Zhang. and H. Yan. Transannularly conjugated tetrameric perylene diimide acceptors containing [2.2] paracyclophane for non-fullerene organic solar cells. Journal of Materials Chemistry A, 8(14), (2020), 6501-6509.

[130] K. Ding., T. Shan., J. Xu., M. Li., Y. Wang., Y. Zhang., Z. Xie., Z. Ma., F. Liu. and H. Zhong. A perylene diimide-containing acceptor enables a high fill factor in organic solar cells. Chemical Communications, 56(77), (2020), 11433-11436.

[131] G. Li., S. Wang., D. Li., T. Liu., C. Yan., J. Li., W. Yang., Z. Luo., R. Ma., X. Wang. and G. Cui. Chalcogen-Fused Perylene Diimides-Based Nonfullerene Acceptors for High-Performance Organic Solar Cells: Insight into the Effect of O, S, and Se. Solar RRL, 4(3), (2020), 1900453.

CHAPTER 3

FUNDAMENTAL THEORY OF PLASMONIC

3.1 Introduction

Over the last few decades, plasmonics has succeeded as a field, spanning a massive spectrum of optical frequencies and showcasing diverse phenomena with potential applications. The study of plasmons, the collective charge oscillations in conducting and semiconducting materials, defines the field of plasmonics at its most fundamental level. The interactions between collective charge oscillations and electromagnetic (EM) radiation at the surface of conductive materials are primarily responsible for the phenomena driving the ever-growing interest in the field of plasmonics. It is to be noted that affordable, abundant, and sustainable energy sources are driving a surge in the pursuit of augmenting solar power and utilizing waste heat from not only industrial plants but also everyday household appliances. The interplay between light and matter is a crucial aspect of energy conversion mechanisms driven by radiation, with the density of states in different materials exerting a profound influence on all forms of optical interactions. The quantity of available 'channels' for containing and directing electromagnetic energy within a given medium is determined by its optical density of states (ODSs). Interestingly, nanostructured materials have the betterment of optical properties that surpass those of conventional isotropic media. These materials can be engineered to exhibit elevated ODS values, leading to improved light trapping and controlled emission spectra. The resulting benefits can be improved across a wide range of energy conversion schemes, including solid-state lighting, solar-thermal technologies, PV, thermophotovoltaic, and photocatalytic applications. Furthermore, possessing an unprecedented sub-wavelength light focusing capability and the ability to modify the ODSs, plasmonic materials have an array of desirable characteristics for numerous applications. Plasmonic materials exhibit unique characteristics that stem from the resonant collective oscillations of charge carriers, which are commonly referred to as plasmons. These plasmons can be stimulated through a diverse range of sources, such as thermal fluctuations, embedded emitters, and external illumination sources, respectively [1-3]. The interplay between long-range Coulomb forces and the spatial distribution of electron plasma plays a crucial role in determining the collective dynamics of volume plasmon oscillations. The surface plasmon polariton (SPP) occurs when the electron plasma oscillation occurs at the interfaces between metals or the metal/dielectric medium under

the influence of an external changing electromagnetic. Exploring the phenomenon of SPP waves arising from plasmons confined to metal-dielectric interfaces and thin metal films that coupled with photons [4,5]. The SPPs exhibit a peculiarly flat dispersion profile, manifesting at wavelengths below those of conventional free-space waves. This property has attracted interest in deploying them for advanced information processing applications [6,7]. However, the flat dispersion is more advantageous and it can probably lead to high ODS readings at certain frequencies that coincide with the excitation of SPP modes. The localized surface plasmon (LSP) modes, exhibiting quantization, are sustained by both wavelength and sub-wavelength-scale particles, resulting in a better ODS, as indicated by sources [8,9]. The LSPR is a phenomenon that occurs when metal NPs, typically of nanometer scale, interact with EM radiation. When these NPs are exposed to EM radiation, such as visible or near-infrared light, the collective oscillation of their conduction electrons, known as surface plasmons, can be excited. This excitation leads to strong resonant absorption and scattering of light at a specific wavelength. The schematic diagram of nanostructure shapes is shown below.

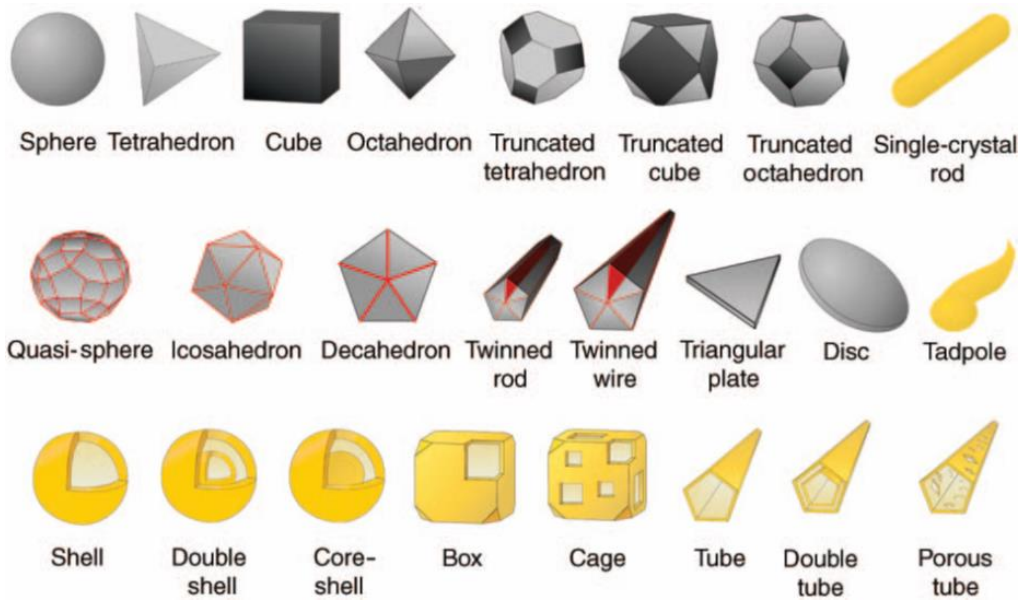

Figure 3.1: The schematic diagram of nanostructure shapes. Reproduced with permission [19].

The uppermost shape row of figure 3.1 unveils single crystals, while the middle row showcases particles decorated with twin defects or stacking faults. The third row prominently introduces the gold shells. Many twinned and single-crystal shapes of crystals can be synthesized in solution, with the exclusion of the octahedron. Controlling the shape of materials, such as wires, tubes, and rods, indeed has a significant impact on their optical, catalytic, and electronic properties. The facets of darkness gracefully signify the (100) planes,

the light gray enveloping them represents the (111) planes, while {111} twin planes are boldly presented in red. The gold shapes stand as symbols of gold particles, while their gray shapes symbolize silver particles. Notably, the spheres, twinned rods, icosahedrons, and cubes, can be gracefully fashioned from gold as well. Plasmonic materials and particles have a desirable ability to induce a substantial ODS in their proximate surroundings. Such better characteristic has proven to be highly advantageous for diverse applications such as in biochemical sensing, fluorescence, and Raman spectroscopy. Notably, the potential of plasmonics in energy applications has sparked significant interest among researchers [10-16]. Plasmonics concerns itself with the localization, routing, and orchestration of EM fields, operating at sub-wavelength dimensions that push beyond the ordinary diffraction limit and into the nanoscale [17,18]. The main constituent of plasmonics is metal due to its support SPP modes exhibited as surface plasmons (SPs), which are EM waves combined with the collective oscillations of the free electrons in the metal. It is important to note that the development of synthetic methodologies has also advanced to a level where nanostructures can be produced from many kinds of materials with quality, quantity, and yield required for the systematic investigation of their peculiar properties, as provided in figure 3.1. The shapes on top row display the single crystal, the second row are particles with stacking fault or twin defect, and third row indicate the gold shells.

3.2 Plasmonic nanomaterials

It is important to acknowledge the significance of the localized surface plasmonic resonance (LSPR) effect, which is a defining intrinsic characteristic of plasmonic materials. According to reports, noble metals have been predominantly engineered for various ranges of applications, leaving room for the emergence of alternative plasmonic nanomaterials [20]. Table 3.1 summarizes the diverse array of materials in which the LSPR effect can be observed, including heavily doped semiconductors, metal oxides, 2D materials, and conducting polymers. These materials show a similar phenomenon to the LSPR effect, highlighting the broad applicability of this attractive optical phenomenon. The resonance wavelength range of such materials is inherent and can be finely tuned by manipulating their morphology and size. Such reasonable characteristic affords the opportunity to achieve extensive spectral coverage, making them highly desirable for a variety of applications. As a result of its intended use and economic benefits, the materials possess the potential to provide a wider range of options that can be integrated with various other materials [20]. Understanding the physics behind the LSPR effect

can play a prominent role in the fabrication and implementation of plasmonic NPs for developing various applications, and numerous quantification approaches such as Mie theory and numerical simulations, respectively [20]. These have gone a long way to describe the LSPR effect phenomena of metallic NPs. In most cases, semiconductors typically display resonance red-shifting beyond the visible and near-infrared (NIR) ranges of prominent metallic materials, with small sizes (<10 nm) of semiconductor particles such as quantum dots - holding great potential for use in biomedical applications. However, the most prominent metallic NPs like Ag reign supreme in resonance intensity, rendering them an ideal choice for applications that require resonance. Interestingly, metallic NPs show impressive benefits because of their sizeable scattering and absorption cross-section, remarkable field augmentation, and effortless ability to adopt various reproducible morphologies.

Table 3.1: Properties of various plasmonic materials [21].

Materials	**Mechanism**	**Examples**	**LSPR range**	**Advantages**	**Comments**
Metallic nanostructures	Free electrons	Au, Ag, Cu, and their alloys	UV-Visible	controllable synthesis methods	Costly, limited permittivity
Semiconductor nanocrystals	Free holes	Cu_{2x}-S, Cu_{2x}-Se, ITO, TiN	Visible-NIR	Broader NIR absorbance	Difficult to dope
2D materials	Electrons and holes	Graphine, MoS_2	NIR	Strong plasmonic effect	Tedious synthesis processing
Conductive polymer	Polaronic charge carriers	Poly(3,4-ethylene-dioxythiophene: sulfate)	NIR	Low cost and flexibility	Low electrical conductivity and high defect density

3.2.1 Electromagnetic interaction with plasmonic nanoparticles

In an EM wave of the incidence, the electric field oscillates perpendicular to the direction of wave propagation. When this wave interacts with metallic NPs, the free electrons in the NPs are driven to move in response to the electric field. However, the direction of the electron

movement is one side having a net positive charge and the other side having a net negative charge for each particle. This effect can have important consequences for the behavior of particles in electric fields. For example, it can help to explain the high conductivity of metals, which arises from the ability of free electrons in the metal to respond to an applied electric field. As a result, the electric field inside the particle is reduced, while the field at its surface is enhanced [22]. For NPs with a diameter smaller than 20 nm, the induced dipole moment may be spatially invariant, meaning that it is distributed uniformly throughout the NPs. However, this induced dipole moment varies with time, following the oscillating electric field of the incident EM wave. The time-varying induced dipole moment, in turn, affects the local EM field around the NPs and contributes to the LSPR. The LSPR phenomenon has many important applications, including in biosensing, catalysis, and plasmon-enhanced spectroscopy. In electrostatics, the charge distribution in a system gives rise to an electric field. The electric field can be calculated using Coulomb's law or the principle of superposition of electric fields. In simple systems, the electric field can be described by a simple formula, such as that of a point charge. However, for larger systems, such as molecules or extended objects, higher-order poles or multipoles must be taken into account to describe the charge-induced field. The collective oscillation of the electron harvest of the optical extinction cross-section (σ_e) is a measure of the total amount of light that is scattered and absorbed by the NPs. The extinction cross-section includes both the scattering cross-section (σ_{scat}) and the absorption cross-section (σ_{abs}). The (σ_{scat}) is the amount of light that is scattered in all directions by the NPs, while the (σ_{abs}) is the amount of light that is absorbed by the NPs [23]. In addition to scattering, metallic NPs can also absorb light through the excitation of surface plasmons, which are collective oscillations of the nanoparticle's free electrons in response to the incident EM field. The absorbed energy is converted into heat through the resistance of the nanoparticle's metallic lattice, which results in an increase in the temperature of the surrounding medium. This phenomenon is known as photothermal heating, and it has important applications in fields such as photothermal therapy and solar energy conversion. In the context of absorbing light, the (σ_{abs}) measures the effective area of absorption. This characteristic can be effectively utilized for targeted heating applications, including hyperthermia in cancer therapy [24]. In short, the (σ_{ext}) can be expressed mathematically as

$$\sigma_{ext} = \sigma_{scat} + \sigma_{abs}\,. \tag{3.1}$$

The above equation corresponds to the extinction cross-section by scattering and absorption when the light is incident in NPs. The wavelength of the incident EM wave also plays a crucial role in determining the optical cross-section. The NPs have different sizes and shapes, and each size and shape has a specific resonance frequency that can interact strongly with certain wavelengths of light. This phenomenon is known as surface plasmon resonance, and it can result in a significant enhancement of the optical cross-section at certain wavelengths. Interestingly, plasmonics can play a vital role due to their scattering, extinction, and absorption cross-sections, which are substantial when the incident light reaches the resonance condition [25].

3.2.2 Permittivity of metals

It is to be noted that the optical properties of metal NPs primarily depend on the dielectric functions of the metal NPs and that of surrounding medium such as, $\varepsilon(\omega)$, which is composed of both real $(\varepsilon_r(\omega))$ and imaginary parts $(\varepsilon_i(\omega))$

$$\varepsilon(\omega) = \varepsilon_r(\omega) + i\varepsilon_i(\omega). \quad (3.2)$$

Where ω is the angular frequency. In general, the position of the resonance peak is mostly determined by the real part while dephasing depends on the imaginary part [22]. According to the statement, the position of the resonance peak is mainly influenced by the real part of a system's response or material's properties. The real part is associated with the system's or material's ability to store and release energy. It affects the frequency at which resonance occurs, meaning that changes in the real part can shift the resonance peak to different frequencies. Therefore, variations in the real part of a system's response or material's properties can have a significant impact on the position of the resonance peak. On the other hand, dephasing, which is the loss of coherence, is influenced by the imaginary part of the system's response or material's properties. The imaginary part is related to the dissipative processes or energy losses within the system. It characterizes the decay or damping of the resonant response. The imaginary part affects the width or broadening of the resonance peak, which is associated with the dephasing phenomenon. Changes in the imaginary part can modify the rate at which coherence is lost and, consequently, influence the dephasing behavior. However, the Drude model is indeed a simple classical model used to describe the behavior of conduction electrons in metals. It was introduced by Paul Drude in the early 20th century and forms the basis for understanding electrical conductivity in metals [26]. In the Drude model, conduction electrons

are treated as free electrons moving through a lattice of positively charged ions. These electrons experience collisions with the ions and other electrons, which cause them to scatter and change direction. However, between collisions, the electrons move freely and can be approximated as a gas of non-interacting particles. Mathematically, such can be expressed as

$$\varepsilon(\omega) = 1 - \frac{\omega_p^2}{\omega(\omega + i\gamma_b)}. \tag{3.3}$$

where ω_p indicates the plasma frequency and γ_b seems to be the bulk damping constant related to the Fermi Velocity V_F and the mean free path l_m can be written mathematically as

$$\gamma_b = \frac{V_F}{l_m}. \tag{3.4}$$

It is to be noted that the quantification of the Fermi velocity hinges on the interplay between electron density, the effective mass of electrons, and the vacuum permittivity, respectively. In summary, while electron density, the effective mass of electrons, and vacuum permittivity play important roles in understanding the behavior of electrons in materials, they are not sufficient to quantify the Fermi velocity. The Fermi velocity is a separate property determined by the electronic band structure of the material. It varies with the electron density of different metals. The electron density in metals is influenced by factors such as the number of valence electrons, the atomic size, and the arrangement of atoms in the crystal lattice. Metals with a higher number of valence electrons and larger atomic sizes tend to have higher electron densities. Additionally, metals with more closely packed crystal structures can have higher electron densities compared to metals with more open structures. The mean free path is a concept commonly used in physics to describe the average distance travelled by a particle, such as a photon or a charged particle before it collides with another particle or interacts with its surroundings. The value of the mean free path depends on several factors, including the nature of the particles involved and the environment in which they are present.

3.2.3 Plasmas and plasmons of metals

The plasmons are collective oscillations of free electrons in a material that can interact strongly with incident light. They arise due to the interaction between the EM field and the free charges (usually electrons) in a solid or a metal surface. When the frequency of the incident light matches the natural frequency of the plasmons, resonance occurs, leading to enhanced light-matter interactions. Interestingly, metals do contain freely mobile charges (electrons), they are

not considered plasmas because the atoms themselves are not ionized. In plasmas, the ionization process separates the electrons from the atoms, creating a mixture of positive and negative charges that behave collectively. Nonetheless, there exists the possibility of maintaining bulk plasma by means of longitudinal plasma oscillations (plasmons), which manifest as oscillatory behavior at frequencies dictated by the restoring force exerted on movable charges due to alterations in the charge distribution when they are displaced from their equilibrium positions. A pertinent example would be the passage of an electron in the vicinity [27,28]. In a bulk plasma, the plasma frequency ω_p can be expressed [29] mathematically as

$$\omega_p^2 = \frac{ne^2}{\varepsilon_0 m}. \tag{3.5}$$

Where n is the density number of mobile charge carriers, e is the charge, m is the mass, and ε_0 represents the permittivity relative to the free space. It is to be noted that when EM radiation, including light, with a frequency below the plasma frequency interacts with plasma, it can induce motion in the charge carriers. This motion of the charges creates an oscillating electric field that acts to screen out the incident field, which is known as the plasma's shielding effect. The plasma frequency is the characteristic frequency at which charged particles in a plasma collectively respond to an external electric field. When the frequency of an incident EM wave is higher than the plasma frequency, the charged particles in the plasma are unable to respond quickly enough to the changing electric field. As a result, they cannot effectively screen out or cancel the incident field, and the wave is transmitted through the plasma.

3.3 Surface plasmon-polaritons

The surface plasmon-polaritons (SPPs) are collective oscillations of free electrons at the interface between a metal and a dielectric material. They arise due to the coupling between the EM field and the collective motion of electrons, known as plasmons. The SPPs have unique properties and can be exploited for various applications in nanophotonics and optoelectronics. They enable strong light confinement below the diffraction limit, leading to enhanced light-matter interactions. SPPs have been utilized in areas such as surface-enhanced spectroscopy, sensing, imaging, and integrated photonics, among others. In contrast to the localized modes associated with the particles, SPP modes associated with a planar interface are extended in nature and may propagate, typically over a few tens of micrometers. The SPP modes are EM waves that are coupled to the collective oscillations of electrons at the interface between a metal and a dielectric medium. Unlike localized modes, such as plasmons confined to individual NPs,

SPP modes are extended along the interface. This has gone a long way to encourage researchers to use SPP as a means of providing better integration of the optical signals than is currently achieved using dielectric light guides [30-33]. To gain insights into the nature of propagating waves within SPPs, it proves enlightening to examine the dispersion relation governing their modes. This can be observed by applying desirable boundary conditions to Maxwell's equations, which is beneficial in observing proper solutions that take the form of a surface wave [29]. This can be written mathematically as

$$K_{SPP} = K_0 \sqrt{\frac{\varepsilon_m \varepsilon_d}{\varepsilon_m + \varepsilon_d}}. \tag{3.6}$$

Where K_{SPP} exhibits the wavevector of the surface plasmon ($K_{SPP} = 2\pi/\lambda_{SPP}$), K_0 represents the free space wavevector ($K_0 = 2\pi/\lambda_{SPP}$), with λ_0 as the wavelength of light in free space, and λ_{SPP} indicates the wavelength of the SPP mode at the same frequency. However, if the square root term in equation (3.6) is usually positive and much greater than one, it suggests that the wavevector of the SPP mode is higher than that of the incident light with the same frequency. The wavevector represents the spatial frequency or the number of wavelengths per unit distance. It is to be noted that Bragg scattering is another method used for SPP excitation. It relies on the periodic modulation of the metal-dielectric interface, creating a grating structure. The incident light interacts with the grating and undergoes scattering, leading to momentum (wavevector) matching with the SPP modes. On the other hand, the frequency (wavelength) of LSPR can be observed by a resonance condition. According to a recent study, particle plasmon resonances exhibit promising prospects as a transformative technology for PV solar cells [34]. The presence of small metallic particles in a material can indeed enhance the absorption of solar light through a phenomenon called particle plasmon resonance. When metallic NPs are exposed to light, the free electrons in the metal can undergo collective oscillations known as plasmons. These plasmons can be excited by incident light and lead to a concentration of the EM field around the particles, increasing their light absorption capability [35,36].

3.3.1 Localized surface plasmon resonance effect

The localized surface plasmonic resonance (LSPR) effect is primarily driven by the attraction between the EMF of the incident light and the electron plasma residing on the surface of metal NPs, which is beneficial in providing unique optical properties and enabling a wide range of applications in nanotechnology. Indeed, LSPR can be supported by a wide range of structures, offering versatility in designing plasmonic systems with tailored optical properties. While the

simplest and most studied structure is a spherical NP, researchers have explored various other shapes such as ellipsoids, rods, stars, and crescents, to achieve specific optical responses [37-39]. Ellipsoidal NPs show anisotropic behavior due to their elongated shape. This anisotropy leads to different resonance properties along different axes, offering control over the spectral response of the LSPR. Nanorods are elongated NPs with rod-like shapes. Their aspect ratio (length-to-width ratio) affects the LSPR wavelength, allowing tuning of the resonance across a wide spectral range. Rod-shaped NPs are particularly useful in applications such as sensing and nonlinear optics. Star-shaped NPs have multiple branches or protrusions extending from a central core. The branches create additional hotspots where plasmonic interactions occur, enhancing the LSPR effects. Star-shaped NPs offer increased EM field enhancements and have been utilized in applications such as surface-enhanced Raman spectroscopy (SERS) and sensing. Crescent-shaped NPs have a curved geometry, resembling a crescent moon. This shape introduces intriguing plasmonic properties, such as asymmetric field distributions and strong near-field enhancements. Crescent NPs have been studied for applications like chiral sensing and optoelectronics.

When particle pairs interact, they can give rise to new resonances or states with specific properties [40]. Resonances are temporary excited states of particles that can decay into other particles. Recent studies suggest that under certain conditions, the aggregation of colloidal particles can lead to the formation of localized modes or regions of high field strength within the random medium [41]. Particles with holes, or toroidal structures, can also exhibit localized modes [42]. Localized modes refer to certain patterns of energy or vibration that are confined to a specific region or structure. These modes can arise in various systems, such as waveguides, optical cavities, or solid-state materials. It is to be noted that the frequency at which the LSPR effect of metallic NPs can indeed be tuned throughout the ultraviolet, visible, and infrared regions of the EM spectrum by adjusting the particle size and shape. This tunability has significant implications in various fields, including sensing, imaging, PVs, and biomedical applications. Interestingly, the absorption and scattering depend on the size of the NPs. As the size increases, more photons interact with the NPs, resulting in a higher probability of absorption and scattering. Consequently, the optical extinction of metallic NPs escalates with increasing particle size. On the other hand, as the size of particles increases, scattering becomes more important in determining the extinction behavior of light, potentially leading to changes in the position and width of the LSPR effect [43]. When the size of a metal NP, such as a sphere, is increased from 10 nm to 90 nm, the plasmonic resonance peak typically shifts to

longer wavelengths, resulting in a redshift. This means that the resonance peak moves from shorter wavelengths (e.g., around 400 nm) towards longer wavelengths (e.g., around 800 nm). Recent studies have shed light on the fascinating alterations that occurs due to the interplay between the polarization field generated by surface charges and the amplitude and relative phase of both the scattered and incident fields [44]. Interestingly, considering the dispersion of the optical properties of the constituent material of the NPs that shift in the frequency is much more important for understanding and controlling the behavior of the LSPR effect, including the resonance frequency and damping characteristics [45]. Indeed, the shape of particles plays a crucial role in various scientific and technological applications, especially in the field of nanotechnology. The development of sophisticated fabrication techniques has enabled researchers to create nanostructures with different shapes, which in turn has opened new opportunities for optical studies. When it comes to fabricating particles, there are various methods employed, and two common approaches are growing particles within a solution and using lithographic techniques with a patterned mask. The goal of various studies in the field of plasmonics is indeed to optimize the localization and enhancement of the LSPR effect.

3.3.2 Light surface

It is to be noted that the metal NPs embedded in a dielectric medium can indeed act as efficient scatterers, leading to various optical phenomena such as light trapping or enhanced light-matter interactions. Interestingly, the light-trapping effects are particularly advantageous in various applications such as photovoltaics, light-emitting devices, and sensors. They can improve the absorption efficiency of solar cells by augmenting the light absorption in the active layer and enhancing the sensitivity and selectivity of optical sensors. Recent studies have reported that the incorporation of plasmonic nanostructures in solution processed TFOSCs devices has attracted much attention in research, which is desirable to augment solar energy harvesting through several mechanisms such as light scattering effect, LSPR effect, and SPP effect [46], as provided in figure 3.2. In the light scattering effect, Plasmonic nanostructures can scatter incident light, causing it to interact with the active layer of the solar cell over a longer path. This increased light-matter interaction enhances the absorption of photons, thereby increasing the overall efficiency of the device. In the LSPR effect, when the dimensions of the nanostructures are tuned to match the wavelength of the incident light, they can resonantly couple with the light, leading to strong electric field enhancements in their vicinity. This enhanced local electric field can increase the absorption of light in the active layer of the solar cell. In the SPP effect, plasmonic nanostructures can also support the propagation of SPPs,

which are coupled states of photons and surface plasmons. These SPPs can help in guiding and trapping light within the active layer of the solar cell, increasing the path length of light and enhancing absorption. Understanding that the metal NP scattering relies not only on the size but also on the shape, as both factors contribute to the overall optical response of the metallic nanostructures [47]. Interestingly, the larger diameter of the NPs, which is greater than 50 nm can scatter light in such a way that enhances the path length travelled by the scattered light within the medium. This is because the scattered light can undergo multiple scattering events as it interacts with the NPs, resulting in an increased path length. This increased path length allows for more interactions between the light and the medium, increasing the chances of absorption and interaction with solar absorbers present in the medium.

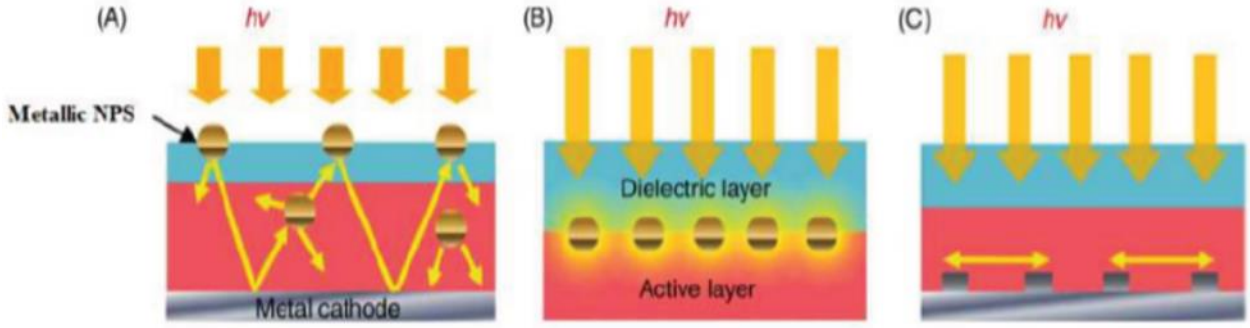

Figure 3.2: The schematic diagram of various mechanisms for plasmonic solar cells to augment the light absorption in the solar cells such as (A) light scattering effect, (B) LSPR effect, and (C) SPP effect, figure from Ref. [46].

Furthermore, the use of metal NPs positioned at the surface of the buffer layer in TFOSCs can indeed have a positive impact on the device performance. These metal NPs can scatter solar energy, particularly the reflected light at the top electrode, back into the active layer of the solar cell [48,49]. This scattering effect can be beneficial for generating more excitons, which are electron-hole pairs responsible for the absorption of light and subsequent electricity generation in the solar cell.

References

[1] J.A. Schuller., E.S. Barnard., W. Cai., Y.C. Jun., J.S. White. and M.L. Brongersma. Plasmonics for extreme light concentration and manipulation. Nature Materials, 9(3), (2010), 193-204.

[2] N.J. Halas. Connecting the dots: Reinventing optics for nanoscale dimensions. Proceedings of the National Academy of Sciences, 106(10), (2009), 3643-3644.

[3] M.I. Stockman. Nanoplasmonics: past, present, and Glimpse into Future. Optics Express, 19(22), (2011), 22029-22106.

[4] S.V. Boriskina., H. Ghasemi. and G. Chen. Plasmonic materials for energy: From physics to applications. Materials Today, 16(10), (2013), 375-386.

[5] F.J. Beck., A. Polman. and K.R. Catchpole. Tunable light trapping for solar cells using localized surface plasmons. Journal of Applied Physics, 105(11), (2009), 114310.

[6] K. Aydin., V.E. Ferry., R.M. Briggs. and H.A. Atwater. Broadband polarization-independent resonant light absorption using ultrathin plasmonic super absorbers. Nature Communications, 2(1), (2011), 517.

[7] M.A. Green. and S. Pillai. Harnessing plasmonics for solar cells. Nature Photonics, 6(3), (2012), 130-132.

[8] O. Neumann., A.S. Urban., J. Day., S. Lal., P. Nordlander. and N.J. Halas. Solar vapor generation enabled by nanoparticles. ACS nano, 7(1), (2013), 42-49.

[9] Z. Fang., Y.R. Zhen., O. Neumann., A. Polman., F.J. García de Abajo., P. Nordlander. and N.J. Halas. Evolution of light-induced vapor generation at a liquid-immersed metallic nanoparticle. Nano letters, 13(4), (2013), 1736-1742.

[10] B. Yan., S.V. Boriskina. and B.M. Reinhard. Design and implementation of noble metal nanoparticle cluster arrays for plasmon-enhanced biosensing. The Journal of Physical Chemistry C, 115(50), (2011), 24437-24453.

[11] A. Gopinath., S.V. Boriskina., B.M. Reinhard. and L. Dal Negro. Deterministic aperiodic arrays of metal nanoparticles for surface-enhanced Raman scattering (SERS). Optics Express, 17(5), (2009), 3741-3753.

[12] A. Polman. Solar steam nanobubbles. ACS nano, 7(1), (2013), 15-18.

[13] A. Kinkhabwala., Z. Yu., S. Fan., Y. Avlasevich., K. Müllen. and W.E. Moerner. Large single-molecule fluorescence enhancements produced by a bowtie nanoantenna. Nature Photonics, 3(11), (2009), 654-657.

[14] S. Lal., S. Link. and N.J. Halas. Nano-optics from sensing to waveguiding. Nature Photonics, 1(11), (2007), 641-648.

[15] J.A. Fan., C. Wu., K. Bao., J. Bao., R. Bardhan., N.J. Halas., V.N. Manoharan., P. Nordlander., G. Shvets. and F. Capasso. Self-assembled plasmonic nanoparticle clusters. *science*, *328*(5982), (2010), 1135-1138.

[16] K.A. Willets. and R.P. Van Duyne. Localized surface plasmon resonance spectroscopy and sensing. Annu. Rev. Phys. Chem., 58, (2007), 267-297.

[17] D.K. Gramotnev. and S.I. Bozhevolnyi. Plasmonics beyond the diffraction limit. Nature Photonics, 4(2), (2010), 83-91.

[18] J.A. Schuller., E.S. Barnard., W. Cai., Y.C. Jun., J.S. White. and M.L. Brongersma. Plasmonics for extreme light concentration and manipulation. Nature Materials, 9(3), (2010), 193-204.

[19] Y. Xia. and N.J. Halas. Shape-controlled synthesis and surface plasmonic properties of metallic nanostructures. MRS Bulletin, 30(5), (2005), 338-348.

[20] G.V. Naik., V.M. Shalaev. and A. Boltasseva. Alternative plasmonic materials: beyond gold and silver. Advanced Materials, 25(24), (2013), 3264-3294.

[21] L. Wang., M. Hasanzadeh Kafshgari. and M. Meunier. Optical properties and applications of plasmonic-metal nanoparticles. Advanced Functional Materials, 30(51), (2020), 2005400.

[22] U. Kreibig. and M. Vollmer. Optical properties of metal clusters (Vol. 25). Springer Science & Business Media, (2013).

[23] J. Olson., S. Dominguez-Medina., A. Hoggard., L.J. Wang., W.S. Chang. and S. Link. Optical characterization of single plasmonic nanoparticles. Chemical Society Reviews, 44(1), (2015), 40-57.

[24] M. Aioub. and M.A. El-Sayed. A real-time surface enhanced raman spectroscopy study of plasmonic photothermal cell death using targeted gold nanoparticles. Journal of the American Chemical Society, 138(4), (2016), 1258-1264.

[25] A.I. Henry., J.M. Bingham., E. Ringe., L.D. Marks., G.C. Schatz. and R.P. Van Duyne. Correlated structure and optical property studies of plasmonic nanoparticles. The Journal of Physical Chemistry C, 115(19), (2011), 9291-9305.

[26] N.W. Ashcroft. and N.D. Mermin. Solid state physics (holt, Rinehart and Winston, new york, 1976). Google Scholar, (2005), 403.

[27] R.A. Alvarez-Puebla., J.F. Li. and X.Y. Ling. Introduction to advances in plasmonics and its applications. Nanoscale, 13(12), (2021), 5935-5936.

[28] J. Gong., L. Yang., K. Tőkési. and Z. Ding. Surface and bulk plasmon excitations of silver by electron impact. The European Physical Journal D, 73, (2019), 1-7.

[29] W.A. Murray. and W.L. Barnes. Plasmonic materials. Advanced materials, 19(22), (2007), 3771-3782.

[30] R. Charbonneau., N. Lahoud., G. Mattiussi. and P. Berini. Demonstration of integrated optics elements based on long-ranging surface plasmon polaritons. Optics Express, 13(3), (2005), 977-984.

[31] S. Jetté-Charbonneau., R. Charbonneau., N. Lahoud., G. Mattiussi. and P. Berini. Demonstration of Bragg gratings based on long-ranging surface plasmon polariton waveguides. Optics Express, 13(12), (2005), 4674-4682.

[32] M.A. Fuentes-Fuentes., D.A. May-Arrioja., J.R. Guzman-Sepulveda., F. Arteaga-Sierra., M. Torres-Cisneros, P.L. Likamwa. and J.J. Sánchez-Mondragón. Suspended LRSPP for the development of highly integrated active plasmonic devices. Optics express, 27(6), (2019), 8858-8870.

[33] R. Guzman-Cabrera. and J.R. Guzman-Sepulveda. Plasmonic-dielectric hybrid interferometric structures for high-sensitivity refractive index sensing. Optik, 220, (2020), 165185.

[34] M. Di Vece. Cluster-assembled devices for solar energy conversion. In Frontiers of Nanoscience (Vol. 15, (2020), 59-86). Elsevier.

[35] B.P. Rand., P. Peumans. and S.R. Forrest. Long-range absorption enhancement in organic tandem thin-film solar cells containing silver nanoclusters. Journal of Applied Physics, 96(12), (2004), 7519-7526.

[36] K. Ding., X. Huang., Y. Li. and S.R. Forrest. Photogeneration and the bulk quantum efficiency of organic photovoltaics. Energy & Environmental Science, 14(3), (2021), 1584-1593.

[37] C. Sönnichsen., T. Franzl., T. Wilk., G. von Plessen., J. Feldmann., O.V. Wilson. and P. Mulvaney. Drastic reduction of plasmon damping in gold nanorods. Physical review letters, 88(7), (2002), 077402.

[38] C.L. Nehl., H. Liao. and J.H. Hafner. Optical properties of star-shaped gold nanoparticles. Nano letters, 6(4), (2006), 683-688.

[39] J.S. Shumaker-Parry., H. Rochholz. and M. Kreiter. Fabrication of crescent-shaped optical antennas. Advanced Materials, 17(17), (2005), 2131-2134.

[40] A.N. Grigorenko., A.K. Geim., H.F. Gleeson., Y. Zhang., A.A. Firsov., I.Y. Khrushchev. and J. Petrovic. Nanofabricated media with negative permeability at visible frequencies. Nature, 438(7066), (2005), 335-338.

[41] A. Degiron. and T.W. Ebbesen. The role of localized surface plasmon modes in the enhanced transmission of periodic subwavelength apertures. Journal of Optics A: Pure and Applied Optics, 7(2), (2005), S90.

[42] W.A. Murray. and W.L. Barnes. Plasmonic materials. Advanced materials, 19(22), (2007), 3771-3782.

[43] V. Jacobsen., P. Stoller., C. Brunner., V. Vogel. and V. Sandoghdar. Interferometric optical detection and tracking of very small gold nanoparticles at a water-glass interface. Optics express, 14(1), (2006), 405-414.

[44] T.A. Estrada-Mendoza., D. Willett. and G. Chumanov. Light Absorption and Scattering by Silver/Silver Sulfide Hybrid Nanoparticles. The Journal of Physical Chemistry C, 124(49), (2020), 27024-27031.

[45] C. Sönnichsen., T. Franzl., T. Wilk., G. von Plessen., J. Feldmann., O.V. Wilson. and P. Mulvaney. Drastic reduction of plasmon damping in gold nanorods. Physical review letters, 88(7), (2002), 077402.

[46] C.H. Chou. and F.C. Chen. Plasmonic nanostructures for light trapping in organic photovoltaic devices. Nanoscale, 6(15), (2014), 8444-8458.

[47] R. Veenkamp., S. Ding., I. Smith. and W.N. Ye. Silicon solar cell enhancement by plasmonic silver nanocubes. In Physics, Simulation, and Photonic Engineering of Photovoltaic Devices III (Vol. 8981, (2014), 211-218). SPIE.

[48] C. Burda., X. Chen., R. Narayanan. and M.A. El-Sayed. Chemistry and properties of nanocrystals of different shapes. Chemical Reviews, 105(4), (2005), 1025-1102.

[49] P. Spinelli., M. Hebbink., R. De Waele., L. Black., F. Lenzmann. and A. Polman. Optical impedance matching using coupled plasmonic nanoparticle arrays. Nano letters, 11(4), (2011), 1760-1765.

CHAPTER 4

Effective energy harvesting in thin-film organic solar cells using Ni/Zn as bimetallic nanoparticles

Journal of Physics and Chemistry of Solids 161 (2022) 110405

Contents lists available at ScienceDirect

Journal of Physics and Chemistry of Solids

journal homepage: www.elsevier.com/locate/jpcs

Effective energy harvesting in thin film organic solar cells using Ni:Zn as bimetallic nanoparticles

Jude N. Ike, Mohammed S.G. Hamed, Genene Tessema Mola *

School of Chemistry & Physics, University of KwaZulu-Natal, Pietermaritzburg Campus, Private Bag X01, Scottsville, 3209, South Africa

ARTICLE INFO

Keywords:
Bimetallic nanoparticles
Acceptors
Donors
Bulk-heterojunction
Power conversion efficiencies

ABSTRACT

This article explores the effect of bimetallic plasmonic nanocomposites in the solar absorber layers of thin-film organic solar cells (TFOSCs) for possible improvement in harvesting solar energy. To achieve this goal, a new nanocomposite composed of Nickel and Zinc (Ni: Zn) was successfully synthesized by the use of a chemical reduction processes. The effect of bimetallic nanocomposites was studied using a photoactive medium, which comprises of poly-(3-hexylthiophene) (P3HT) [6,6]-phenyl C61 butyric acid methyl ester (PC61BM) blend and doped with Ni:Zn at different concentrations. Consequently, an improved power conversion efficiency value up to 4.78% was found at 1% Ni:Zn bimetallic concentration by weight compared to reference solar cell. This is a clear indication of the influence of Ni:Zn bimetallic nanoparticles on the performance of TFOSC. These effects have been realized by the occurrence of local surface plasmon resonance (LSPR) phenomenon caused by Ni: Zn nanoparticles in polymer medium.

4.1 Abstract

This article explores the effect of bimetallic plasmonic nanocomposites in the solar absorber layers of thin-film organic solar cells (TFOSCs) for possible improvement in harvesting solar energy. To achieve this goal, a new nanocomposite composed of Nickel and Zinc (Ni/Zn) was successfully synthesized using a chemical reduction process. The effect of bimetallic nanocomposites was studied using a photoactive medium, which comprises of poly-(3-hexylthiophene) (P3HT)/[6,6]-phenyl C61 butyric acid methyl ester (PC61BM) blend and doped with Ni/Zn at different concentrations. Consequently, an improved power conversion efficiency value of up to 4.78% was found at 1% Ni/Zn bimetallic concentration by weight compared to reference solar cells. This is a clear indication that the effect of Ni/Zn bimetallic nanoparticles doped with active layer is favorable to augment the performance of TFOSC. These effects have been realized by the occurrence of the localized surface plasmon resonance (LSPR) phenomenon caused by Ni/Zn nanoparticles in a polymer medium.

4.2 Introduction

It is well noted that fossil fuel has been the leading source of energy for humanity's day-to-day livelihood for centuries. However, recent studies have reported that the residual from the use of fossil fuel harmfully impacts the mere existence of life on Earth due to the emission of carbon dioxide (CO_2) and poisonous gases into the Earth's atmosphere [1]. On this note, the current predictions have suggested that the three types of fossil fuels, including oil, coal, and as well as natural gas, can possibly be exhausted in the next few decades. Therefore, there is an urgent desire to find adequate alternative energy sources for a sustainable and suitable energy supply to the global need. Interestingly, solar energy conversion into electricity by way of the photovoltaic effect is one of the possibilities and impressive methodologies to cope with energy shortage worldwide. It has been reported recently that thin-film organic solar cells (TFOSCs) seem to be inspiring materials and beneficial to convert photon energy into electricity [2,3]. Hence, the TFOSCs are the most promising light-harvesting devices in producing and providing sufficient cheap renewable energy due to their possible lightweight, flexibility, low cost, and easy fabrication processes via solution processing compared to their inorganic counterparts [4-9]. Nevertheless, the recorded power conversion efficiency (PCE) value for high-performance TFOSCs based on fullerene derivative has increased dramatically above 10%, which seems to be adequate to generate much electricity for domestic use in our societies based on the literature [10-12]. However, it has been reported by recent studies that the unsteadiness of the particles in the ambient surroundings makes device fabrication unproductive due to oxygen and humidity that harshly impact the solar absorber layer for sunlight conversion ability [13-15]. Regardless of these challenges, the TFOSCs still play a vital role and become more favorable in providing several advantages such as flexibility, lightweight, and cheap device fabrication via roll-to-roll processing techniques.

It is to be noted that the bulk-heterojunction (BHJ) is the most suitable and successful solar absorber layer of TFOSCs, which is formed by the blend of the acceptor (A) material and donor (D) polymer molecules. The BHJ absorber layers are sandwiched between two electrodes to collect- photon-generated charges [16,17]. Captivatingly, the interfacial buffer layers among solar absorber medium and electrodes have significantly enriched the charge carrier mobility in the devices, which is beneficial to optimize the ability to measure photocurrent [14]. Holes and electrons are the two main leading charge carriers, which are transported along the donor and acceptor (D/A) domain to be collected by the electrodes in

the TFOSC, respectively. The most used hole transport layer in TFOSCs structural is Poly (3,4-ethylene dioxythiophene): Polystyrene-para-sulfonic acid (PEDOT/PSS). It is promising to escalate both the collection and charge transport of holes from the solar absorber to the anode electrode [14]. The PEDOT/PSS is a suitable water-soluble conducting polymer, which consists of a sustainable work function (5.1 eV), transparency to light (> 85%), and favorable electrical conduction [18]. Despite the strengths mentioned above, PEDOT/PSS negatively led to a reduction of device performances and stability of TFOSCs due to its acidic and hygroscopic nature [19-21]. To address this issue, several metallic nanocomposites/nanoparticles were employed as a considerable mechanism to alleviate the disadvantage of PEDOT/PSS, and this will go a long way to boost the high performance in TFOSC applications [14,22-26]. Fascinatingly, the nanoparticles' electrical and optical properties seem to be favorable to harvesting sufficient photo-current because of the localized surface plasmon resonance effect (LSPR) of the metal nanoparticles [27]. It is important to note that the surface plasmon resonance (SPR) and LSPR of noble metal nanocomposites have attracted much attention for research due to their wide range of application potential in the fields of photonics, sensor, medicine, photocatalysis, and solar energy harvesting, etc. The interaction between the electromagnetic (EM) field of the incident light and the surface electron plasma of the metal nanoparticles is the main reason for the occurrence of LSPR and SPR. Both LSPR and SPR are dependent on the size and shape of the metal nanoparticles. Figure 4.1 demonstrates the occurrence of plasmon resonances for various shapes of metal nanocomposites, for example, resonances occur near the UV range for spherical shape nanoparticles while resonances occur in the far infrared regions for nano-rice-like structures. It is to be noted here that the size of the nanoparticles must be smaller than the wavelength of the incident light for LSPR to occur in the medium as depicted in figure 4.1. The electric field component of the incident EM radiation polarizes the surface charge of the metal nanoparticles that leads to charge oscillation which eventually cause resonances. Such resonance absorption leads to the generation of electron-hole pairs due to (i) the hot electrons produced by LSPR absorption, or (ii) propagation of light on the surface nanoparticles, which serve as waveguides due to SPR or as antennas to convert sunlight into the localized electrical field [28]. Photocatalysis is one of the key application areas which has emerged as a promising technology for various applications, including water splitting, energy generation, and device fabrication [29]. Similarly, plasmon metal nanoparticles have been successfully used in harvesting photons in various thin-film solar cell technologies.

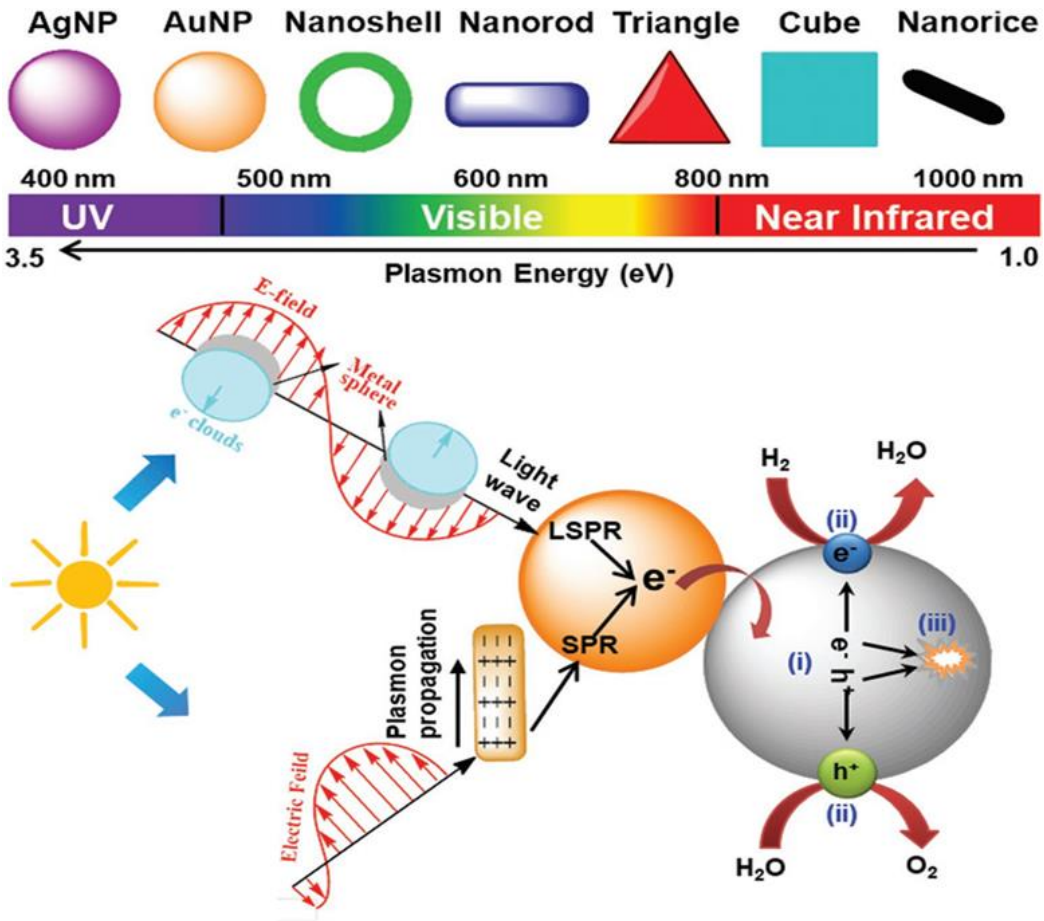

Figure 4.1: The plasmon resonances for various nanocomposites, SPR, and the LSPR, and different stages during the process of solar water splitting. (i) generation of electron-hole pairs by solar irradiation. (ii) migration of electrons and holes to the surface-active sites for hydrogen and oxygen evolution reactions. (iii) recombination of electrons and holes. Reproduced with permission [28].

The generation of hot electron-hole pairs and/or the formation of an intense electromagnetic field in the vicinity of metal nanoparticles are some of the mechanisms required to improve the formation and separation of excitons within the absorber medium [30]. Some metallic nanocomposites, including zinc (Zn), gold (Au), and silver (Ag) have recently been invested in the synthesis of single or mono-metallic nanoparticles due to their LSPR effect to assist in harvesting more photo-current [14]. However, bimetallic nanoparticles, which consist of two different elements, can offer suitable exciting properties, which can lead to superior characteristics compared to their counterpart mono-metallic nanoparticles [27, 31].

In this study, nickel/zinc (Ni/Zn) bimetallic nanoparticles were effectively synthesized to augment the processes of charge carrier mobility and exciton dissociations by way of considerable high light scattering and long-range LSPR effect. The Ni/Zn bimetallic nanoparticle was further incorporated into the poly-(3-hexylthiophene) (P3HT)/[6,6]-phenyl

C61 butyric acid methyl ester (PC61BM) as a solar absorber in conventional TFOSCs to harvest sufficient photo-current. The TFOSC devices are well fabricated using Ni/Zn bimetallic with a mixture of P3HT/PC61BM as a solar absorber. Consequently, the substantial PCE value of around 4.78% was recorded at 1% concentration by weight compared to the Pristine (2.56%) un-doped layer. Such remarkable improvement is largely accredited to boosting photo-current harvesting because of the desirable mixture of Ni/Zn bimetallic nanoparticles within the active layer. Therefore, the experimental details will be presented and discussed in the following sections.

4.3 Experimental sections

4.3.1 Resources

In this study, the chemicals and necessary materials were purchased and used without any additional processing except the synthesis of nickel/zinc (Ni/Zn) as bimetallic nanoparticles. The chemicals including poly (3,4-ethylene dioxythiophene): poly (styrene-sulfonate) (PEDOT/PSS), Poly (3-hexylthiophene) (P3HT) 95 %, and [6,6]-phenyl-C61-butyric acid methyl ester (PC61BM) 95 % purity were bought from Ossila Co. Ltd. Nickel nitrate hexahydrate (> 99% ($Ni(NO_3)_2$ $6H_2O$), zinc nitrate hexahydrate (> 99.98% $Zn(NO_3)_2$ $6H_2O$), sodium borohydride (> 99.98% $NaBH_4$), indium tin oxide (ITO) treated glasses were bought from Merck, Germany.

4.3.2 Synthesis of nickel/Zinc (Ni/Zn) bimetallic nanoparticles

The bimetallic nanoparticles of Ni/Zn were synthesized using a chemical reduction approach, which was achievable using a similar procedure as reported by other investigators [32,33]. The materials employed involve 0.2 M of ($Ni(NO_3)_2$ $6H_2O$), 0.1 M of ($Zn(NO_3)_2$ $6H_2O$), and 0.5 M of $NaBH_4$, respectively. The 0.5 M of $NaBH_4$ was used and served as a reducing agent. The above chemicals were dissolved in each 50 mL deionized water in three separate flasks and stirred suitably for 10 min. After that, the solutions were further mixed up, commencement with ($Ni(NO_3)_2$ $6H_2O$) solution followed by dropwise adding of ($Zn(NO_3)_2$ 6H2O) and $NaBH_4$ solutions under stirring to prepare Ni/Zn bimetallic nanoparticles. The mixtures were then stirred continuously on a hot plate with a magnetic stirrer at the temperature of 40 ^oC for 3 hours. The resultant precipitate was then filtered and washed thoroughly with deionized water and ethanol several times to eliminate sodium ions. However, the resultant Ni/Zn bimetallic nanoparticles were further dried up in the oven for 2 hours at the temperature of 70 ^oC. The

powder of Ni/Zn bimetallic nanoparticles was also characterized based on their optical, structural, and morphological properties using ultraviolet-visible (UV-Vis) absorption spectroscopy, scanning electron microscopy (SEM), transmission electron microscopy (TEM), and X-ray diffraction (XRD) measurements.

4.3.3 Device preparation

The TFOSCs were successfully fabricated using un-patterned ITO-coated glass substrates. Initially, the substrates with a sheet resistance of 15 Ω/sq were partially etched with the warm acid solutions, which include hydrochloric acid, hydrogen-2-oxide, and trinitrate-5-acid ($HCL/H_2O/HNO_3$ at a concentration of 48%: 48%: 4%) by volume to remove part of the ITO. After etching, the substrates were thoroughly cleansed using an ultrasonic cleaner with deionized water, acetone, and isopropanol for 10 min in each solution, respectively. The substrates were then dehydrated with a nitrogen air gun and further dried up in the oven for 20 min at 100 ^oC. After that, the thin-film transparent layer of PEDOT/PSS was spin-coated on the substrates at 3500 rpm for 60 seconds and was further desiccated in the oven for 20 min under an ambient atmosphere at 100 ^oC. The solar absorbers were then processed in chloroform solvent with and without Ni/Zn bimetallic nanoparticles. The pristine active layer solution was suitably prepared from P3HT with PC61BM polymers blend, at the stoichiometric ratio of 1:1, in chloroform solvent at a 20 mg/ml concentration. A similar composition of active layer solutions was also prepared using P3HT/PC61BM with Ni/Zn bimetallic nanoparticles at different concentrations (1% and 3%) by weight, respectively. After that, the solutions were further sonicated for 3 hours on a hot plate with a magnetic stirrer to ensure adequate miscibility of the particles in the intermixing at 40 ^oC. The solutions of the photoactive layers were then spin-coated on dried PEDOT/PSS for 40 seconds at 1200 rpm. The samples were then desiccated in the furnace under nitrogen gas for 10 min at 100 ^oC before being conveyed into a deposition chamber, which is beneficial for depositing lithium fluoride (LiF) and aluminium (Al) electrodes, respectively. A remarkably thin layer of LiF (0.5 nm) and 80 nm thickness of Al electrode was entirely deposited using Edward Auto 306 deposition unit at a pressure of 10^{-6} mbar. The conventional device structure implemented in this study is given as GLASS/ITO/PEDOT/PSS/P3HT/PC61BM/Ni/Zn bimetallic nanoparticles/LiF/Al. After short post-deposition annealing for 5 min at 100 ^oC, the device was then characterized in the ambient environment using a computer interfaced Keithley HP2420 source meter under an AM1.5 solar simulator (model SS50AAA) operating at an integrated light intensity of 100 mW/cm^2. The resulting diodes in this work have an effective area of 0.042 cm^2 or 4.2 mm^2. Then, the charge

mobility properties were also investigated using space charge limited current (SCLC), which was highly collected from current-voltage (J-V) data underneath dark environments. However, the device properties of thin-film absorption based on Ni/Zn bimetallic were explored by means of UV-Vis absorption spectra found via (T80-PG-Instrument limited) an absorption meter. Therefore, the device structure, which consists of numerous layers of conventional TFOSCs, is shown in figure 4.2.

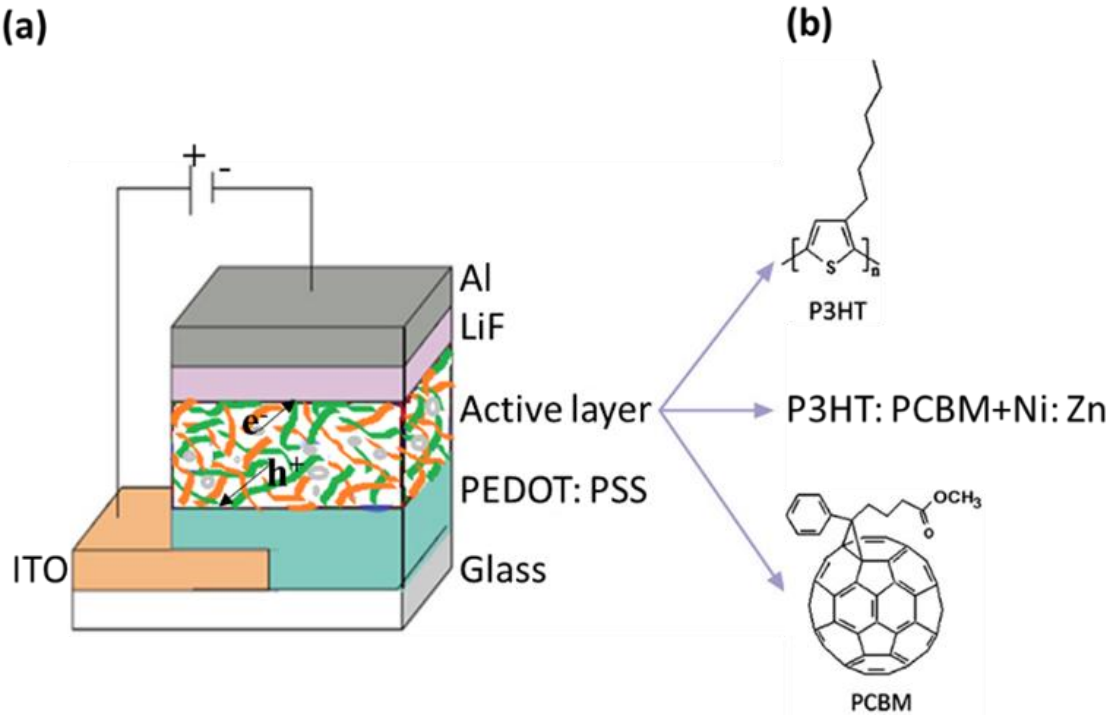

Figure 4.2: (a) The conventional structure of TFOSC and (b) the components structure of the photoactive layer.

4.4 Result and discussion sections

4.4.1 Characterizations of Ni/Zn bimetallic nanocomposites

The newly synthesized Ni/Zn bimetallic nanoparticles were characterized for their physical, morphological, and structural properties. The HRTEM images presented in figure 4.3 depict the existence of several shapes and sizes of Ni/Zn bimetallic nanocomposites in the powder form, which is beneficial to influence the electrical and optical properties of the composite. The images in (figure 4.3a and (b)) show that the Ni/Zn bimetallic nanoparticles appeared to have some sort of disc like geometry distributed on the background of sheet like structures. In fact, the Ni/Zn do exist at different phases such as φ-phase and γ-phase as reported in the

literature [34]. The existence of the different phases depends on the nickel content in the Zn matrix.

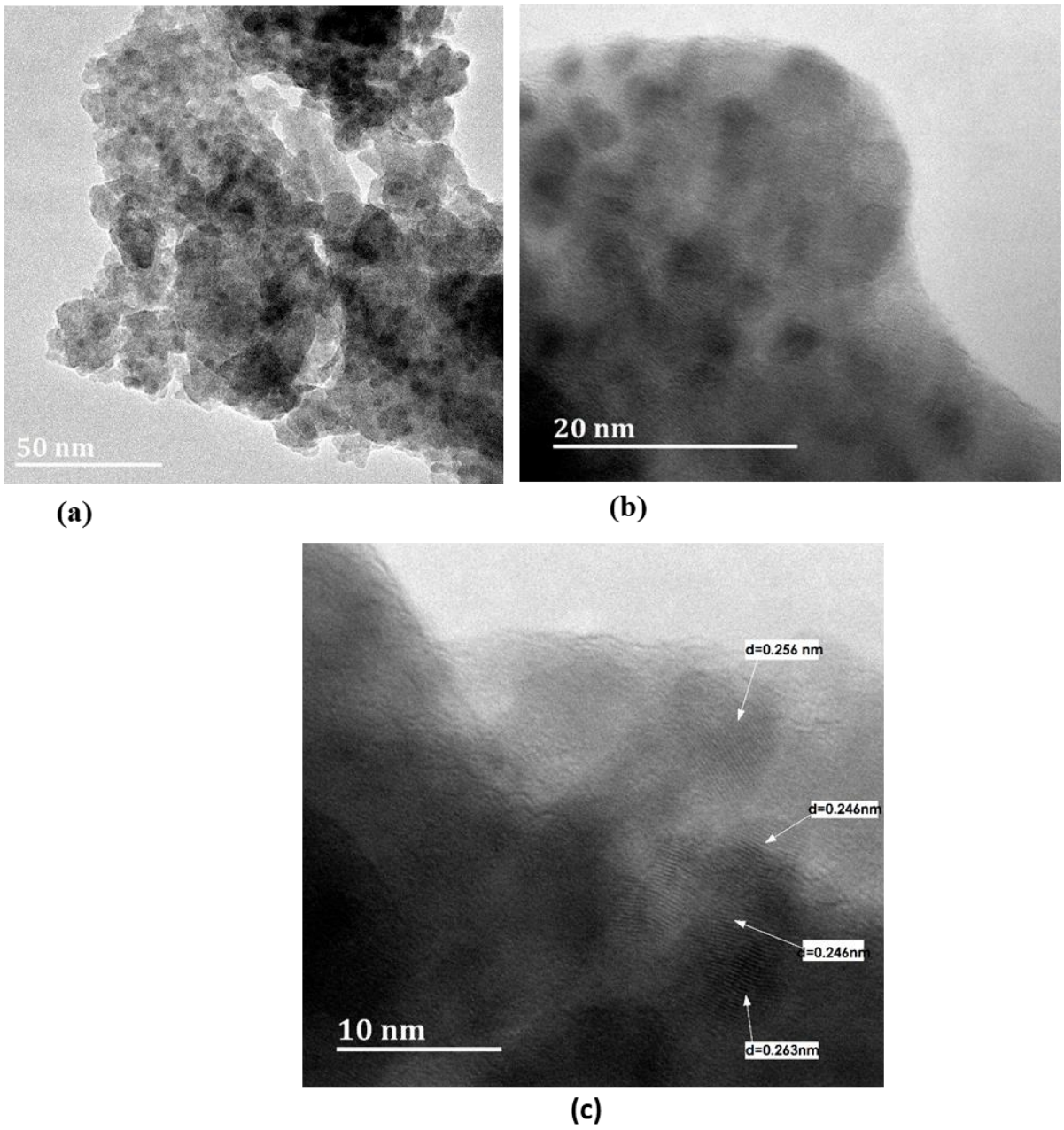

Figure 4.3: (a,b) HRTEM images of Ni/Zn bimetallic nanoparticles at different magnifications. (c) The crystallite fringes taken from Ni/Zn powder indicate lattice spacing and crystallinity of the nanostructures.

It is not even to mention the existence of single phases of Ni and Zn. However, additional investigations using different spectroscopy methods are needed to study the structure of the Ni/Zn. It is to be noted though that disc-like structures have different sizes as provided in figure 4.3 (a) and (b). The TEM images further displayed crystal fringes, which is attributed to the

existence of a well-aligned crystalline structure in the medium. However, the measured lattice spacing corresponding to the value d = 0.263 nm is attributed to the **a**-axis of the hexagonal closed packed (hcp) structure of Zn single phase while d =0.246 nm and d = 256 nm could be attributed to Ni doped Zn hcp structure.

4.4.2 Optical absorption of Ni/Zn bimetallic nanocomposites

It is to be noted that the light-harvesting is critically dependent on the optical absorption width of the solar absorber medium of the TFOSCs. Then, the optical properties of Ni/Zn bimetallic nanoparticles were enormously probed using optical absorption measurements collected from the respective solar absorber films and the particle suspension in deionized water solutions. However, the UV-Vis data were taken from solar absorber films composed of P3HT/PC61BM blend with and without the inclusion of Ni/Zn bimetallic nanocomposites as displayed in figure 4.4a. The two new prominent peaks were clearly observable at 1% and 3% loading of Ni/Zn bimetallic films as pointed out by the arrows compared to the pristine reference film (See figure 4.4a). Furthermore, the Ni/Zn bimetallic doped films demonstrated a slight redshift in the maximum peak of the absorbances, which is favorable to enhance photons harvesting at the more intense emission of the solar radiation.

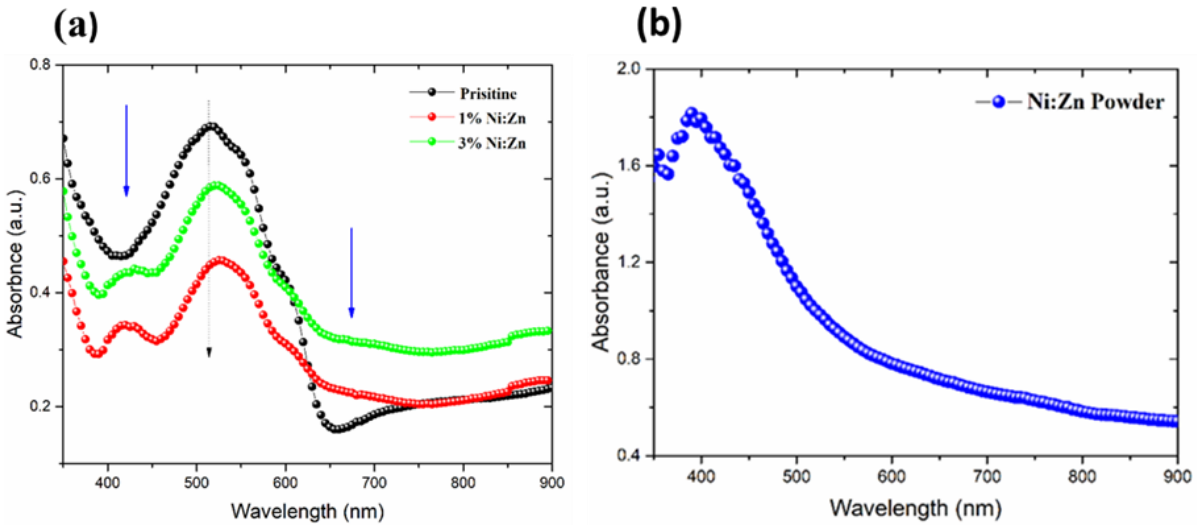

Figure 4.4: (a) UV-Vis absorption spectra taken at a different doping level of Ni/Zn NPs in absorber layers of TFOSC (b) the UV-Vis absorption spectrum of the Ni/Zn bimetallic powder in water suspension.

In light of this, the first arrow points to absorption bumps that range from 425 to 450 nm, while the second one is between 630 and 700 nm, near infra-red regions. Interestingly, the broadband

optical absorption of the new intensity peaks indicates the presence of various sizes and shapes of the Ni/Zn bimetallic nanoparticles in the medium, which is consistent with the distribution of particles observed from TEM morphology. Moreover, the absorbency of Ni/Zn bimetallic powder suspension presented in figure 4.4b shows a broad absorption spectrum centered at 400 nm. The long tail of the absorption spectrum in figure 4b is attributed to the light scattering processes that took place in the aqueous medium. The absorption peak near 400 nm is associated with a band-to-band transition of electrons in the metal nanoparticles. However, the new absorbance peaks observed in metal nanoparticles doped absorber films could be attributed to the occurrence of LSPR and far-field scattering of the incident radiation in the dielectric medium.

4.4.3 Organic Solar cells doped with Ni/Zn nanocomposites

The effects of Ni/Zn bimetallic nanocomposite on the performance of the P3HT/PC61BM-based thin film solar cell were investigated by way of the measured J-V characteristics of the devices. The J-V curve plotted in figure 4.5 clearly exhibited considerable changes in the measured photocurrent from the solar cells doped with Ni/Zn bimetallic nanocomposites. Moreover, the device parameter derived from the measured electrical properties of the conventional TFOSCs is also provided in Table 4.1. It is to be noted that the performance of the solar cells is clearly dependent on the concentration of Ni/Zn bimetallic nanoparticles in the absorber layers of the solar cells. Consequently, the short-circuit voltage (J_{sc}) and open-circuit voltage (V_{oc}) measured at the doping level of 1% and 3% of Ni/Zn by weight significantly improved compared to that of the pristine. The short-circuit current and device fill factor (FF) have increased by 48% and 19%, respectively, from the reference cell and at 1% concentration of Ni/Zn bimetallic nanocomposites within the active layer. This is a clear indication of the improved light harvesting ability of the absorber layer by the LSPR effect, which is obviously exhibited on the UV-Vis absorption spectra as displayed in Fig. 4.4a. The best PCE value achieved in this investigation was 4.78% at 1% Ni/Zn bimetallic concentration by weight. This is a clear indication of the optimum concentration of the bimetallic nanoparticles for the best performance of the solar cells (See Table 4.1). It should be noted that the enhanced efficiency is mainly accredited to the measured high photocurrent from the devices because of the Ni/Zn bimetallic nanocomposites.

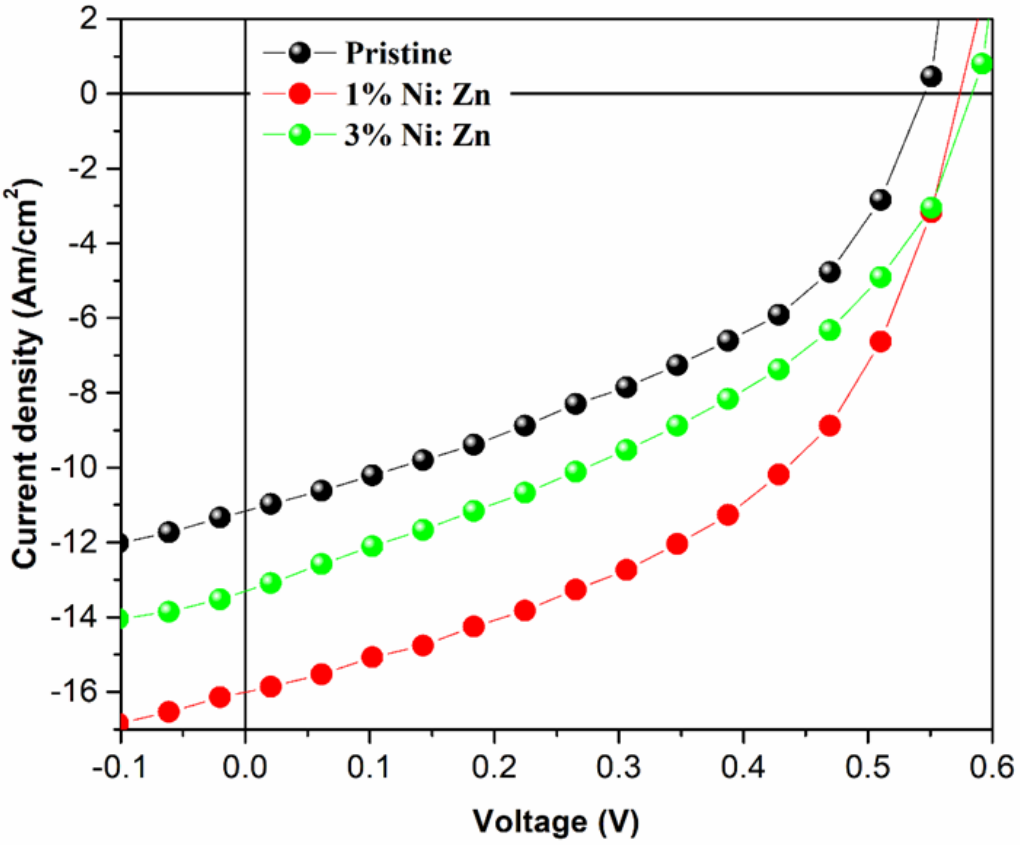

Figure 4.5: J-V characteristic of the solar cells fabricated using P3HT/PC61BM blend active layer containing Ni/Zn bimetallic nanoparticles at different concentrations.

Recent studies have reported the effect of Ag/Cu bimetallic nanocomposites blended with an active layer and discovered that PCE augmentation is the main reason for optical absorption in solar absorbers [35]. The same observation was remarkably found by Oseni and Mola [27] based on improved absorption efficiency by blending Ag/Zn nanoparticles with PTB7/PC61BM. According to the results achieved in this work, it is interesting to note that the devices blended with Ni/Zn bimetallic nanocomposites depicted a desirable performance compared to pristine, which is favorable to optimize charge dissociations, charge mobility, and collection processes. Such improvements are reflected due to enhanced FF, J_{sc}, and PCE, respectively. These were partially originated from the reduction of the series resistance (R_s) [14]. Moreover, another approach to improve the exciton dissociation is by forming a near-strong field in the vicinity of the composite, and far-field scattering is an additional mechanism to enhance light harvesting ability in TFOSC [36-39].

Table 4.1: The TFOSCs device parameters fabricated at different concentrations of Ni/Zn bimetallic with the best performance.

Ni/Zn (wt%)	**V_{oc} (V)**	**J_{sc} (mA/cm^2)**	**FF (%)**	**PCE (%)**	**R_s (Ω cm^2)**
0% (Pristine)	0.54	11.27	41.75	2.56	256
1%	0.58	16.71	49.79	4.78	130
3%	0.56	13.86	44.23	3.36	119

4.4.4 Charge carrier transport

The charge mobility in the polymer medium plays an important role in determining the collection of photons-generated charge carriers in solar cells. The space charge limited current (SCLC) measured in the absence of photon generated current is one of the methods to study the charge transport properties of the polymer medium. The SCLC is J-V data measured in the absence of light (dark condition) (figure 4.6b). However, the SCLC is the right flank of the figure right after injection limited current ($\geq$ 0.82 V). It is a region where the current reaches close to saturation and it is a region that all traps are filled in the medium, the charge transport property is mainly reliant on the nature of the medium. Therefore, the measured SCLC data were fitted to Mott-Gurney's law to derive important transport parameters, which uses field dependent mobility equation of the form: $\mu(E) = \mu_0 exp\ (\gamma\sqrt{E})$. Thus, the SCLC data can be described in terms of Mott-Gurney law presented as

$$J = \frac{9}{8}\varepsilon\varepsilon_o\mu_o\frac{V^2}{L^3}exp\left(0.89\gamma\sqrt{\frac{V}{L}}\right). \quad (4.1)$$

Where μ_o is the zero-field mobility, ε_o signifies the permittivity of free space, ε displays the relative dielectric permittivity of the material, L denotes the thickness of photoactive layer, γ is the field activation factor, and V is the voltage drop across the sample, which is possibly corrected via the built-in voltage (V_{bi}).

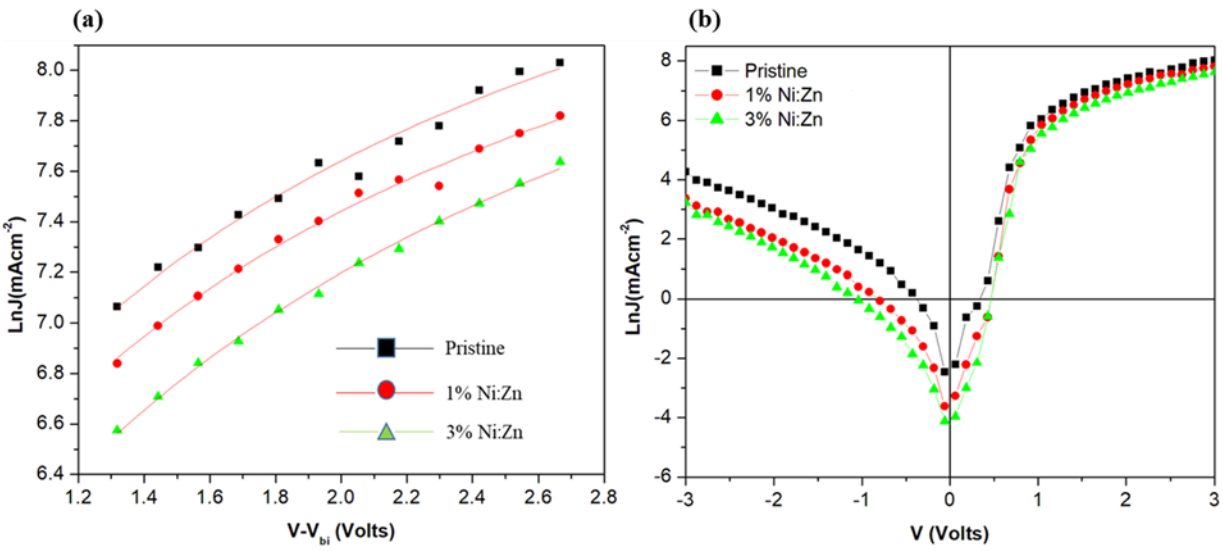

Figure 4.6: (a) The SCLC data taken from TFOSC devices containing different concentrations of Ni/Zn and the solid line is a computer fits of equation (4.1) to the data (b) J-V measured under dark condition at different concentrations.

The field activation factor, $\gamma = B\left(\frac{1}{k_B T} - \frac{1}{k_B T_0}\right)$, is dependent on temperature (T) and constant parameters T_0 and B determined by nature of the material [40,41]. The negative value of γ suggest that mobility decreases at high applied electric field in the polymer medium [41]. According to the result provided in figure 4.6a the SCLC data are in a very good agreement with the prediction of Mott-Gurney's law. The transport parameters attained from the analysis were found to be similar to the values reported in literature for polymer medium. Thus, the zero-field mobilities of Ni/Zn bimetallic doped devices were observed to be one order of magnitude higher than that of the pristine solar cell (See Table 4.2).

Table 4.2: The charge transport parameters of TFOSCs fabricated with photoactive layer doped with Ni/Zn bimetallic nanoparticles at different concentrations.

(P3HT/$PC_{61}BM$/ Ni/Zn) (wt%)	**μ_o (Zero-field mobility) ($cm^2S^{-1}V^{-1}$)**	**γ (Field activation factor) (cmV^{-1})**
0% (Pristine)	3.46×10^{-4}	-3.02×10^{-4}
1%	2.86×10^{-3}	-2.49×10^{-4}
3%	1.66×10^{-3}	-2.66×10^{-4}

This is clear evidence of the effect of Ni/Zn bimetallic nanocomposites doped with an active layer, which is favorable in augmenting the charge transport processes and the promotion of charge dissociation in TFOSCs.

4.5 Conclusion

In conclusion, we have synthesized Ni/Zn bimetallic nanoparticles using wet chemistry procedures. The Ni/Zn bimetallic nanoparticles were doped in P3HT/PC61BM blend bulk-heterojunction solar absorber films at different concentrations. The fabricated solar cells doped with Ni/Zn bimetallic nanocomposites showed remarkable improvement in device performance because of the occurrence of the LSPR effect in the photoactive layer. This is due to the fact that LSPR/SPR phenomena assisted in improving the light-harvesting ability of TFOSCs. Subsequently, the best device parameters recorded from these investigations were PCE value up to the rate of 4.78%, a J_{sc} of 16.71 $mAcm^{-2}$, and a high FF of 50.0% were measured at 1% concentration of Ni/Zn by weight. This is clear evidence of the effect of Ni/Zn bimetallic nanocomposites on the performance of thin film organic solar cells play an indispensable role to improve the charge transport and collection processes. The Ni/Zn bimetallic is environmentally stable and suitable for roll-to-roll printing methods for large-scale device fabrication.

Authors statement

All authors in the list are equally involved in the preparation of this manuscript submitted to the Journal of Physics and Chemistry of Solids. The authors have acknowledged the organizations that support this research work financially.

Declaration of competing interest

The authors declare that they have no known competing financial interests or personal relationships that could have appeared to influence the work reported in this paper.

Acknowledgments

This manuscript work is financially supported by the National Research Foundation (NRF), South Africa (Grant numbers: 113835, 85589, and 93562). The authors further acknowledge the members of staff in the microscopic and microanalysis unit (MMU) at the University of KwaZulu-Natal (UKZN), Pietermaritzburg Campus, South Africa, for TEM, SEM, and EDX analyses.

References

[1] E.A. Arbab., B. Taleatu. and G.T. Mola. Environmental stability of PTB7: PCBM bulk heterojunction solar cell. Journal of Modern Optics, 61(21), (2014), 1749-1753.

[2] C.J. Brabec., S. Gowrisanker., J.J. Halls., D. Laird., S. Jia. and S.P. Williams. Polymer–fullerene bulk-heterojunction solar cells. Advanced Materials, 22(34), (2010), 3839-3856.

[3] Y. Liang., Z. Xu., J. Xia., S.T. Tsai., Y. Wu., G. Li., C. Ray. and L. Yu. For the bright future-bulk heterojunction polymer solar cells with a power conversion efficiency of 7.4%. Advanced materials, 22(20), (2010), E135-E138.

[4] S.O. Oseni. and G.T. Mola. The effect of uni-and binary solvent additives in PTB7: PC61BM based solar cells. Solar Energy, 150, (2017), 66-72.

[5] Z. Zhang., J. Miao., Z. Ding., B. Kan., B. Lin., X. Wan., W. Ma., Y. Chen., X. Long., C. Dou. and J. Zhang. Efficient and thermally stable organic solar cells based on small molecule donor and polymer acceptor. Nature communications, 10(1), (2019), 1-8.

[6] Y. Li., G. Xu., C. Cui. and Y. Li. Flexible and semitransparent organic solar cells. Advanced Energy Materials, 8(7), (2018), 1701791.

[7] P.K. Nayak., S. Mahesh., H.J. Snaith. and D. Cahen. Photovoltaic solar cell technologies: analysing the state of the art. Nat Rev Mater, 4(4), (2019), 269-285.

[8] W.J. Hou., Y.M. Xiao., G.Y. Han., J.Y. Lin. The applications of polymers in solar cells: a review. Polymers, 11(1), (2019), 143.

[9] L. Jhamba., D. Wamwangi. and Z. Chiguvare. Dark and illuminated J (V) characteristics of thin layered bulk heterojunction P3HT: PCBM sandwich solar cells after thermal treatment. Optical and Quantum Electronics, 52(9), (2020), 1-15.

[10] F.C. Hsu., J.W. Luo., Y.W. Su., C.S. Yang., Y.A. Lin., J.Y. Lin., C.Y. Chang., Y.F. Chen. and C.P Li. Efficient Charge Transfer and Carrier Extraction in All-Polymer Solar Cells Using an Acceptor Filler. ACS Applied Energy Materials, 3(5), (2020), 4217-4225.

[11] C.C. Chen., W.H. Chang., K. Yoshimura., K. Ohya., J. You., J. Gao., Z. Hong. and Y. Yang. An efficient triple-junction polymer solar cell having a power conversion efficiency exceeding 11%. Advanced materials, 26(32), (2014), 5670-5677.

[12] J. You., L. Dou., K. Yoshimura., T. Kato., K. Ohya., T. Moriarty., K. Emery., C.C. Chen., J. Gao., G. Li. and Y. Yang. A polymer tandem solar cell with 10.6% power conversion efficiency. Nature communications, 4(1), (2013), 1-10.

[13] Elhadi A. A. Arbab, Bidini Teleatu, Genene Tessema Mola, Environmental stability of PTB7/PCBM bulk heterojunction solar cell, J. Mod. Optics, 61(21), (2014)1749-1753.

[14] Genene Tessema Mola, Elhadi A. A. Arbab, Bidini A. Taleatu, K. Kaviyarasu, Ishaq Ahmad and M. Maaza. Growth and characterization of V_2O_5 thin film on the conductive electrode, J. Microscopy, 265 (2), (2017), 214-221.

[15] E.A. Arbab., B. Gebremichael., A. Kumar. and G.T. Mola. Morphology-dependent performance of thin film organic solar cells. Journal of Modern Optics, 66(4), (2019), 399-406.

[16] A. Aguiar., J. Farinhas., W. da Silva., M. Susano., M.R. Silva., L. Alcácer., S. Kumar., C.M. Brett., J. Morgado. and A.J. Sobral. Simple BODIPY dyes as suitable electron donors for organic bulk heterojunction photovoltaic cells. Dyes and Pigments, 172, (2020), 107842.

[17] T.R. Hopper., D. Qian., L. Yang., X. Wang., K. Zhou., R. Kumar., W. Ma., C. He., J. Hou., F. Gao. and A.A. Bakulin. Control of Donor-Acceptor Photophysics through Structural Modification of a “Twisting” Push–Pull Molecule. Chemistry of Materials, 31(17), (2019), 6860-6869.

[18] M.S. Hamed., S.O. Oseni., A. Kumar., G. Sharma. and G.T. Mola. Nickel sulphide nano-composite assisted hole transport in thin film polymer solar cells. Solar Energy, 195, (2020), 310-317.

[19] S. Rafique., S.M. Abdullah., M.M. Shahid., M.O. Ansari. and K. Sulaiman. Significantly improved photovoltaic performance in polymer bulk heterojunction solar cells with graphene oxide/PEDOT: PSS double-decked hole transport layer. Scientific Reports, 7(1), (2017), 1-10.

[20] B. Xu., S.A. Gopalan., A.I. Gopalan., N. Muthuchamy., K.P. Lee., J.S. Lee., Y. Jiang., S.W. Lee., S.W. Kim., J.S. Kim. and H.M. Jeong. Functional solid additive modified PEDOT: PSS as an anode buffer layer for enhanced photovoltaic performance and stability in polymer solar cells. Scientific reports, 7(1), (2017), 1-13.

[21] K. Bini., X. Xu., M.R. Andersson. and E. Wang. Alcohol-soluble conjugated polymers as cathode interlayers for all-polymer solar cells. ACS Applied Energy Materials, 1(5), (2018), 2176-2182.

[22] X.G. Mbuyise., E.A. Arbab., K. Kaviyarasu., G. Pellicane., M. Maaza. and G.T. Mola. Zinc oxide doped single wall carbon nanotubes in hole transport buffer layer. Journal of Alloys and Compounds, 706, (2017), 344-350.

[23] Saheed O. Oseni, Genene Tessema Mola, Effects of metal-decorated nanocomposite on inverted thin film organic solar cell, Journal of Physics and Chemistry of Solids, 130 (2019), 120-126.

[24] Y. Thaver., S.O. Oseni., K. Kaviyarasu., R.P. Dwivedi. and G.T. Mola. Metal nano-composite assisted photons harvesting in thin film organic photovoltaic. Physica B: Condensed Matter, 582, (2020), 411844.

[25] S. Liu., R. Jiang., P. You., X. Zhu., J. Wang. and F. Yan. Au/Ag core-shell nanocuboids for high-efficiency organic solar cells with broadband plasmonic enhancement. Energy & Environmental Science, 9(3), (2016), 898-905.

[26] K. Yao., H. Zhong., Z. Liu., M. Xiong., S. Leng., J. Zhang., Y.X. Xu., W. Wang., L. Zhou., H. Huang. and A.K.Y. Jen. Plasmonic metal nanoparticles with the core-shell structure for high-performance organic and perovskite solar cells. ACS nano, 13(5), (2019), 5397-5409.

[27] S.O. Oseni. and G.T. Mola, G.T. Bimetallic nanocomposites and the performance of the inverted organic solar cell. Composites Part B: Engineering, 172, (2019), 660-665.

[28] A. Zada., P. Muhammad., W. Ahmad., Z. Hussain., S. Ali., M. Khan., Q. Khan. and M. Maqbool. Surface Plasmonic-Assisted Photocatalysis and Optoelectronic Devices with Noble Metal Nanocrystals: Design, Synthesis, and Applications. Advanced Functional Materials, 30(7), (2020), 1906744.

[29] M. Wang., M. Ye., J. Iocozzia., C. Lin. and Z. Lin. Plasmon-mediated solar energy conversion via photocatalysis in noble metal/semiconductor composites. Advanced Science, 3(6), (2016), 1600024.

[30] H.H. Kyaw., M.T.Z. Myint., S.H. Al-Harthi., T. Maekawa., K. Yanagisawa., A. Sellai. and J. Dutta. Observation of exchanging the role of gold and silver nanoparticles in the bimetallic thin film upon annealing above the glass transition temperature. Materials Research Express, 4(8), (2017), 086409.

[31] S.Y. Kok., Z.C. Hsieh., C.H. Chou., S.S. Yang., M.K. Chuang., Y.T. Lin., S.S. Yap., T.Y. Tou. and F.C. Chen. Plasmonic effects on bulk heterojunction polymer solar cells: A transient

photovoltage and differential charging Study. Science of Advanced Materials, 9(8), (2017), 1435-1439.

[32] X.G. Mbuyise., E.A. Arbab. and G.T. Mola. The effect of a trimetallic nanocomposite in the solar absorber layer of organic solar cells. RSC advances, 9(11), (2019), 6070-6076.

[33] L. Jia., J. Yu., Y. Chen., P. Ning., Q. Guan., J. Gu., R. Miao. and Q. Chen. Noble-metal-free bimetallic alloy nanoparticle-catalytic gasification of phenol in supercritical water. The Journal of Supercritical Fluids, 126, (2017), 79-88.

[34] A. Petrauskas., L. Grincevičienė., A. Češūnienė. and R. Juškėnas. Studies of phase composition of Zn–Ni alloy obtained in the acetate-chloride electrolyte by using XRD and potentiodynamic stripping. Electrochimica acta, 50(5), (2005), 1189-1196.

[35] P. Tonui. and G.T. Mola. Improved charge extraction in polymer solar cell using metal nanocomposite. Physica E: Low-dimensional Systems and Nanostructures, 107, (2019), 154-159.

[36] M.S. Hamed. and G.T. Mola. Copper sulfide as a mechanism to improve energy harvesting in thin film solar cells. Journal of Alloys and Compounds, 802, (2019), 252-258.

[37] E. Stratakis. and E. Kymakis. Nanoparticle-based plasmonic organic photovoltaic devices. Materials Today, 16(4), (2013), 133-146.

[38] R. Chowdhury., L. Tegg., V.J. Keast., N.P. Holmes., N.A. Cooling., B. Vaughan., N.C. Nicolaidis., W.J. Belcher., P.C. Dastoor. and X. Zhou. Plasmonic enhancement of aqueous processed organic photovoltaics. RSC Advances, 11(31), (2021), 19000-19011.

[39] J.A. Bartelt., Z.M. Beiley., E.T. Hoke., W.R. Mateker., J.D. Douglas., B.A. Collins., J.R. Tumbleston., K.R. Graham., A. Amassian., H. Ade. and J.M. Fréchet. The importance of fullerene percolation in the mixed regions of polymer–fullerene bulk heterojunction solar cells. Advanced Energy Materials, 3(3), (2013), 364-374.

[40] M.W. Dlamini. and G.T. Mola. Near-field enhanced performance of organic photovoltaic cells. Physica B: Condensed Matter, 552, (2019), 78-83.

[41] Veaceslav Coropceanu, Je´roˆme Cornil, Demetrio A. da Silva Filho, Yoann Olivier, Robert Silbey, and Jean-Luc Bre´das, Charge Transport in Organic Semiconductors, Chem. Rev., 107 (2007), 926-952.

CHAPTER 5

Plasmon assisted optical absorption and reduced charge recombination for improved device performance in polymer solar cells

Journal of Physics and Chemistry of Solids 165 (2022) 110662

Contents lists available at ScienceDirect

Journal of Physics and Chemistry of Solids

journal homepage: www.elsevier.com/locate/jpcs

Plasmon assisted optical absorption and reduced charge recombination for improved device performance in polymer solar cell

Jude N. Ike [a], Mpilo Wiseman Dlamini [a], Ram P. Dwivedi [c], Yong Zhang [b], Genene Tessema Mola [a,*]

[a] School of Chemistry & Physics, University of KwaZulu-Natal, Pietermaritzburg Campus, Private Bag X01, Scottsville, 3209, South Africa
[b] School of Materials Science and Engineering, Harbin Institute of Technology, Harbin, 150001, China
[c] Faculty of Engineering and Technology, Shoolini University, Bajhol, HP, 173229, India

ARTICLE INFO

Keywords:
Bimetallic nanoparticles
Acceptors
Donors
Bulk-heterojunction
Plasmonic resonance

ABSTRACT

Silver and Calcium (Ag:Ca) bi-metallic nano-partices have been successfully synthesized using a chemical reduction processes. The nano-partices were intended to be used in the solar absorber layer of thin film organic solar cell (TFOSC) to assist in improving optical absorption and charge transport processes in polymers blend medium. The nanocomposite (Ag:Ca) is expected to exhibit local surface plasmon resonance (LSPR) and far-field scattering from the interaction with the incident photons. The absorber layer of TFOSC, in this investigation, is prepared from the mixture of poly-(3-hexylthiophene) (P3HT): [6,6]-phenyl C61 butyric acid methyl ester (PC61BM). Devices were fabricated at various concentration of metal nano-particles in the solar absorber layer, as 1%, 3%, and 5% by weight, to be able to determine the optimum concentration of the dopant. Hence, the experimental evidences clearly showed that performance of the solar cell is dependent on the concertation of the metal nano-particles. Consequently, the power conversion efficiency (PCE) value has increased by 75% with a remarkable improvement in device fill factor of 53.4% at an optimum doping level of 3%. The optical and morphological properties of the synthesized nano-particles are well presented and discussed in terms of the data collected using transmission and scanning electron microscopy (TEM & SEM) and other complimentary methods.

5.1 Abstract

Silver and Calcium (Ag/Ca) bi-metallic nanoparticles have been successfully synthesized using chemical reduction processes. The nanoparticles were intended to be used in the solar absorber layer of thin-film organic solar cells (TFOSC) to assist in improving optical absorption and charge transport processes in a polymer blend medium. The nanocomposite (Ag/Ca) is expected to exhibit localized surface plasmon resonance (LSPR) and far-field scattering from the interaction with the incident photons. The absorber layer of TFOSC, in this investigation, is prepared from the mixture of poly-(3-hexylthiophene) (P3HT)/[6,6]-phenyl C61 butyric acid methyl ester (PC61BM). Devices were fabricated at various concentrations of metal nanoparticles in the solar absorber layer, as 1%, 3%, and 5% by weight, to be able to determine the optimum concentration of the dopant. Hence, the experimental evidence clearly showed

that the solar cell's performance depends on the concentration of the metal nanoparticles. Consequently, the power conversion efficiency (PCE) value has increased by 75% with a remarkable improvement in the device fill factor of 53.4% at an optimum doping level of 3%. The optical and morphological properties of the synthesized nanoparticles are well presented and discussed in terms of the data collected using transmission and scanning electron microscopy (TEM & SEM) and other complementary methods.

5.2 Introduction

Conducting polymers have attracted tremendous attention in the last three decades because of their potential application in flexible electronics. Thin-film organic solar cell (TFOSC) is one of the highly sought for areas of application with the view to producing lightweight and flexible solar panels. The introduction of bulk-heterojunction (BHJ) design in the preparation of TFOSC resulted in the realization of the desirable high-performance polymer solar cells [1]. BHJ design of OSC offers an enhanced interfacial area for efficient charge separation and collection [2,3]. The donor and acceptor molecules in the BHJ medium form an interpenetrating network to facilitate the charge transport processes. However, the effectiveness of BHJ is highly dependent on the film morphology of the absorber layer, which can be controlled by solvent additive as well as post-device production annealing. The progress of fullerene-based organic solar cells is limited by the narrow optical absorption band of the fullerene acceptor molecules that hamper solar energy harvesting. Moreover, the optoelectronic properties of the fullerene-based absorber film suffer from poor charge transport mobility, poor optical absorption in the visible and near-infrared region of the PCBM, and low open-circuit voltage (V_{oc}) as well as poor device stability. These effects are often attributed to the deep-lying lowest unoccupied molecular orbital (LUMO) levels of PCBM [4-6]. Plasmon metal nanoparticles have been introduced in OSC research to improve photon harvesting and charge transport processes in the medium [7-10]. Consequently, the incorporation of metallic nanoparticles in the solar absorber layer, which is composed of a mixture of poly-(3-hexylthiophene) (P3HT) and [6,6]-phenyl C61 butyric acid methyl ester (PC61BM), is expected to boost power conversion efficiency (PCE) of the devices [11-16]. This is due to the occurrence of local surface plasmonic resonance (LSPR) from the interaction of the incident light with the surface electron plasma of the metal nanoparticles located in a dielectric medium. Near-field light scattering by metal nanoparticles is also used as a mechanism to trap light in the polymer medium.

Furthermore, several metallic nanoparticles have been employed recently as a promising mechanism to boost the high performance of TFOSCs devices [17-22]. Such metallic nanoparticles are mostly prepared from novel metals such as gold (Au), copper (Cu), silver (Ag), zinc (Zn), and nickel (Ni), respectively. The metal NPs play a significant role in photon harvesting in TFOSCs polymer medium, which is advantageous for promoting exciton dissociation and improving charge transport processes due to the occurrence of several phenomena from the interaction with the incident radiation. The most popular metal nanoparticles in OSC research are Au and Ag due to their strong influence in generating LSPR and light scattering properties in the dielectric medium. In the light of this, Au exhibits a long-range plasmonic effect, and it mainly depicts low light scattering ability. At the same time, Ag nanoparticles display high light-scattering properties with the short-range LSPR effect [22, 23]. In the current investigations, Calcium (Ca) is used in the synthesis of Ag/Ca bimetallic nanoparticles to exploit the optoelectronic properties of both metals for solar energy harvesting. Calcium is a transition metal that possesses favorable optical and electrical properties and can be used as a nanoparticle mechanism to augment photons harvesting and the charge transport process, respectively [20]. Interestingly, the bimetallic nanoparticles are more favorable to absorb photo-current than mono-metallic nanoparticles because the former has high light-scattering and long-range LSPR effect in TFOSCs. Additionally, bimetallic nanoparticles are promising to induce the LSPR effect in the solar absorber layer and produce a strong local electromagnetic field (EMF), which induces light scattering that promotes trapping and assists in the dissociation of excitons in the polymer medium [24-27]. The interaction of electromagnetic radiation with metal nanoparticles in the polymer medium results in the occurrence of several phenomena such as plasmonic light-scattering, dipole-dipole coupling, plasmonic heating effect, hot-electron injection, and local electromagnetic field enhancement. All these processes are depicted in the schematic diagram provided in figure 5.1. We summarize each phenomenon briefly, and details can be found in the cited references.

Generally, the incident EMF can liberate an electron from metal, which is known as a hot electron, and eject it into the semiconductor. The hot electron having enough momentum can overcome the Schottky barrier produced within the metal nanocrystals and semiconductor through direct contact; hence can be injected into the CB of the semiconductor (See figure 5.1D). Furthermore, the electric field component of the incident photon can induce dipole moment in the metal by surface charge polarization that can store energy. This induced dipole moment would oscillate at the frequency of the incident photons, which leads to resonance absorption by way of surface plasmon resonance (SPR) (figure 5.1A). The formed metal dipole

moment can also induce another dipole at the polymer-metal interfaces that create the so-called dipole-dipole interaction between metal nanoparticles and neighboring semiconductors (figure 5.1B). The energy stored in the process can be transformed by way of phonon-electron relaxation during the decay of LSPR produces a photo-thermal process, and then, the gained energy of mobile carriers turns into heat [28]. This effect can probably occur during the non-radiative decay process of LSPR (See figure 5.1C). Interestingly, the oscillating plasma eventually dephases by way of energy transfer to the nearest molecules or compounds in the form of heat (figure 5.1C). Finally, the interaction of EMF with surface electron plasma of the metal can generate a local electromagnetic field in the vicinity of the metal that can cause near field scattering (figure 5.1E). All these phenomena would assist in harvesting more photons and exciton dissociation processes leading to the collection of more photocurrent.

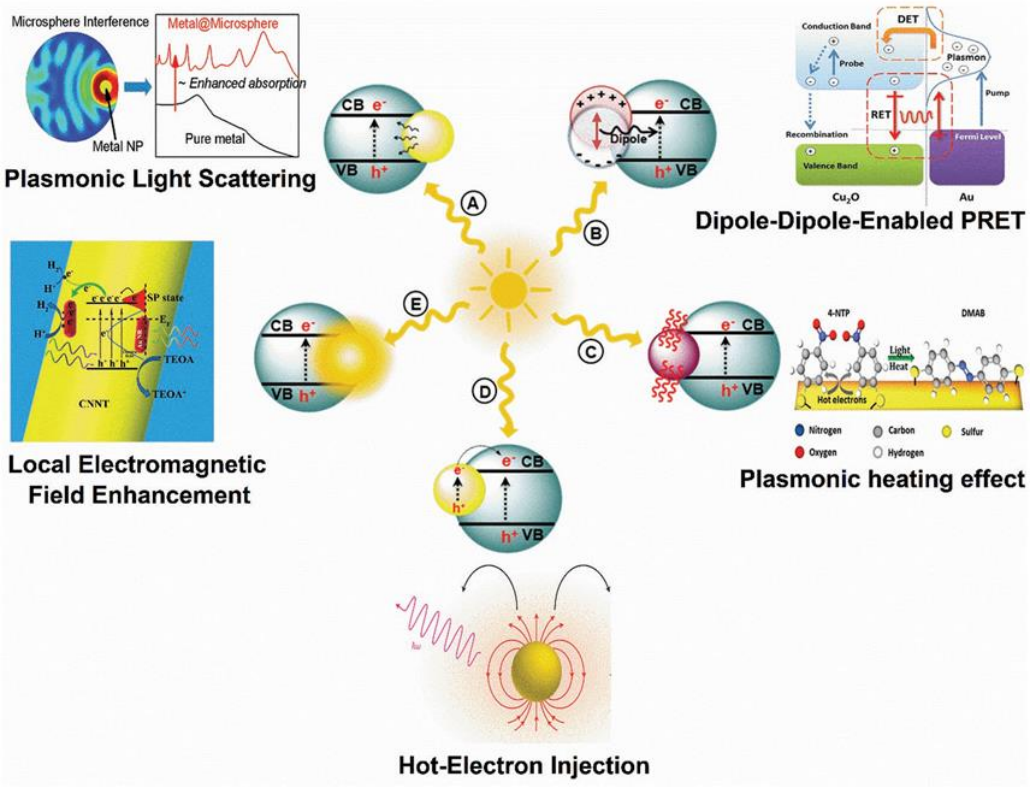

Figure 5.1: The mechanisms proposed for plasmonic assisted water splitting and optoelectronics devices. Such mechanisms are (A) plasmonic light-scattering, (B) dipole-dipole coupling, (C) plasmonic heating effect, (D) hot-electron injection, and (E) local electromagnetic field enhancement. Reproduced with permission [29,30].

This article reports a considerable device performance improvement by employing newly synthesized Ag/Ca as bimetallic nanocomposites in the solar absorber layer of P3HT/PCBM based on TFOSCs. The solar cells were fabricated at various doping levels such as 1%, 3%,

and 5% Ag/Ca by weight, which permitted the determination to display significant improvement in terms of charge collection, which is beneficial in increasing power conversion efficiency compared to pristine (undoped layer). Therefore, the achievable results from several device structures are analyzed and presented in the appropriate section of this new article.

5.3 Experimental sections

5.3.1 Material

The chemical materials for synthesizing silver/calcium (Ag/Ca) as bimetallic nanocomposites were obtained from a commercial source and used as received. Such chemical materials include silver nitrate hexahydrate (> 99.5% $AgNO_3$), calcium nitrate hexahydrate (> 99.9% $Ca(NO_3)_2.H_2O$), and sodium borohydride (> 99.98% $NaBH_4$) were purchased from Merck, Germany. The polymer molecules, which include the poly-(3,4-ethylene dioxythiophene): poly-(styrene-sulfonate) (PEDOT/PSS), Poly-(3-hexylthiophene) (P3HT), and [6,6]-phenyl-C61-butyric acid methyl ester (PC61BM) 95% purity were procured from Ossila Co. Ltd. Uk. All the reagents were rightfully used without any further purification as appropriately received.

5.3.2 Synthesis of Ag/Ca bimetallic nanocomposites

The synthesis of Ag/Ca bimetallic nanocomposites starts with preparing several chemical solutions in 50 mL of deionized water solvent. The chemical solutes such as 40 mM of silver nitrate, 20 mM of calcium nitrate, and 0.5 M of sodium borohydride, which acts as a reducing agent, were dissolved in 50 mL of deionized water solvent in three separate clean flasks. Subsequently, the solutions were successfully mixed up, starting with $AgNO_3$ followed by dropwise adding ($Ca(NO_3)_2.H_2O$) and $NaBH_4$ solutions under stirring, which is beneficial to process the needful substantial Ag/Ca bimetallic nanoparticles. The mixture was thoroughly stirred for 3-4 h on a hot plate at a temperature of about 40 ^oC with a magnetic stirrer. At the same time, the resultant suspension was further filtered and cleaned up with deionized water several times to remove sodium ions. However, the resultant precipitate of Ag/Ca was dried for 2 h at 80 ^oC in the vacuum oven to ensure functional bimetallic nanocomposites. After that, the powder of Ag/Ca bimetallic nanoparticles was effectively characterized using ultraviolet-visible (UV-Vis) absorption spectroscopy, transmission electron microscopy (TEM), scanning electron microscopy (SEM), X-ray diffraction (XRD), and energy dispersion (EDX) analysis.

5.3.3 Device fabrication of Ag/Ca bimetallic nanocomposites

The TFOSC devices were fabricated on indium tin oxide (ITO) coated glass substrates, which were suitably cut to the size of 30 mm x 30 mm. The ITO-coated glass substrates were successfully etched with acid solutions containing hydrochloric acid (HCl), hydrogen-2-oxide (H_2O), and trioxonitrate-5-acid (HNO_3) at concentrations of 48%: 48%: 4% by volume to remove part of ITO from the substrate. The substrates were cleaned with an ultrasonic cleaner with different solutions, including deionized water, acetone, and isopropanol, for 10 min each. The substrates were then dried up in an oven for 20 min at 120 ^oC before coating PEDOT/PSS at the rate of 3500 rpm for one min (60 sec) and was further dehydrated in the oven for 20 min at 120 ^oC under the ambient atmosphere. The solar absorber was prepared in chloroform solvent at 20 g/mL of P3HT/PC61BM at the respective weight ratio of 1:1. Another solution was further prepared by adding Ag/Ca bimetallic nanoparticles to P3HT/PC61BM solution at the doping level of 1%, 3%, and 5% concentrations, respectively. In the light of this, the solutions were later stirred on the hot plate with a magnetic stirrer for 3 h at the average temperature of 40 ^oC to ensure the effective miscibility of the molecules in the blend.

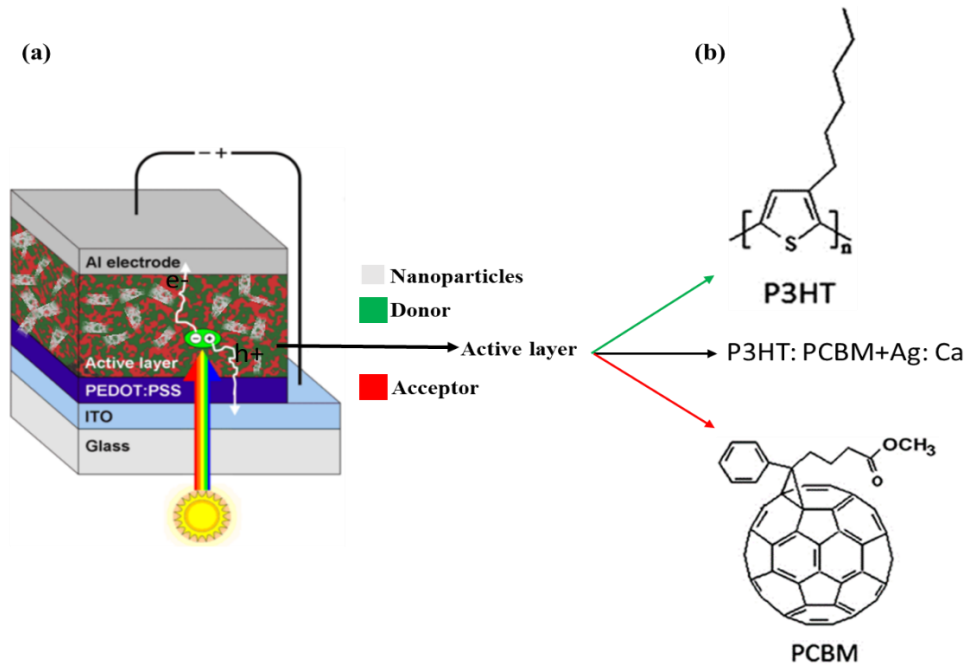

Figure 5.2: (a) The conventional device architecture of TFOSC and (b) the structure of the components of the photoactive layer.

After that, the solutions of the active layer were successfully spin-coated on desiccated PEDOT/PSS at the rate of 1200 rpm for 40 min. The respective samples were suitably annealed

in the furnace under a nitrogen gas for 10 min at 120 ^{o}C and then transferred into the deposition chamber. Finally, the electron transport layer (LiF) and aluminium electrodes were deposited at the respective thicknesses of 0.5 nm and 100 nm using a vacuum Edward Auto 306 deposition unit at the appropriate pressure of 10^{-6} mbar. The samples were successfully annealed at 120 ^{o}C in the furnace for 5 min under nitrogen gas. In the process, the current density-voltage (J-V) characteristic was measured under ambient conditions using a computer-interfaced Keithley (HP2420) source meter with AM 1.5 Global solar simulator (model SS50AAA), which operates at a reasonable light intensity rate of 100 mW/cm^2. However, the Ag/Ca bimetallic photoactive films' optical absorption characteristics were examined employing a UV-Vis absorption photo-spectrometer (T80-PG-Instrument limited). The conventional device architecture, which consists of several layers of materials as provided in figure 5.2, is given by GLASS/ITO/PEDOT/PSS/ACTIVE-LAYER/Ag/Ca/LIF/AL. The devices have an effective area of given as 0.04 cm^2 or 4.0 mm^2.

5.4. Result and discussion sections

5.4.1 Characterizations of Ag/Ca bimetallic nanoparticles

Surface morphology

The surface morphology and composition of silver/calcium (Ag/Ca) bimetallic nanocomposites were satisfactorily probed using transmission electron microscopy (TEM) and scanning electron microscopy (SEM), respectively. The TEM, EDX, and SEM images are taken from the powder form of Ag/Ca bimetallic nanoparticles, as presented in figure 5.3. As reported in the literature, the bimetallic nanoparticles of Ag/Ca do exist at different structural phases [31]. The TEM images presented in figure 5.3a and b exhibited a remarkable structure pattern of the Ag/Ca bimetallic nanocomposites taken from the powder form. The particle sizes range from 10 nm to about 50 nm. The TEM image in figure 5.3a demonstrated the crystal fringes, which could probably be due to the medium's well-aligned crystalline structure. On the

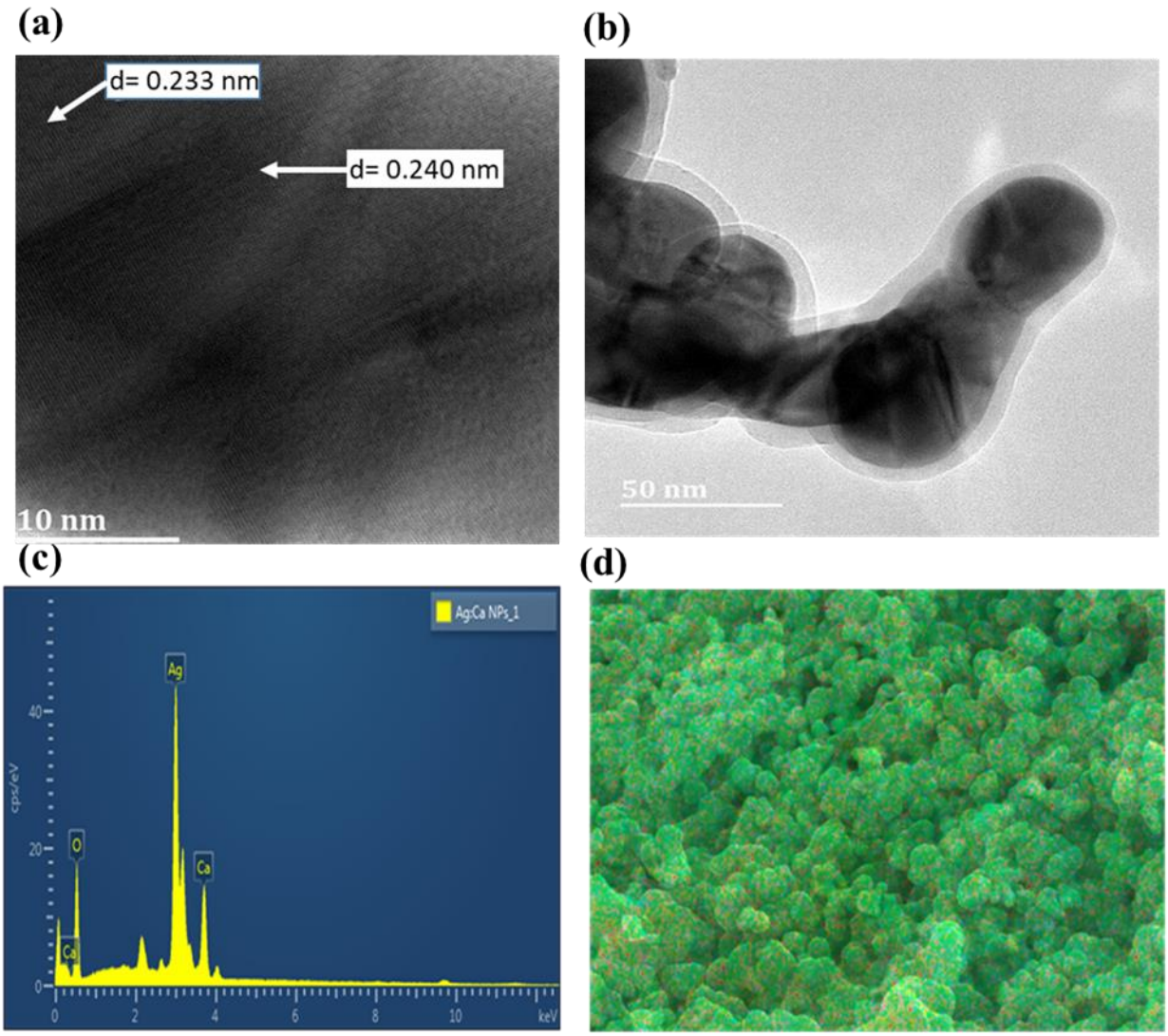

Figure 5.3: The desirable morphology of the synthesized Ag: Ca bimetallic nanoparticles; (a) and (b) are TEM images at different magnifications, (c) Energy dispersion (EDX) analysis, and (d) the SEM image of bimetallic nanoparticles with elemental mapping representing elements Ag Ca O.

other hand, it was found that the measured lattice spacing matching to the actual value of d = 0.233 nm which is effectively attributed to the a-axis of the hexagonal closed packed (hcp) of Ca single phase, while d = 0.240 nm could be probably accredited to Ag-doped with Ca hcp structure. In contrast, the TEM image provided in figure 5.3b indicates the core-shell-like structure of the bimetallic nanoparticles, in which Ag is a core and Ca appears to be the shell. This is evident by the dominant greenish color on the surface of the SEM images in figure 5.3d representing Ca on the surface. The elemental composition of bimetallic nanoparticles was studied using energy dispersion (EDX) data provided in figure 5.3c, which revealed the existence of characteristic peaks of silver, calcium, and a slight trace of oxygen content in the medium. The existence of oxygen can probably be due to the background of the samples and

possible partial oxidation of Ca because of the exposure to the ambient laboratory conditions. However, the SEM image in figure 5.3d indicates the existence of several forms of clusters, which appeared to be composed of the same interconnected bud-like structure of Ag/Ca bimetallic nanoparticles. It can also be witnessed that the elemental mapping taken from the same powder displayed the uniform distribution of elements of silver (Ag) and calcium (Ca) in the medium. The domination of green colour representing the Ca element in is suggesting that Ca is covering a shell in the Ag core.

5.4.2 X-ray diffraction study of Ag/Ca bimetallic nanoparticles

The Seifert X-ray diffractometer with Cu-Kα radiation (λ = 1.5418 Å) was used to probe the powder sample of Ag/Ca bimetallic nanocomposites. The XRD pattern collected from Ag/Ca bimetallic nanocomposites are present at the diffraction angles ranging from 30^{o} to 85^{o}, as shown in figure 5.4. The XRD pattern consists of distinct peaks near 38.2^{o}, 44.5^{o}, 65.5^{o}, 78.5^{o}, and 82.5^{o}, respectively. These peaks can be attributed to diffraction from the crystal planes (111), (200), (220), (311), and (222) of Ag/Ca bimetallic nanocomposites. Interestingly, the corresponding peaks achieved are promising in confirming the crystalline structure of synthesized Ag/Ca bimetallic nanoparticles, which is beneficial in promoting charge transport and enhancing the device performance of thin-film organic solar cells.

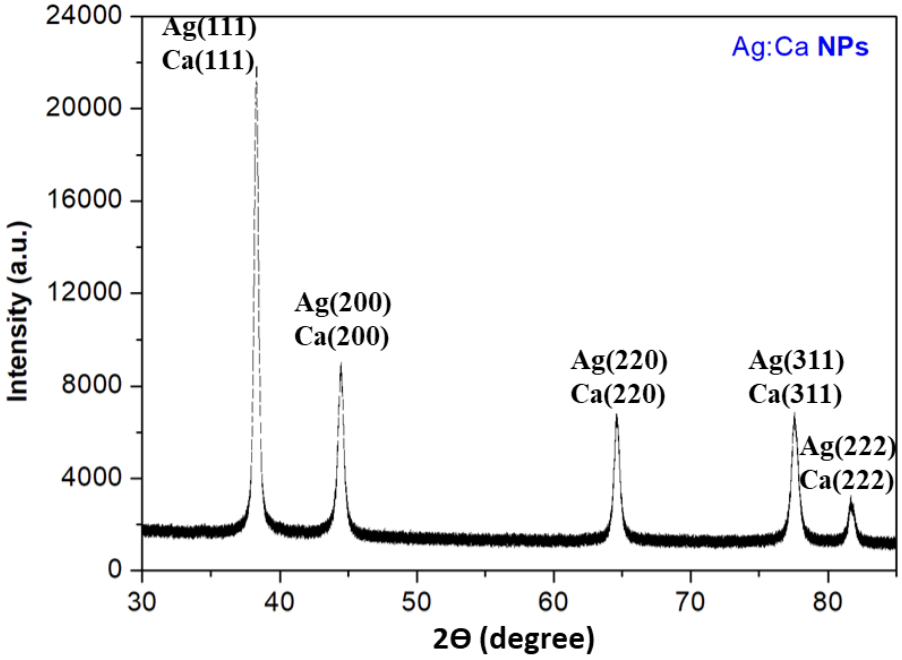

Figure 5.4: The X-ray diffraction pattern of Ag/Ca bimetallic nanocomposites.

5.4.3 Optical properties of Ag/Ca bimetallic nanoparticles

The optical absorption properties of the solar absorber films are one of the main factors that can determine the amount of photon-generated current in OSC devices. Nevertheless, the UV-Vis measurements were successfully conducted from solar absorber layers for the P3HT/PCBM blends with and without the addition of Ag/Ca nanoparticles, as provided in figure 5.5a. The absorption spectra of the doped films incorporated with Ag/Ca bimetallic nanocomposites displayed two desirable prominent peaks at the doping level of 1%, 3%, and 5%, respectively. The absorption peak centred around 512 nm is the absorbency of a P3HT/ PCBM blends as depicted in the pristine film. The new absorption bumps near 400 nm clearly come from the incorporation of Ag/Ca in the absorber layers as it is evident in comparison to the pristine counterparts (See figure 5.5a). The intensity of the optical absorption changes with the concentration of the metal-nanoparticles in the medium, where the maximum intensity peak is observed from 3% wt doping level of Ag/Ca in the absorber layer. However, as the concentration increases to 5% then the intensity peak drops once again which is attributed to the formation of high-level defect concentration in the absorber layer that has promoted charge recombination. The high charge non-radiative charge recombination leads to the reduction of the absorbance peaks. The existence of defects is evident by the measured high series resistance from a solar cell with 5% doping level, which has resulted in lower device performances, i.e., low J_{sc}, FF, and PCE values. On the other hand, the best device performance recorded in this investigation is from devices at a doping level of 3% that exhibited lower series resistance and better photons harvesting, which are beneficial to boost the performance of thin-film organic solar cells. The intensity of the absorbency generally increases with the doping level of 1%, 3%, and 5% of Ag/Ca in the film and a slight redshift is also visible on the vibrionic shoulder of P3HT. On the other hand, the optical absorbance spectrum of synthesized Ag/Ca was also taken from deionized water suspension, as provided in figure 5.5b. The broad absorption spectrum observed in figure 5.5b is significantly situated at 400 nm. This is likely to be a band-to-band transition of the Ag atom in the composite.

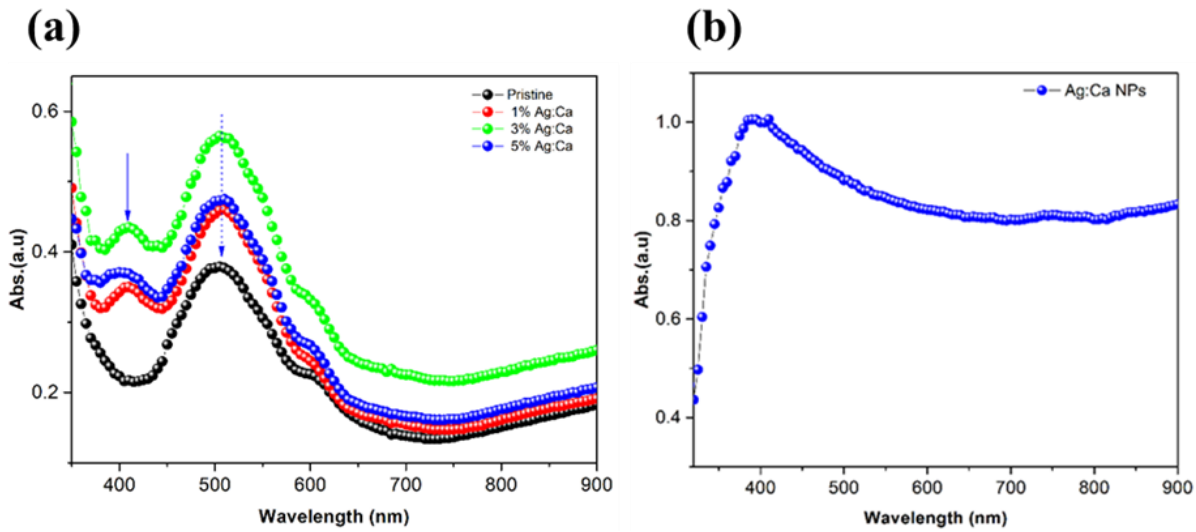

Figure 5.5: (a) UV-Vis absorption spectra taken at a different doping level of Ag/Ca bimetallic nanocomposites in absorber layers of TFOSC (b) the UV-Vis absorption spectrum of the Ag/Ca bimetallic powder in water suspension.

However, the broad absorption band is a clear testimony of enhanced scattering processes in the medium. It is to be noted that the plasmonic metallic nanocomposites in the solar absorber of TFOSCs are promising in improving optical absorption through light scattering and localized surface plasmonic resonance (LSPR) effects, which is beneficial to the light-harvesting ability, as reported by recent studies [32,33]. Due to the influence of LSPR of Ag/Ca bimetallic nanocomposites, optical absorption enhancement was effectively achieved in the visible and near-infrared regions at different concentrations.

5.4.4 Device characterization doped with Ag/Ca nanoparticles

In this section, the electrical properties of P3HT/PCBM blend-based thin-film organic solar cells with and without Ag/Ca bimetallic nanocomposites were investigated. The current-voltage (J-V) characteristics of the solar cells are presented in figure 5.6, which clearly shows the concentration-dependent performance of the solar cells. The photocurrents measured from the devices have been enhanced by the presence of the nanoparticles in the absorber layer compared to the reference cells at the doping level of 1%, 3%, and 5%, which display remarkable high device performance, as shown in figure 5.6 and Table 5.1, respectively. According to the information derived from the J-V characteristic curves, the effects of Ag/Ca bimetallic nanocomposites are evident in the photo-voltaic performance of TFOSC devices. The results further indicate that the parameters, including open-circuit voltage (V_{oc}), short-circuit current (J_{sc}), power conversion efficiency (PCE), and fill factor (FF), attained at the

respective doping level of 1%, 3%, and 5% of Ag/Ca nanoparticles are found to be higher than that of pristine (undoped-layer). Considering this, the measured J_{sc} values enhance dramatically from 8.7 mA/cm^2 for the pristine solar absorber to 11.3, 13.7, and 11.6 mA/cm^2 for the devices doped with Ag/Ca bimetallic nanocomposites at concentrations of 1%, 3%, and 5%, respectively.

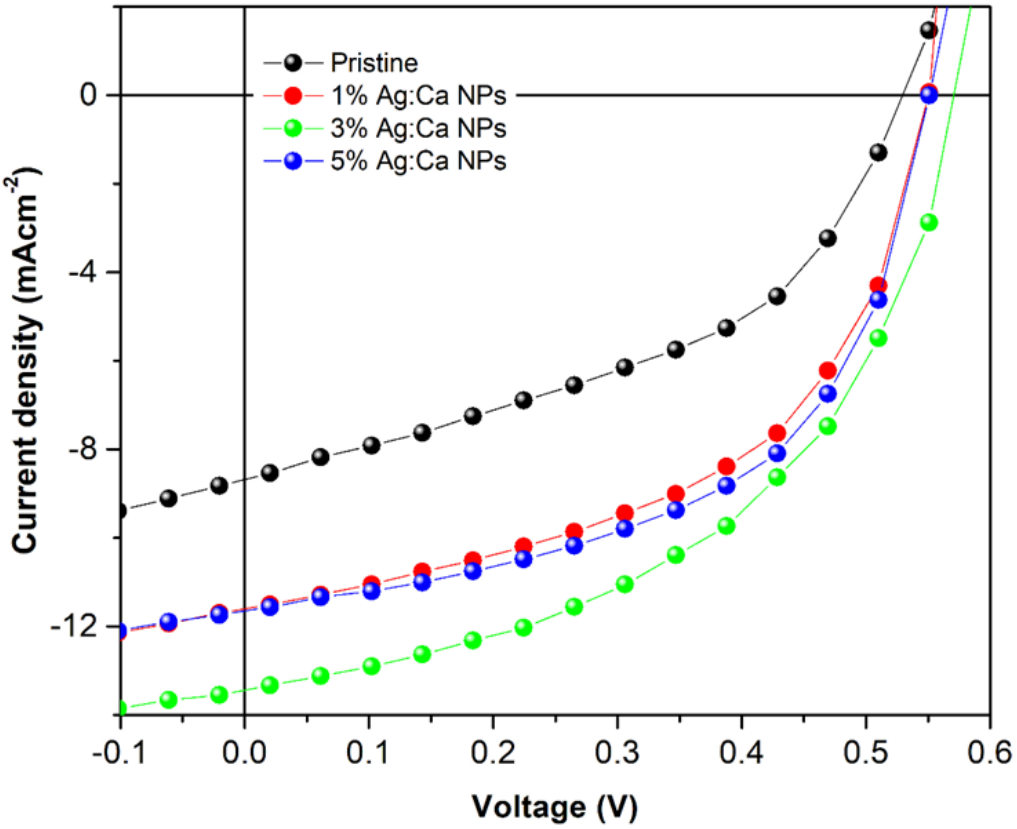

Figure 5.6: J-V characteristic of the solar cells fabricated using P3HT/PC61BM blend photo-active layer containing Ag/Ca bimetallic nanocomposites at the respective doping level of 1%, 3%, and 5% concentrations.

Such enhancements partly originate from the reduction of the series resistance (R_s), as reported by recent studies [9] that reduces charge recombination in the medium. The maximum PCE recorded in the current investigation was 4.13%, which corresponds to a high J_{sc} of 13.7 mA/cm^2 at the doping level of 3% (See Table 5.1). Such changes in the device performance are attributed to the occurrence of LSPR effects and light trapping through scattering, which was effectively displayed on the UV-Vis optical absorption spectra, as provided in figure 5.5. Recent studies have reported that the formation of a strong electromagnetic field (EMF) in the vicinity of the metal NPs would also contribute to effective dissociations of excess excitons at the metal-polymer interfaces.

Table 5.1: Photo-voltaic parameters observed for the devices with the best performance at the doping level of 1%, 3%, and 5% concentrations of Ag/Ca bimetallic nanoparticles.

Ag: Ca (wt%)	**V_{oc} (V)**	**J_{sc} (mA/cm^2)**	**FF (%)**	**PCE (%)**	**R_s (Ωcm^2)**
0% (Pristine)	0.51	8.7	36.7	1.99	395
1%	0.55	11.3	51.3	3.22	247
3%	0.57	13.7	53.4	4.13	134
5%	0.55	11.6	52.8	3.47	151

The local EMF produced by the metallic nanoparticles can probably promote the diffusion of excitons and charge separation, which is beneficial in promoting the photocurrent [34,35]. In general, the Ag/Ca bimetallic nanocomposites can play a vital role in enhancing the electrical conductivity of the polymer medium and promoting charge carriers.

5.4.5 Charge transport properties analysis of Ag/Ca bimetallic nanoparticles

It is to be noted that the space charge limited current (SCLC) is an effective method used to investigate the charge transport properties of the absorber medium of a solar cell device. The SCLC data were taken under the dark conditions when the photon-induced charge generations were suppressed, and traps were filled in the medium. The SCLC is a significant region where the amount of current extracted can probably rely on the bulk properties of the solar absorber. However, it has been reported that numerous efforts have led to the detection of very desirable parameters of the charge transport properties in several semiconductor mediums, especially zero charge mobility and field activation factors, respectively [36]. The measured SCLC data is often compared to the Mott-Gurney law used to be able to determine the transport parameters. However, we employed field-dependent charge transport mobility equation of the form: $\mu(E)=\mu_o \exp-(\gamma\sqrt{E})$. Considering this, the SCLC can be explained by the Mott-Gurney law coupled with the field-dependent mobility equation.

$$J = \frac{9}{8}\varepsilon\varepsilon_o\mu_o\frac{V^2}{L^3}exp\left(0.89\gamma\sqrt{\frac{V}{L}}\right). \quad (5.1)$$

where ε_o in equation (5.1) shows the permittivity of free space, μ_o exhibits the significant zero-field mobility, ε depicts the desirable relative dielectric permittivity of the material, L denotes the suitable thickness of solar absorber, γ displays the field activation factor, and V indicates the voltage drop across the sample, and it can probably be rectified via the built-in voltage (V_{bi}). Therefore, the experimental data were suitably fitted to theoretical equation (5.1), and it was observed to be in good agreement with experimental data, as displayed in figure 5.7. It has been reported that the field activation factor; $\gamma = B\left(\frac{1}{k_BT} - \frac{1}{k_BT_0}\right)$, can be attributed to temperature (T) dependence, while the constant parameters T_0 and B can probably be achievable due to the nature of the material [37].

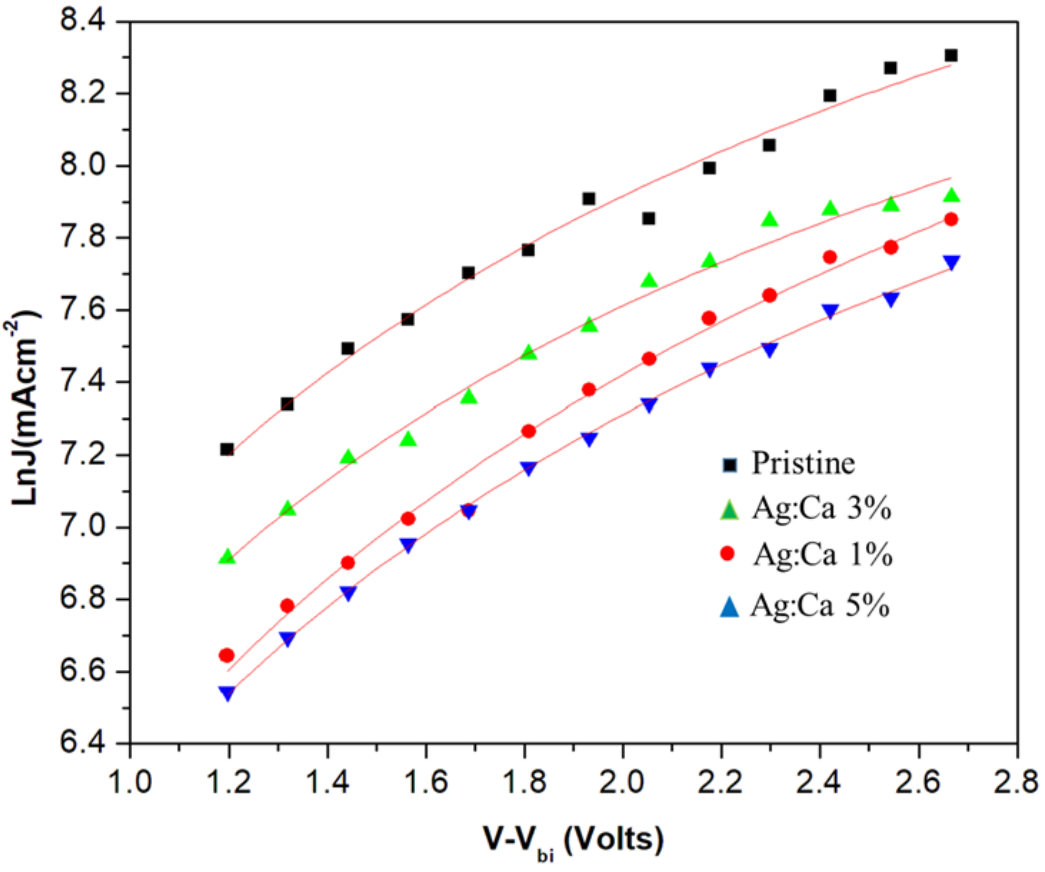

Figure 5.7: The space charge limited current data taken from solar cells fabricated with Ag/Ca doped solar absorbers at the concentration of 1%, 3%, and 5%.

Moreover, the zero-field mobility and field activation factor derived from the analysis are observed to be comparable with the expected values observed in the literature, as provided in Table 5.2. The results further indicate that the zero-field mobility μ_o values measured at the

doping level of 1%, 3%, and 5% concentrations of Ag/Ca bimetallic nanoparticles are effectively observed to be one order of magnitude much higher compared to the pristine device, which displays the remarkable enhancement in their respective short-circuit current and fill factor values. Considering this, the zero-field mobility obtained from the fit displayed those values observed at the doping level of 3% and 5% concentrations of Ag/Ca bimetallic nanoparticles are much higher than that of 1% concentration. This could be probably due to low recombination in the devices with 3% and 5% concentrations, which is also evident in their improved fill factors. However, the observed zero-field mobility values agree better with the reduction of series resistance for devices with 3% and 5% concentrations. In general, it is a clear indication of the effect of Ag/Ca bimetallic nanocomposites doped with solar absorbers at different concentrations, which is beneficial in improving the charge transport properties and enhancing the charge dissociation in thin-film organic solar cells.

Table 5.2: The charge carrier transport parameters of TFOSCs based on photo-active layer doped with Ag/Ca bimetallic nanocomposites at the respective 1%, 3%, and 5% concentrations.

(P3HT:$PC_{61}BM$: Ag: Ca) (wt%)	**μ_o (Zero-field mobility) ($cm^2S^{-1}V^{-1}$)**	**γ (Field activation factor) (cmV^{-1})**
0% (Pristine)	4.69×10^{-4}	-3.65×10^{-4}
1%	1.87×10^{-3}	-1.43×10^{-4}
3%	3.66×10^{-3}	-2.85×10^{-4}
5%	1.98×10^{-3}	-1.54×10^{-4}

5.5 Conclusion

The silver/calcium bimetallic nanocomposites were successfully synthesized and suitably employed into P3HT/PC61BM solar absorber films with the view to improving energy harvesting and charge transport processes in thin-film organic solar cells. The metal nanoparticles were incorporated into the absorber layer at a concentration of 1%, 3%, and 5% by weight, which displayed enhanced device performances compared to the undoped. This is attributed to improved optical absorption and charge transport processes by the occurrence of local surface plasmon resonance effect and far-field scattering assisted light trapping in the medium. Consequently, the best device performance parameters measured in this investigation

are PCE = 4.13%, J_{sc} = 13.7 $mAcm^{-2}$, V_{oc} = 0.57 V, and FF = 53.4% at the doping level of 3% by weight. Generally, all the solar cells doped with metal nanoparticles have exhibited improved device performance compared to undoped devices. However, excessive use of the NPs is unfavorable to the performance of solar cells as evidenced by the lower PCE of the devices at 5% doping level. Finally, the use of bimetallic nanocomposites has a significant influence on the charge transport processes in TFOSC and reduces the recombination rate to harvest more photocurrent. The Ag/Ca is environmentally stable and can be used for solution processing of devices to produce low-cost and flexible solar panels.

Authors statement

All authors are equally involved in the preparation of this manuscript submitted to the Journal of Physics and Chemistry of Solids. The authors have acknowledged the organizations that support this research work financially.

Declaration of competing interest

The authors declare the following financial interests/personal relationships which may be considered as competing interests: Prof. Genene Tessema Mola reports financial support was provided by National Research Foundation South Africa.

Acknowledgments

G.T. Mola acknowledges the financial support received from South Africa-China Joint Research Program (2021) and the National Research Foundation (NRF) (Grant numbers: 93562 and 132786), South Africa. Y. Zhang acknowledges the support from the National Key Research and Development Program (2021YFEO105800), China.

References

[1] S. Park., S.W. Heo., W. Lee., D. Inoue., Z. Jiang., K. Yu., H. Jinno., D. Hashizume., M. Sekino., T. Yokota. and K. Fukuda. Self-powered ultra-flexible electronics via nano-grating-patterned organic photovoltaics. Nature, 561(7724), (2018), 516-521.

[2] Q. Gan., F.J. Bartoli. and Z.H. Kafafi. Plasmonic-enhanced organic photovoltaics: Breaking the 10% efficiency barrier. Advanced materials, 25(17), (2013), 2385-2396.

[3] E. Stratakis. and E. Kymakis. Nanoparticle-based plasmonic organic photovoltaic devices. Materials Today, 16(4), (2013), 133-146.

[4] G. Zhao., Y. He. and Y. Li. 6.5% Efficiency of polymer solar cells based on poly (3-hexylthiophene) and indene-C60 bisadduct by device optimization. Advanced Materials, 22(39), (2010), 4355-4358.

[5] M.W. Dlamini., M.S. Hamed., X.G. Mbuyise. and G.T. Mola. Improved energy harvesting using well-aligned ZnS nanoparticles in bulk-heterojunction organic solar cells. Journal of Materials Science: Materials in Electronics, 31(12), (2020), 9415-9422.

[6] S.R. Gollu., R. Sharma., G. Srinivas., S. Kundu. and D. Gupta. Incorporation of SiO2 dielectric nanoparticles for performance enhancement in P3HT: PCBM inverted organic solar cells. Organic Electronics, 24, (2015), 43-50.

[7] Y. Cui., H. Yao., J. Zhang., T. Zhang., Y. Wang., L. Hong., K. Xian., B. Xu., S. Zhang., J. Peng. and Z. Wei. Over 16% efficiency organic photovoltaic cells enabled by a chlorinated acceptor with increased open-circuit voltages. Nature communications, 10(1), (2019), 1-8.

[8] Z. Zhou., W. Liu., G. Zhou., M. Zhang., D. Qian., J. Zhang., S. Chen., S. Xu., C. Yang., F. Gao. and H. Zhu. Subtle molecular tailoring induces significant morphology optimization enabling over 16% efficiency organic solar cells with efficient charge generation. Advanced Materials, 32(4), (2020), 1906324.

[9] L. Meng., Y. Zhang., X. Wan., C. Li., X. Zhang., Y. Wang., X. Ke., Z. Xiao., L. Ding., R. Xia. and H.L. Yip. Organic and solution-processed tandem solar cells with 17.3% efficiency. Science, 361(6407), (2018), 1094-1098.

[10] Z. Luo., R. Ma., T. Liu., J. Yu., Y. Xiao., R. Sun., G. Xie., J. Yuan., Y. Chen., K. Chen., G. Chai., H. Sun., J. Min., J. Zhang., Y. Zou., C. Yang., X. Lu., F. Gao. and H. Yan. Fine-

tuning energy levels via asymmetric end groups enables polymer solar cells with efficiencies of over 17%. Joule, 4 (6), (2020), 1236−1247.

[11] G. Kakavelakis., E. Stratakis. and E. Kymakis. Aluminum nanoparticles for efficient and stable organic photovoltaics. RSC Advances, 3(37), (2013), 16288-16291.

[12] W.F. Fu., X. Chen., X. Yang., L. Wang., Y. Shi., M. Shi., H.Y. Li., A.K.Y. Jen., J.W. Chen., Y. and H.Z. Chen. Optical and electrical effects of plasmonic nanoparticles in high-efficiency hybrid solar cells. Physical Chemistry Chemical Physics, 15(40), (2013),17105-17111.

[13] G.D. Spyropoulos., M.M. Stylianakis., E. Stratakis. and E. Kymakis. Organic bulk heterojunction photovoltaic devices with surfactant-free Au nanoparticles embedded in the active layer. Applied Physics Letters, 100(21), (2012), 213904.

[14] G.D. Spyropoulos., M. Stylianakis., E. Stratakis. and E. Kymakis. Plasmonic organic photovoltaics doped with metal nanoparticles. Photonics and Nanostructures-Fundamentals and Applications, 9(2), (2011), 184-189.

[15] G. Kakavelakis., E. Stratakis. and E. Kymakis. Synergetic plasmonic effect of Al and Au nanoparticles for efficiency enhancement of air-processed organic photovoltaic devices. Chemical Communications, 50(40), (2014), 5285-5287.

[16] B. Paci., D. Bailo., V.R. Albertini., J. Wright., C. Ferrero., G.D. Spyropoulos., E. Stratakis. and E. Kymakis. Spatially resolved in-situ structural study of organic electronic devices with nanoscale resolution: the plasmonic photovoltaic case study. Advanced Materials, 25(34), (2013), 4760-4765.

[17] Y. Hao., Y. Hao., Q. Sun., Y. Cui., Z. Li., T. Ji., H. Wang. and F. Zhu. Broadband EQE enhancement in organic solar cells with multiple-shaped silver nanoparticles: Optical coupling and interfacial engineering. Materials Today Energy, 3, (2017), 84-91.

[18] R. Koutavarapu., B. Babu., C.V. Reddy., K. Yoo., M. Cho. and J. Shim. A novel one-pot approach of ZnWO 4 nanorods decorated onto gC 3 N 4 nanosheets: 1D/2D heterojunction for enhanced solar-light-driven photocatalytic activity. Journal of Materials Science, 55(3), (2020), 1170-1183.

[19] M.S. Hamed., M.A. Adedeji., Y. Zhang. and G.T. Mola. Silver sulphide nanoparticles enhanced photo-current in polymer solar cells. Applied Physics A, 126(3), (2020), 1-9.

[20] X.G. Mbuyise. and G.T. Mola. Polycrystal metals nano-composite assisted photons harvesting in thin film organic solar cell. Solar Energy, 208, (2020), 930-936.

[21] Elhadi A. A. Arbab, Bidini Teleatu, Genene Tessema Mola, Environmental stability of PTB7: PCBM bulk heterojunction solar cell, J. Mod. Optics, Vol. 61(21), (2014)1749-1753.

[22] E.A.A. Arbab. and G.T. Mola. Metals decorated nanocomposite assisted charge transport in polymer solar cell. Materials Science in Semiconductor Processing, 91, (2019), 1-8.

[23] S.O. Oseni. and G.T. Mola. Bimetallic nanocomposites and the performance of the inverted organic solar cell. Composites Part B: Engineering, 172, (2019), 660-665.

[24] Genene Tessema Mola, Elhadi A. A. Arbab, Bidini A. Taleatu, K. Kaviyarasu, Ishaq Ahmad and M. Maaza, Growth and characterization of V_2O_5 thin film on the conductive electrode, J. Microscopy, Vol. 265 (2), (2017) 214-221

[25] P.T. Sah., W.C. Chang., J.H. Chen., H.H. Wang. and L.H. Chan. Bimetallic Ag–Au–Ag nanorods are used to enhance the efficiency of polymer solar cells. Electrochimica Acta, 259, (2018), 293-302.

[26] S.H. Jeong., H. Choi., J.Y. Kim. and T.W. Lee. Silver-based nanoparticles for surface plasmon resonance in organic optoelectronics. Particle & Particle Systems Characterization, 32(2), (2015), 164-175.

[27] A.O. Juma., E.A. Arbab., C.M. Muiva., L.M. Lepodise. and G.T.Mola. Synthesis and characterization of CuO-NiO-ZnO mixed metal oxide nanocomposite. Journal of alloys and compounds, 723, (2017), 866-872.

[28] L. Zhou., Y. Tan., J. Wang., W. Xu., Y. Yuan., W. Cai., S. Zhu. and J. Zhu. 3D self-assembly of aluminium nanoparticles for plasmon-enhanced solar desalination. Nature Photonics, 10(6), (2016), 393-398.

[29] N. Zhang., C. Han., X. Fu. and Y.J. Xu. Function-oriented engineering of metal-based nanohybrids for photoredox catalysis: exerting plasmonic effect and beyond. Chem, 4(8), (2018), 1832-1861.

[30] A. Zada., P. Muhammad., W. Ahmad., Z. Hussain., S. Ali., M. Khan., Q. Khan. and M. Maqbool. Surface Plasmonic-Assisted Photocatalysis and Optoelectronic Devices with Noble

Metal Nanocrystals: Design, Synthesis, and Applications. Advanced Functional Materials, 30(7), (2020), 1906744.

[31] S. Saha., A. Pal., S. Kundu., S. Basu. and T. Pal. Photochemical green synthesis of calcium-alginate-stabilized Ag and Au nanoparticles and their catalytic application to 4-nitrophenol reduction. Langmuir, 26(4), (2010), 2885-2893.

[32] D.H. Wang., D.Y. Kim., K.W. Choi., J.H. Seo., S.H. Im., J.H. Park., O.O. Park. and A.J. Heeger. Enhancement of donor-acceptor polymer bulk heterojunction solar cell power conversion efficiencies by addition of Au nanoparticles, Angew. Chem. 123(24), (2011), 5633-5637.

[33] X. Li., W.C.H. Choy., H. Lu., W.E.I. Sha. and A.H.P. Ho. Efficiency enhancement of organic solar cells by using shape-dependent broadband plasmonic absorption in metallic nanoparticles, Adv. Funct. Mater. 23(21), (2013), 2728-2735.

[34] D. Zhang., W.C.H. Choy., F. Xie., W.E.I. Sha., X. Li., B. Ding., K. Zhang., F. Huang. and Y. Cao. Plasmonic electrically functionalized TiO2 for high-performance organic solar cells, Adv. Funct. Mater. 23(34), (2013), 4255-4261.

[35] X. Ren., J. Cheng., S. Zhang., X. Li., T. Rao., L. Huo., J. Hou. and W.C.H. Choy. High efficiency organic solar cells achieved by the simultaneous plasmon-optical and plasmon-electrical effects from plasmonic asymmetric modes of gold nanostars, Small 12(37), (2016), 5200-5207.

[36] G. Tessema. Charge transport across bulk heterojunction organic thin film. Applied Physics A, 106(1), (2012), 53-57.

[37] Veaceslav Coropceanu, Je´roˆme Cornil, Demetrio A. da Silva Filho, Yoann Olivier, Robert Silbey, and Jean-Luc Bre´das, Charge Transport in Organic Semiconductors, Chem. Rev., 107 (2007), 926-952.

CHAPTER 6

Silver doped ZnS core-shell nanocomposites to promote photon harvesting in polymer solar cells

Physica B 646 (2022) 414347

Contents lists available at ScienceDirect

Physica B: Physics of Condensed Matter

journal homepage: www.elsevier.com/locate/physb

Silver doped ZnS core-shell nanocomposites to promote photon harvesting in polymer cells

Jude N. Ike, Michael A. Adedeji, Genene Tessema Mola *

School of Chemistry & Physics, University of KwaZulu-Natal, Pietermaritzburg Campus, Private Bag X01, Scottsville, 3209, South Africa

ARTICLE INFO

Keywords:
Metal nanoparticles
Charge transport
Solar absorber medium
Photovoltaic
Optical absorption

ABSTRACT

Silver doped zinc sulfide (ZnS:Ag) metal nanoparticles (NPs) were successfully synthesized and used as a dopant in thin-film organic solar cells (TFOSCs). Core-shell structured ZnS:Ag nano-particle is expected to improve photon harvesting in solar absorber medium. Polymers blend composed of poly-(3-hexylthiophene) (P3HT): [6,6]-phenyl C61 butyric acid methyl ester (PC61BM) were used as absorber medium with and without ZnS:Ag metal NPs. The concentrations of the metal NPs were varied to investigate the effect of doping level in the generation photocurrent. Significant device performances were recorded with short-circuit current (J_{sc}) of 14.30 $mAcm^{-2}$, fill factor (FF) of 52.63%, and PCE performance of 4.50% was achieved at 3% concentration by weight. Such an improvement is likely attributed to the presence of localized surface plasmonic resonance (LSPR) effect at the metal/polymer interfaces, which plays an essential role in augmenting the charge transport processes and augmenting the optical absorption. The results further indicate that PCE value has enhanced dramatically by 98% compared to the pristine reference cell. The finding of our investigation will be deliberated based on the measured optoelectronic and morphological properties of newly synthesized ZnS:Ag metal NPs and device performances.

6.1 Abstract

Silver-doped zinc sulfide (ZnS/Ag) metal nanoparticles (NPs) were successfully synthesized and used as a dopant in thin-film organic solar cells (TFOSCs). Core-shell structured ZnS/Ag nanoparticle is expected to improve photon harvesting in solar absorber medium. Polymers blend composed of poly-(3-hexylthiophene) (P3HT): [6,6]-phenyl C61 butyric acid methyl ester (PC61BM) was used as absorber medium with and without ZnS/Ag metal NPs. The concentrations of the metal NPs were varied to investigate the effect of doping levels in the generation of photocurrent. Significant device performances were recorded with short-circuit current (J_{sc}) of 14.30 $mAcm^{-2}$, fill factor (FF) of 52.63%, and PCE performance of 4.50% was achieved at 3% concentration by weight. Such an improvement is likely attributed to the localized surface plasmonic resonance (LSPR) effect at the metal/polymer interfaces, which

plays an essential role in augmenting the charge transport processes and optical absorption. The results further indicate that the PCE value was enhanced dramatically by 98% compared to the pristine reference cell. The findings of our investigation will be deliberated based on the measured optoelectronic and morphological properties of newly synthesized ZnS/Ag metal NPs and device performances.

6.2 Introduction

Polymer photovoltaic (PV) is a promising technology that can effectively use semiconducting organic molecules as solar absorber layers in solar cells, which is beneficial in converting photon energy into electricity for energy needs worldwide. Interestingly, the demand for more renewable solar energy sources for electricity and electronic devices has led to polymer organic photovoltaic attraction due to challenges arising from our continued reliance on fossil fuels. The thin-film organic solar cells (TFOSCs) are solar cells fabricated from conducting organic molecules, which are among the most promising solar cell technologies available today to produce affordable and flexible solar panels. The TFOSCs have various advantages compared to inorganic solar cells like amorphous silicon (a-Si) and Cadmium Telluride (CdTe). These advantages include the lightweight, cheap device manufacturing cost, mechanical flexibility, semitransparency, portability, and easy fabrication process through solution processing [1-8]. This investigation employs polymer blend composed of poly-(3-hexylthiophene) (P3HT)/ [6,6]-phenyl C61 butyric acid methyl ester (PC61BM). The certified recorded power conversion efficiency (PCE) value of organic solar cells has exceeded 17%, which is beneficial in harvesting much photon energy to boost the device performance in TFOSCs [9-12]. In TFOSCs research, the main challenges are augmenting the PCE of the devices without compromising the low-cost device fabrication and achieving a longer lifetime [13]. Several solvent additives, metal nanostructured particles (NPs), and semiconductor oxides have been employed to address the challenges of charge transport and collection processes in the polymer medium. These approaches complement the improving conductivity of the medium, reducing energy losses through the synthesis of low band gap conducting polymer and synchronizing energy levels, which are desirable to promote the device performance in TFOSCs [14]. On the other hand, the use of metallic NPs has attracted much attention in various research field such as sensors, photocatalysis, and solar energy conversion that contribute to increasing the device performance in TFOSCs [15,16]. The inclusion of metallic NPs in TFOSC improves the optical absorption of the active layer and creates a better conducive environment for exciton dissociation and charge transport process, which is favorable in reducing the high charge

recombination and augmenting overall performance due to localized surface plasmonic resonance (LSPR) effect [13, 17-19]. It is to be noted that some metal NPs have been used in most of the functional layers of TFOSCs structures because of their effective excitation of LSPR and their light scattering effect, respectively. These effects promote photon-to-electron conversion efficiency. The LSPR effect of the metal NPs could produce a local electromagnetic field in a polymer matrix, which expedites the respective generation and splits of excitons. In contrast, light scattering by NPs can probably increase the optical path length that enhance light trapping and generate more exciton [20-22].

In plasmonics, it is to be noted that metal NPs can effectively serve as plasmonic antennas, which induce intense localized electric fields to desired locations with nanometer precision [23]. Therefore, two types of effects exhibited by plasmonic excitations due to the electric field component of the incident light with wave vector (K) are presented in figure 6.1. Process (A) shows the occurrence of polarized charges on metal atoms that induce dipole moment when the wavelength of the incident wave is much larger than the size the nanoparticles. The surface electron could be displaced from the positive ions core by the action of the electric field of the incident wave, which collectively oscillates in resonance with the frequency of the wave, commonly referred to as the LSPR effect [23]. In the process (B), as provided in figure 6.1, shows a one-dimensional nanowire, which is much longer than that of the wavelength of the incident light. In this case, the light coupled to the nanostructure can excite the free electrons to generate a propagating surface plasmon (PSP), which travels along the surface of the metal nanostructure. Each phenomenon was recapitulated in brief, and many specifics could be observed in the cited reference [23]. It is to be noted that the purpose for the existence of plasmonic is the surface electron plasma of the metal NPs, which respond to the electromagnetic field of incident light. Among the metals, silver (Ag) has played a vital role in producing enhanced plasmons, making it one of highly desirable for several plasmonic applications [23,24]. Metal NPs in the polymer blend medium can produce a strong local electromagnetic field near the vicinity of the NPs, which is vital for exciton splitting and charge carrier transport to boost the device performance in TFOSCs. Furthermore, it has been reported that zinc sulfide (ZnS) NPs seem to be a stable transition metal sulfide that can be easily synthesized using low-temperature colloidal chemistry [25].

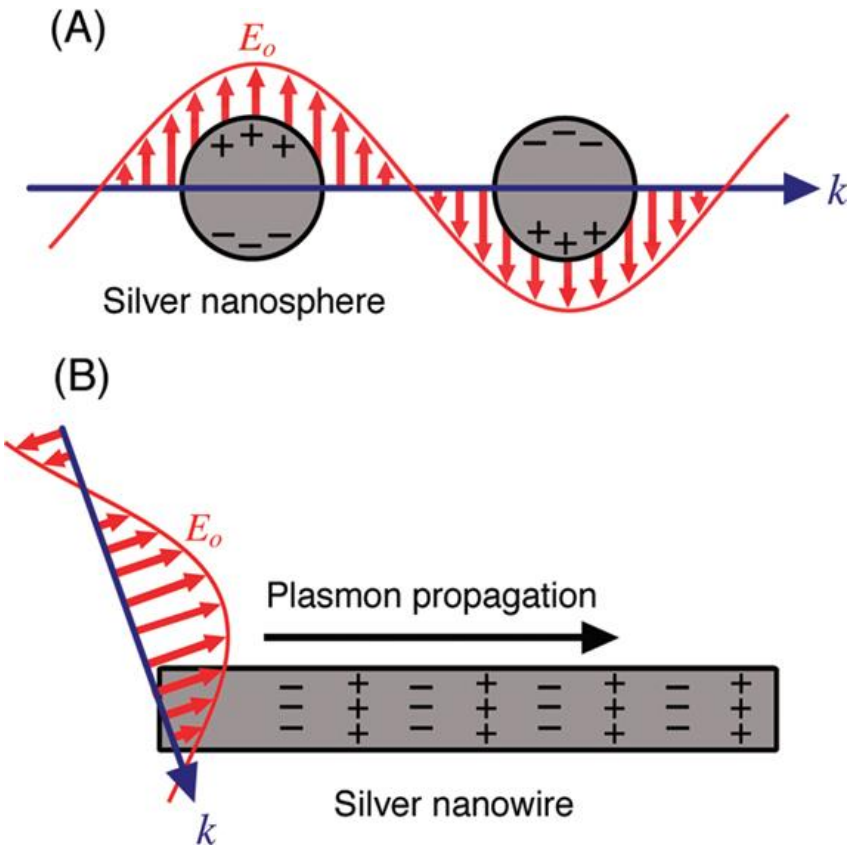

Figure 6.1: The two types of plasmonic nanostructure that shows possible plasmon excitations by the electric field (E_o) component of the incident light with wave vector (K). Reproduced with permission [23].

The ZnS NPs further indicate unique photoelectric properties, such as good electroluminescence and photoluminescence, respectively [26]. More details about ZnS semiconductor and their properties have been reported recently by Bredol *et al.* [27] and Dlamini *et al.* [28]. In this current research, we are reporting the effect of silver-doped zinc sulfide metal NPs as a dopant in the active layer of P3HT/PCBM at different concentrations by weight to improve the overall device performance in TFOSCs.

6.3 Experimental and methods

6.3.1 Materials used

The zinc sulfide doped with a silver (ZnS/Ag) metal NPs were successfully synthesized using the following chemical materials such as zinc nitrate hexahydrate (> 99.98% $Zn(NO_3)_2$ $6H_2O$), sodium sulfide nonahydrate ((Na_2S. $6H_2O$), 98.0%), silver nitrate hexahydrate (> 99.5% $AgNO_3$), and Polyvinyl Pyrrolidone (PVP, $(C_6H_9NO)_n$ of molecular weight (MW) of 25000-

30000), and such materials were bought from Merck, Germany. The Poly-(3-hexylthiophene) (P3HT), and [6,6]-phenyl-C61-butyric acid methyl ester (PC61BM), and poly-(3,4-ethylene dioxythiophene): poly-(styrene-sulfonate) (PEDOT/PSS) were also bought from Ossila Co. Ltd UK.

6.3.2 ZnS/Ag metal nanoparticles synthesis

The synthesis of ZnS/Ag metal NPs begun with the preparation of precursor solutions in 50 mL of deionized water. The solutes such as 0.5 M of Zn, 0.5 M of Na_2S, 0.2 M of Ag, and 3.0 g of PVP were dissolved in 50 mL of deionized water each in separate flasks. The solutions were stirred at room temperature and mixed up one by one into the Zn solution in droplet form under continuous stirring. The solution of the mixture was further stirred on a hot plate at an average temperature of about 40 ^oC for 3 h to ensure better miscibility. The resultant suspension was finally rinsed and filtered at different times using deionized water, which is beneficial to get rid of sodium ions to ensure pure ZnS/Ag metal NPs and it was then further dried up at 70 ^oC for 2 h in the vacuum oven. The ZnS/Ag metal NPs were then characterized using a UV-Vis absorption spectroscopy (T80-PG-Instrument limited), a transmission electron microscopy (TEM), a scanning electron microscopy (SEM), an energy dispersing X-ray (EDX) analysis, and X-ray diffraction (XRD).

6.3.3 ZnS/Ag metal nanoparticles device preparation

Conducting polymer blend-based solar cells were fabricated on Indium tin oxide (ITO) coated glass substrates and doping the absorbers with ZnS/Ag NPs at different concentrations. Initially, the substrates were etched with an acid solution consisting of $HCl/H_2O/HNO_3$ at the concentrations of 48%: 48%: 4% by volume. This is followed by thoroughly rinsing the substrate up sequentially in detergent, deionized water, acetone, and isopropanol using ultrasonic bath for 10 min each. They were then desiccated in the oven for 20 min at 120 ^oC before spin coating the hole transport layer PEDOT/PSS at 3500 rpm for 60 s. In the process, the hole transport layer (HTL) coated substrates were further annealed again in an oven for 20 min at 120 ^oC. The active layer was appropriately prepared in chloroform solvent from polymer blend P3HT/PC61BM blend at 1:1 at a 20 mg/mL concentration. The other three active layer solutions were separately prepared with the addition of 1%, 3%, and 5% concentrations of ZnS/Ag NPs by weight into the P3HT/PC61BM pristine solution. Then, the solutions were stirred on the hot plate at an average temperature of 40 ^oC for 3 h to ensure better dispersion of

the ZnS/Ag metal NPs and miscibility of the molecules in the active layer blend. In the process, the photoactive layer was then spin-coated on top of the HTL at the rate of 1200 rpm for 40 min and dehydrated in a furnace at 120 ^{o}C for 10 min under a nitrogen atmosphere before being transported into the deposition chamber (Edward Auto 306 deposition unit) at a suitable pressure of 10^{-6} mbar. Finally, the top electrode aluminium and electron transport layer (ETL) was deposited on the solar absorber film with thicknesses of 80 nm and 0.5 nm (See figure 6.2). Moreover, the solar cells were effectively characterized using a computer interfaced Keithley HP2420 source meter and solar simulator (model SS50AAA), which operate at air mass of about 1.5AM and 100 mW/cm^2. Meanwhile, the ZnS/Ag photoactive films' optical absorption characteristics were investigated using UV-Vis absorption spectra, which was attainable with a photo-spectrometer (T80-PG-Instrument limited).

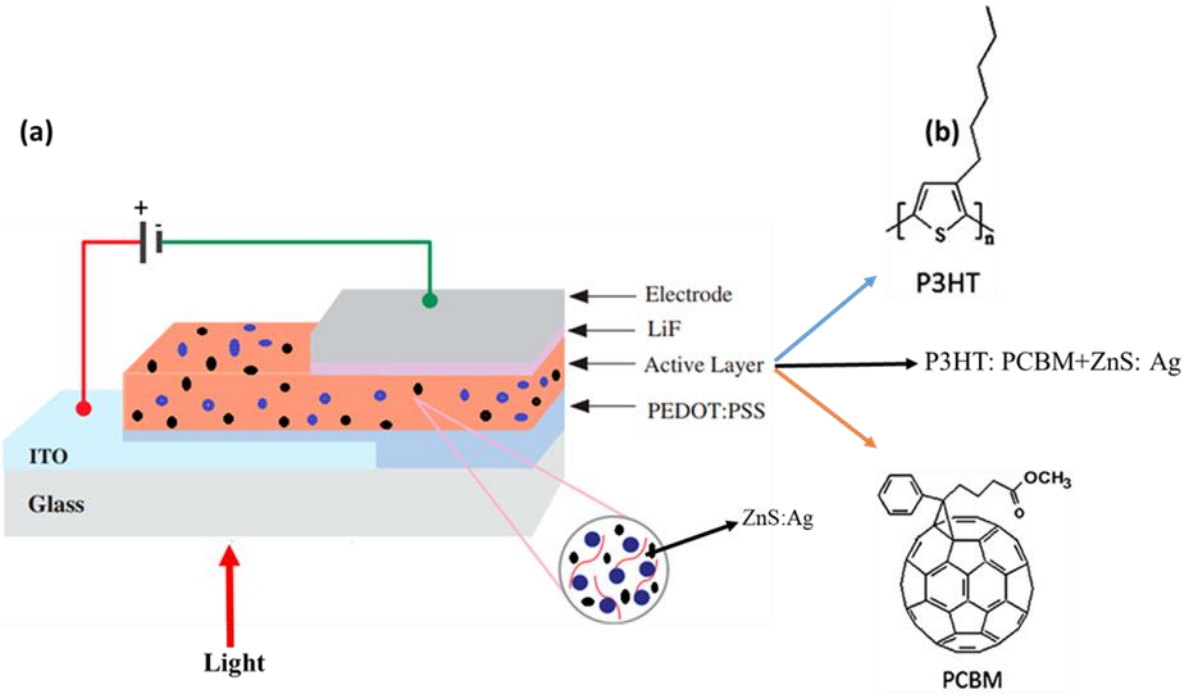

Figure 6.2: (a) and (b) show the schematic diagram of the TFOSCs with the ZnS/Ag metal NPs incorporated into the solar absorber medium.

6.4 Results and discussion

6.4.1 Morphology studies

In this section, transmission, and scanning electron microscopy (TEM and SEM) were used to investigate the morphology and composition of the synthesized ZnS/Ag metal NPs. The images provided in figure 6.3 were taken from the ZnS/Ag metal NPs powder form, which clearly showed the nature of the nanoparticles.

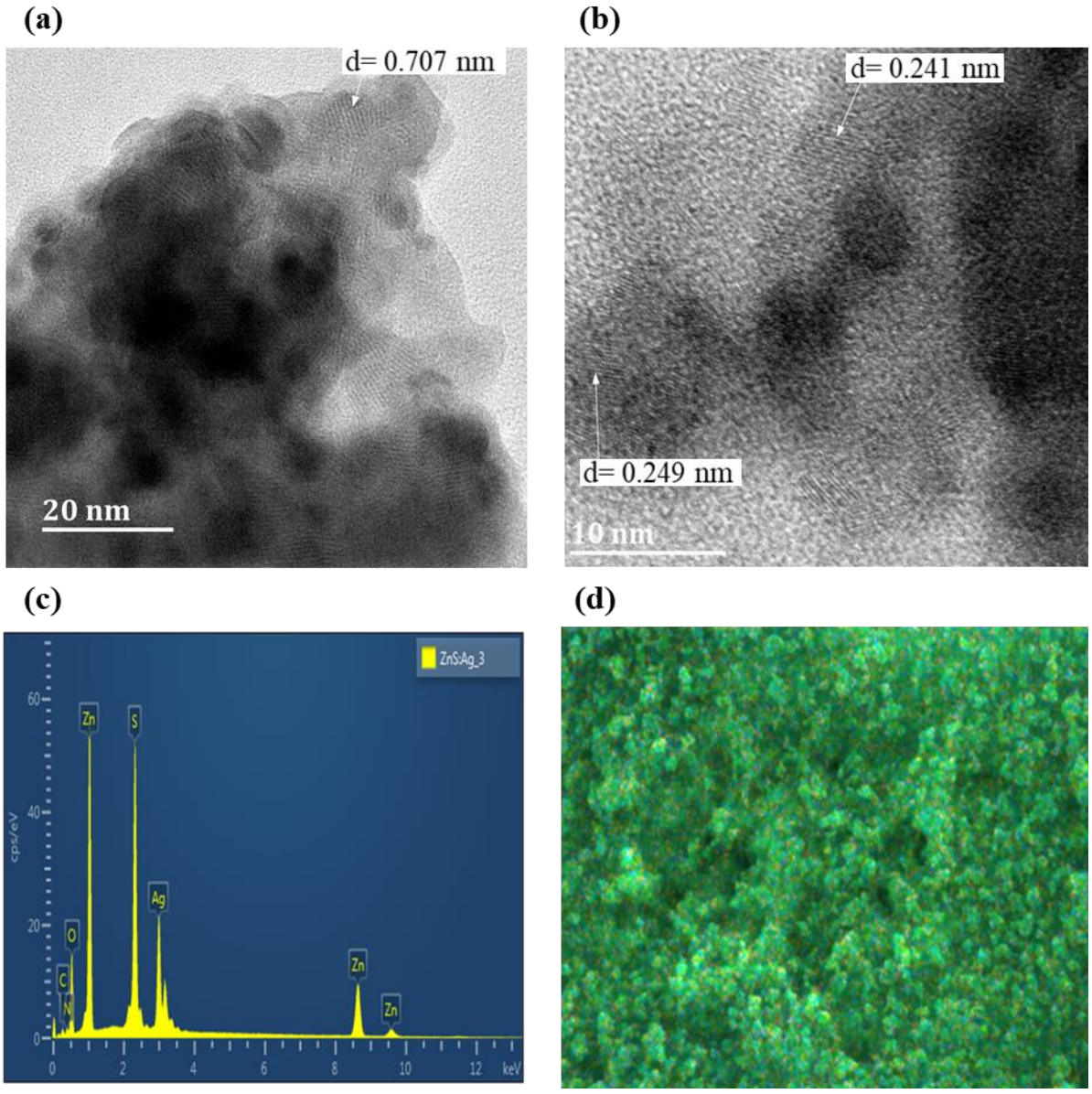

Figure 6.3: ZnS/Ag powder TEM images (a & b), (c) Energy Dispersive X-ray (EDX), and the SEM image (d).

According to the literature, the metal NPs of ZnS/Ag can be found/incorporated in various structural phases [29,30]. The TEM images provided in figure 6.3a and b display a core-shell structure pattern of the silver doped ZnS with different sizes where ZnS as a core and Ag as a shell. The sizes and shapes of the NPs play a vital role in promoting light-scattering processes in the solar absorber medium, which improves the value of short-circuit current (J_{sc}) in TFOSCs. The crystalline fringes were observed from the TEM image provided in figure 6.3a. It indicates the existence of well-defined crystalline planes with a spacing of d = 0.707 nm, which contributed to the **a**-axis of the ZnS hexagonal closed-packed (hcp) structure. The d

=0.241 nm and d = 0.249 nm are attributed to Ag planes enveloping the ZnS core. This is a clear indication of a predominantly green color on the surface of the SEM image, as provided in figure 6.3d showing Ag on the surface. The domination of the green color signifying the Ag element implies that Ag is covered as a shell in the ZnS core. Interestingly, the elemental composition of ZnS/Ag NPs was investigated using energy dispersing X-ray (EDX) analysis, as shown in figure 6.3c. It provided the presence of characteristic peaks of zinc, sulfur, silver, and a slight trace of carbon, nitrogen, and oxygen, respectively. It is to be noted that the presence of carbon, nitrogen, and oxygen is because of the partial oxidation of metal elements due to exposure to an ambient environment. The SEM images presented in figure 6.3d exhibited a well-defined formation of a metal NPs cluster-like structure in prolonged space, indicating agglomeration.

6.4.2 X-ray diffraction

The X-ray diffraction (XRD) analysis examined from zinc sulfide doped with silver (ZnS/Ag) metal NPs was effectively probed in terms of crystallographic structure. The diffraction pattern was scanned from 10^{o} to 90^{o} at 2θ values, which produced several prominent peaks as noted in figure 6.4. The obtained X-ray diffraction pattern was successfully matched with standard diffraction patterns JCPDS Card No. 231-0813 for ZnS [31], and JCPDS Card No. 900-8459 for Ag [32]. The ZnS composites exhibited a trigonal structure with cell parameters a = 3.82 Å and c = 150.24 Å and belong to space group R 3 m:H, while the Ag composite is a cubic structure, belonging to space group F m -3 m, with cell parameter a = 4.0862 Å. The average crystallite size of the ZnS/Ag NPs were determined to be 16.1 nm using Debye-Scherer's equation as given below:

$$D = \frac{K\lambda}{\beta cos\theta}. \quad (6.1)$$

Where *k* as provided in equation (6.1) indicates the Scherer constant (*k* = 0.89), λ is the wavelength of the X-ray (1.5405 Å), β is the full width at half maximum (FWHM) of the diffraction peak in radians, and θ depicts the corresponding Bragg angle at the maximum peak in degrees. The detailed of XRD analysis is summarized in Table 6.1, showing the numerous lattice planes to which the various lattice reflections were matched.

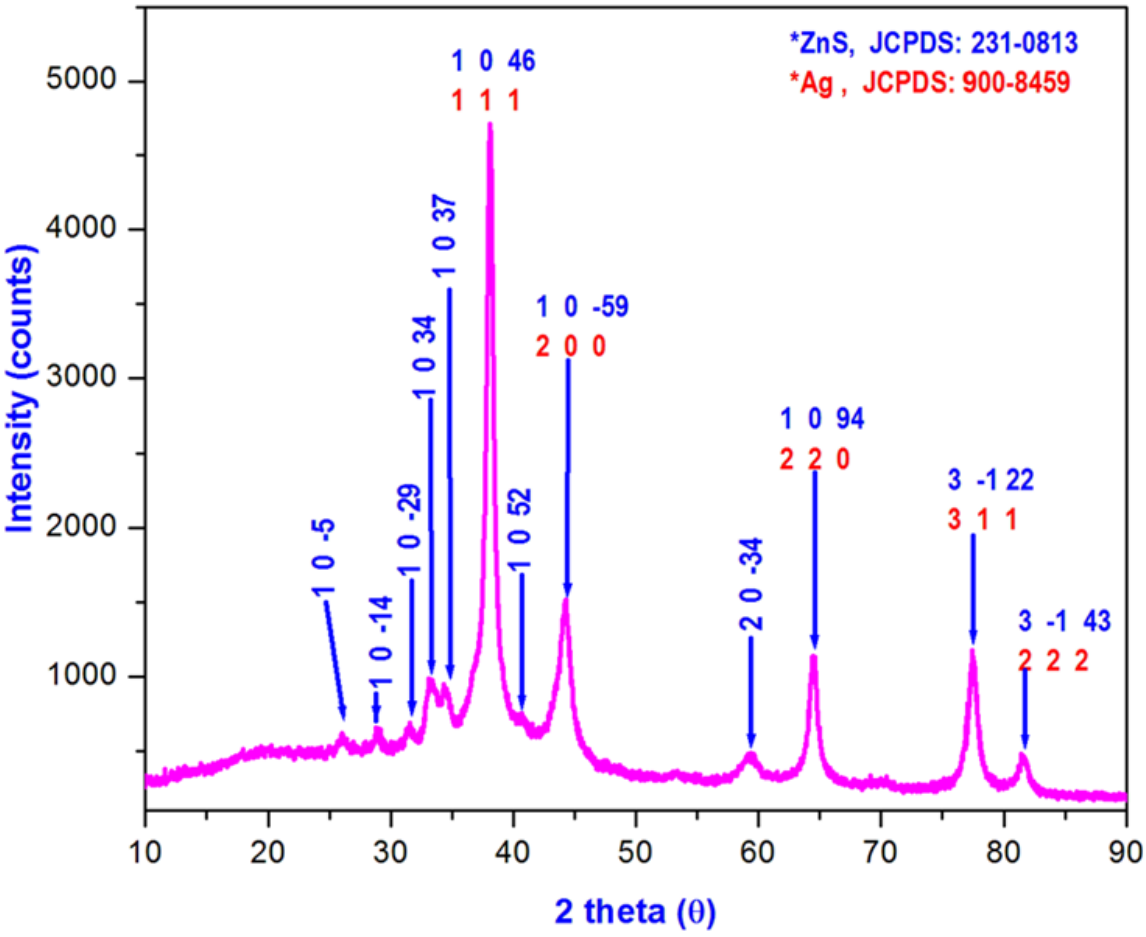

Figure 6.4: Powder XRD spectrum for ZnS/Ag metal NPs structural recognition.

Table 6.1: The analysis of XRD of ZnS/Ag metal NPs.

Peak no	**2θ (º)**	**hkl (ZnS)**	**hkl (Ag)**	**FWHM (β)**	**D (nm)**
1	27.06	1 0 -5	---	0.30	26.96
2	27.88	1 0 -14	---	0.34	23.81
3	31.56	1 0 -29	---	0.48	17.01
4	33.10	1 0 34	---	0.94	8.72
5	34.28	1 0 37	---	0.70	11.74
6	38.08	1 0 46	1 1 1	0.50	16.62
7	40.66	1 0 52	---	0.52	16.11
8	44.24	1 0 59	2 0 0	0.62	13.68
9	59.38	2 0 -34	---	0.88	10.28
10	64.42	1 0 94	2 2 0	0.56	16.58
11	77.36	3 -1 22	3 1 1	0.60	16.77
12	81.36	3 -1 43	2 2 2	0.72	14.39

6.4.3 Optical properties of ZnS/Ag metal nanoparticles

The amount of photon-generated current in the devices can be investigated using optical absorption properties of the photoactive layer based on P3HT/PCBM. However, the optical absorption characteristics of the several films were effectively probed using UV-Vis spectra, as shown in figure 6.5a. The peak at 520 nm corresponds to the electronic excitation of the P3HT in the blend upon photon absorption film. The absorption spectra of the doped films with ZnS/Ag metal NPs depicted three suitable prominent peaks at 1%, 3%, and 5% concentrations. The absorption spectra of the doped films incorporated demonstrated significant bumps ranging from 400 to 450 nm and above 750 nm. It seems that the absorption spectra peaks are mostly red shifted with respect to the pristine film (See figure 6.5a). This implies that the crystallinity of the solar absorber medium was not disturbed by incorporating with ZnS/Ag metal NPs at 1%, 3%, and 5% concentrations by weight. The red shift observed is not only desirable but also

seems as a promising in repositioning the absorption peak to a high intense emission spectrum of solar radiation.

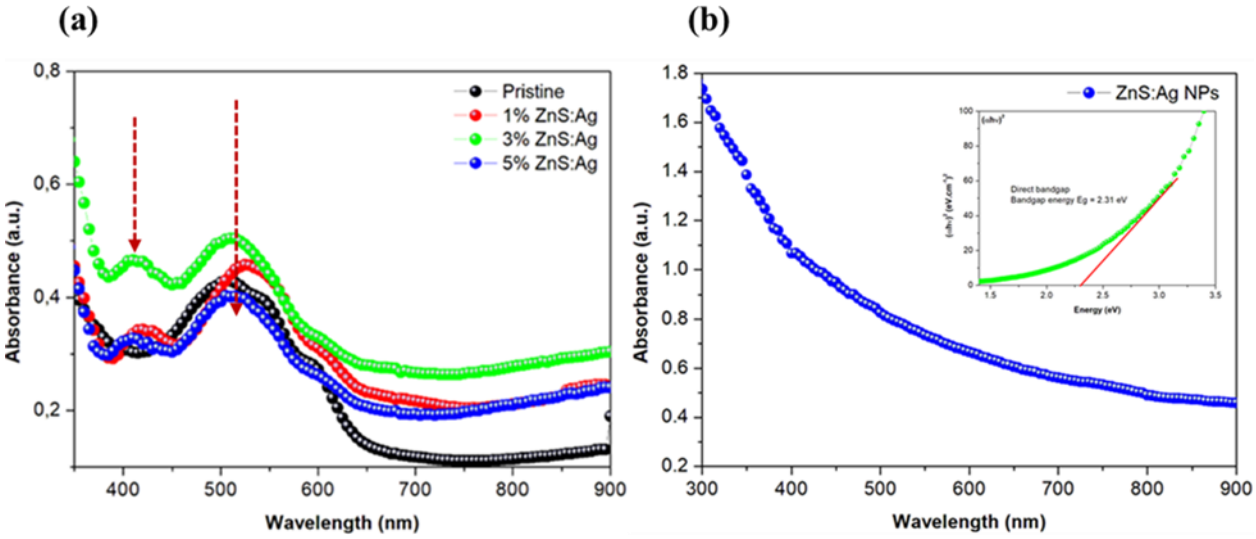

Figure 6.5: (a) Absorption spectra of the solar devices prepared with ZnS/Ag metal NPs at different concentrations (b) Absorption spectrum of the ZnS/Ag metal NPs suspension in deionized water with energy band gap (inset).

The occurrence of the new absorbance peaks is attributed to ZnS/Ag in the film and a slight redshift is also visible on the vibrionic shoulder located at 590 nm. Moreover, variations in the intensity of the prominent absorption peaks are evident with the concentration of the metal nanocomposites in absorber layers. The maximum absorbance peak was achieved at the optimum 3% concentration of ZnS/Ag metal NPs in the photoactive layer. Nevertheless, as the concentration enhances at the doping level of 5% by weight, the intensity peak decreases. This can be probably due to high defect concentration in the solar absorber layer that has augmented charge recombination. The decrease of absorbance peak at 5% doping level is due to non-radiative recombination, which leads to high series resistance that diminishes the device performance of FF, PCE, and J_{sc}, respectively. It is to be noted that the extensive absorption band in the infrared regions is probably due to the dependence of the LSPR effect on the nature, size, and shape of ZnS/Ag metal NPs in the medium, which is consistent with the distribution of the particles observed from TEM morphology. However, the wide absorption band is remarkable evidence in promoting light scattering processes and the LSPR effect in the medium, which is beneficial in augmenting photon harvesting in TFOSCs [33-35]. Figure 6.5b was recorded from the ZnS/Ag metal NPs powder in a deionized water suspension. Consequently, a broad absorption spectrum was observed, ranging from 350 nm to 900 nm.

The absorption peak ranging from 350 nm to 450 nm is associated with a band-to-band transition of electrons in the Ag metal nanocomposites. On the other hand, the peak is probably the presence of inter-band transition and transverse mode of the LSPR effect, which is promising in enhancing the photon harvesting ability within the solar absorber layer.

Moreover, the energy bandgap of the nanocomposite (ZnS/Ag) is determined from the onset of the optical absorption of the powder suspension, as provided in figure 6.5b (inset). One of the most prominent mechanisms to investigate the energy band gap is Tauc's plot, which can be quantified using the equation

$$\alpha h\nu = \beta(h\nu - E_g)^n. \tag{6.2}$$

where α signifies the absorption coefficient, h represents the Planck constant, ν exemplifies the photon's frequency, β denotes the constant, E_g is the energy gap, and n is the value depending on the nature of the transition. Recent studies reported that the value of n is equal to half for allowed direct transition and two for allowed indirect transition [36-37]. It is to be noted that E_g can be observed from the intercept of the tangent line of the curve at $(\alpha h\nu)^2 = 0$ in $(\alpha h\nu)$ versus the hν plot. Consequently, the achievable direct energy bandgap of ZnS/Ag nanoparticles is around 2.31 eV. Generally, the observation of improvement of optical absorption above 750 nm at 1%, 3%, and 5% concentrations of ZnS/Ag metal NPs can probably be attributed to the light trapping mechanisms via scattering. This can provide multiple reflections of light within the solar absorber layer, leading to trapping and enhanced light-harvesting performance in TFOSCs [35].

6.4.4 J-V characteristics of ZnS/Ag metal nanoparticles

The influence of ZnS/Ag metal nanoparticles on the performance of P3HT/PCBM based thin-film organic solar cells (TFOSCs) was studied using the measured current-voltage characteristics (J-V) of the devices. Fig. 6.6 represents J-V characteristics of TFOSC devices at different concentrations of ZnS/Ag nanoparticles in the photoactive layer. The data were taken under illumination with 100 mW/cm^2 in the ambient environment. The respective photovoltaic device parameters are summarized in Table 6.2. According to the results obtained on the photovoltaic parameters, the open-circuit voltage (V_{oc}) value displayed minor changes ranging from 0.55 as pristine to 0.55, 0.53, and 0.56 volts for doping levels 1%, 3%, and 5%, respectively. A slight increment on V_{oc} was observed in pristine compared to 3% concentration of ZnS/Ag metal nanoparticles, as provided in Table 6.2, but it suffers from a low short-circuit

current (J_{sc}), which resulted in relatively poor device performance. This could be the influence of the nanoparticles on the energy band structure of the active layer and electrodes.

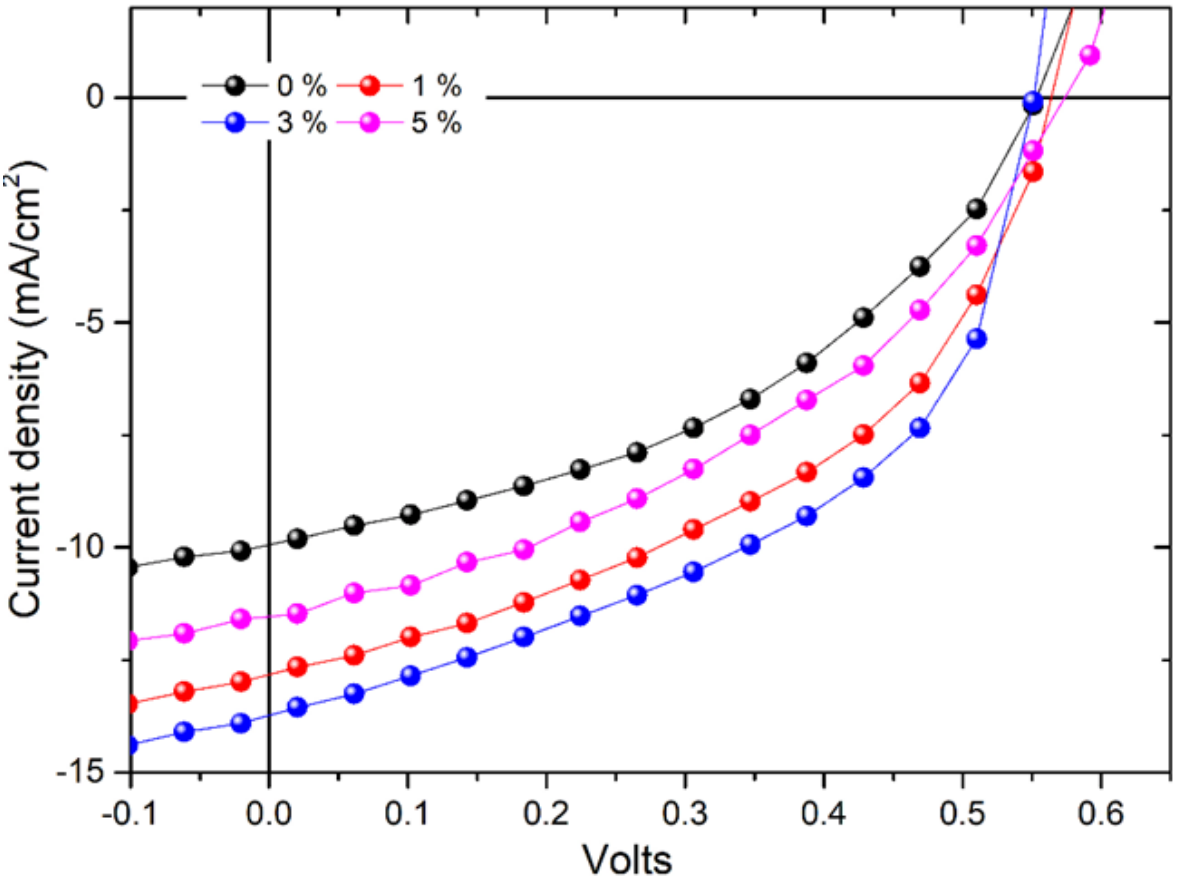

Figure 6.6: J-V characteristics of the devices produced as reference and ZnS/Ag metal NPs doped solar cells.

Moreover, the J_{sc} achieved at 1% (13.77 mAcm^{-2}), 3% (14.30 mAcm^{-2}), and 5% (12.22 mAcm^{-2}) concentrations are much higher than that of pristine value (10.31 mAcm^{-2}). The results further indicate that incorporating ZnS/Ag metal nanoparticles in photoactive layer enhances of the device J_{sc} and fill factor (FF), respectively. However, the J_{sc} improvements at 1%, 3%, and 5% concentrations are probably attributed to enhanced charge transport processes and augmenting the optical absorbance. Such improvements are probably due to the reduction of the series resistance (R_s), as reported recently by researchers [38] that decreases charge recombination in the medium, which is promising not only to improve the electrical conductivity of the polymer medium but also to augment the charge carriers.

Table 6.2: The J-V parameters of TFOSCs for the reference and the doped photoactive medium.

ZnS/Ag (wt%)	**V_{oc} (V)**	**J_{sc} (mA/cm^2)**	**FF (%)**	**PCE (%)**	**R_s (Ωcm^2)**
0% (Pristine)	0.55	10.31	39.43	2.14	827
1%	0.55	13.77	45.54	3.49	390
3%	0.53	14.30	52.63	4.50	149
5%	0.56	12.22	43.98	3.15	630

Recent studies have reported that the charge carrier mobility imbalance in P3HT/PCBM TFOSCs can negatively affect their device performance [39]. Interestingly, the improvement of J_{sc} and FF achieved, in the current experiment, suggests that incorporating ZnS/Ag metal nanoparticles at the doping level of 1%, 3%, and 5% assisted in enhancing the charge carrier mobility imbalance between the electron and hole mobility. The results further indicate that the achievable power conversion efficiency (PCE) of devices with ZnS/Ag improve dramatically from 2.14% as pristine to 3.49%, 4.50%, and 3.15% for 1%, 3%, and 5% concentrations, respectively. This is a significant improvement for devices fabricated under an ambient environment without using the glove box filled with inert gases. Nevertheless, the highest J_{sc}, FF, and PCE were observed from the solar cells at 3% concentration of ZnS/Ag metal NPs (see Table 6.2). Interestingly, the performance of PCE had improved by 98% with an augmentation in device FF to 52.63% at 3% concentration. Such enhancements on the device performance probably contributed to boosting the J_{sc} and low series resistances in the devices. It is to be noted that the low series resistance and a consequential leakage current are promising in leading to non-generation recombination and augmenting the charge transport mobility. Furthermore, it has been reported that incorporating metal nanoparticles in the solar absorber layer leads to enhanced performance and gives rise to the boosted structural stability of the blend [40]. However, the performance improvement can probably be attributed to the augmentation of the solar absorber morphology due to the existence of metal nanoparticles in TFOSCs.

6.4.5 Charge carrier transport of ZnS/Ag metal nanoparticles

The charge transport characteristics of the devices was effectively probed using the space charge limited current (SCLC), and it was taken under dark conditions. Figure 6.7b shows the measured J-V data under dark conditions. The dark current sharply increases above the Ohmic region and gets to a steady-state condition as it approaches to SCLC where most traps filled. This is the necessary condition to investigate the property of charge transport in polymer medium. It is to be noted that the examined SCLC data is compared to the Mott-Gurney law which is promises to determining the transport parameters. However, it has been reported that the SCLC data is fitted [41] with an equation-based Mott-Gurney's model law and field-dependent mobility equation.

$$J = \frac{9}{8}\varepsilon\varepsilon_o\mu_o\frac{V^2}{L^3}exp\left(0.89\gamma\sqrt{\frac{V}{L}}\right). \quad (6.3)$$

Where Ɛ and $Ɛ_o$ as provided in equation (6.3) exhibit the suitable relative dielectric permittivity of the polymer medium and free space. μ_o is a zero-field mobility, L demonstrates the active layer thickness, γ represents the field activation factor, and V indicates the applied voltage across the device, which could be corrected through the built-in potential voltage (V_{bi}) as stated by recent studies [19, 42-43]. The field activation factor $\gamma = B\left(\frac{1}{k_BT} - \frac{1}{k_BT_0}\right)$ is reliant on temperature (T), while the constant parameters T_0 and B could probably be relied on the nature of the material [38].

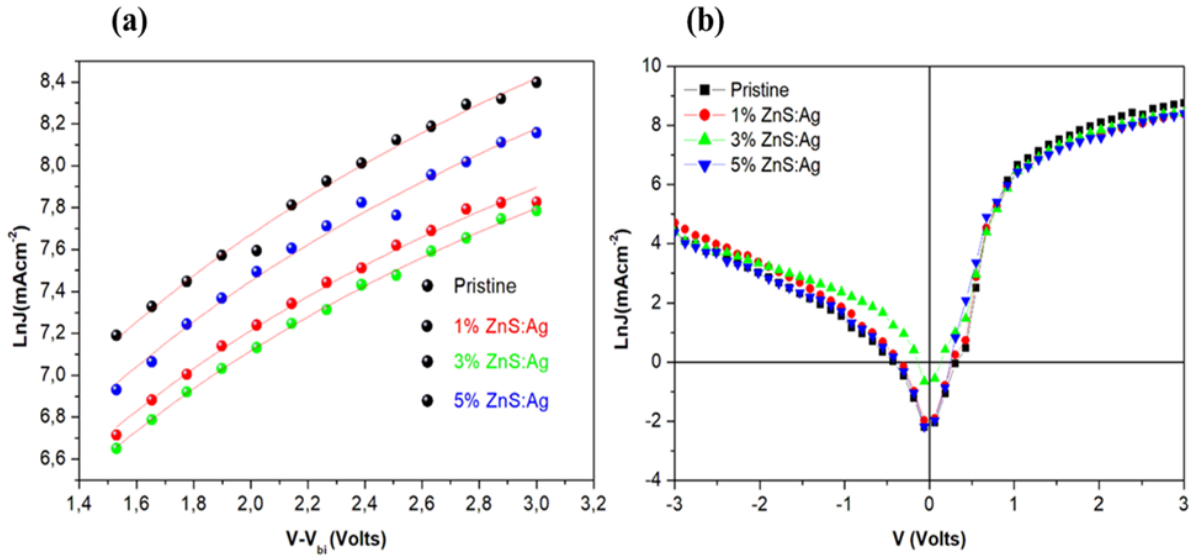

Figure 6.7: (a) The SCLC curve of devices fabricated with ZnS/Ag at different concentrations and (b) J-V measured under dark conditions.

According to the results presented in Table 6.3, it was found that the measured SCLC data were fitted with equation (6.3), which are well in agreement between the experiment and the prediction of Mott-Gurney's law. The experimental data further agreed significantly with the model, as provided in figure 6.7a.

Table 6.3: The charge transport parameters found from new organic solar cell devices fabricated with ZnS/Ag metal NPs.

P3HT/$PC_{61}BM$ ZnS/Ag (wt%)	**μ_o ($cm^2S^{-1}V^{-1}$)**	**γ (cmV^{-1})**
0.0%	5.15×10^{-5}	-4.04×10^{-5}
1%	1.07×10^{-3}	-3.67×10^{-5}
3%	1.11×10^{-3}	-3.55×10^{-5}
5%	1.05×10^{-3}	-3.49×10^{-5}

It was also observed that the respective zero-field mobility (μ_o) and the field activation factor (γ) derived from the analysis are in good agreement with the literature, as provided in Table 6.3. Recent studies reported that the negative values observed at the field activation factor propose that the mobility decreases at the high applied electric field in the polymer medium [38]. As displayed in Table 6.3, the zero-field mobility values of the devices with ZnS/Ag at 1%, 3%, and 5% by weight are two orders of magnitude higher than that of pristine TFOSC due to desirable enhancement in their J_{sc} values. This observation probably be attributed to the fact that the germination recombination in the devices was effectively reduced due to enhanced miscibility and crystallinity of the ZnS/Ag metal nanoparticles doped with solar absorber layer, which is clear evidence in their improved FF and the promotion of charge dissociation in TFOSCs.

6.5 Conclusion

In conclusion, ZnS/Ag metal nanoparticles were successfully synthesized using wet chemistry procedures. The nanoparticles were used in the photoactive layer of TFOSCs at various doping levels of 1%, 3%, and 5% by weight. It was found that all the devices fabricated with ZnS/Ag at different concentrations have shown a significant device performance improvement

compared to that of pristine material. Such an improvement due to the presence of metal nanoparticles is attributed to the existence of LSPR effect and light scattering phenomena, which are beneficial in assisting photon harvesting by solar absorber layer of TFOSC. The best performance recorded in this work was at 3% concentration by weight, which resulted in a maximum J_{sc} of 14.30 mA/cm^2 with the highest FF of 52.63% and PCE value of 4.50%. Finally, the ZnS/Ag metal nanoparticles are stable and suitable for roll-to-roll printing device fabrication, which is aimed at producing solar cells at low cost.

Declaration of competing interest

The authors declare that they have no known competing financial interests or personal relationships that could have appeared to influence the work reported in this paper.

Data availability

Data will be made available on request.

Acknowledgments

This work is financially supported by the National Research Foundation (NRF), South Africa (Grant numbers: 113835, 132786). The authors further recognize the members of staff in the microscopic and microanalysis unit (MMU) at UKZN for various TEM and SEM measurements.

References

[1] M.C. Scharber. and N.S. Sariciftci. Efficiency of bulk-heterojunction organic solar cells. Progress in polymer science, 38(12), (2013), 1929-1940.

[2] Genene Tessema Mola, Makhosazane Mthethwa, Mohammed Hamed, Micheal Adedeji, Xolani Mbuyesi, Amit Kumar; Gaurav Sharma, Yong Zang, Local surface plasmon resonance assisted energy harvesting in thin film organic solar cells, Journal of Alloys and Compounds, 856, (2020) 158172

[3] S.O. Oseni. and G.T. Mola. Properties of functional layers in inverted thin-film organic solar cells, Sol. Energy Mater. Sol. Cell., 160, (2017), 241-256.

[4] P. Tonui., S.O. Oseni., G. Sharma., Q. Yan. and G.T. Mola. Perovskites photovoltaic solar cells: An overview of current status, Renew. Sustain. Energy Rev., 91, (2018) 1025–1044.

[5] Z. Liu., S.Y. Lee. and E.C. Lee. Copper nanoparticle incorporated plasmonic organic bulk-heterojunction solar cells, Appl. Phys. Lett.,105(22), (2014), 179.

[6] A. Singh., A. Dey. and P.K. Iyer. Influence of molar mass ratio, annealing temperature and cathode buffer layer on power conversion efficiency of P3HT: PC71BM based organic bulk heterojunction solar cell. Organic Electronics, 51, (2017), 428-434.

[7] H. Yao., F. Bai., H. Hu., L. Arunagiri., J. Zhang., Y. Chen., H. Yu., S. Chen., T. Liu., J.Y.L. Lai. and Y. Zou. Efficient all-polymer solar cells based on a new polymer acceptor achieving 10.3% power conversion efficiency. ACS Energy Letters, 4(2), (2019), 417-422.

[8] X. Li., W.C.H. Choy., L. Huo., F. Xie., W.E.I. Sha., B. Ding., X. Guo., Y. Li., J. Hou., J. You. and Y. Yang. Dual plasmonic nanostructures for high performance inverted organic solar cells, Adv. Mater., 24(22), (2012), 3046-3052.

[9] Q. Liu., Y. Jiang., K. Jin., J. Qin., J. Xu., W. Li., J. Xiong., J. Liu., Z. Xiao., K. Sun. and S. Yang. 18% Efficiency organic solar cells. Science Bulletin, 65(4), (2020), 272-275.

[10] Y. Cui., H. Yao., J. Zhang., K. Xian., T. Zhang., L. Hong., Y. Wang., Y. Xu., K. Ma., C. An. and C. He. Single-junction organic photovoltaic cells with approaching 18% efficiency. Advanced Materials, 32(19), (2020), 1908205.

[11] C. Li., J. Zhou., J. Song., J. Xu., H. Zhang., X. Zhang., J. Guo., L. Zhu., D. Wei., G. Han. and J. Min. Non-fullerene acceptors with branched side chains and improved molecular packing to exceed 18% efficiency in organic solar cells. Nature Energy, 6(6), (2021), 605-613.

[12] F. Liu., L. Zhou., W. Liu., Z. Zhou., Q. Yue., W. Zheng., R. Sun., W. Liu., S. Xu., H. Fan. and L. Feng. Organic Solar Cells with 18% Efficiency Enabled by an Alloy Acceptor: A Two-in-One Strategy. Advanced Materials, (2021), 2100830.

[13] S.O. Oseni. and G.T. Mola. The effect of uni-and binary solvent additives in PTB7/PC61BM based solar cells. Solar Energy, 150, (2017), 66-72.

[14] B. Bouthinon, R. Clerc, J. Vaillant, J.M. Verilhac, J. Faure-Vincent, D. Djurado, I. Ionica, G. Man, A. Gras, G. Pananakakis, Impact of Blend Morphology on Interface State Recombination in Bulk Heterojunction Organic Solar Cells, Advanced Functional Materials, 25 (2015) 1090 1101.

[15] J.M. Lee., J. Lim., N. Lee., H.I. Park., K.E. Lee., T. Jeon., S.A. Nam., J. Kim., J. Shin. and S.O. Kim. Synergistic concurrent enhancement of charge generation, dissociation, and transport in organic solar cells with plasmonic metal–carbon nanotube hybrids. Advanced Materials, 27(9), (2015), 1519-1525.

[16] H.C. Liao., C.S. Tsao., T.H. Lin., M.H. Jao., C.M. Chuang., S.Y. Chang., Y.C. Huang., Y.T. Shao., C.Y. Chen., C.J. Su. and U.S. Jeng. Nanoparticle-tuned self-organization of a bulk heterojunction hybrid solar cell with enhanced performance. ACS nano, 6(2), (2012), 1657-1666.

[17] A. Foertig., J. Kniepert., M. Gluecker., T. Brenner., V. Dyakonov., D. Neher. and C. Deibel. Nongeminate and geminate recombination in PTB7: PCBM solar cells, Advanced Functional Materials, 24(9), (2014) 1306-1311.

[18] G.T. Mola., W.E. Dlamini. and S.O. Oseni. Improving optical absorption bandwidth using bilayer bulkheterojunction organic photoactive medium. Journal of Materials Science: Materials in Electronics, 27(11), (2016), 11628-11633.

[19] S.O. Oseni., K. Kaviyarasu., M. Maaza., G. Sharma., G. Pellicane. and G.T. Mola. ZnO: CNT assisted charge transport in PTB7: PCBM blend organic solar cell. Journal of Alloys and Compounds, 748, (2018), 216-222.

[20] L. Lu., Z. Luo., T. Xu. and L. Yu. Cooperative plasmonic effect of Ag and Au nanoparticles on enhancing performance of polymer solar cells. Nano letters, 13(1), (2013), 59-64.

[21] S.H. Jeong., H. Choi., J.Y. Kim. and T.W. Lee. Silver-based nanoparticles for surface plasmon resonance in organic optoelectronics. Particle & Particle Systems Characterization, 32(2), (2015), 164-175.

[22] X. Li., W.C. Choy., L. Huo., F. Xie., W.E. Sha., B. Ding., X. Guo., Y. Li., J. Hou., J. You. and Y. Yang. Dual plasmonic nanostructures for high performance inverted organic solar cells. Advanced Materials, 24(22), (2012), 3046-3052.

[23] M. Rycenga., C.M. Cobley., J. Zeng., W. Li., C.H. Moran., Q. Zhang., D. Qin. and Y. Xia, Y., 2011. Controlling the synthesis and assembly of silver nanostructures for plasmonic applications. Chemical reviews, 111(6), (2011), 3669-3712.

[24] A.L. Pyayt., B. Wiley., Y. Xia., A. Chen. and L. Dalton. Integration of photonic and silver nanowire plasmonic waveguides. Nature nanotechnology, 3(11), (2008), 660-665.

[25] T.A. Kareem. and A.A. Kaliani. Fabrication and characterization of ZnSCubic/P3HT, ZnSHexa: P3HT and ZnSHexa/P3HT/PVAAg bulk heterojunction solar cells. J. Nano Electr. Phys. 7(2), (2015), 1-6.

[26] Y.Y. She., Y.A.N.G. Juan. and K.Q. Qiu. Synthesis of ZnS nanoparticles by solid–liquid chemical reaction with ZnO and Na2S under ultrasonic. Trans. Nonferr. Metals Soc. China 20, (2010), s211-s215.

[27] M. Bredol., K. Matras., A. Szatkowski., J. Sanetra. and A. Prodi-Schwab. P3HT/ZnS: a new hybrid bulk heterojunction photovoltaic system with very high open circuit voltage. Sol. Energy Mater. Sol. Cells 93(5), (2009), 662-666.

[28] M.W. Dlamini., X.G. Mbuyise. and G.T. Mola. Improved energy harvesting using well-aligned ZnS nanoparticles in bulk-heterojunction organic solar cell. Journal of Materials Science. Materials in Electronics, 31(12), (2020), 9415-9422.

[29] S.I Sadovnikov. Synthesis, properties, and applications of semiconductor nanostructured zinc sulfide. Russian Chemical Reviews, 88(6), (2019), 571.

[30] S. Mazhar., U.Y. Qazi., N. Nadeem., M. Zahid., A. Jalil., F. Khan., I. Ul-Hasan. and I. Shahid. Photocatalytic degradation of methylene blue using polyaniline-based silver-doped zinc sulfide (PANI-Ag/ZnS) composites. Environmental Science and Pollution Research, 29(6), (2022), 9203-9217.

[31] S. Mardix., E. Alexander., O. Brafman. and I.T. Steinberger. Polytype families in zinc sulphide crystals. Acta Crystallographica, 22(6), (1967), 808-812.

[32] R.W.G. Wyckoff. and R.W. Wyckoff. 1963. Crystal structures (Vol. 1, p. 312). New York: Interscience publishers. (1963).

[33] D.H. Wang., D.Y. Kim., K.W. Choi., J.H. Seo., S.H. Im., J.H. Park., O.O. Park. and A.J. Heeger. Enhancement of donor-acceptor polymer bulk heterojunction solar cell power conversion efficiencies by addition of Au nanoparticles, Angew. Chem. 123(24), (2011), 5633-5637.

[34] X. Li., W.C.H. Choy., H. Lu., W.E.I. Sha. and A.H.P. Ho. Efficiency enhancement of organic solar cells by using shape-dependent broadband plasmonic absorption in metallic nanoparticles, Adv. Funct. Mater. 23(21), (2013), 2728-2735.

[35] M.S. Hamed., M.A. Adedeji., Y. Zhang. and G.T. Mola. Silver sulphide nanoparticles enhanced photo-current in polymer solar cells. Applied Physics A, 126(3), (2020), 1-9.

[36] P. Makuła., M. Pacia. and W. Macyk. How to correctly determine the band gap energy of modified semiconductor photocatalysts based on UV–Vis spectra. The Journal of Physical Chemistry Letters, 9(23), (2018), 6814-6817.

[37] S.B. Aziz., O.G. Abdullah. and M.A. Rasheed. A novel polymer composite with a small optical band gap: new approaches for photonics and optoelectronics. Journal of Applied Polymer Science, 134(21), (2017).

[38] J.N. Ike., M.S. Hamed. and G.T. Mola, G.T. Effective energy harvesting in thin film organic solar cells using Ni: Zn as bimetallic nanoparticles. Journal of Physics and Chemistry of Solids, 161, (2022), 110405.

[39] M.W. Dlamini. and G.T. Mola. Near-field enhanced performance of organic photovoltaic cells. Physica B: Condensed Matter, 552, (2019), 78-83.

[40] B. Paci., G.D. Spyropoulos., A. Generosi., D. Bailo., V.R. Albertini., E. Stratakis. and E. Kymakis. Enhanced structural stability and performance durability of bulk heterojunction photovoltaic devices incorporating metallic nanoparticles. Advanced Functional Materials, 21(18), (2011), 3573-3582.

[41] G. Tessema. Charge transport across bulk heterojunction organic thin film. Applied Physics A, 106(1), (2012), 53-57.

[42] M.S. Hamed., J.N. Ike. and G.T. Mola. Plasmonic nanoparticles mediated energy harvesting in thin-film organic solar cells. Journal of Physics D: Applied Physics, 55(1), (2021), 015102.

[43] M.A. Adedeji., M.S. Hamed. and G.T. Mola. Light trapping using copper decorated nanocomposite in the hole transport layer of organic solar cell. Solar Energy, 203, (2020), 83-90.

CHAPTER 7

The impact of Ag/Co nanocomposite on organic charge transport medium for improved photocurrent in polymer solar cell

Received: 1 May 2023 | Revised: 27 June 2023 | Accepted: 10 July 2023
DOI: 10.1002/pol.20230275

RESEARCH ARTICLE

JOURNAL OF POLYMER SCIENCE WILEY

The impact of Ag/Co nanocomposite on organic charge transport medium for improved photocurrent in polymer solar cell

Jude N. Ike[1] | Ncedo Jili[1] | Amit Kumar[2] | Gaurav Sharma[2] | Genene Tessema Mola[1]

[1]School of Chemistry & Physics, University of KwaZulu-Natal, Pietermaritzburg, Scottsville, South Africa
[2]International Research Centre of Nanotechnology for Himalayan Sustainability (IRCNHS), Shoolini University, Solan, India

Correspondence
Genene Tessema Mola, School of Chemistry & Physics, University of KwaZulu-Natal, King Edward Avenue, Pietermaritzburg Campus, Private Bag X01, Scottsville 3209, South Africa.
Email: genene.mola@gmail.com

Funding information
National Research Foundation South Africa, Grant/Award Numbers: 113835, 132786

Abstract
Tuning charge transport properties using silver-cobalt bimetallic nanoparticles is investigated to enhance the photo-current collection in polymer solar cells. The silver-cobalt nanoparticles were not only augmenting the charge transport processes but also expected to trap light by way of reflection. The polymers blend consisting of poly-(3-hexylthiophene) (P3HT):[6,6]-phenyl C61 butyric acid methyl ester (PC61BM) is used in the fabrication of polymer solar cells. The experimental results indicated that the solar cells' performance depended on the concentration of Ag/Co in the hole transport layer (HTL). Nevertheless, the high-power conversion efficiency value of up to 4.21% was observed, at the concentration of 0.1% by weight, which is much higher than pristine solar cells due to improved measured photocurrents from the devices. This is a significant improvement in PCE by 66.4% compared to the undoped transport medium. Ag/Co nanocomposite is found to be more stable under ambient laboratory conditions.

KEYWORDS
bimetallic nanoparticles, device fabrication, hole transport layer, light-scattering process, polymer solar cell

7.1 Abstracts

Tuning charge transport properties using silver-cobalt bimetallic nanoparticles is investigated to enhance the collection of photo-current in polymer solar cells. The silver-cobalt nanoparticles were not only augmenting the charge transport processes but also expected to trap light by way of reflection. The polymers blend consisting of poly-(3-hexylthiophene) (P3HT): [6,6]-phenyl C61 butyric acid methyl ester (PC61BM) is used in the fabrication of polymer solar cells. The experimental results indicated that the solar cell's performance depended on the concentration of Ag/Co in the hole transport layer (HTL). Nevertheless, the

high-power conversion efficiency value of up to 4.21% was observed, at the concentration of 0.1% by weight, which is much higher than pristine solar cells due to improved measured photocurrents from the devices. This is a significant improvement in PCE by 66.4% compared to the undoped transport medium. Ag/Co nanocomposite is found to be more stable under ambient laboratory conditions.

7.2 Introduction

The thin-film organic solar cells (TFOSCs) have attracted a lot of research attention as a potential source of green energy due to their many advantages of low cost, lightweight, mechanical flexibility, cheap device fabrication, and portability over inorganic counterparts [1-8]. TFOSCs can be fabricated using solution processing techniques, which are generally easy to scale up, for mass production using roll to roll printing method. This makes them a promising alternative to inorganic solar cells, which are more expensive and produce environmentally hazardous chemicals from device processing. The advantages of TFOSCs have led to a lot of research and development in this field, and the efficiency has increased significantly in recent years. The power conversion efficiency (PCE) of polymer solar cells has increased dramatically by well over 19% with the introduction of small acceptor molecules [9-10]. This is a significant milestone, as it makes them competitive with other types of solar cells. With continued research and development, it is possible that even higher PCE values could be achieved, making TFOSCs an even more promising source of green energy for the future. The development of highly efficient and stable TFOSCs has been the subject of intense research over the years. One approach to achieving this goal solution processes TFOSCs, which has led to significant achievements in synthesizing conducting polymer molecules and designing various device structures. One important factor that impacts device performance is the thickness of the solar absorber. To effectively capture all the incident photons, it is important to minimize the thickness of the polymer layer without compromising efficiency [11]. Despite this, recent research has demonstrated that the thickness of the photoactive layer in TFOSCs can be reduced to as little as 150-200 nm [11-12]. The inadequate charge generation and collection in TFOSCs are likely due to low optical absorption of the absorber layer, which has been partially eased via the use of plasmon metal nanoparticles (NPs), reflective surfaces, etc. On the other hand, interfacial buffer layers between the solar absorber medium and electrodes have gained popularity as a promising technique to improve the charge carrier transport process and boost device performance [8]. Despite the availability of alternative materials, the Poly (3,4-ethylene dioxythiophene): Polystyrene-para-sulfonic acid (PEDOT/PSS) remains unrivaled as the

preeminent hole transport layer (HTL) in the conventional architecture of TFOSCs. Its unique properties facilitate the efficient transportation and collection of holes from the solar absorber to the anode electrode. Over the last two decades, PEDOT/PSS has captured significant research interest due to its impressive characteristics. Its high work function of approximately 5.2 eV, along with its smooth morphology, exceptional electrical conductivity, and high optical transmittance of more than 85%, have been found to effectively decrease the roughness of indium tin oxide (ITO) electrodes, thereby boosting the performance of TFOSCs. PEDOT/PSS, despite its observed benefits, remains a technical challenge in device fabrication due to its interaction with the underlying hydrophobic solar absorber. The hydrophilic nature of PEDOT/PSS can lead to severe wettability upon contact, which has been noted in previous studies [13-14]. In a recent publication, Fang, Jeng, Lim, *et al.* (2012) [15] revealed that discarding PEDOT/PSS as the hole transport layer (HTL) is not a viable solution to rectify the malfunction, as doing so can leave the solar absorber vulnerable to moisture and oxygen, ultimately compromising the device's performance in thin-film organic solar cells (TFOSCs).

Furthermore, as per recent research, the lack of an optimal hole transport layer (HTL) could result in inadequate device output during fabrication and even instigate device instability in TFOSCs [16]. To overcome the limitation of PEDOT/PSS, a variety of techniques have been explored to enhance the performance of TFOSCs [17-20]. Among these methods, thermal annealing, solvent additives, and the incorporation of metal NPs have emerged as the most promising strategies. The substitution of PEDOT/PSS with metal NPs as the HTL during device fabrication has emerged as a focal point in research, achieving significant attention. This novel approach offers multiple benefits, such as enhanced light absorption and improved device performance in TFOSCs [21-22]. One cannot overlook the fact that the localized surface plasmonic resonance (LSPR) and surface plasmonic resonance (SPR) owe their existence to the significant interplay between the electromagnetic (EM) field of the incident photon and the surface electron plasma of the metal nanocomposites [23]. The potential impact of LSPR and SPR may vary based on the size and geometry of metal nanoparticles (NPs). It is to be noted that the resonance condition can be fascinatingly observed when the frequency of light aligns with the frequency of oscillating electrons, commonly referred to as LSPR, in the context of nano-sized structures. Mathematically, the plasmon energy in a free electron model can be explained, as depicted in equation [24]

$$E_p = \hbar\sqrt{\frac{ne^2}{m\varepsilon_0}} = \hbar\omega_p. \tag{7.1}$$

Where *n* is the number free electrons per a unit volume, *e* is the charge of elementary, *m* is the mass of an electron, ε_0 indicates the permittivity of free space, ħ is the ratio of Planck constant to 2π ($h/2\pi$), and ω_p is the bulk plasmon frequency. The Drude model has revealed that metals with low inter-band absorption have relatively high conductivities with a small imaginary part of the dielectric constant. This is evident in the response of damped, free electrons under the influence of a frequency to an applied electromagnetic field, as shown in equation [24]

$$\varepsilon_r(\omega) = 1 - \frac{\omega_p}{\omega^2 + i\gamma\omega}. \tag{7.2}$$

Where $\tau = \frac{1}{\gamma}$ denotes the relaxation time and ω is the angular frequency of an applied electromagnetic field. When metallic nanoparticles have diameters smaller than the wavelength of light, they can be effectively characterized by a point dipole model, which accurately predicts their absorption and scattering behavior in response to the electromagnetic field. Mathematically, the scattering and absorption cross-sections are provided in equation [25].

$$C_{scat} = \frac{1}{6\pi}\left(\frac{2\pi}{\lambda}\right)^4 |\alpha|^2;\ C_{abs} = \left(\frac{2\pi}{\lambda}\right) Im|\alpha|. \tag{7.3}$$

On this note, the α can be quantified using the equation.

$$\alpha = 3V\frac{\omega_p^2}{\omega_p^2 - 3\omega^2 - i\gamma\omega} = 3V\left[\frac{\varepsilon_p/\varepsilon_m - 1}{\varepsilon_p/\varepsilon_m + 1}\right]. \tag{7.4}$$

Where α represents the polarizability of the particle, *V* is the particle volume, ε_p is the dielectric function of the particle and ε_m is the dielectric function of the embedding medium. Moreover, it is to be noted that the interaction of electromagnetic radiation with metal nanocomposites in polymer solar cells caused by the occurrence of various phenomena such as far-field scattering, near-field coupling, hot-electron transfer, plasmon resonant energy transfer and the remarkable processes are explained, as provided in figure 7.1. Each phenomenon is well summarized in brief, but enough details can be observed from the cited references.

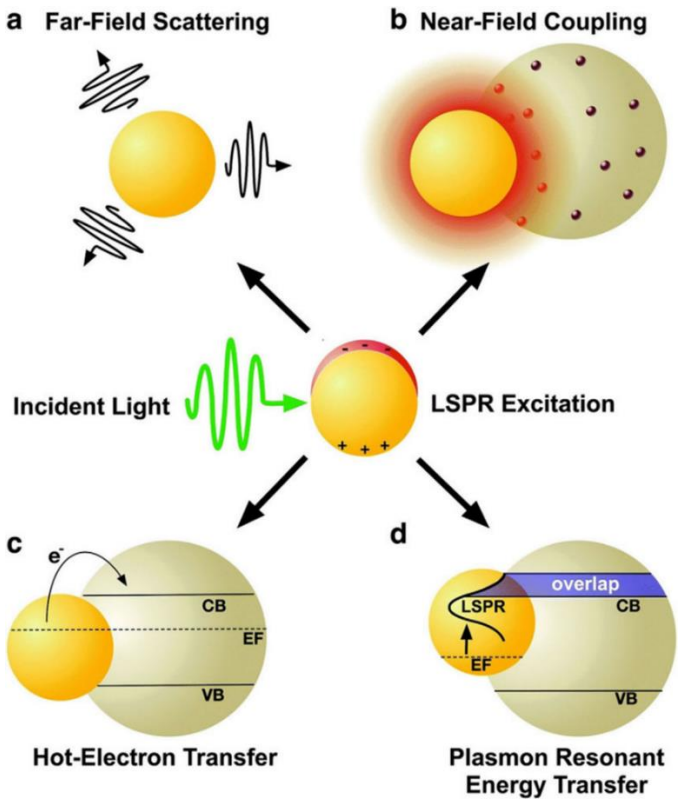

Figure 7.1: The excitation of the LSPR effect and different energy transfer mechanisms responsible for plasmon-driven performance augmentation. Reproduced by permission from (Willian *et al.*, 2016) [26].

It is to be noted that the energy transfer mechanisms, which are accountable for plasmon-driven performance improvement can be split into two categories namely radiative and nonradiative [26,27].

In the radiative process, the energy can be transferred to an adjacent semiconductor via far-field scattering (See figure 7.1a) and near-field coupling (See figure 7.1b). In the far-field scattering, the nano-plasmonic geometry gets activated upon excitation and radiates its energy as a secondary source, which is known as the light scattering process. On the other hand, near-field light confinement, which is referred to as optical coupling is responsible for absorption augmentation in the metal-semiconductor nanoparticles. These energy transfers can play a vital role in providing light absorption for the adjacent environment. However, these phenomena are not only directly responsible for photocurrent increase, but they also provide conditions in which photoactive material generates many hole and electron carriers, respectively. Interestingly, one of the mechanisms responsible for nonradiative energy transfer is hot electron injection, as provided in figure 7.1c. In the process of the excitation of plasmonic

metal, the LSPR gets excited and nonradiative decay of the LSPR effect can be beneficial in generating hot carriers. Plasmon-induced resonance energy transfer (PIRET), as depicted in figure 7.1d, constitutes an alternative mechanism accountable for the nonradiative energy transfer of hot electrons. As the surface plasmons decay, they generate a transient exciton through dipole-dipole interactions, which in turn directly induces the formation of electron-hole pairs in the semiconductor. It is worth noting that the integration of metal nanoparticles within hole transport layers has proven to be advantageous in enhancing the device's overall functionality by means of the LSPR effect and light-scattering, as stated in reference [28]. The utilization of prominent synthesized metal NPs, such as silver (Ag), copper (Cu), nickel (Ni), zinc (Zn), and gold (Au), has been predominantly limited to mono-metal NPs, which are competent at capturing incident photons through the LSPR effect. However, the emergence of bimetallic nanoparticles (BMNPs), composed of two distinct elements, presents a unique opportunity to achieve optimal photonic device properties compared to their mono-metallic NP counterparts [23, 29-33]. Likewise, the optoelectronic properties of BMNPs in TFOSCs outshine that of their mono-metallic counterparts, due to their impressive light-scattering capabilities and far-reaching LSPR effects. In this novel investigation, the crown jewel of metal NPs in TFOSCs is silver (Ag), which has impressive LSPR effect and light-scattering properties in the dielectric medium, to be reckoned with for enhanced photons harvesting. To harness the potential of the NPs, the synthesis of Ag/Co BMNPs is carried out, where cobalt (Co) is introduced to exploit the optoelectronic properties of both metals in TFOSCs [30, 34]. Nevertheless, Co may have functioned as a transitional metal, encompassing not just desirable optical characteristics but also electrical traits to enhance both charge transfer mechanisms and the absorption of incident photons in TFOSCs. Within this piece of article, we have accomplished the successful synthesis and characterization of bimetallic silver-cobalt (Ag/Co) NPs, which were subsequently implemented at various locations within the device architecture. The strategic use of these NPs facilitated a considerable enhancement in the hole transport process of TFOSCs, and furthermore, we are reporting for the first time the direct influence of Ag/Co on the performance of TFOSCs. Presumably utilized at distinct strata within the device architecture, the Ag/Co BMNPs functioned as a solar absorber, a dopant within the HTL, and a co-buffer layer, synergistically enhancing charge transport to effectively boost the performance of the TFOSC.

7.3 Experimental

7.3.1 Materials

In this latest investigation, every chemical element utilized as a foundation for TFOSCs was procured from commercial sources and used as received, except for the production of cobalt-doped silver (Ag/Co) BMNPs. The polymer molecules, including poly-(3,4-ethylene dioxythiophene): poly-(styrene-sulfonate) (PEDOT/PSS), Poly-(3-hexylthiophene) (P3HT), and [6,6]-phenyl-C61-butyric acid methyl ester (PC61BM) with a purity of 95%, were acquired from Ossila Co. Ltd. based in the United Kingdom. Meanwhile, Sigma-Aldrich supplied the ingredients for this experiment in the form of silver nitrate hexahydrate (> 99.5% $AgNO_3$), sodium borohydride (> 99.98% $NaBH_4$), chloroform, and cobalt nitrate hexahydrate (> 98% $Co(NO_3)_2$). To initiate the device fabrication process, the un-patterned indium tin oxide (ITO) coated glass with a sheet resistance of roughly 15 Ω/sq underwent a partial etching. Afterward, the substrates underwent a thorough purification process, undergoing a sequence of ultrasonic cleansing utilizing a range of solutions including detergent, distilled water, acetone, and isopropanol for a duration of 10 min per solution to rid them of any stubborn impurities. To eliminate any lingering moisture, the samples were then subjected to annealing in an oven, for 30 min of baking at 100 ^oC. During the procedure, the Ag/Co BMNPs powder underwent a successful integration into the PEDOT/PSS aqueous solution through varying weight ratios of 0.05%, 0.1%, and 0.15% while maintaining a constant weight of PEDOT/PSS. To guarantee optimal miscibility of Ag/Co BMNPs within PEDOT/PSS, the amalgamated solution was vigorously stirred for an extended period (10 hours). The combination of Ag/Co/PEDOT/PSS solution was deposited onto ITO-coated glass substrates by spin coating at 3500 rpm for one minute. The resulting film was then dried in an oven at 100 ^oC for 20 min, producing the expected hole transport film. The photo-active layers of TFOSCs were prepared from P3HT/ PC61BM mixture at the ratio of 1:1 by weight and dissolved in a chloroform solvent. The binary polymer blend solution was maintained at the 20 mg/ml concentration. The solution is then sonicated for three hours and stirred at 40 ^oC, to achieve desirable miscibility within the blend. Following this progression, the solution of the solar absorber was spin-coated onto a desiccated Ag/Co/PEDOT/PSS substrate at 1200 rpm for a duration of 40 minutes. Following heat treatment of the films in nitrogen atmosphere for 10 min at 120 ^oC, the individual samples underwent a metamorphic process. Finally, thin buffer layer consisting of (LiF) and Al electrodes are deposited on the photo-active layers at unique thicknesses of 0.5 nm and 90 nm,

respectively. The deposition was carried out using Edward Auto 306 deposition unit, operating at an optimal pressure of 10^{-6} mbar. The devices with the structure GLASS/ITO/PEDOT/PSS+Ag/Co/ACTIVE-LAYER/LIF/AL were transferred into the furnace and successfully annealed at 120 ºC for 5 minutes under nitrogen gas. A schematic diagram of this device structure can be seen in figure7. 2.

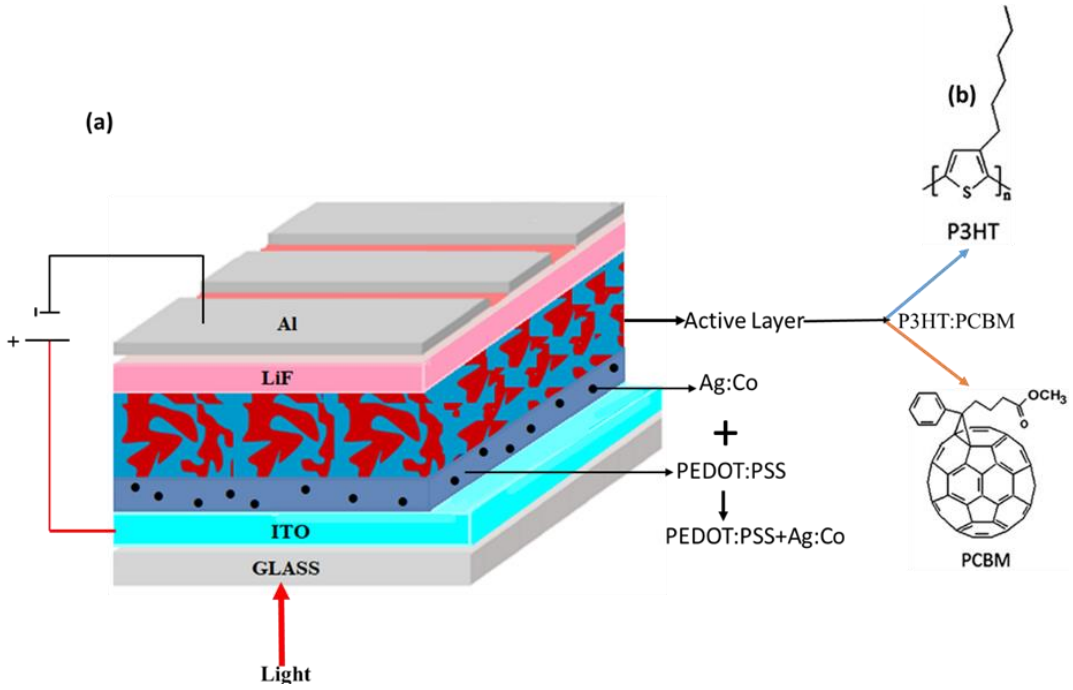

Figure 7.2: (a) The conventional architecture of TFOSC and (b) the structure of the components of the solar absorber layer.

7.3.2 Synthesis and characterization of Ag/Co bimetallic nanoparticles

The chemical reduction method was employed in the synthesis of Ag/Co BMNPs. The required chemicals were 40 mM of silver nitrate and 20 mM of cobalt nitrate and 0.1 M of sodium borohydride used as the reducing agent in the aqueous solution. Two separate solutions were prepared from 40 mM of $Ag(NO_3)_2$, and 20 mM of $Co(NO_3)_2$, respectively, in 25 ml of distilled water and each containing 0.1 M of $NaBH_4$. The solutions underwent a productive agitation at ambient temperature and were safely amalgamated through a meticulous dropwise addition technique while the mixture was stirred continuously. After three hours of stirring on a hot plate at 40 °C, the amalgam needed some purification. The mixture underwent filtration and was thoroughly rinsed with distilled water to extract any lingering sodium ions. The end result was a suspension that was devoid of any unwanted particles. The Ag/Co BMNPs precipitate

was then left to dry for two hours in a vacuum oven set to 70 °C. This ensured the amalgam would be free of moisture, making it a highly desirable product. Eventually, the Ag/Co BMNPs powder underwent comprehensive optical and morphological characterization, using ultraviolet-visible (UV-Vis) absorption spectroscopy, transmission electron microscopy (TEM), scanning electron microscopy (SEM), energy dispersive analysis (EDX), X-ray diffraction (XRD), Photoluminescence (PL), and Fourier transform infrared region (FTIR) analysis.

7.4 Results and discussion sections

7.4.1 Particle morphologies

The surface morphology and structure of silver-doped with cobalt (Ag/Co) BMNPs were appropriately investigated through the utilization of transmission electron microscopy (TEM) and scanning electron microscopy (SEM), respectively. Figure 7.3a and 7.3b show TEM images of the Ag/Co BMNPs, revealing the sizes of the NPs ranging from 5 nm to 50 nm. These particle sizes are much more suitable for enhancing the light-scattering process in a solar absorber layer. Notably, the lattice spacing as investigated from the measured fringes was measured to be 0.236 nm (See figure 7.3b), which was attributed to the existence of well aligned crystalline structure in the medium. The TEM images as provided in figure 7.3a, and b indicate that the Ag/Co BMNPs appeared to be composed of several sizes of disc-like and spherical-like geometrical objects distributed on the background of sheet-like structures. These TEM images affirm the presence of a core-shell configuration composed of Ag-doped Co at diverse sizes and shapes, in which Ag serves as the nucleus and Co as the shell. The hexagonal closed-packed (hcp) structure of the Ag/Co BMNPs phase appears to play a key role in this phenomenon, most likely through the orientation of the a-axis. Figure 7.3c displays the energy-dispersive X-ray (EDX) results, which enabled us to gain valuable insights into the elemental composition of Ag/Co BMNPs. The presence of silver and cobalt is clearly demonstrated by the measured peaks, which stand out amidst a total absence of oxygen or carbon. This indicates that the metal elements have not undergone even partial oxidation because of exposure to ambient conditions.

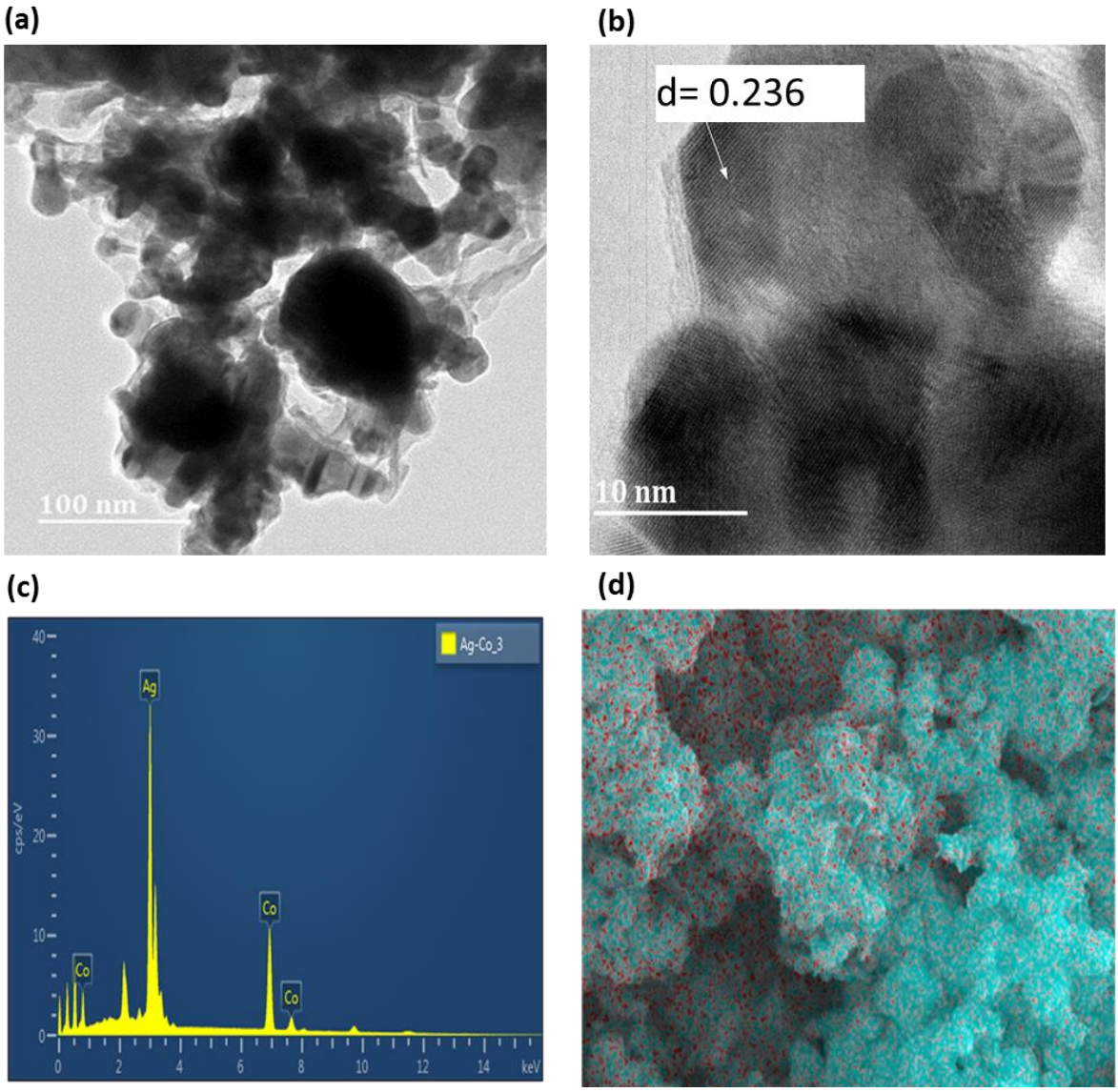

Figure 7.3: The remarkable morphology of the synthesized Ag/Co metal NPs; (a) and (b) are TEM images at different magnifications, (c) the energy dispersive X-ray (EDX) results, and (d) the SEM image of metal NPs with elemental mapping signifying elements Ag Ag Co Co.

The SEM image, illustrated in figure 7.3d, depicts a silver and cobalt composition with a uniform distribution of elements in the medium. The red color corresponds to cobalt, while the light blue color represents silver, suggesting that cobalt is enveloped as a shell on the silver core. Recent literature [34, 35-36] confirms the existence of various structural phases of Ag/Co BMNPs.

7.4.2 XRD analysis of Ag/Co BMNPs

The synthesized Ag/Co BMNPs powder was characterized for both its optical and morphological properties. Notably, the compound's XRD pattern, depicted in figure 7.4, diffraction peaks exhibited by the Ag/Co BMNPs powder.

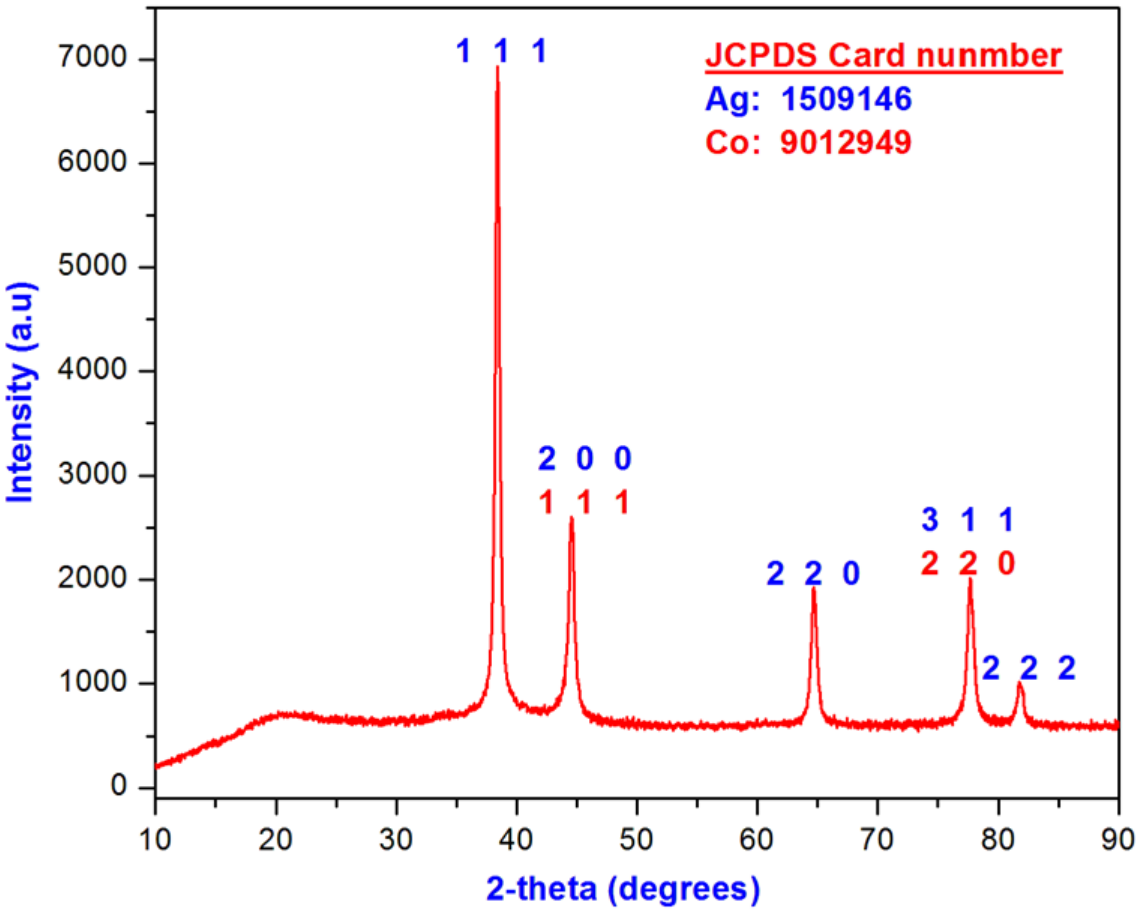

Figure 7.4: X-ray diffraction pattern for Ag/Co BMNPs.

The diffraction patterns were found to match exceptionally well with JCPDS Card number 150-9146 for Ag [37] and JCPDS Card number 901-2949 for Co. However, Ag exhibited a significant cubic structure with a cell parameter of a = 4.0710 Å and an F M -3 M space group. The Co possesses a cubic structure, which belongs to the F M -3 M space group and has a cell parameter of a = 3.5441 Å. The diffractogram of the Ag/Co BMNPs produced five peaks at 2-theta values of 38.5°, 44.5°, 65°, 78°, and 82°, which correspond to beams reflected from the (1 1 1), (2 0 0; 1 1 1), (2 2 0), (3 1 1; 2 2 0), and (2 2 2) planes of the cubic space. The average size of the Ag/Co BMNPs was found to be 25.90 nm, as determined by the Debye-Scherrer equation.

$$D_{size} = \frac{0.89\lambda}{\beta cos\theta}. \quad (7.5)$$

where λ (1.5405 Å) depicts the X-ray wavelength, beta (β) is the full width at half maximum (FWHM) in radians, and theta (θ) is the Bragg angle at the maximum peak in degrees.

Table 7.1: The analysis of XRD of Ag/Co BMNPs.

Peak no	**2θ (º)**	**hkl (Ag)**	**hkl (Co)**	**FWHM (β)**	**D (nm)**
1	38.38	1 1 1	---	0.32	25.99
2	44.50	2 0 0	1 1 1	0.38	22.34
3	64.68	2 2 0	---	0.38	24.47
4	77.60	3 1 1	2 2 0	0.52	19.39
5	81.68	2 2 2	---	0.28	37.09

7.4.3 Optical properties of Ag/Co BMNPs interfacial layer

The optical absorption properties of the hole transport layers were studied using UV-Vis spectra taken at room temperature and different doping levels of Ag/Co in HTL. Figure 7.5a exhibits the attractively derived spectra of the ITO/PEDOT/PSS-Ag/Co/P3HT/PCBM/LiF/Al films with varied concentrations of Ag/Co BMNPs in HTL. Similarly, figure 7.5b is the absorption spectrum of Ag/Co BMNPs in deionized water suspension, which displays an extended absorbency due to large scattering and electron band transitions. Consequently, the fingerprint of the presence of Ag/Co in HTL is clearly visible in figure 7.5a by absorbance peak spanning from 350 nm to 480 nm. These absorption peaks, observed within the UV region, are a consequence of the band-to-band transition in the Ag/Co nanocomposites. In addition, the optical absorption pattern of the pristine film, depicted in figure 7.5a, displays a distinct peak at 518 nm. Nevertheless, the PEDOT/PSS film infused with Ag/Co BMNPs at concentrations of 0.05%, 0.1%, and 0.15% by weight in the HTL displayed conspicuous absorption peaks within the visible and infrared regions, due to the localized surface plasmonic resonance phenomenon and enhanced light scattering processes arising from the inclusion of Ag/Co BMNPs.

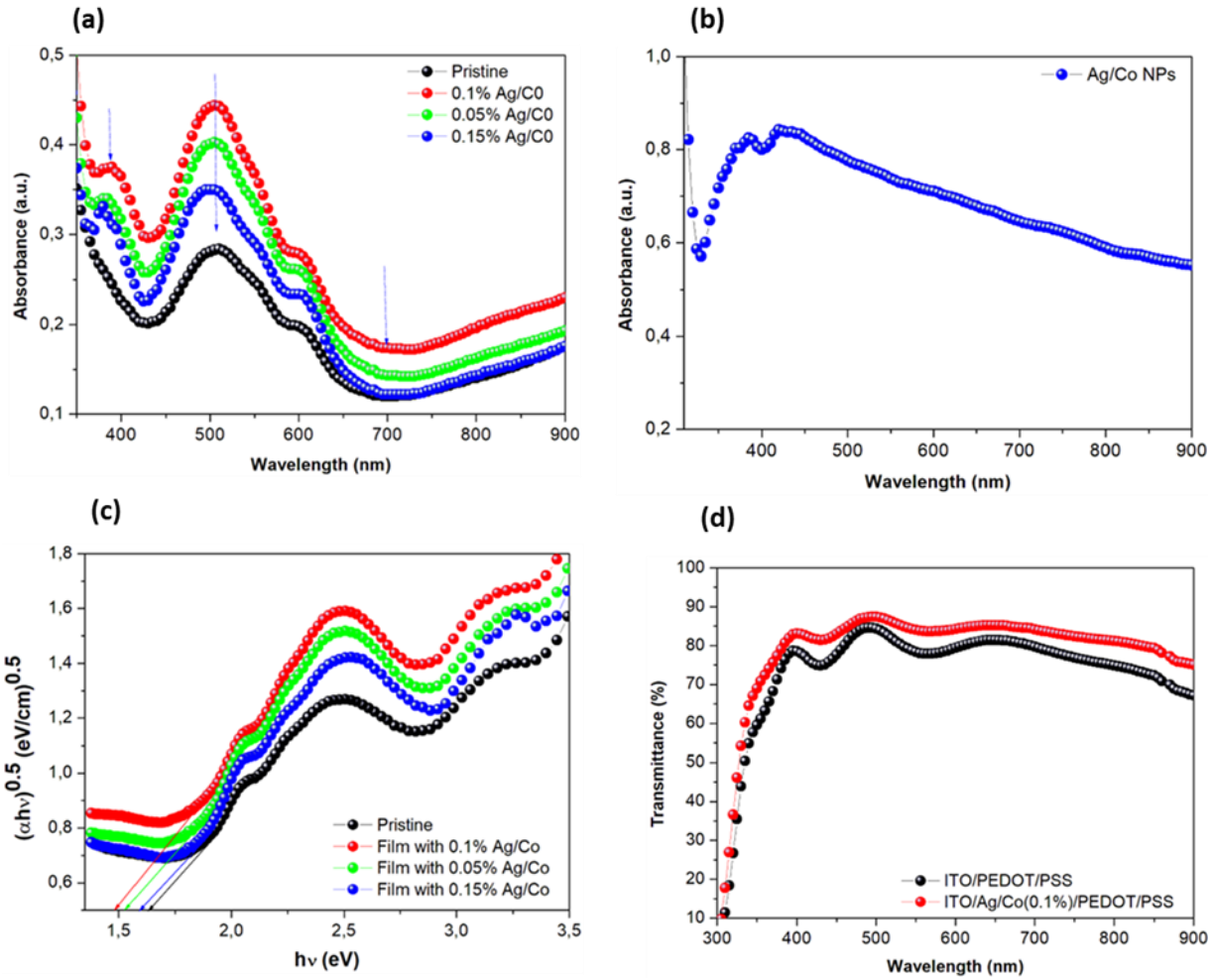

Figure 7.5: Optical absorption spectra of (a) P3HT/PCBM of solar absorber coated on PEDOT/PSS/Ag/Co hole transport layer for Ag/Co BMNPs concentration. (b) the Ag/Co BMNPs nanocomposite powder in deionized water suspension. (c) Tau-Tau plot of the optical absorbance of the various films and observation of the energy band gap. (d) the optical transmission spectra of the Ag/Co BMNPs doped with PEDOT/PSS films.

Generally, the spectra in figure 7.5a clearly suggest that absorbency is dependent on the concentration of Ag/Co in HTLs, with the most prominent effect being observed at 0.05% concentration. This finding is consistent with the performance of solar cells discussed in the following sections. Moreover, the doped films' absorption spectra, featured noteworthy undulations ranging from 400 to 500 nm and exceeding 800 nm, possibly linked to the existence of the LSPR phenomenon. Surprisingly, it was noted that all doped devices exhibited considerably improved optical absorption compared to the pristine ones.

According to figure 7.5c, the energy band gaps of the absorber films were determined based on the onset of absorptions, which suggests that the band gap changes with the concentration

of Ag/Co in HTL. It should be emphasized that the relationship between photon energy's absorption coefficient (α) can be mathematically expressed by the equation.

$$\alpha = \frac{ln\left(1/T\right)}{d} = 2.303 \times \left(\frac{A}{d}\right). \quad (7.6)$$

Where A represents the absorption data, T signifies the transmittance, and d denotes the thickness of the Ag/Co BMNPs [38]. The correlation between the incident photon energy and the absorption coefficient (α) is revealed in the equation.

$$\alpha h\nu = k(h\nu - E_g)^m. \quad (7.7)$$

Where *k* is the constant, E_g is the energy separation between the valence and conduction bands (the energy band gap), h is the Planck constant, *ν* is a frequency, and *m* is the value that depends on the nature of the transition. Recent studies [39,40] report that the plot of α*hν* versus h*ν* corresponds to the direct allowed transition, even though *m* is 2 for allowed direct transition and equal to 0.5 for allowed indirect transition. Figure 7.5c demonstrated the energy band gap of the TFOSCs, both with and without NPs. Meanwhile, quantifying the photon energy loss of polymer solar cells, which can be accomplished by utilizing the equation.

$$E_{loss} = E_g - qV_{oc}. \quad (7.8)$$

The relationship between the energy band gap (E_g), the elementary charge (q), and open circuit voltage (V_{oc}) in polymer solar cells is a delicate, one in which energy loss can drastically impact the performance of the cell. This is particularly evident in TFOSC, where the value of PCE is limited by the constraints imposed by the V_{oc}. Indeed, recent reports suggest that the high energy loss suffered by organic solar cells with losses ranging from 0.6 eV to 1.3 eV is a major problem that must be overcome if these cells are to reach their full potential [41,42].

Furthermore, the optical transmission spectra, as depicted in figure 7.5d, were analyzed for the ITO/PEDOT/PSS/Ag/Co film structure at the doping concentration and compared with the absorption of the pristine ITO/PEDOT/PSS film. The concentration of 0.1wt% Ag/Co BMNPs blended with PEDOT/PSS was found to greatly enhance optical transmission, particularly in the 370 nm to 480 nm range, surpassing even pristine ITO/PEDOT/PSS film. Interestingly, the optical transmission at 0.1wt% film was consistently high, ranging from 82 to 87% in the wavelength of 370-900 nm range. This improvement is attributed to the LSPR effect and has promising implications for enhancing charge transport processes and harvesting photon energy in TFOSCs. However, the film with ITO/PEDOT/PSS exhibited a reduction in transmission

from 77-80% in the wavelength ranging from 330 nm to 900 nm. Generally, the absorption in the infrared region is attributed to absorbance by different sizes of metal NPs situated at the HTL of the devices.

7.4.4 Photoluminescence and FTIR spectra of Ag/Co BMNPs

It is to be noted that the photoluminescence (PL) spectrum is the emission of light as a result of excitation from the source of light. This phenomenon involves the absorption of photons by the sample from a monochromatic light source, such as a laser or Xe lamp, which facilitates electron excitation from the valence to the conduction bands. According to reports, delving into the study of PL at room temperature may yield valuable insights into the diverse energy states present in both the valence and conduction bands. These energy states are believed to be responsible for the phenomenon of radiative recombination, as per sources cited in reference [43]. The PL spectrum emission of the synthesized Ag/Co bimetallic nanoparticles (BMNPs) is shown in figure 7.6(a). The PL spectrum shows emission from 440 nm to 490 nm, which agrees with band-to-band transition described by optical absorbency of Ag/Co in deionized water suspension (figure 7.5b). Through these wondrous displays, we have come to understand that the intensity of the visible emission owes its very existence to the photocatalytic activity that arises from the presence of Ag/Co BMNPs. The chemical structure of the prepared Ag/Co bimetallic nanoparticles (BMNPs) was investigated with a Fourier transform infrared spectrophotometer (FTIR), as depicted in figure 7.6b. FTIR is a notable technique, which is basically used to ascertain additional aspects of the prepared nanostructures based on the identification of their characteristic peaks [44]. However, several FTIR spectrum peaks at wavenumber 3850 cm^{-1}, 2750 cm^{-1}, 2327 cm^{-1}, 2081 cm^{-1}, 1221 cm^{-1}, 560 cm^{-1}, and 481 cm^{-1} were observed in the synthesized Ag/Co BMNPs. Recent studies have reported that the FTIR spectrum can probably confirm the polymer synthesized and the other components in the composites [45]. Therefore, the FTIR spectrum of the Ag/Co BMNPs confirmed the effective formation of the significant bonds in the composites. Consequently, the broad peak situated at wavenumber 2750 cm^{-1} is attributed to the (Ag-O) stretching vibration functional group [46]. The peak located at wavenumber 560 cm^{-1} was assigned/attributed to the (Co-N) bending vibration functional group, which is similar as cited in reference [47].

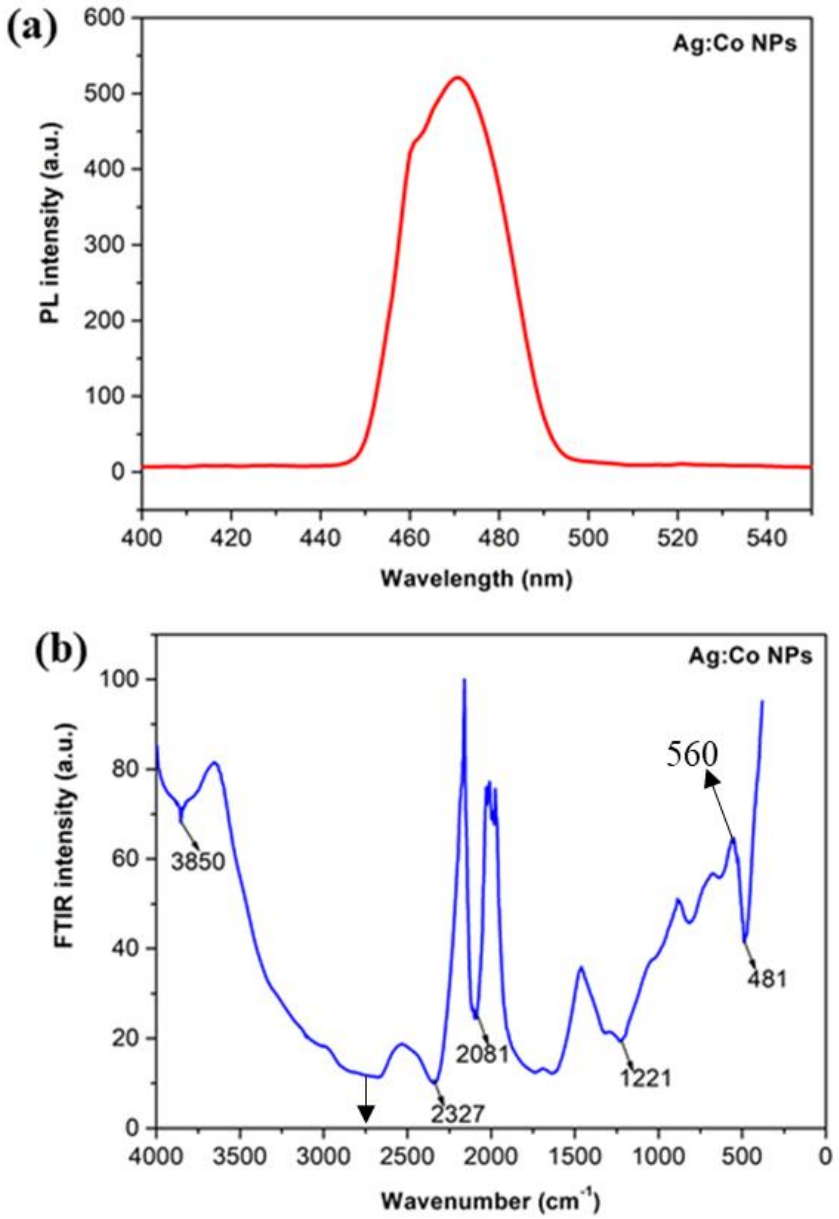

Figure 7.6: (a) Photoluminescence (PL) and (b) Fourier transform infrared (FTIR) spectrum of Ag/Co BMNPs.

7.4.5 Electrical properties of Ag/Co BMNPs interfacial layer

In this section, thin film polymer solar cells are fabricated at different concentrations of Ag/Co BMNPs in the HTL. The device performance as determined from J-V data taken from different solar cells are given in figure 7.7. According to the figure there is high surge of photocurrent collection depending on the concentration of Ag/Co in the HTL.

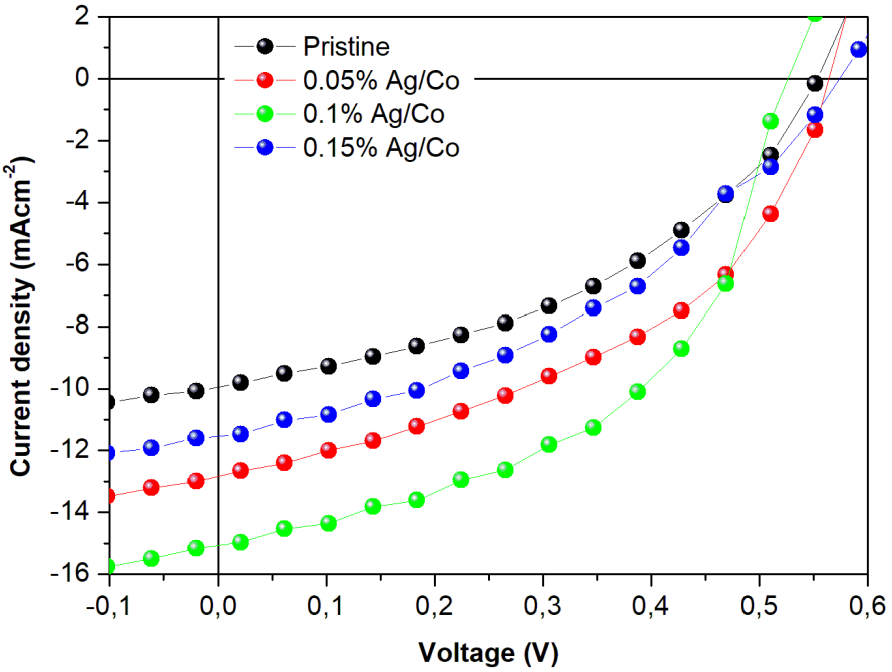

Figure 7.7: The J-V characteristics of the best-performing devices.

The concentration levels of Ag/Co BMNPs varied from 0%, 0.05%, 0.1%, and 0.15%, which resulted in remarkable power conversion efficiency values compared to undoped device. The improvement is attributable to the amplified photocurrents measured from the devices. The PCE values of all Ag/Co doped HTL devices are surpassing those of the pristine PEDOT/PSS hole transport layer, as shown in Table 7.2. This positive improvement is directly linked to the changes in optical properties detailed in the preceding section. Additionally, the findings suggest that the best PCE value recorded here 4.21% was achieved at 0.1% doping level, yielding a high short-circuit current (J_{sc}) of approximately 15.30 mA/cm^2, as provided in Table 7.2. This change in PCE is 66.4% growth from undoped HTL. This enhancement serves as a testament to the exceptional influence of Ag/Co BMNPs in the HTL, which facilitates an unprecedented augmentation of the charge dissociation and collection processes in thin-film organic solar cells. The device parameter augmentation unequivocally demonstrates that the photoactive films likely have the capacity to extract holes due to the emergence of Ag/Co BMNPs in the PEDOT/PSS hole transport layer. This provides a distinct signal that the incorporation of Ag/Co BMNPs in the HTL has boosted the device performance by effective collection of photo-generated current.

Table 7.2: The J-V parameters of the best-performed devices.

Ag/Co (wt%)	E_g	E_{loss} (eV)	V_{oc} (V)	J_{sc} (mA/cm^2)	FF (%)	PCE (%)	R_s (Ωcm^2)
Pristine	1.65	1.10	0.55	10.31	39.43	2.53	827
0.05%	1.56	1.03	0.53	13.20	48.70	3.44	622
0.1%	1.49	0.94	0.53	15.30	51.81	4.21	494
0.15%	1.59	1.07	0.52	11.94	44.72	2.87	691

7.4.6 Charge transport properties analysis of Ag/Co BMNPs interfacial layer

Figure 7.8 sheds light on the charge transport properties examined in this section. By measuring the dark current of pristine and solar cells made with 0.05%, 0.1%, and 0.15%wt Ag/Co BMNPs in the HTL, we gained significant insight into the transport behaviour. Take note that the space charge limited current (SCLC) present in the HTL of polymer solar cells has been probed with great effectiveness. This approach is quite advantageous in comprehending the impact of Ag/Co BMNPs on charge transport processes and examining charge carrier mobility. What is truly fascinating is that the SCLC mechanism, governed by the Mott-Gurney Law, has been harnessed to effectively investigate charge mobility. On a related note, the current density can be quantified using the following equation.

$$J = \frac{9}{8}\varepsilon\varepsilon_o\mu_o\frac{V^2}{L^3}. \tag{7.9}$$

Where Ɛ and $Ɛ_o$ display the relative dielectric permittivity of the solar cell device fabrication and free space; μ_o is zero-field mobility; L is the thickness of the solar absorber, which is 100 nm; V is the applied voltage across the device, which can probably be rectified via the built-in potential voltage (V_{bi}) as stated by recent studies [28, 48-51] to be

$$V=V_{ap}-V_{bi}. \tag{7.10}$$

Where V_{bi} displays the bias voltage. On the other hand, the μ is basically reliant on the electric field, which can be computed using the Poole-Frenkel equation.

$$\mu = \mu_o exp\left(\gamma\sqrt{E}\right). \tag{7.11}$$

Where μ_o is zero-field mobility; γ is the field activation factor. As we combine equations (7.9) and (7.11), the field dependent on the SCLC can be clarified by Mott-Gurney Law [19,29,52]

$$J = \frac{9}{8}\varepsilon\varepsilon_o\mu_o\frac{V^2}{L^3}exp\left(0.89\gamma\sqrt{\frac{V}{L}}\right). \quad (7.12)$$

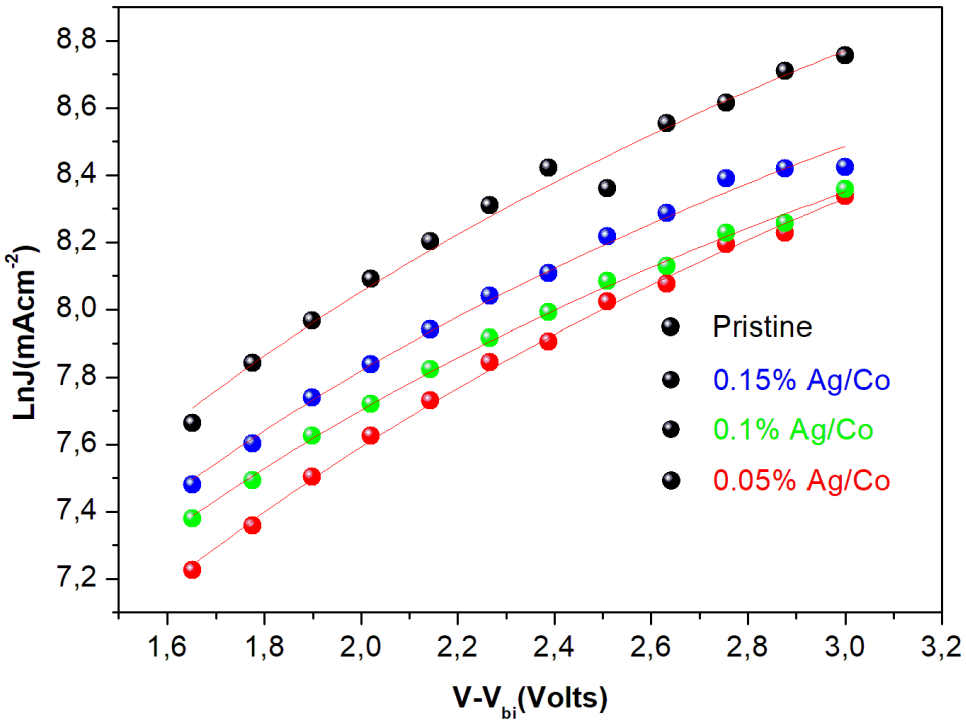

Figure 7.8: The SCLC curves of device solar cells fabricated with different concentrations of PEDOT/PSS/Ag/Co BMNPs in the hole transport layer and pristine device.

According to the findings, figure 7.8 demonstrates that the SCLC data sourced from dark current agree well with the Mott-Gurney equation. Interestingly, the present study has also identified that the zero-field mobility (μ_o), and the field activation factor (γ) obtained from the devices align precisely with the SCLC data. These results are given in Table 7.3. The findings additionally revealed that Ag/Co BMNPs integrated into PEDOT/PSS as the hole transport layer exhibited substantially elevated zero-field mobilities compared to the unaltered reference. Notably, at concentrations of 0.05%, 0.1%, and 0.15%wt of Ag/Co BMNPs, the zero-field mobilities in the HTL surpassed the pristine value by one order of magnitude. The marked improvement in hole and electron mobilities, coupled with the significant attainment of a more harmonized charge transport process, bears witness to the profound impact of Ag/Co BMNPs on the HTL. By enhancing the charge transport processes in TFOSC device performance, this accomplishment stands as a testament to the commendable contribution of Ag/Co BMNPs.

Table 7.3: The charge transport parameters of TFOSCs.

Hole transport layer (wt%)	**μ_o ($cm^2S^{-1}V^{-1}$)**	**γ (cmV^{-1})**
Pristine	8.09×10^{-4}	-7.39×10^{-5}
0.05% Ag: Co	2.08×10^{-3}	-1.89×10^{-4}
0.1% Ag: Co	2.05×10^{-3}	-1.87×10^{-4}
0.15% Ag: Co	1.39×10^{-3}	-1.27×10^{-4}

7.5 Conclusion

In summary, the silver/cobalt (Ag/Co) BMNPs were effectively synthesized and dispersed into PEDOT/PSS hole transport layer (HTL) at various concentrations of 0.05%, 0.1%, and 0.15% by weight, which was beneficial in boosting the performance of thin-film organic solar cells. Interestingly, the fabricated devices using Ag/Co doped in the HTL demonstrated a desirable enhancement compared to pristine PEDOT/PSS (undoped HTL) based solar cell. The Optimum Ag/Co blending in PEDOT/PSS was observed to be 0.1% by weight and yielded the highest power conversion efficiency value of 4.21% under ambient laboratory environment. Such improvement is assigned/attributed to the occurrence of local surface plasmon resonance effect at the interface between active layer and HTL, which is supporting the charge transport and light-scattering processes in TFOSCs. Moreover, the optical absorption properties with PEDOT/PSS doped with Ag/Co BMNPs by weight in the HTL exhibited remarkably high absorption peaks intensities, in the visible and infrared regions, which is a reason for improved photocurrent. Such achievement is a clear indication that the solar cell performance seemed to be reliant on the doping level of Ag/Co BMNPs in the HTL. Finally, the facile synthesis of Ag/Co BMNPs makes suitable for large scale device production.

Acknowledgments

The authors express their sincere gratitude to the National Research Foundation (NRF), South Africa (Grant numbers: 113835, 132786) for the financial support throughout this study. Additionally, the authors would like to recognize the exceptional contributions of the members of staff in the microscopic and microanalysis unit (MMU) at UKZN for their meticulous and

comprehensive characterization of TEM and SEM measurements, which were crucial to the success of this research endeavour.

Conflicts of interests/Competing interests.

In this study, the authors affirm that there are no competing interests to declare.

References

[1] J. You., L. Dou., K. Yoshimura., T. Kato., K. Ohya., T. Moriarty., K. Emery., C.C Chen., J. Gao., G. Li. and Y. Yang. A polymer tandem solar cell with 10.6% power conversion efficiency. Nature Communications, 4(1), (2013), 1-10.

[2] O. Inganäs. Organic photovoltaics over three decades. Advanced Materials, 30(35), (2018), 1800388.

[3] H. Wang., J. Cao., J. Yu., Z. Zhang., R. Geng., L. Yang. and W. Tang. Molecular engineering of central fused-ring cores of non-fullerene acceptors for high-efficiency organic solar cells. Journal of Material Chemistry A, 7(9), (2019), 4313-4333.

[4] J. Hou., O. Inganas., R.H. Friend. and F. Gao. Organic solar cells based on non-fullerene acceptors. Nature Materials, 17(2), (2018), 119-128.

[5] H. Kim., S. Nam., J. Jeong., S. Lee., J. Seo., H. Han. and Y. Kim, Y., 2014. Organic solar cells based on conjugated polymers: history and recent advances. Korean Journal of Chemical Engineering, 31(7), (2014), 1095-1104.

[6] Y. Cui., H. Yao., J. Zhang., T. Zhang., Y. Wang., L. Hong., K. Xian., B. Xu., S. Zhang., J. Peng. and Z. Wei. Over 16% efficiency organic photovoltaic cells enabled by a chlorinated acceptor with increased open-circuit voltages. Nature Communications, 10(1), (2019), 1-8.

[7] K. Kaviyarasu., G.T. Mola., S.O. Oseni., K. Kanimozhi., C. Maria Magdalane. J. Kennedy. and M. Maaza. ZnO doped single wall carbon nanotube as an active medium for gas sensor and solar absorber. Journal of Materials Science: Materials in Electronics, 30(1), (2019), 147158.

[8] E. Abdalla. and G.T. Mola. Metals decorated nanocomposite assisted charge transport in polymer solar cell. Materials Science in Semiconductor Processing, 91, (2019), 1-8.

[9] J. Yuan., Y. Zhang., L. Zhou., G. Zhang., H.L. Yip., T.K. Lau., X. Lu., C. Zhu., H. Peng., P.A. Johnson., M. Leclerc., Y. Cao., J. Ulanski., Y. Li. and Y. Zou. Single-junction organic solar cell with over 15% efficiency using fused-ring acceptor with an electron-deficient core. Joule 3, (2019), 1140-1151.

[10] L. Meng., Y. Zhang., X. Wan., C. Li., X. Zhang., Y. Wang., X. Ke., Z. Xiao., L. Ding., R. Xia., H-L. Yip., Y. Cao. and Y. Chen. Organic and solution-processed tandem solar cells with 17.3% efficiency. Science, 361(6407), (2018), 1094-1098.

[11] M.J. Beliatis., S.J. Henley., S. Han., K. Gandhi., A.A.D.T. Adikaari., E. Stratakis., E. Kymakis. and S.R.P. Silva. Organic solar cells with plasmonic layers formed by laser nanofabrication. Physical Chemistry Chemical Physics, 15(21), (2013), 8237-8244.

[12] Q. Gan, F.J. Bartoli, Z.H. Kafafi, Plasmonic-enhanced organic photovoltaics: breaking the 10 % efficiency barrier, Advanced Materials, 25(17), (2013) 2385-2396.

[13] S. Lattante. Electron and hole transport layers: their use in inverted bulk heterojunction polymer solar cells. Electronics, 3(1), (2014), 132-164.

[14] T.H. Lai., S.W. Tsang., J.R. Manders., S. Chen. and F. So. Properties of interlayer for organic photovoltaics. Materials Today, 16(11), (2013), 424-432.

[15] Fang Jeng, Lim, Krishnamoorthy Ananthanarayanan, Joachim Luther, and Ghim Wei Ho. Influence of a novel fluorosurfactant modified PEDOT: PSS hole transport layer on the performance of inverted organic solar cells. Journal of Materials Chemistry, 22(48), (2012), 25057-25064.

[16] J.D. Servaites., M.A. Ratner. and T.J. Marks. Organic solar cells: A new look at traditional models. Energy & Environmental Science, 4(11), (2011), 4410-4422.

[17] X.G. Mbuyise., E.A.A. Arbab., K. Kaviyarasu., G. Pellicane., M. Maaza. and G.T. Mola. Zinc oxide doped single wall carbon nanotubes in hole transport buffer layer, Journal of Alloys and Compounds, 706 (2017) 344-350.

[18] G. Sai-Anand., B. Han., B.H. Kang., S.W. Kim., S.W. Lee., J.S. Lee., H.M. Jeong. and S.W. Kang. Incorporation of gold nanodots into poly (3, 4-ethylene dioxythiophene): poly (styrene sulfonate) for an efficient anode interfacial layer for improved plasmonic organic photovoltaics. Journal of Nanoscience and Nanotechnology, 15(9), (2015), 7092-7098.

[19] G.T. Mola. and E.A.A. Arbab. Bimetallic nanocomposite as hole transport co-buffer layer in organic solar cell, Applied Physics A, 123(12), (2017), 1-6.

[20] S.J. Lee., H. Kim., A.R.M. Yusoff. and J. Jang. Organic photovoltaic with PEDOT: PSS and V2O5 mixture as the hole transport layer. Solar Energy Materials and Solar Cells, 120, (2014), 238-243.

[21] J.M. Lee., J. Lim., N. Lee., H.I. Park., K.E. Lee., T. Jeon., S.A. Nam., J. Kim., J. Shin. and S.O. Kim. Synergistic concurrent enhancement of charge generation, dissociation, and transport in organic solar cells with plasmonic metal-carbon nanotube hybrids. Advanced Materials, 27(9), (2015), 1519-1525.

[22] H.C. Liao., C.S. Tsao., T.H. Lin., M.H. Jao., C.M. Chuang., S.Y. Chang., Y.C. Huang., Y.T. Shao., C.Y. Chen., C.J. Su. and U.S. Jeng. Nanoparticle-tuned self-organization of a bulk heterojunction hybrid solar cell with enhanced performance. ACS nano, 6(2), (2012), 1657-1666.

[23] J.N. Ike., M.S. Hamed. and G.T. Mola. Effective energy harvesting in thin-film organic solar cells using Ni: Zn as bimetallic nanoparticles. Journal of Physics and Chemistry of Solids, 161, (2022), 110405.

[24] S.A., Maier. Plasmonics: fundamentals and applications. New York: springer. New York, 1, (2007), 245.

[25] M. Notarianni., K. Vernon., A. Chou., M. Aljada., J. Liu. and N. Motta. Plasmonic effect of gold nanoparticles in organic solar cells. Solar Energy, 106, (2014), 23-37.

[26] William R, Erwin, Holly F. Zarick, Eric M. Talbert, and Rizia Bardhan. Light trapping in mesoporous solar cells with plasmonic nanostructures. Energy & Environmental Science, 9(5), (2016), 1577-1601.

[27] A.M. Brown., R. Sundararaman., P. Narang., W.A. Goddard III. and H.A. Atwater. Nonradiative plasmon decay and hot carrier dynamics: effects of phonons, surfaces, and geometry. ACS nano, 10(1), (2016), 957-966.

[28] J.L. Wu., F.C. Chen., Y.S. Hsiao., F.C. Chien., P. Chen., C.H. Kuo., M.H. Huang. and C.S. Hsu. Surface plasmonic effects of metallic nanoparticles on the performance of polymer bulk heterojunction solar cells. ACS nano, 5(2), (2011), 959-967.

[29] S.O. Oseni. and G.T. Mola, G.T. Bimetallic nanocomposites and the performance of the inverted organic solar cell. Composites Part B: Engineering, 172, (2019), 660-665.

[30] J.N. Ike., M.W. Dlamini., R.P. Dwivedi., Y. Zhang. and G.T. Mola. Plasmon assisted optical absorption and reduced charge recombination for improved device performance in polymer solar cells. Journal of Physics and Chemistry of Solids, 165, (2022), 110662.

[31] M. Lanzi., E. Salatelli., L. Giorgini., M. Marinelli. and F. Pierini. Effect of the incorporation of an Ag nanoparticle interlayer on the photovoltaic performance of green bulk heterojunction water-soluble polythiophene solar cells. Polymer, 149, (2018) 273-285.

[32] M.A. Al-Azawi., N. Bidin., M. Bououdina. and S.M. Mohammad. Preparation of gold and gold-silver alloy nanoparticles for enhancement of plasmonic dye-sensitized solar cells' performance. Solar Energy, 126, (2016) 93-104.

[33] M. Tang., B.I. Sun., D. Zhou., Z. Gu., K. Chen., J. Guo., L. Feng. and Y. Zhou. Broadband plasmonic Cu-Au bimetallic nanoparticles for organic bulk heterojunction solar cells. Organic Electronics, 38, (2016) 213-221.

[34] X.G. Mbuyise. and G.T. Mola. Polycrystal metals nano-composite assisted photons harvesting in thin film organic solar cell. Solar Energy, 208, (2020), 930-936.

[35] P. Mahajan., A. Sharma., B. Kaur., N. Goyal. and S. Gautam. Green synthesized (Ocimum sanctum and Allium sativum) Ag-doped cobalt ferrite nanoparticles for antibacterial application. Vacuum, 161, (2019), 389-397.

[36] Z. Kanwal., M.A. Raza., S. Riaz., S. Manzoor., A. Tayyeb., I. Sajid. and S. Naseem. Synthesis and characterization of silver nanoparticle-decorated cobalt nanocomposites (Co@ AgNPs) and their density-dependent antibacterial activity. Royal Society open science, 6(5), (2019), 182135.

[37] E. A. Owen. and G. I. Williams. A low-temperature X-ray camera. Journal of Scientific Instruments, 31(2), (1954), 49.

[38] S.B. Aziz., O.G. Abdullah. and M.A. Rasheed. A novel polymer composite with a small optical band gap: New approaches for photonics and optoelectronics. Journal of Applied Polymer Science, 134(21), (2017).

[39] T. Watanabe., Y. Iso., T. Isobe. and H. Sasaki. Photoluminescence color stability of green-emitting InP/ZnS core/shell quantum dots embedded in silica prepared via hydrophobic routes. RSC advances, 8(45), (2018), 25526-25533.

[40] D.A. Granada-Ramirez., J.S. Arias-Cerón., M.L. Gómez-Herrera., J.P. Luna-Arias., M. Pérez-González., S.A. Tomás., P. Rodríguez-Fragoso. and J.G. Mendoza-Alvarez. Effect of the indium myristate precursor concentration on the structural, optical, chemical surface, and electronic properties of InP quantum dots passivated with ZnS. Journal of Materials Science: Materials in Electronics, 30, (2019), 4885-4894.

[41] X. Wang., Y. Yang., Z. He., H. Wu. and Y. Cao. Influence of the acceptor crystallinity on the open circuit voltage in PTB7-Th: ITIC organic solar cells. Journal of Material Chemistry C, 7(47), (2019), 14861-14866.

[42] Q. Fan., W. Su., S. Chen., W. Kim., X. Chen., B. Lee., T. Liu., A.U. Mendez-Romero., R. Ma., T. Yang. and W. Zhuang. Mechanically robust all-polymer solar cells from narrow band gap acceptors with hetero-bridging atoms. Joule, 4(3), (2020), 658-672.

[43] P. Bindu. and S. Thomas. Estimation of lattice strain in ZnO nanoparticles: X-ray peak profile analysis. Journal of Theoretical and Applied Physics, 8(4), (2014), 123-134.

[44] N. Thakur. and K. Kumar. Effect of (Ag, Co) co-doping on the structural and antibacterial efficiency of CuO nanoparticles: A rapid microwave-assisted method. Journal of Environmental Chemical Engineering, 8(4), (2020), 104011.

[45] M. Rouhi., M. Babamoradi., Z. Hajizadeh., A. Maleki. and S. T. Maleki. Design and performance of polypyrrole/halloysite nanotubes/Fe3O4/Ag/Co nanocomposite for photocatalytic degradation of methylene blue under visible light irradiation. Optik, 212, (2020), 164721.

[46] D.A. Köse. and H. Necefoğlu. Synthesis and characterization of bis (nicotinamide) m-hydroxybenzoate complexes of Co (II), Ni (II), Cu (II), and Zn (II). Journal of Thermal Analysis and Calorimetry, 93, (2008), 509-514.

[47] B.S. Aziz., G. Hussein., M.A. Brza., J.S. Mohammed., T.R. Abdulwahid., S. Raza Saeed. and A. Hassanzadeh, A., 2019. Fabrication of interconnected plasmonic spherical silver nanoparticles with enhanced localized surface plasmon resonance (LSPR) peaks using quince leaf extract solution. Nanomaterials, 9(11), (2019),1557.

[48] M. S. Hamed., S. O. Oseni., A. Kumar., G. Sharma. and G. T. Mola. Nickel sulfide nano-composite assisted hole transport in thin film polymer solar cells. Solar Energy, 195, (2020), 310-317.

[49] M. S. Hamed., J. N. Ike. and G. T. Mola. Plasmonic nanoparticles mediated energy harvesting in thin-film organic solar cells. Journal of Physics D: Applied Physics, 55(1), (2021), 015102.

[50] M. W. Dlamini and G.T. Mola, 2019. Near-field enhanced performance of organic photovoltaic cells. Physica B: Condensed Matter, 552, (2019), 78-83.

[51] G. T. Mola., M. C. Mthethwa., M. S. Hamed., M. A. Adedeji., X. G. Mbuyise., A. Kumar., G. Sharma. and Y. Zang. Local surface plasmon resonance assisted energy harvesting in thin-film organic solar cells. Journal of Alloys and Compounds, 856, (2020),158172.

[52] J.N. Ike., M.A. Adedeji. and G.T. Mola. Silver-doped ZnS core-shell nanocomposites to promote photon harvesting in polymer cells. Physica B: Condensed Matter, 646, (2022), 414347.

CHAPTER 8

CONCLUSION AND FUTURE WORK

8.1 Conclusion

In this thesis, we were able to probe different routes of augmenting photo-absorption, exciton generation, and charge transport processes through the use of metal NPs in P3HT/PC61BM blends photoactive layers and charge transport layers, respectively. The main observation comprised of the use of BHJ, solvent additive, and synthesized metal NPs has a positive impact on the performance of TFOSCs. This could lead to more efficient and effective solar cell devices, which are vital for the advancement of renewable energy technologies. Metal NPs are basically used as a mechanism to assist in harvesting the photon energy due to the presence of LSPR effect. The inclusion of metal NPs can play a crucial role in improving optical absorption of the solar absorber layer and further create a conducive environment for exciton dissociation and charge transport processes, respectively. Based on experimental results, four different articles have been published in international journals with high impact factors. The articles were published with different respective NPs such as Ni/Zn, Ag/Ca, ZnS/Ag, and Ag/Co.

The effects of incorporating Ni/Zn bimetallic nanoparticles (BMNPs) into the P3HT/PC61BM blend BHJ solar absorber films at various concentrations is beneficial in enhancing the performance of the solar cells. The fabricated solar cells doped with Ni/Zn BMNPs showed remarkable improvement in device performance at the doping level of 1% and 3% compared to pristine solar cells. The recorded device parameters showed promising improvements in terms of PCE value, which reached up to 4.78%. The J_{sc} of 16.71 mA/cm^2, and a high FF of 50.0% were significantly attained at 1% concentration making the device more efficient due to the presence of LSPR effect to augment the absorption and charge transport processes. On the other hand, the synthesis of silver/calcium (Ag/Ca) BMNPs was successful, and these NPs were integrated into the active layer films of organic solar cells made from P3HT and PC61BM. This integration aimed to enhance energy harvesting and charge transport processes within the solar cells, potentially leading to improved overall performance and efficiency in the TFOSCs. The metal NPs were incorporated into the solar absorber layer at different concentrations by weight (1%, 3%, and 5%), which had a positive impact on the efficiency or other relevant parameters of the solar device. The best device performance was achieved from 3% doping level with high PCE of 4.13%, with J_{sc} of 13.7 mA/cm^2, V_{oc} of 0.57 V, and FF of 53.4%. This

achievement is attributed/assigned to augment optical absorption and charge transport processes by the occurrence of the LSPR effect and far-field scattering, which have assisted light trapping in the medium. However, excessive use of NPs in the solar cells can have a negative impact on their performance, as indicated by the lower PCE observed in devices with a 5% doping level. Moreover, ZnS/Ag metal NPs were strategically dispersed at 1%, 3%, and 5% by weight within the photoactive layer of TFOSCs. An observation revealed that the utilization of ZnS/Ag composites at different concentrations led to noteworthy improvements in device performance, surpassing that of the pristine counterparts. The achievable best results at doping level of 3% concentration by weight, which resulted in a solar cell with a high J_{sc} of 14.30 mA/cm^2, a high FF of 52.63%, and a PCE of 4.50%. These are promising results in the context of solar cell performance. The ZnS/Ag metal NPs can indeed be stable and suitable for various applications, including roll-to-roll printing device fabrication for solar cell production. Furthermore, the silver/cobalt (Ag/Co) BMNPs were effectively synthesized and dispersed into the PEDOT/PSS hole transport layer at various concentrations of 0.05%, 0.1%, and 0.15% by weight, which was beneficial in enhancing the performance of TFOSCs. Interestingly, the fabricated devices using Ag/Co doped in the HTL showed a desirable improvement compared to pristine PEDOT/PSS (undoped HTL) based solar cells. The optimum Ag/Co blending in PEDOT/PSS was found to be 0.1% by weight and produced the highest PCE value of 4.21% under an ambient laboratory environment. Such advancement is assigned to the presence of the LSPR effect at the interface between the solar absorber layer and HTL, which supports the charge transport and light-scattering processes in TFOSCs. Among Ni/Zn, Ag/Ca, ZnS/Ag, and Ag/Co metal NPs, the PCE value of 4.78% was observed at the doping level of 1% Ni/Zn concentration with higher J_{sc} of 16.71 mA/cm^2 compared to other metal NPs due to low series resistance (R_s). In comparison with Table 4,2 5.2, 6.3, and 7.3. The Table 6.3 seems to be in two orders of magnitude higher than that of pristine compared to other tables, which is clear evidence of the effect of ZnS/Ag metal NPs doped with active layer is favorable in increasing the charge transport processes and promoting charge dissociation in TFOSCs. Conclusively, the inclusion of metal NPs in TFOSC device structure plays significant role in improving the performances of polymers blend based solar cell. The metal NPs are environmentally stable and suitable to roll to roll device fabrication.

8.2 Future Work

The donor polymers and fullerene derivative-based acceptors have been classically employed as the absorption medium in thin-film organic solar cells (TFOSCs) with power conversion efficiencies (PCEs) up to 13% being reported in the literature [1]. However, these solar cells have weak absorption in the visible region and have limited possibilities for energy band gap tuning. Non-fullerene acceptors (NFAs), on the other hand, possess various advantages such as tunable energy levels and broader absorption range that covers as far as the near infra-red (NIR) regions and have consequently achieved PCEs up to 19% [1,2]. The collective effect of metal nanoparticles (NPs) results into enhanced optical absorption, thereby augmenting the overall performance of the devices. The use of metal NPs in the device structures of various solar cells has demonstrated remarkable results in the past few years [3.4]. However, the incorporation of metal NPs in the electron transport layer (ETL) of NFA-based organic solar cells (OSCs) have not been demonstrated to the best of my knowledge. I would conduct and report the successful incorporation of metal NPs into NFA-based TFOSCs for further investigation, as a potential research future work.

References

[1] G.T. Mola., A.Y. Ahmed., J.N. Ike., M. Liu., M.S. Hamed. and Y. Zhang. Engineering non-fullerene acceptors as a mechanism to control film morphology and energy loss in organic solar cells. Energy & Fuels, 36(9), (2022), 4691-4707.

[2] Y. Cui., Y. Xu., H. Yao., P. Bi., L. Hong., J. Zhang., Y. Zu., T. Zhang., J. Qin., J. Ren. and Z. Chen. Single-junction organic photovoltaic cell with 19% efficiency. Advanced Materials, 33(41), (2021), 2102420.

[3] Jude N. Ike, Jili Ncedo, Kumar Amit, Sharma Gaurav, Genene Tessema Mola. The impact of Ag/Co nanocomposite on organic charge transport medium for improved photocurrent in polymer solar cells. Journal of Polymer Science (2023).

[4] Mohammed S.G. Hamed, Jude N. Ike, Yilin Wang, Ke Zhou, Wei Ma. and Genene Tessema Mola. Reducing Energy Loss in Polymer Solar Cell through Optimization of Novel Metal Nanocomposite. Energy & Fuels, 37(8), (2023), 6129-6137.